AD_____

AWARD NUMBER: W81XWH-05-1-0115

TITLE: Angiogenesis Research to Improve Therapies for Vascular Leak Syndromes, Intra-Abdominal Adhesions, and Arterial Injuries

PRINCIPAL INVESTIGATOR: Donald Ingber, M.D., Ph.D.

CONTRACTING ORGANIZATION: Children's Hospital
Boston, MA 02115

REPORT DATE: April 2009

TYPE OF REPORT: Addendum to Final

PREPARED FOR: U.S. Army Medical Research and Materiel Command
Fort Detrick, Maryland 21702-5012

REPORT DOCUMENTATION PAGE

Form Approved
OMB No. 0704-0188

1. REPORT DATE	2. REPORT TYPE	3. DATES COVERED
1 April 2009	Addendum to Final	24 Mar 2008 – 23 Mar 2009

4. TITLE AND SUBTITLE

Angiogenesis Research to Improve Therapies for Vascular Leak Syndromes, Intra-Abdominal Adhesions, and Arterial Injuries

5a. CONTRACT NUMBER

5b. GRANT NUMBER
W81XWH-05-1-0115

5c. PROGRAM ELEMENT NUMBER

6. AUTHOR(S)

Donald Ingber, M.D., Ph.D.

E-Mail: donald.ingber@childrens.harvard.edu

5d. PROJECT NUMBER

5e. TASK NUMBER

5f. WORK UNIT NUMBER

7. PERFORMING ORGANIZATION NAME(S) AND ADDRESS(ES)

Children's Hospital
Boston, MA 02115

8. PERFORMING ORGANIZATION REPORT NUMBER

9. SPONSORING / MONITORING AGENCY NAME(S) AND ADDRESS(ES)
U.S. Army Medical Research and Materiel Command
Fort Detrick, Maryland 21702-5012

10. SPONSOR/MONITOR'S ACRONYM(S)

11. SPONSOR/MONITOR'S REPORT NUMBER(S)

12. DISTRIBUTION / AVAILABILITY STATEMENT
Approved for Public Release; Distribution Unlimited

13. SUPPLEMENTARY NOTES

14. ABSTRACT
The three goals of this project are: (i) to discover and develop novel drugs which could prevent or reverse the vascular leak syndrome; (ii) to develop angiogenesis inhibitors which would inhibit post-operative abdominal adhesions; and, (iii) to isolate endothelial progenitor cells from blood, capable of being expanded in vitro and applied to vascular grafts. Progress has been made in each category: we have made considerable progress in determining the efficacy of three anti-angiogenic agents in preventing vascular permeability in experimental model systems; we have developed a new blood cleansing platform that may have great value for treatment of infected patients with sepsis; we established that sunitinib prevents and reduces postoperative intra-abdominal adhesions in rabbits at a dose of 10 mg/kd/day; we determined that sunitinib reduces bowel anastomotic bursting pressure when used at the current dose and duration of treatment; we have shown that the human EPC/MPC system for building vascular networks is versatile in that it occurs in a variety of 3-dimensional environments, and that a transient influx of murine neutrophils 1-2 days after implantation of EPCs/MPCs/Matrigel is an important contributor to vasculogenesis.

15. SUBJECT TERMS
Lodamin; doxycycline; Caplostatin; vascular leak; sunitinib; adhesions; circulating endothelial cells; mesenchymal and endothelial progenitor cells; mesenchymal stem cells; tissue-engineering

16. SECURITY CLASSIFICATION OF:			17. LIMITATION OF ABSTRACT	18. NUMBER OF PAGES	19a. NAME OF RESPONSIBLE PERSON
a. REPORT	b. ABSTRACT	c. THIS PAGE			USAMRMC
U	U	U	UU	176	19b. TELEPHONE NUMBER *(include area code)*

Table of Contents

DOD Congressional Annual Report *(04/24/08 – 04/23/09)*

Project I: New Therapy for Vascular Leak Syndromes

Donald Ingber, M.D., Ph.D., *Principal Investigator*
Kwan-Hyuck Baek, Ph.D., *Research Fellow*
Ofra Benny-Ratsaby, *Research Fellow*
Ofer Fainaru, Ph.D., *Research Fellow*
Kashi Javaherian, Ph.D., *Research Associate*
Tong-Young Lee, Ph.D., Research Fellow
Sandra Ryeom, Ph.D., *Research Associate*
Chong Yung, Ph.D., *Research Fellow*
Alexander Zaslavsky, Ph.D., *Research Fellow*

I. ABSTRACT:

During combat, soldiers suffer from a number of different vascular leak syndromes after injuries, burns, or asphyxiation. These syndromes lead to progressive pulmonary edema, swelling of limbs or other edematous tissues. This proposal has been investigating the application of angiogenesis inhibitors as novel therapies to prevent or reverse vascular leak syndromes. Angiogenesis inhibitors function to block the increased permeability of capillary blood vessels, which is the underlying cause of vascular leak syndromes. Using mouse models of vascular permeability and *in vitro* assays, we have made continuous progress in understanding the role of both endogenous angiogenesis inhibitors and novel anti-angiogenic therapies in blocking and reversing vascular permeability. In addition, we have extended our research in new directions, including development of new therapies based on mimicry of microvascular structure and function for isolation of patient's circulating stem cells for treatment of military casualties caused by injury, as well as for clearance of pathogens in patients with sepsis.

II. INTRODUCTION:

This past year we have made considerable progress in determining the efficacy of three anti-angiogenic agents in preventing vascular permeability in experimental model systems. These therapies include the following: (i) a newly developed nanoparticle-based oral delivery system for TNP470 called Lodamin; (ii) the well-known antibiotic doxycycline; and (iii) a stabilized peptide fragment of the endogenous angiogenesis inhibitor endostatin. We also have begun to explore the mechanism of action of these therapies by investigating the role of the potent endogenous angiogenesis inhibitor thrombospondin-1 in mediating the effects of these anti-angiogenic therapies. The development of rapidly acting, non-toxic therapies for the treatment of vascular leak syndromes holds great significance for soldiers during combat for the immediate treatment of vascular leak syndromes sustained due to blast

injuries, burns or asphyxiation, among others. In addition, we have extended our work to develop methods to isolate circulating stem cells from a patient's blood to facilitate the vascular regeneration effort being pursued by Dr. Bischoff in Task 3 of this grant. In the course of these studies, we have developed a new blood cleansing platform that may have great value for treatment of infected patients with sepsis.

III. BODY:

As outlined in the Statement of Work, our research accomplishments this past year include the following:

Aim 1: To examine the mechanism by which a TNP470-conjugate inhibits vascular leakage. We proposed to examine the efficacy of Lodamin in preventing vascular permeability and determine whether the endogenous angiogenesis inhibitors thrombospondin-1 and/or endostatin are necessary for the anti-permeability properties of Lodamin.

This past year we have optimized the dosing of Lodamin *in vivo* for the treatment of a number of angiogenic-dependent diseases in mouse models. These diseases include tumor growth, a surgically-induced model of endometriosis, a laser-induced model of macular degeneration and the Miles permeability assay. Our studies demonstrate that Lodamin effectively suppresses tumor growth and decreases microvessel density, as well as inhibiting the expansion of endometriotic lesions. Further, Lodamin treatment of a laser-induced model of macular degeneration demonstrated a 65% inhibition in retinal permeability as assessed by Evans blue.

To confirm whether Lodamin may be an effective single agent therapy for the treatment of vascular leak syndrome, we utilized the Miles permeability assay with VEGF as an agonist to induce vascular permeability. Our studies demonstrated that after 5 days of oral Lodamin treatment, vascular permeability was inhibited by 57% as assessed by the Miles assay. These studies suggest that Lodamin could potentially be used as a single agent therapy for preventing vascular leak syndromes.

To determine whether the anti-vascular permeability actions of Lodamin are mediated by the endogenous angiogenesis inhibitors thrombospondin-1 (TSP-1) and/or endostatin, we utilized transgenic mice with targeted deletions of both *Tsp-1* and *Collagen XVIII* (the precursor to endostatin). In our preliminary studies, we used a surgically induced model of endometriosis, which has been shown to be an angiogenesis-dependent disease in both wild-type and *Tsp-1/endostatin* double null mice. The results of these studies indicate that treatment with Lodamin is equally effective in wild-type mice and mice lacking both TSP-1 and endostatin suggesting that the anti-angiogenic action of Lodamin is not dependent on either of these endogenous angiogenesis inhibitors.

Aim 2: To determine whether an endostatin peptide conjugated to the Fc domain of IgG, protects endothelial barrier function and inhibits vascular leakage.

We have investigated whether a stabilized peptide fragment derived from the endogenous angiogenesis inhibitor endostatin is effective in protecting against vascular leak. Stabilization of endostatin was achieved by conjugation to an Fc peptide, as previously described. Previous studies have demonstrated that full-length endostatin, consisting of 330 amino acids, is an effective inhibitor of vascular permeability. However, the generation of full-length recombinant endostatin for treatment would be cost prohibitive.

This past year, we analyzed the size of circulating endostatin detected in the blood to determine whether full-length endostatin was produced. We found that smaller fragments of endostatin, consisting of 187 and 250 amino acids, were circulating endogenously in the body under physiological conditions. To determine the efficacy of these smaller fragments of endostatin in suppressing vascular leak, it is first nessary to obtain large quantities of endostatin peptide to treat mice for 1 week before performing a Miles permeability assay to assess vascular permeability. This year we have cloned these smaller fragments of endostatin into a lentivirus expression system. This strategy has allowed us to produce milligram quantities of the 187 amino acid fragment of endostatin, which may be used for *in vivo* testing in the future in tumor growth and vascular permeability models.

<u>Aim 3:</u> To investigate the use of the antibiotic doxycycline to protect against vascular leak syndromes.

The tasks outlined for the completion of this Aim included the investigation of the well-characterized antibiotic doxycyline in the prevention of vascular permeability. Other studies proposed to compare the efficacy of doxycycline to Lodamin treatment in both *in vitro* and *in vivo* assays in suppressing vascular permeability. Our *in vitro* assays utilized an endothelial cell line and assessed permeability by the passage of the macromolecule FITC-dextran through the endothelial cell monolayer. Doxycycline treatment significantly inhibited permeability of FITC-dextran through human endothelial cells *in vitro.* Our *in vitro* studies further identified the upregulation of the adherens junction protein, VE-cadherin after doxycycline treatment of endothelial cells. VE-cadherin plays a critical role in maintaining the barrier function of epithelial and endothelail cells. These data suggest that one possible mechanism by which doxycycline may block vascular permeability is through the upregulation of adherens junction proteins.

Our *in vivo* studies utilized the Miles assay with VEGF as an agonist for induction of vascular permeability. These studies revealed that treatment with doxycycline inhibits the permeability of Evans blue, which is an indicator of vascular permeability. We have also investigated the effectiveness of combination therapy using both doxycycline and Lodamin. To test whether combining both anti-angiogenic agents potentiated their anti-angiogenic actions as compared to the use of either therapy alone, we tested the combination of doxycycline treatment and Lodamin in the suppression of tumor growth. Our data indicate that the combination of both treatments is more effective than either alone in suppressing tumor growth using a transplantable tumor model.

To determine whether the anti-angiogenic actions of doxycyline required the presence of the endogenous angiogenesis inhibitor TSP-1, we utilized *Tsp-1* null mice. We have previously demonstrated that doxycycline effectively suppresses tumor growth using a transplantable flank tumor model. This past year, we treated tumor-bearing wild type and *Tsp-1* null mice with either doxycycline or vehicle alone. Tumorigenesis was equally inhibited in both cohorts of mice treated with doxycycline indicating that the loss of TSP-1 did not affect the anti-angiogenic function of doxycycline.

New Aim 4: To develop new therapies based on mimicry of microvascular structure and function for tre atment of mi litary causalities that are caused b y trauma or infection.

New studies have been initiated in collaboration with Dr. Bischoff in Task 3 to help isolate circulating vascular stem cells, or 'endothelial precursor cells' (EPCs), from a patient's blood that might be used for blood vessel tissue engineering in the injured soldier. This same platform technology may be used to cleanse a septic patient's blood of infectious pathogens.

The initial objective of this aim was to develop a biomedical device that can continuously harvest large quantities of circulating stem cells (e.g. EPC and MPC) directly from the bloodstream of wounded patients for therapeutic tissue engineering purposes (as described in Task 3). Our concept was to adapt and improve a prototype blood cleansing device we previously developed in another short duration DoD (CIMIT)-funded project to remove pathogens for sepsis therapy (*1, 2*) for this stem cell harvesting application. As sepsis therapy is also critical for the medical care of the soldier, and our other CIMIT grant funding ended in early 2008, we decided to extend the aim of this Task to include development of new therapies for treatment of military casualties caused by infection as well as major trauma, and hence continued work on the blood cleansing device for sepsis applications as well as stem cell harvesting for tissue regeneration.

The prototype blood cleansing device was based on mimicry of microvascular structure and function, but these engineered devices utilize microfluidics and micromagnetic beads to selective bind and magnetically remove cells from flowing whole blood, rather than molecular opsonins in the microcapillary network of the spleen. In our past work, we showed that the microfluidic-micromagnetic blood cleansing device could remove 80% of living fungal cells from human whole blood flowing at 20 mL/hr (*2*). Magnetic opsonins were created by coating 1 μm microbeads with pathogen-specific antibodies. However, one drawback of this device was that ~13% of flowing blood was lost in the saline collection stream during the separation process. Over the past year, we developed a greatly improved device design inspired by the native architecture of the spleen that virtually eliminates blood loss while further enhancing separation efficiency (Fig 1). This Biomimetic Spleen has three microfluidic layers that replicate the microvasculature, sinusoids, and lymphoid follicles of the native organ. By controlling the back-pressure of saline fluid in the lymphoid-channels, this fluid only flows periodically and there is little opportunity to mix with flowing blood in the vascular

channels. The result is a simple and yet robust device that can clear 85-95% of living fungi from human whole blood flowing at similar flow rates (5 to 20 mL/hr) with virtually no blood loss or dilution. Once we confirmed the functionality of this novel platform technology, we began to adapt it for selective collection of circulating stem cells from flowing whole blood. In initial proof-of-principles trials, the biomimetic spleen demonstrated an ability to selective separate and retain circulating EPC tagged with 2.7-μm beads (conjugated with anti-CD31 antibodies) in its sinusoid- and lymphoid-channels (Fig 2). Additional studies are underway to explore the potential utility for both medical applications (sepsis and stem cell harvesting for vascular tissue regeneration).

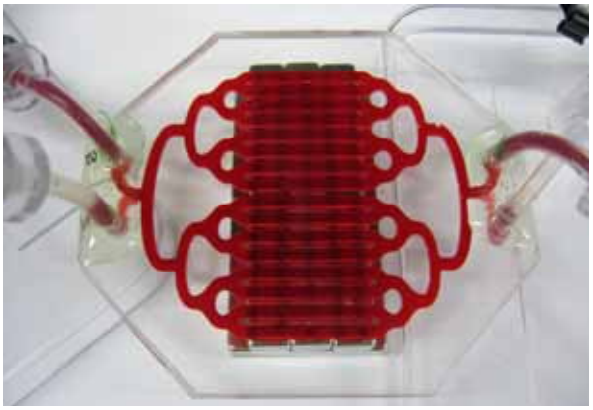

Fig 1. (Top View) Multiplexed Biomimetic Spleen borrows the architecture of the native organ (i.e. microvasculature, sinusoids, and lymphoid follicle) to improve pathogen clearance (85% at 20 mL/hr or 95% at 5 mL/hr) while virtually eliminating blood loss and dilution.

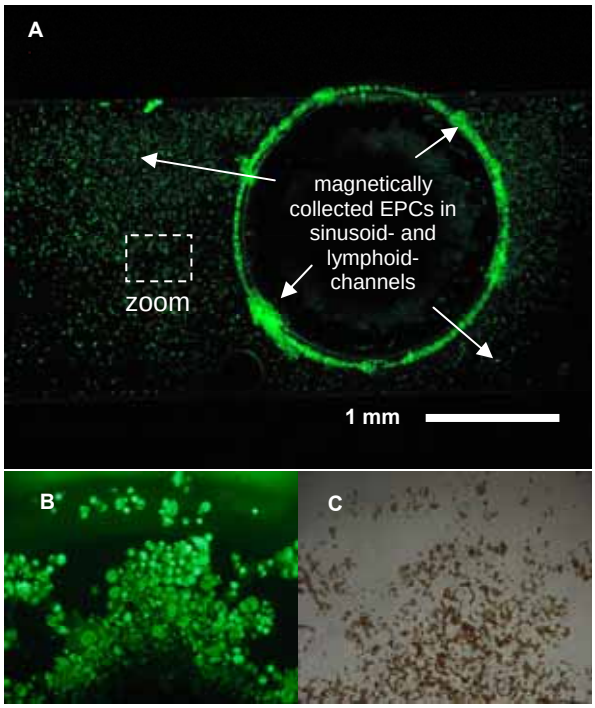

Fig 2. (A) EPC cells (green fluorescent) tagged with 2.7-μm beads coated with anti-CD31 antibodies (brown dots) were selectively separated from flowing human whole blood and retained in the sinusoid- and lymphoid-channels of the biomimetic spleen. **(B)** Zoomed in view of fluorescent EPC cells. **(C)** EPC and beads in brightfield.

IV. KEY RESEARCH ACCOMPLISHMENTS:

Bulleted list of key research accomplishments emanating from this research:

- optimized the anti-tumor dosing and treatment schedule for two of the anti-angiogenic inhibitors utilized in this study: Lodamin and an Fc-conjugated endostatin fragment.
- investigated the efficacy of Lodamin (a nanoparticle-based oral delivery system for TNP470) for use as a single agent in protection against VEGF-induced vascular permeability

- identified the size of circulating endogenous endostatin in human blood and generated Fc-conjugated peptides of 3 different fragments of endostatin.
- cloned truncated forms of endostatin consisting of 187 and 250 amino acids (full length endostatin consists of 330 amino acids) into a lentivirus expression vector.
- generated milligram quantities of the 187 amino acid fragment of endostatin. This fragment is referred to as the NC1 fragment of collagen XVIII.
- confirmed the anti-permeability properties of doxycycline *in vitro.* We assessed the permeability of the macromolecule FITC-dextran through human endothelial cell monolayers after treatment with doxycycline.
- demonstrated the doxcycline-dependent upregulation of the adherens junction protein VE-cadherin, which plays a critical role in maintaining the barrier function of endothelial cell monolayers. Our studies show that doxycycline increases VE-cadherin expression in endothelial cells but decreases levels of phosphorylated VE-cadherin.
- compared the anti-angiogenic efficacy of combination therapy with two of the anti-angiogenic inhibitors utilized in this proposal: Lodamin (a nanoparticle-based oral delivery system for TNP470) and doxycycline using a transplantable tumor model in mice.
- examined the expression of the anti-angiogenic protein thrombospondin-1 (TSP-1) in circulating platelets harvested from wild-type mice after 5 days of treatment with doxycycline.
- developed a Microfluidic-Micromagnetic Cell Separator Device that successfully removed 80% of all fungal cells from flowing whole human blood (20 mL/hr, 10 mL)
- developed prototype biomimetic spleen device that has even higher separation efficiency with minimal blood loss (85% at 20 mL/hr or 95% at 5 mL/hr)
- tested proof-of-concept in magnetically separating EPCs from flowing human whole blood in biomimetic spleen device.

V. REPORTABLE OUTCOMES:

Manuscripts:

1. Lee TL, Sjin RMT, Movahedi S, Ahmed B, Pravda EA, Lo KM, Gillies SD, Folkman J and Javaherian K. (2008) Linking antibody Fc domain to endostatin significantly improves endostatin half-life and efficacy**.** Clin Cancer Res. 2008 Mar 1;14(5):1487-93.
2. Fainaru O, Hornstein MD, Folkman J. Doxycycline inhibits vascular leakage and prevents ovarian hyperstimulation syndrome in a murine model. Fertil Steril. 2008 Oct 18.

3. Fainaru O, Adini I, Benny O, Bazinet L, Pravda E, D'Amato R, Folkman J. Doxycycline induces membrane expression of VE-cadherin on endothelial cells and prevents vascular hyperpermeability. FASEB J. 2008 Oct;22(10):3728-35.
4. Benny O, Fainaru O, Adini A, Cassiola F, Bazinet L, Adini I, Pravda E, Nahmias Y, Koirala S, Corfas G, D'Amato RJ, Folkman J. An orally delivered small-molecule formulation with antiangiogenic and anticancer activity. Nat Biotechnol. 2008 Jul;26(7):799-807.
5. Tong-Young Lee, Stefan Muschal, Elke A. Pravda, Judah Folkman, Amir Abdollahi, and Kashi Javaherian. Angiostatin regulates the expression of antiangiogenic and pro-apoptotic pathways via targeted inhibition of mitochondrial proteins. Blood 2009. *In press.*

Patents:

1. Yung CW, Ingber DE (Inventors), Biomimetic Spleen for Filtration of Blood and Other Flowing Fluids. (pending, 2008)

Honors:

- Publication featured on cover and cited as “Hot Article” in May issue of Lab On A Chip
- Research reviewed in Chemical Technology, Feb 25, 2009
- Research reviewed in MIT Technology Review, May 23, 2008
- Received Surgical Research Council - Translational Research Award (2008, Yung)
- Received Dr. M. Judah Folkman Research Day Award (2008, Yung)

Invited Presentations:

O. Benny:

Nanotechnology strategy for suppressing angiogenic cancer metastases. The Angiogenesis Foundation Presents the 6th Annual International Symposium. The Judah Folkman Conference. Cambridge MA U.S.A.

Lodamin- an oral formulation for the antiangoigenic drug TNP-470. 35th Annual Meeting & Exposition of the Controlled Release Society. New York

An Antiangiogenic Nanotechnology strategy for suppressing cancer and metastases. M. Judah Folkman Children's Hospital Research Day, Children’s Hospital Boston

O. Fainaru:

Poster presentation - Doxycycline inhibits vascular leakage and prevents the development of pulmonary edema. 26th Army Science Conference. December 2008, Orlando, FL, USA.

Oral Presentation - Doxycycline Inhibits Vascular Leakage and Prevents Ovarian Hyperstimulation Syndrome (OHSS) in a Murine Model. American Society of Reproductive Medicine. 2007 annual meeting, Washington DC, USA.

D. Ingber:

Biodesign Principles to Bioinspired Nanotechnologies, School of Biomedical Engineering Lecture Series, Purdue University

Biological Design Principles for the Nanotechnologist, INBT Symposium, Johns Hopkins University

Biomimetic Microsystems for Sepsis Therapy and other Bioinspired Medical Devices, NICHD Workshop on Safe and Effective Devices for use in the NICU, NICHD, Bethesda, MD

From Biological Design Principles to Bioinspired Nanotechnologies, Center for Cancer Nanotechnology Excellence Seminar Series*,* Stanford University Bio X Program

From Biodesign Principles to Biologically Inspired Engineering, Dept of Biomedical Engineering Seminar Series, University of Caifornia, Berkeley

From Biological Design Principles to Bioinspired Nanotechnologies, California Nanosystems Institute Seminar Series, UCLA

T.Y. Lee:

Efficacy of Fc-angiostatin and Fc-endostatin in vascular permeability. Children's Hospital Boston, Harvard Medical School.

C.W. Yung:

Biomimetic Spleen for Sepsis Therapy, MA Life Sciences Innovation Day 2009, Boston

VI. CONCLUSIONS:

These studies confirm the potential therapeutic importance of angiogenesis modulators and devices that mimic microvascular structure and function for treatment of injured soldiers. The finding that FDA-approved angiogenesis inhibitors a potent suppressors of vascular permeability offers a new approach to prevent or reverse vascular leak syndrome in patients following trauma, and the new blood cleansing platform may be of great utility in patients with systemic infections and sepsis when combined with conventional antibiotic therapy.

"SO WHAT SECTION"

The finding that these non-toxic anti-angiogenic drugs prevent increases in vascular permeability induced by various stimuli raise the possibility that they might be used to prevent vascular leak syndromes or reverse complications in injured solders.

The use of orally available anti-angiogenic therapies such as Lodamin and doxycycline, raises the possibility that these drugs might be carried by soldiers and administered just prior to entering into combat to prevent potential pulmonary complications, or be self-administered immediately after injury. The fact that doxycycline is a commercial drug that already FDA-approved warrants further exploration of this compound for treatment of vascular leak syndromes in the clinic. The biomimetic artificial spleen approach described here may be used to create a new type of portable, extracorporeal blood cleansing device that could be used to filter the entire blood volume of an injured patient to selective collect stem cells for regenerative medical applications, or to remove pathogens and toxins and thereby, save the lives of septic patients in the field, as well as in a hospital setting.

VII. REFERENCES:

1. Yung CW, Fiering J, Mueller AJ, Ingber DE. Micromagnetic-microfluidic blood cleansing device. Lab Chip 2009;9(9):1171-7.
2. Yung CW, and Ingber DE; Septic Solution. Medical Device Developments, Oct 1, 2008.

Project II: The Prevention of Post-operative and Traumatic Abdominal Adhesions

Mark Puder, M.D. Ph.D., *Primary Investigator*
Hau Le, M.D., *Research Fellow*
Jonathan Meisel, M.D., *Research Fellow*

I. ABSTRACT:

Objective: To investigate the effect of sunitinib, an angiogenesis inhibitor, on the prevention and reduction of intra-abdominal adhesion.

Background: Postoperative intra-abdominal adhesions are a major cause of morbidity and mortality in surgical patients. They are the number one cause of bowel obstruction and infertility, and a major source of excess surgical costs and hospitalizations. Adhesion formation has been shown to be angiogenesis dependent. We previously demonstrated the inhibitory effect of sunitinib, a vascular endothelial growth factor receptor antagonist, on postoperative adhesion formation in murine model. We therefore hypothesized that sunitinib may prevent or reduce postoperative adhesions in a leporine, large animal model.

Methods: Twenty New Zealand white rabbits underwent a standard uterine adhesion procedure. One day prior to surgery, the rabbits were randomized to daily treatment with sunitinib (10 mg/kg) or saline control for ten days. On postoperative day ten, the rabbits were sacrificed and their adhesions scored. To assess the effect of sunitinib on wound healing, an additional sixteen rabbits underwent a large bowel transection with immediate re-anastamosis. These rabbits were sacrificed on postoperative day 10, and bowel bursting strength was measured.

Results: Thirty-eight percent of the sunitinib treated rabbits were completely adhesion free. The sunitinib treated rabbits had a median tenacity score of 1.0 [inter-quartile range (IQR) 0-1.75], compared to 3.25 (IQR 3-3.5) in the control animals (P=0.004). Median percent involvement score for the sunitinib treated rabbits vs. controls was 1.0 (IQR 0-1.0) and 4.0 (IQR 4.0-4.0), respectively (P=0.003). Collectively, the sunitinib treated rabbits had a median total adhesion score of 2 (IQR 0-2.75) compared to 7 (IQR 6-7.5) in the control group (P=0.003). Bowel bursting strength appeared to be weaker in the sunitinib treated rabbits. Final results are still pending.

Conclusion: Sunitinib significantly reduces postoperative adhesions in a leporine model. Anti-angiogenic therapy may improve adhesion related morbidity and mortality after general and gynecological surgery.

II. INTRODUCTION:

Postoperative intra-abdominal adhesions are a major health problem causing high morbidity in the general surgery and trauma patient populations. Adhesions cost the U.S. hundreds of millions of dollars annually. Several approaches have been attempted to inhibit intra-abdominal adhesion formation, most with limited success [1, 2]. Most recently, our attention has been turned towards a recently FDA approved class of drugs called tyrosine kinase inhibitors that have both anti-angiogenic and anti-tumor properties. In clinical practice, this class of drugs is approved for use in advanced stages of renal cell carcinoma and gastrointestinal stromal tumors. Sunitinib (sunitinib malate or SU11248; Pfizer Inc.) is a tyrosine kinase inhibitor that also inhibits vascular endothelial growth factor receptors 1 and 2 (VEGFR). VEGFR's are angiogenesis mediators involved in adhesion formation. We proposed that the inhibition of VEGFR will prevent or reduce surgical adhesions, as VEGF, among other factors, is up-regulated in adhesion formation.

III. BODY:

Our previous work with sunitinib has shown promising results in preventing postoperative adhesions in a murine model [3]. In this study, the rabbit uterine horn abdominal adhesion model was utilized as described. A lower midline abdominal incision is made and the uterine horns brought out through the incision. Using a number 10 scalpel, the uterus and fallopian tubes are abraded until punctuate hemorrhages appear. A small collateral blood vessel in the mesosalpinx is occluded with a 5-0 silk tie. The uterus is then returned to normal anatomic position and the peritoneum and skin are closed.

First, a pilot study was performed to determine a non-toxic dose of sunitinib in the rabbits. Results showed that 10 mg/kg/day was safe and efficacious at preventing adhesions and was well tolerated. We then moved on to our full experiment.

Twenty rabbits were randomly assigned to receive either sunitinib (10mg/kg/day) once a day, or a placebo. The medication was mixed with water and given by orogastric gavage. The control rabbits were gavaged with water only. All rabbits received the first dose 24 hours prior to surgery and continued daily for 10 days postoperatively. The rabbits were sacrificed on postoperative day 10 and the adhesions were blindly scored by 2 individual scorers based on a well accepted scoring system: tenacity to the uterine horns (none = 0, fell apart = 1, lysed with traction = 2, lysed with blunt dissection = 3, lysed with sharp dissection = 4) and percent covered (0 = 0, <25% = 1, 25-50% = 2, 50-75% = 3, >75% = 4) [4].

Nine out of the ten control rabbits developed adhesions. Two of the sunitinib treated rabbits died during the gavaging process due to an injury to the mediastinum. However, three of the remaining 8 sunitinib treated rabbits (38%) were completely adhesion free.

Figure 1 shows a representative image of a control uterus and a uterus treated with sunitinib at the time of sacrifice. Four out of ten control rabbits had other organs involved in the uterine adhesions. In two rabbits, the uterus was strongly adhered to the colon, while two others were adhered to loops of small intestine. The uterus was adhered to the incision in the peritoneum in three additional rabbits as well. In sharp contrast, none of the sunitinib treated rabbits had any extra-uterine involvement of adhesions.

The control animal adhesions had a median tenacity score of 3.25 (IQR 3.0-3.5), while the adhesions from the sunitinib treated animals had a median tenacity score of 1.0 (IQR 0-1.75; *P* = 0.004). When determining the extent of the uterus involved in adhesions, the control rabbits had a median score of 4.0 (IQR 4.0-4.0), while the sunitinib treated rabbits had a median score of 1.0 (IQR 0-1.0; *P* = 0.003). Collectively, the control rabbits had a median total adhesion score of 7.0 (IQR 6.0-7.5), while the sunitinib treated rabbits had a median score of 2.0 (IQR 0-2.75) (*P* = 0.003; **Table 1**).

Figure 1: Appearance of a control (left) and sunitinib treated (right) uterus at necropsy. Control uterus is adhered to itself and to the bladder, while the sunitinib treated uterus is adhesion free.

Table 1: Adhesion scores of control versus sunitinib treated rabbits at sacrifice.

	Saline Control (*n*=10)	Sunitinib (*n*=8)	*P*-value
Tenacity to uterus	3.25 (3.0 – 3.5)	1.0 (0-1.75)	0.004
Extent of uterus covered	4.0 (4.0 – 4.0)	1.0 (0-1.0)	0.003
Total score	7.0 (6.0 – 7.5)	2.0 (0.2.75)	0.003
Adhesion free rabbits (*n*)	1	3	

Results expressed as medians with inter-quartile range (IQR)

To determine adequacy of wound healing, we tested bowel anastomotic bursting strength. Sixteen additional rabbits underwent a laparotomy and complete transection of the large bowel approximately 15 cm distal to the ileocecal valve. The animals then underwent an end-to-end re-anastomosis using a single layer of interrupted 4-0 PDS sutures. One day prior to surgery, the rabbits were randomly assigned to be treated daily with sunitinib at a dose of 10 mg/kg (suspended in 10 ml of normal saline) or saline control via orogastric gavage. At the time of sacrifice the anastomoses were inspected. There was no evidence of disruption or leak. Clinically, all the rabbits did well. When the rabbits were sacrificed at POD 10, the anastomoses were tested to determine their bursting pressure using a previously described method [5]. Briefly, a 12 cm segment of colon with the suture line in the middle, was removed from the rabbit and gently irrigated with water to remove any remaining feces. A bowel clamp was used to occlude one end, while the other end of the bowel was cannulated with an infusion tube. A pressure transducer was inserted distal to the anastomosis and attached to a monitor. Water was then slowly infused into the bowel and the pressure at which the bowel burst was recorded. The last six rabbits are currently undergoing experimentation and the results will be final in the next 2 weeks. Preliminary results point to a weakening of the bowel bursting strength when treated with sunitinib.

IV. KEY RESEARCH ACCOMPLISHMENTS:

- Established that sunitinib prevents and reduces postoperative intra-abdominal adhesions in rabbits at a dose of 10 mg/kd/day.

- Determined that sunitinib reduces bowel anastomotic bursting pressure when used at the current dose and duration of treatment.

V. REPORTABLE OUTCOMES:

Manuscript:

Meisel, J., Le, H., De Meijer, V.E., Puder, M. *Sunitinib Inhibits Postoperative Adhesions in a Large Animal Model.* – Manuscript submitted to Annals of Surgery, May 2009.

Abstracts/Presentations:

Meisel, J., Le, H., de Meijer, V.E., Puder, M. *Inhibition of Intra-abdominal Adhesion Formation in a Rabbit Model with the Angiogenesis Inhibitor Sunitinib*. American Pediatric Surgical Association – 40th Annual Meeting, Fajardo, Puerto Rico – Oral/Poster Presentation, May 2009.

Meisel, J., Le, H., de Meijer, V.E., Puder, M. *Inhibition of Intra-abdominal Adhesion Formation in a Rabbit Model with the Angiogenesis Inhibitor Sunitinib*. Massachusetts Chapter of the American College of Surgeons 55th Annual Meeting, Boston, MA – Poster Presentation, December 2008.

Dr. M. Judah Folkman Research Day, Invited speaker: *Short and Long-term Inhibition of Intra-abdominal Adhesion Formation with the Angiogenesis Inhibitor Sunitinib*. Grand Rounds, Children's Hospital, Boston. May 21, 2008. – Awarded one of top four oral presentations.

VI. CONCLUSIONS:

Sunitinib significantly reduces postoperative adhesions in a leporine model. Anti-angiogenic therapy may be able to improve adhesion related morbidity and mortality after general and gynecological surgery. However, caution may be needed when bowel resection is indicated.

Future work will be directed towards determining the optimal dose and duration of use in order to minimize any potential harmful side effects of antiangiogenic therapy.

"SO WHAT SECTION"

Adhesions are the major cause of intestinal obstruction, which can lead to prolonged hospital stays and often additional abdominal operations, which perpetuates the problem itself. Adhesions also increase the morbidity and mortality of each subsequent operation because they lead to increased blood loss and injury to internal organs. In the United States, the total cost from complications from adhesions is over $1 billion a year, and accounts for over 846,000 inpatient care days [6]. The prevention of adhesions would profoundly decrease the morbidity and reduce health care costs across a broad range of medical disciplines [7].

VII. REFERENCES:

1. Montz FJ, Holschneider CH, Bozuk M, Gotlieb WH, Martinez-Maza O (1994) Interleukin 10: ability to minimize postoperative intraperitoneal adhesion formation in a murine model. Fertil Steril 61: 1136-1140.

2. Rodgers KE, Johns DB, Girgis W, Campeau J, diZerega GS (1997) Reduction of adhesion formation with hyaluronic acid after peritoneal surgery in rabbits. Fertil Steril 67: 553-558.

3. Kim S, Lee S, Greene AK, Arsenault DA, Le H, Meisel J, Novak K, Flynn E, Heymach JV, Puder M (2008) Inhibition of intra-abdominal adhesion formation with the angiogenesis inhibitor sunitinib. J Surg Res 149(1):115-9.

4. Rodgers K, Girgis W, diZerega GS, Johns DB. Intraperitoneal tolmetin prevents postsurgical adhesion formation in rabbits. Int J Fertil 1990; 35(1):40-5.

5. de Hingh IH, de Man BM, Lomme RM, et al. Colonic anastomotic strength and matrix metalloproteinase activity in an experimental model of bacterial peritonitis (2003) Br J Surg; 90(8):981-8.

6. Ray NF, Denton WG, Thamer M, Henderson SC, Perry S (1998) Abdominal adhesiolysis: inpatient care and expenditures in the United States in 1994. J Am Coll Surg 196: 1-9.

7. Menzies D, Parker M, Hoare R, Knight A (2001) Small bowel obstruction due to postoperative adhesions: treatment patterns and associated costs in 110 hospital admissions. Ann R Coll Surg Engl 83: 40-46.

Project III: Creating New Blood Vessels using Blood-derived Endothelial and Mesenchymal Progenitor Cells

Joyce Bischoff, Ph.D., *Principal Investigator*
Elisa Boscolo, Ph.D., *Research Fellow*
Juan Martin-Melero, Ph.D., *Research Fellow*

I. ABSTRACT:

Tissue-engineering of blood vessels holds promise as a new approach to revascularize tissues and organs that have been damaged or impaired by disease. We postulated that human EPCs and MPCs could be isolated from blood or bone marrow, expanded ex vivo and used to build new vascular networks in vivo. With this funding from the DOD, we have shown that human EPCs isolated from either umbilical cord blood or from adult peripheral blood, combined with human MPCs, isolated from either umbilical cord blood or adult bone marrow, form functional blood vessel networks, de novo, within 7 days after implantation into immune-deficient mice(1, 2). This demonstration of robust vasculogenesis using normal human cells has brought us one step closer to our goal of building blood vessel networks from human progenitor cells obtained without sacrifice of healthy tissues, veins or arteries.

Our specific goals for the past year have been to devise strategies to accelerate the de novo formation of vascular networks in our model system so that this approach(s) could be used to quickly revascularize ischemic tissue, preferably within a matter of 24-48 hours. To pursue this goal, we conducted a detailed analysis of the cellular events beginning one day after the EPCs and MPCs are implanted into immune-deficient mice. (In previous work, our standard time point for analyses was 7 days.) The time course experiment revealed a striking influx of murine neutrophils into the cell/Matrigel implant at days 1 and 2 followed by an apparent efflux beginning at day 4 and continuing to day 7. This observation raised the question of whether the neutrophil influx was a critical parameter for vasculogenesis in this model. We tested this by depleting murine neutrophils with an antibody known as anti-Gr-1, and found a statistically significant decrease in microvascular density. This result shows that the neutrophil influx contributes significantly to the vascular network formation in this model.

II. INTRODUCTION:

Our goal is to build vascular networks from human endothelial progenitor cells (EPCs) and mesenchymal progenitor cells (MPCs) to re-vascularize damaged tissues and organs. We and others have shown that human EPCs and MPCs can be obtained from blood or bone marrow and expanded in the laboratory without difficulty. Our published work demonstrates the vasculogenic capability of these cells in vivo using a Matrigel model and immunodeficient mice. In the future, we envision use of a soldier's own EPCs and MPCs for a variety of tissue-engineering (TE) applications and for in situ

regeneration of vascular networks in ischemic tissue. For TE, vascular networks created from EPCs/MPCs would be incorporated into TE constructs in vitro such that upon implantation in vivo, anastomoses with the host circulation would occur rapidly to establish blood flow. For tissue regeneration in situ, EPCs/MPCs would be delivered to the site in vivo where they would undergo vasculogenesis, as we have demonstrated can occur in vivo in our Matrigel-based model system. Our overall hypothesis is that EPCs and MPCs applied to either a TE organ or in situ to ischemic tissue will establish an adequate blood supply and thereby promote resident cells to undergo appropriate tissue development and regeneration. The beneficiary population would be patients/soldiers with injuries that require new tissue formation or regeneration. Soldiers are well-suited to this proposed strategy because it should be straightforward to isolate EPCs and MPCs from their peripheral blood or bone marrow because of overall good health and relatively young age. In summary, advancing this research could lead to strategies for creating tissue-engineered blood vessels as needed for damaged organs and tissues suffered by injured soldiers.

III. BODY:

Objective 1: To determine key parameters to accelerate the vasculogenic process to a time frame of 24-48 hours using the in vivo model we have established with human EPCs and MPCs.

We performed a time course experiment in which cbEPCs and bmMPCs were implanted in nude mice, as described in our model, and explanted at Day 1, 2, 3, 4, 5, 6, 7 and 14. The degree of vascularization at each of these time points can be seen in Figure 1A, which shows macroscopic views of representative Matrigel explants from each time point. The onset of vascularization can be seen as early as Day 3 after implantation. The microvessell density (microvessels defined as lumens containing red blood cells) at each time point is shown in Figure 1B. Histology of sections from each Matrigel explant revealed an influx of neutrophils, and possibly other polymorphonuclear leukocytes at Day 1, 2 and 3 that appeared to subside beginning at Day 4. Sections were immunostained with anti-CD11b, a marker for macrophages and granulocytes (granulocytes include neutrophils, basophils and eosinophils). Figure 1C shows the dramatic influx of CD11b+ cells at Day 2 that is largely absent at Day 7. Three different magnifications are shown to provide low, medium and high power views.

In experiments not shown, we tested whether or not the CD11b cellular influx could be attributed to the 1) matrigel alone, 2) either EPCs alone or MPCs alone, 3) mouse strain or 4) human cells. None of these parameters appear to be mediating the neutrophil influx. Instead, it appears that the combination of the two cell types that engage in vasculogenesis induces the neutrophil influx.

To test the functional significance of this influx on ability of human EPCs and MPCs to form vascular networks, we performed two experiments. The first was to add human leukocytes to the cbEPCs/bmMPC/Matrigel implant and measure effect of vasculogenesis. This did not augment or inhibit the degree of vascularization (data not shown). The second experiment was to deplete the granulocyte/monocyte population in

the mice using an anti-Gr-1 antibody, which has been used by many laboratories to deplete murine granulocytes from mice for a specified window of time(3, 4). Figure 1D shows that intraperitoneal injection of anti-Gr-1 at Day -2, Day 0 and Day 2 caused a dramatic depletion of Gr-1-positive granulocytes in the murine blood at Day 0, Day 2. By Day 7, Gr-1 positive cells were returning to normal levels. I. p. injection of an isotype-matched control IgG had no effect. (Note: in panels D, E and F, open bars are controls treated with isotype-matched control IgG, black bars are mice treated with anti-Gr-1 (200ug/injection). Panel E shows results of differential white blood cell analysis of neutrophils, lymphocytes and monocytes at Day 2 and Day 7 to verify neutrophil depletion. (n=5 for each group). Matrigel implants were removed on Day 7 for histology and quantification of vessel density. The neutrophil depletion caused a 48% decrease in microvessel density, showing that the neutrophils play a positive role in vasculogenesis in this model.

In summary, this is an important result as it demonstrates an unforeseen role of granulocytes/monocytes in this model system. However, a critical role for CD11b+/Gr-1+ cells in tumor angiogenesis has emerged based on reports from several laboratories(5-7). Our results points towards a strategy for potentially enhancing and accelerating vasculogenesis. We are currently preparing a manuscript to report our findings on these early events in vasculogenesis in this model.

Figure 1 - Early events in vessel formation from human EPCs and MPCs - participation of murine neutrophils

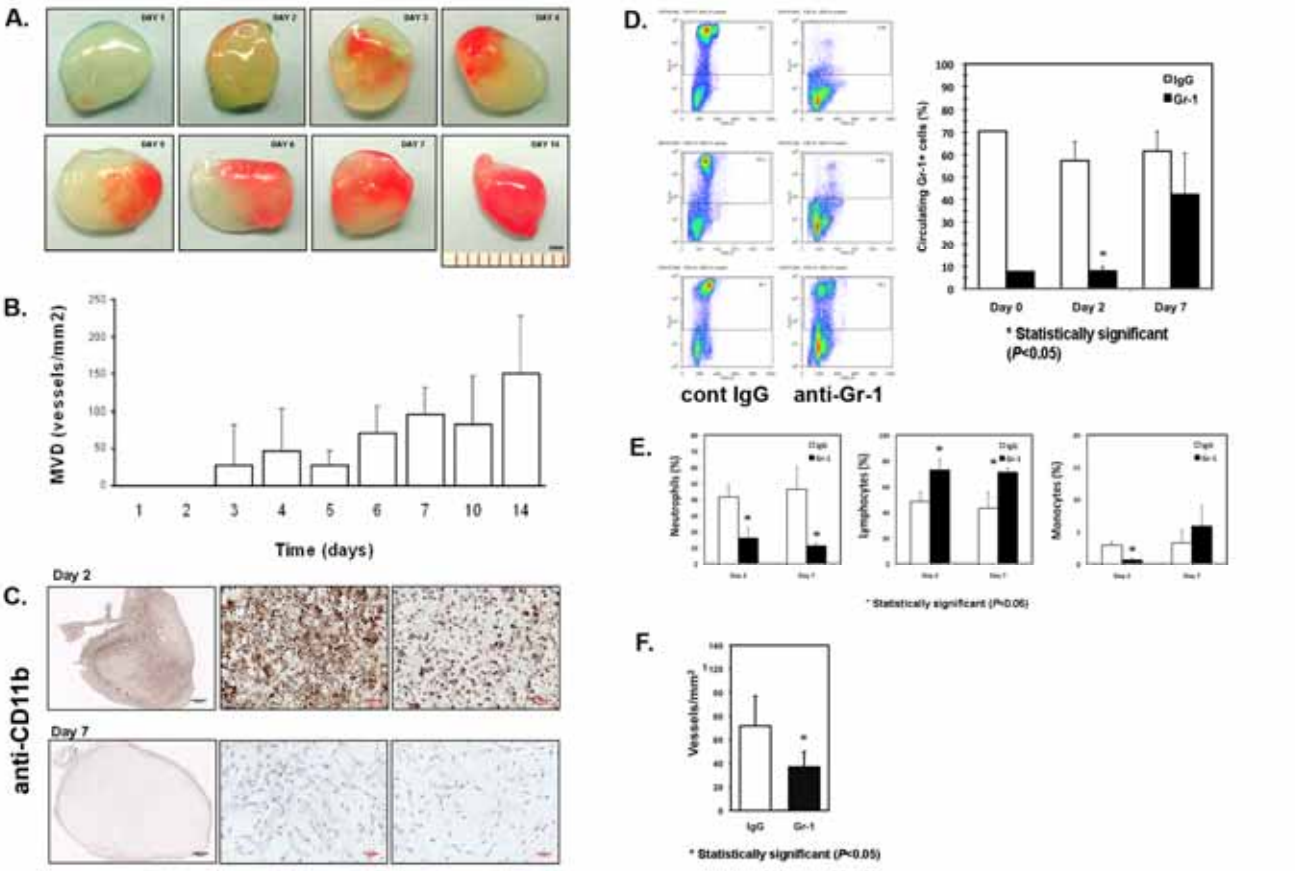

Objective 2: To test vasculogenic activity of human EPCs and MPCs in a variety of different matrices to determine how widely adaptable this two-cell system will be to different tissues/organs wherein functional blood vessels are needed.

This objective has been tested by substituting three different types of extracellular matrix (ECM) for Matrigel in our in vivo model. We tested type I collagen, commercially available from rat tail tendons, human fibrin produced by thrombin-induced cleavage of fibrinogen, and a peptide hydrogel known as PuraMatrix (available from BD Biosciences). PuraMatrix self assembles into a 3-d hydrogel with fibrous structure when exposed to physiological salt concentrations. The results are summarized in Figure 2 (see next page). The top panels show H&E stained sections from each each type of ECM. Red blood cell-filled vessels are evident in each; quantification of red blood cell-filled vessels (microvessel density) is shown in the bar graph below. The middle panels show sections stained with anti-human CD31 antibody. The bottom panels show confocal fluorescence of sections double-labeled with anti-CD31 (red) and anti-alpha smooth muscle actin (SMA) (green). Red stained human endothelial cells line the lumens of the vessels; green-stained alpha-SMA perivascular cells surround the CD31+ vessels. Microvessel density achieved with 7 mg/ml type I collagen and 2.5 mg/ml PuraMatrix was lower than microvessel density achieved by the control – Matrigel. All other concentrations of type I collagen, PuraMatrix and Fibrin were similar to Matrigel, demonstrating that human EPCs and MPCs can form vessels in a variety of ECM environments.

Figure 2 - Human EPCs and MPCs form vessels in a variety of matrices.

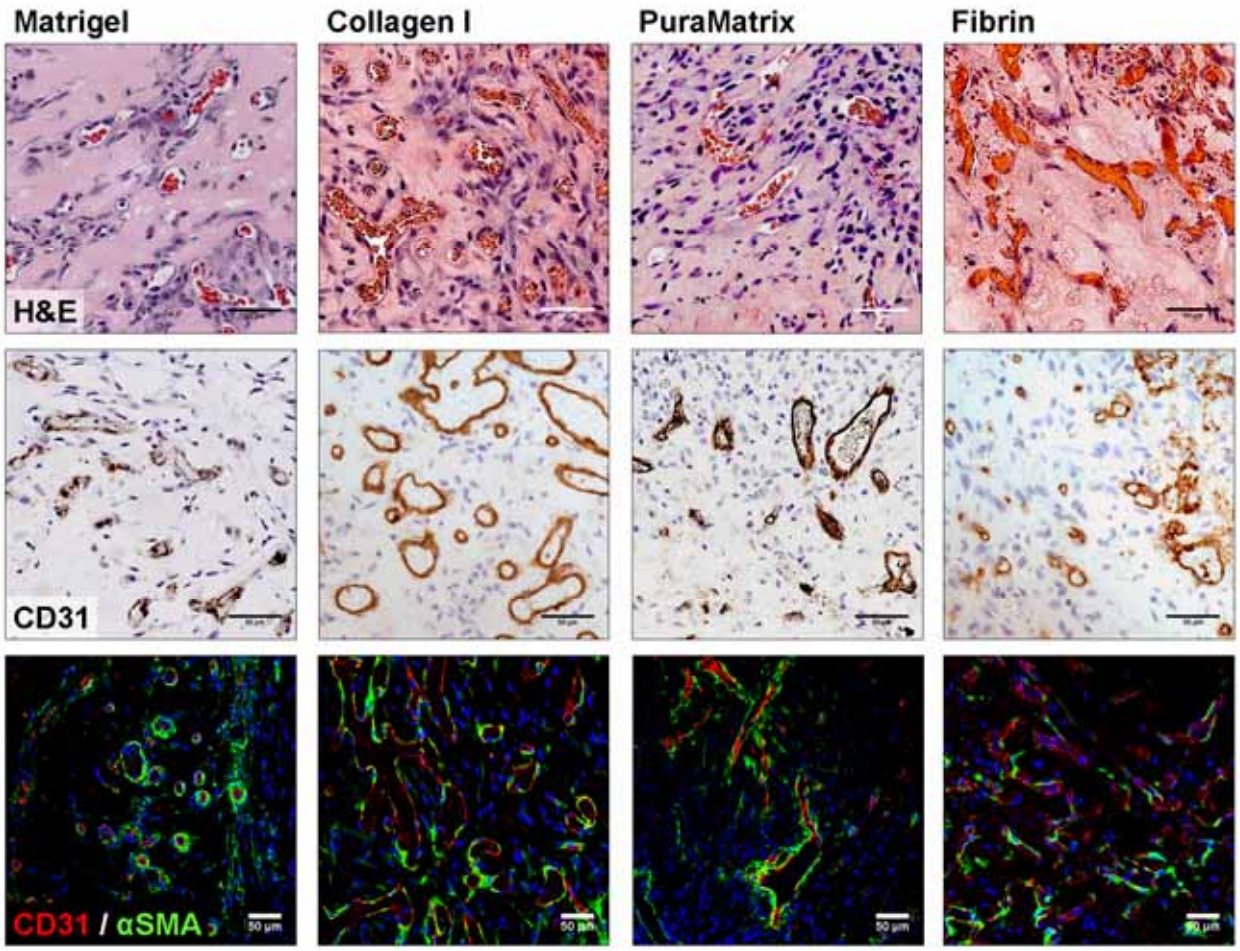

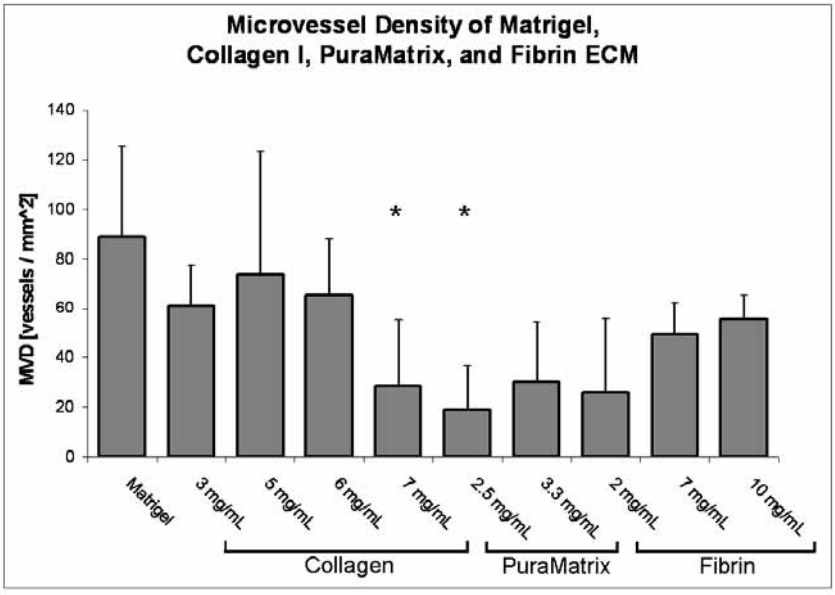

* denotes P ≤ 0.05 compared to Matrigel and 3-6 mg/mL collagen, n = 4-12 animals

Objective 3 : To further optimize cell culture conditions for expansion of human progenitor cell populations to demonstrate the feasibility of translating this technology to clinical application.

We tested whether human EPCs and MPCs could be expanded more rapidly and easily using CultiSphereG (Sigma) macroporous microcarrier beads. The idea is that the beads provide greater surface area for cell adhesion and expansion compared to a 2-dimensional cell culture plate. Our initial studies showed that human EPCs adhered, proliferated and maintained their endothelial phenotype when cultured on these beads, but the increase in expansion potential was modest – approximately 1.6 fold.

IV. KEY RESEARCH ACCOMPLISHMENTS:

- Conducted detailed time course experiment in the in vivo vasculogenesis model
- Showed functional significance of the granulocyte/monocyte influx
- Tested whether human granulocyte/monocytes would augment vasculogenesis in this model
- Showed that human EPCs/MPCs form vascular networks in a variety of 3-dimensional microenvironments – type I collagen gels, fibrin gels and a peptide hydrogel (PuraMatrix)
- Tested expansion potential of human EPCs and MPCs on microcarrier beads

V. REPORTABLE OUTCOMES:

1) Manuscripts April 2008 – April 2009:

1. Melero-Martin JM, Obaldia ME, Kang S-Y, Khan ZA, Yuan L, Oettgen P and Bischoff J. 2008, Engineering robust and functional vascular networks in vivo with human adult and cord blood-derived progenitor cells. Circ. Res. 103: 194-202. (*highlighted in Circ. Res. Editorial "Therapeutic Vasculogenesis: It takes two"*)

2. Melero-Martin JM and Bischoff J. Chapter 13 An *in vivo* experimental model for postnatal vasculogenesis. Methods Enzymol. 2004. 445:303-329

3. Melero-Martin JM, Santhalingam S, and Al-Rubeai M. 2009, Methodology for Optimal In Vitro Cell Expansion in Tissue Engineering. Adv Biochem Engin/Biotechnol 112: 209–229

2) Presentations April 2008 – April 2009:

Bischoff J. Seminar, Department of Biomedical Engineering,
University of California – Irvine April 2008
Title: Blood-derived Progenitors as Cellular Building Blocks for Cardiovascular Tissue-Engineering

Bischoff J. Seminar, Graduate Program in Cell Biology,
Cleveland Clinic Foundation, Cleveland, Ohio October 2008
Title: Tissue Vascularization using Blood- and Bone Marrow-derived Progenitor Cells

Bischoff J. Seminar, Vascular Biology and Transplantation Program,
Yale University, New Haven, CT November 2008
Title: Tissue Vascularization using Blood- and Bone Marrow-derived Progenitor Cells

Melero-Martin JM, Invited Talk, Experimental Biology 2008: North America
Vascular Biology Organization (NAVBO) Blood Vessel Club. San Diego, CA April 2008.
Title: Engineering vascular networks in vivo with human postnatal progenitor cells

Melero-Martin JM, Seminar, Vascular Research Division/Department of Pathology.
Brigham & Women's Hospital/Harvard Medical School, Boston, MA September 2008.
Title: Engineering vascular networks in vivo with human postnatal progenitor cells

Melero-Martin JM, Seminar, Department of Molecular, Cellular and Biomedical Sciences, University of New Hampshire, Durham, NH December 2008
Title: Engineering vascular networks in vivo with human postnatal progenitor cells

Melero-Martin JM, Poster Presentation, 26th Army Science Conference, Orlando, Florida, December 2008
Title: Engineering robust and functional vascular networks in vivo with human adult and cord blood-derived progenitor cells

Melero-Martin JM, Poster Presentation, 5th Annual Symposium in Cellular, Molecular and Clinical Research in Surgery, Children's Hospital Boston December 2008
Title: Engineering robust and functional vascular networks *in vivo* with human adult and cord blood-derived progenitor cell

3) Patents – see publication date of 26.06.2008

Pub. No.:	WO/2008/077094	**International Application No.:**	PCT/US2007/088110
Publication Date:	26.06.2008	**International Filing Date:**	19.12.2007

IPC: ***A61K 35/12*** (2006.01), ***A61L 27/38*** (2006.01), ***A61P 9/10*** (2006.01)

Applicants: **CHILDREN'S MEDICAL CENTER CORPORATION** [US/US]; 55 Shattuck Street, Boston, MA 02115 (US) *(All Except US)*.
MELERO-MARTIN, Juan, M. [ES/US]; 91 Bynner Street, Apartment 2, Jamaica Plain, MA 02130 (US) *(US Only)*.
BISCHOFF, Joyce, E. [US/US]; 59 Shady Hill Road, Weston, MA 02493 (US) *(US Only)*.

Inventors: **MELERO-MARTIN, Juan, M.** [ES/US]; 91 Bynner Street, Apartment 2, Jamaica Plain, MA 02130 (US).
BISCHOFF, Joyce, E. [US/US]; 59 Shady Hill Road, Weston, MA 02493 (US).

Agent: **RESNICK, David S.**; Nixon Peabody LLP, 100 Summer Street, Boston, MA 02110-2131 (US).

Priority Data: 60/875,737 19.12.2006 US

Title: METHODS FOR PROMOTING NEOVASCULARIZATION

Abstract:

The success of tissue engineering and therapeutic neovascularization depends on the development of a microvascular network. The present invention provides methods for promoting neovascularization in tissue engineering constructs, tissue repair, and wound healing comprising endothelial and mesenchymal progenitor cells.

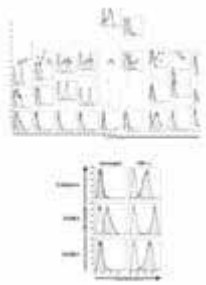

4) Funding obtained:

2008-2012 National Institutes of Health $895,024 direct costs
R01 HL094262
Title: Tissue vascularization using blood and bone marrow-derived progenitor cells
Test ability of human and mesenchymal progenitor cells to form vascular networks in ischemic and non-ischemic myocardium *in vivo*.
Principal Investigator: Joyce Bischoff

This grant, which started October 2008, is a direct outgrowth from the DOD-funded Project III. In this NIH grant, we propose to develop and test strategies to accelerate and fine tune the building of vascular networks using progenitor cells and to determine whether our system can be applied to both ischemic and non-ischemic myocardium.

5) Employment/research opportunities/training.

Dr. Juan Melero-Martin, a post-doctoral fellow on Project III for 3.5 years, was recruited to be an independent investigator by the Department of Cardiac Surgery at Children's Hospital Boston, as of September 1, 2008. This is important and exciting step in his career development.

VI. CONCLUSIONS:

Our two major accomplishments over the past year have been 1) that the human EPC/MPC system for building vascular networks is versatile in that it occurs in a variety of 3-dimensional environments and 2) that a transient influx of murine neutrophils 1-2 days after implantation of EPCs/MPCs/Matrigel is an important contributor to vasculogenesis. This result is summarized in the schematic in Figure 3.

Figure 3 - granulocyte/monocyte cells play an important role in the formation of vascular networks from human progenitor cells

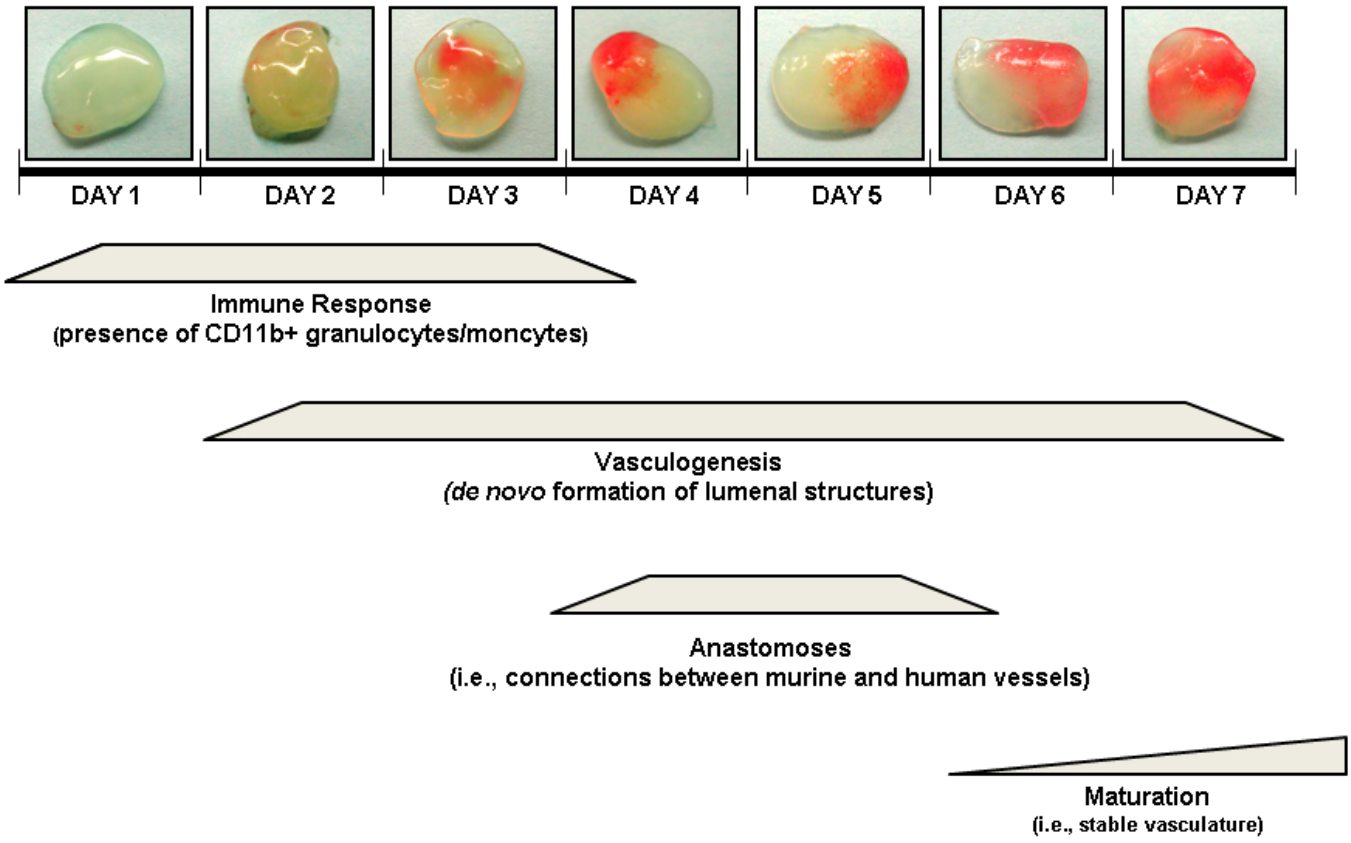

"SO WHAT SECTION"

Our goal is to build vascular networks from human endothelial progenitor cells (EPCs) and mesenchymal progenitor cells (MPCs) to re-build damaged tissues and organs. We have shown that human EPCs and MPCs can be obtained from blood or bone marrow and expanded in the laboratory without difficulty. Our published data demonstrate the vasculogenic capability of these cells in vivo. In the future, we envision use of a patient's own EPCs and MPCs for a variety of tissue-engineering (TE) applications and for in situ regeneration of vascular networks in ischemic tissue. For tissue-engineering (TE), vascular networks created from EPCs/MPCs would be incorporated into tissue-engineered constructs in vitro such that upon implantation in vivo, anastomoses with the host circulation occur rapidly to establish blood flow. For tissue regeneration in situ, EPCs/MPCs would be delivered to the site in vivo where they will undergo vasculogenesis. In summary, we envision our two-cell system as an *enabling technology* that can be applied to many different tissues/organs wherein functional blood vessels are needed.

VII. REFERENCES:

1. Melero-Martin, J.M., Khan, Z.A., Picard, A., Wu, X., Paruchuri, S., and Bischoff, J. 2007. In vivo vasculogenic potential of human blood-derived endothelial progenitor cells. *Blood* 109:4761-4768.

2. Melero-Martin, J.M., De Obaldia, M.E., Kang, S.Y., Khan, Z.A., Yuan, L., Oettgen, P., and Bischoff, J. 2008. Engineering robust and functional vascular networks in vivo with human adult and cord blood-derived progenitor cells. *Circ Res* 103:194-202.

3. Kaipainen, A., Kieran, M.W., Huang, S., Butterfield, C., Bielenberg, D., Mostoslavsky, G., Mulligan, R., Folkman, J., and Panigrahy, D. 2007. PPARalpha deficiency in inflammatory cells suppresses tumor growth. *PLoS ONE* 2:e260.

4. Muhs, B.E., Gagne, P., Plitas, G., Shaw, J.P., and Shamamian, P. 2004. Experimental hindlimb ischemia leads to neutrophil-mediated increases in gastrocnemius MMP-2 and -9 activity: a potential mechanism for ischemia induced MMP activation. *J Surg Res* 117:249-254.

5. Shojaei, F., Wu, X., Zhong, C., Yu, L., Liang, X.H., Yao, J., Blanchard, D., Bais, C., Peale, F.V., van Bruggen, N., et al. 2007. Bv8 regulates myeloid-cell-dependent tumour angiogenesis. *Nature* 450:825-831.

6. Shojaei, F., and Ferrara, N. 2008. Refractoriness to antivascular endothelial growth factor treatment: role of myeloid cells. *Cancer Res* 68:5501-5504.

7. Ahn, G.O., and Brown, J.M. 2008. Matrix metalloproteinase-9 is required for tumor vasculogenesis but not for angiogenesis: role of bone marrow-derived myelomonocytic cells. *Cancer Cell* 13:193-205.

VIII: APPENDICES:

Project I:

1. Lee TL, Sjin RMT, Movahedi S, Ahmed B, Pravda EA, Lo KM, Gillies SD, Folkman J and Javaherian K. (2008) Linking antibody Fc domain to endostatin significantly improves endostatin half-life and efficacy**.** Clin Cancer Res. 2008 Mar 1;14(5):1487-93.
2. Fainaru O, Hornstein MD, Folkman J. Doxycycline inhibits vascular leakage and prevents ovarian hyperstimulation syndrome in a murine model. Fertil Steril. 2008 Oct 18.
3. Fainaru O, Adini I, Benny O, Bazinet L, Pravda E, D'Amato R, Folkman J. Doxycycline induces membrane expression of VE-cadherin on endothelial cells and prevents vascular hyperpermeability. FASEB J. 2008 Oct;22(10):3728-35.
4. Benny O, Fainaru O, Adini A, Cassiola F, Bazinet L, Adini I, Pravda E, Nahmias Y, Koirala S, Corfas G, D'Amato RJ, Folkman J. An orally delivered small-molecule formulation with antiangiogenic and anticancer activity. Nat Biotechnol. 2008 Jul;26(7):799-807.
5. Tong-Young Lee, Stefan Muschal, Elke A. Pravda, Judah Folkman, Amir Abdollahi, and Kashi Javaherian. Angiostatin regulates the expression of antiangiogenic and pro-apoptotic pathways via targeted inhibition of mitochondrial proteins. Blood 2009. In press.
6. Yung CW, Fiering J, Mueller AJ, Ingber DE. Micromagnetic-microfluidic blood cleansing device. Lab Chip 2009;9(9):1171-7.
7. Yung CW, and Ingber DE; Septic Solution. Medical Device Developments, Oct 1, 2008.

Project II:

None

Project III:

8. Melero-Martin JM, Obaldia ME, Kang S-Y, Khan ZA, Yuan L, Oettgen P and Bischoff J. 2008, Engineering robust and functional vascular networks in vivo with human adult and cord blood-derived progenitor cells. Circ. Res. 103: 194-202. (*highlighted in Circ. Res. Editorial "Therapeutic Vasculogenesis: It takes two"*)
9. Melero-Martin JM and Bischoff J. Chapter 13 An *in vivo* experimental model for postnatal vasculogenesis. Methods Enzymol. 2004. 445:303-329

10. Melero-Martin JM, Santhalingam S, and Al-Rubeai M. 2009, Methodology for Optimal In Vitro Cell Expansion in Tissue Engineering. Adv Biochem Engin/Biotechnol 112: 209–229

Linking Antibody Fc Domain to Endostatin Significantly Improves Endostatin Half-life and Efficacy

Tong-Young Lee,[1] Robert M. Tjin Tham Sjin,[1] Shahla Movahedi,[1] Bissan Ahmed,[1] Elke A. Pravda,[1] Kin-Ming Lo,[2] Stephen D. Gillies,[2] Judah Folkman,[1] and Kashi Javaherian[1]

Abstract

Purpose: The half-life of the antiangiogenic molecule endostatin that has been used in clinical trial is short (~2 h). In addition, ~50% of the clinical grade endostatin molecules lack four amino acids at their NH_2 termini. Lack of these amino acids gives rise to a molecule that is devoid of zinc, resulting in no antitumor activity. Our goal was to develop a new version of endostatin that does not show such deficiency.

Experimental Design: A recombinant human endostatin conjugated to the Fc domain of IgG was constructed and expressed in mammalian cell culture. The presence of Fc has been shown by previous investigators to play a major role in increasing the half-life of the molecule. Fc-endostatin was tested in tumor-bearing mice, and its half-life was compared with the clinical grade endostatin.

Results: The antitumor dose of Fc-endostatin was found to be ~100 times less than the clinical grade endostatin. The half-life of Fc-endostatin in the circulation was found to be weeks rather than hours, as observed for endostatin alone. In addition, a U-shaped curve was observed for antitumor activity of endostatin as a function of endostatin concentration delivered to the animals.

Conclusion: Fc-endostatin is a superior molecule to the original clinical endostatin. Due to its long half-life, the amount of protein required is substantially reduced compared with the clinically tested endostatin. Furthermore, in view of the U-shaped curve of efficacy observed for endostatin, we estimate that the requirement for Fc-endostatin is ~700-fold less than endostatin alone. The half-life of endostatin is similar to that of vascular endothelial growth factor–Trap and Avastin, two other antiangiogenic reagents. We conclude that a new clinical trial of endostatin, incorporating Fc, may benefit cancer patients.

Endostatin, a proteolytic fragment from collagen 18, has been shown to be a potent antiangiogenic protein (1, 2). The antitumor activity of endostatin is well-established. At the time of this writing, there are >950 publications on endostatin. The antitumor properties of endostatin have been confirmed in the vast majority of these publications using a large variety of tumor models (2). The protein does not cause toxicity in patients.

The mechanism of endostatin action is still not clear. Integrin $\alpha5\beta1$ has been implicated by binding endostatin and inhibiting angiogenesis (3). Its generation from collagen 18 is regulated by cell pathways initiated by the master tumor suppressor p53 (4, 5). P53 up-regulates transcription of α (II) collagen prolyl-4-hydroxylase, releasing tumstatin and endostatin from collagen 4 and 18, respectively.

Clinical trials of human endostatin in phase I and II used a recombinant molecule that was expressed in yeast. This formulation of endostatin carried two major handicaps. The half-life of the protein in circulation was very short. The decay of endostatin represented a biexponential model that resulted in a half-life ($t_{1/2}$) of 42.3 min and a β $t_{1/2}$ of 12.9 h (6). The second problem, which has not been appreciated, is the fact that ~50% of the injected recombinant human endostatin used in the original clinical trials lacked four amino acids at the NH_2 terminus of the molecule (7). Deletion of these four amino acids gave rise to a molecule which did not bind zinc and consequently showed a relatively decreased antitumor activity (8).

To overcome these two deficiencies, we have constructed a molecule of endostatin that is fused to the Fc region of an IgG molecule (9, 10). The presence of Fc increases the half-life to longer than a week, analogous to the two angiogenesis inhibitors Avastin and vascular endothelial growth factor (VEGF)-Trap. Both of these reagents contain an Fc domain that increases the half-lives of the proteins to weeks rather than hours (11, 12). In this connection, it is relevant to point out that a Fab fragment of Avastin, which lacks Fc, has a half-life of ~2 h [the molecule is called Lucentis (Ranibizumab) and is produced by Genentech for the treatment of age-related macular degeneration; ref. 13].

Authors' Affiliations: [1]Vascular Biology Program, Department of Surgery, Children's Hospital Boston and Harvard Medical School, Boston, Massachusetts and [2]EMD Lexigen Research Center, Billerica, Massachusetts

Received 6/20/07; revised 10/18/07; accepted 12/7/07.

Grant support: Breast Cancer Research Foundation, Department of Defense grant W81XWH-05-1-0115, and NIH grant RO1 CA064481 (J. Folkman).

The costs of publication of this article were defrayed in part by the payment of page charges. This article must therefore be hereby marked *advertisement* in accordance with 18 U.S.C. Section 1734 solely to indicate this fact.

Requests for reprints: Kashi Javaherian, Karp Family Research Laboratories, Room 11.213, 1 Blackfan Circle, Boston, MA 02115. Phone: 617-919-2392; Fax: 617-730-0231; E-mail: kashi.javaherian@childrens.harvard.edu.

doi:10.1158/1078-0432.CCR-07-1530

Another aspect of endostatin, its biphasic, U-shaped antitumor activity (14, 15), is also revealed for recombinant human Fc-endostatin (hFc-endostatin) here. We show here that Fc-endostatin, when its biphasic, U-shaped antitumor activity is taken into account, can achieve optimum antitumor efficacy when administered at doses that are at least 100-fold lower than endostatin lacking Fc.

We anticipate that by using Fc-endostatin, it should be possible to reach endostatin concentrations in tens of μg/mL in the circulation of patients, analogous to Avastin and VEGF-Trap (11, 16). Finally, we report the antitumor activities for two endostatin mutants. One of the mutants has alanine substitutions of two histidines responsible for its zinc binding (H1A and H3A). The second mutant lacks heparin binding due to replacement of two critical arginines by alanines (R27A and R139A). Both of these mutants decrease antitumor activity of the native endostatin. The zinc-deficient mutant is more effective than the heparin-deficient endostatin. The improved formulation of endostatin reported here may provide for more effective clinical trials.

Materials and Methods

Expression and purification. Construction, expression, and purification of hFc-endostatin and mouse Fc-endostatin (mFc-endostatin) have been described previously (9, 10). The recombinant constructs were prepared by placing the Fc regions at the NH_2 terminus of endostatin. Stable cell lines of these constructs were produced in NS/0 murine myeloma cells. The proteins were expressed and secreted into the medium. Protein A was used for purification of the recombinant proteins (at least 90% purity; refs. 9, 10). We obtained ~50 mg/liter of Fc-endostatin by using fermentors of 10- to 18-liter capacity.

hFc-endostatin (H1A and H3A) is a mutant in which the histidines 1 and 3 of endostatin are substituted by alanines, resulting in a molecule that lacks zinc binding. The expression plasmid for hFc-endostatin (H1A and H3A) was constructed by using a synthetic HindIII-SexA1 oligonucleotide duplex containing the two codon substitutions to replace the corresponding restriction fragment in pdCs-Fc(D4K)-endostatin (9). The sense strand has the sequence 5′-AGCTT**GCT**AGC**GCA**CGCGACTTCCAGCCGGTGCTCCA, and the nonsense strand has the sequence 5′-CCAGGTGGAGCACCGGCTG-GAAGTCGCG**TGC**GCT**AGC**A, where the H1A and H3A codons and anticodons are in bold. The resultant construct was used to transfect NS/0 murine myeloma cells. hFc-endostatin (H1A and H3A) was purified from conditioned medium of stable clones as previously described (9). Construction, expression, and purification of endostatin deficient in heparin binding have been previously described (17). We have previously reported the inhibition of endothelial cell migration *in vitro* and the reduction of tumor vessel density *in vivo* by Fc-endostatin (8, 14).

Animal studies. All animal procedures were carried out in compliance with Children's Hospital Boston guidelines. Protocols were approved by the Institutional Animal Care and Use Committee. Male (24-27 g) immunocompetent C57Bl/6J (Jackson Laboratory) and immunocompromised severe combined immunodeficiency (SCID) mice (Massachusetts General Hospital) were used. Mice were ages 7 to 9 weeks. Mice were acclimated, caged in groups of five in a barrier care facility, and fed animal chow and water *ad libitum*. Animals were euthanized by CO_2 inhalation.

ELISA determination of Fc-endostatin. Serum samples were obtained by retroorbital puncture with nonheparinized capillary tubes under

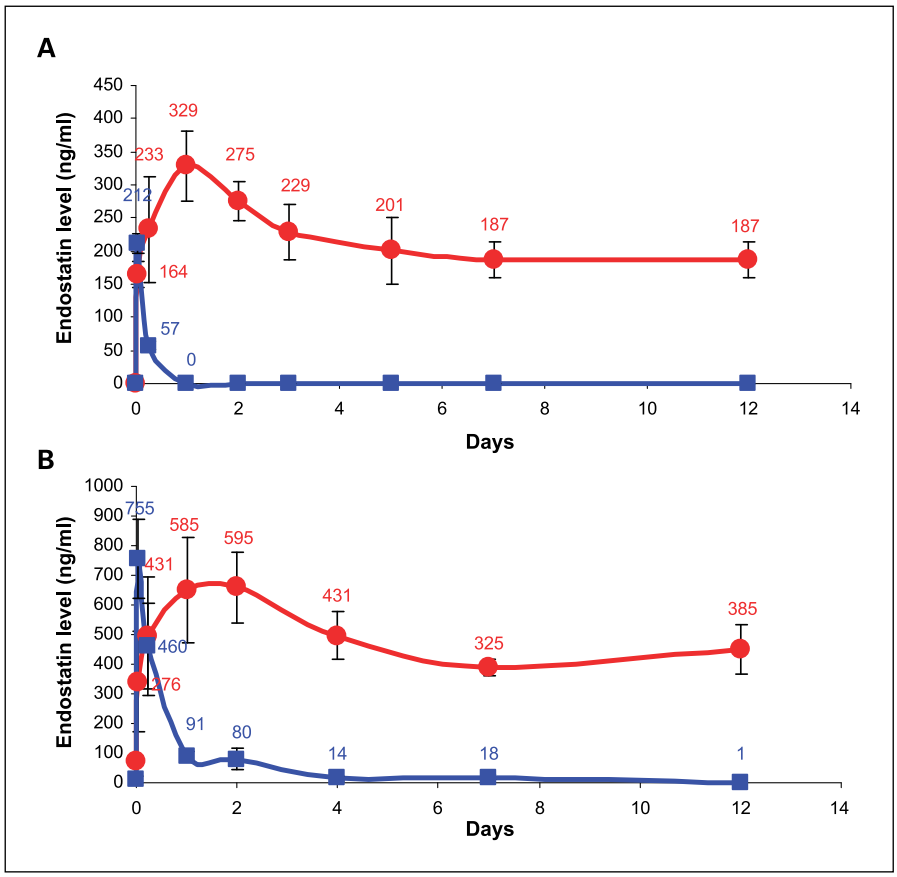

Fig. 1. Pharmacokinetics of endostatin and Fc-endostatin. Endostatin (100 μg/0.2 mL) was injected s.c. into C57Bl/6J.mice, and concentrations of the circulating protein were monitored by ELISA (Cytimmune). Three mice were in each group. *A,* hFc-endostatin (●) and human endostatin (■). *B,* mFc-endostatin (●) and mouse endostatin (■). The measured concentrations of mouse endostatin were corrected for baseline endostatin (60 ng/mL). Mouse endostatin was prepared by treating mFc-endostatin with enterokinase and purified on Pharmacia Sepharose S-100 (9).

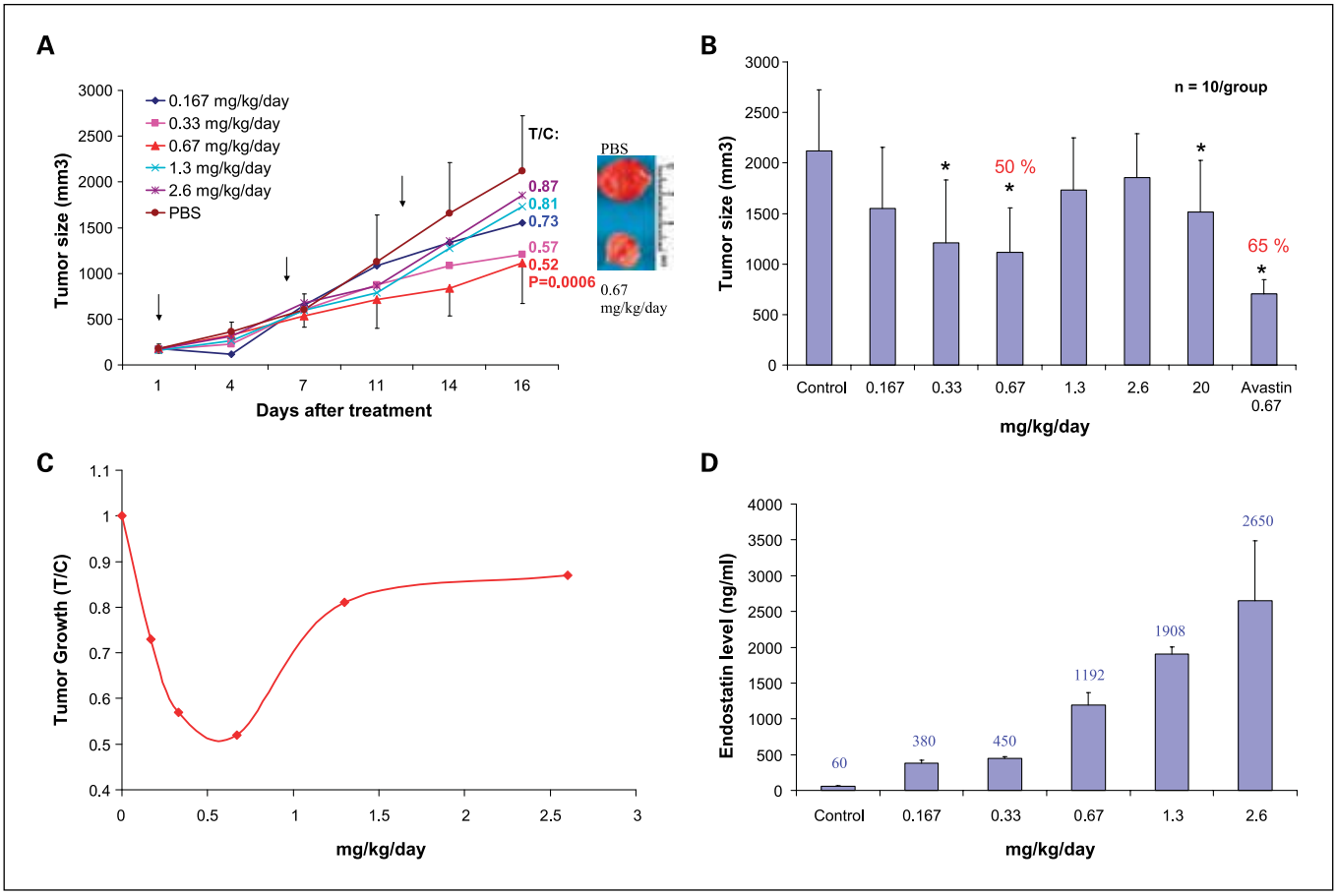

Fig. 2. Treatment of human melanomas (A2058) with hFc-endostatin. Ten SCID mice in each group. S.c. injections were delivered in 0.2 mL volume of PBS once every 6 days; (↓) $n = 10$. *A,* tumor size as a function of time and concentration of endostatin. The ratio of T/C is shown for each group. *B,* tumor size is plotted as a function of concentration of the delivered protein. The Avastin dose is the same as endostatin at its optimum efficacy (0.67 mg/kg/d). Daily injection of clinical grade endostatin at 0.5 mg per mouse day (20 mg/kg/d). *C,* the U-shaped curve for data of *B*. *D,* ELISA of endostatin 3 days after the last injection.

anesthesia. Samples were placed at 4°C overnight, and serum was collected after centrifugation at 10,000 rpm for 10 min. Concentrations were determined by competition ELISA (Cytimmune Sciences) following the manufacturer's protocol.

Tumor models. Human melanoma A2058 and ASPC-1 (a human pancreatic tumor cell line) were cultured in DMEM and RPMI 1640 with L-glutamine, respectively and supplemented with 10% FCS and antibiotics. SCID mice were shaved and the dorsal skin was cleaned with ethanol before cell injection. A suspension of 5×10^6 tumor cells in 0.1 mL of PBS was injected s.c. into the dorsa of mice at the proximal midline. Mice were weighed and tumors were monitored twice a week in 2 diameters with a digital calipers. Tumor volumes were determined using $a^2 \times b \times 0.52$ (where a is the shortest and b is the longest diameter). Tumors were allowed to grow to ~100 mm^3 and mice were randomized. Treatment was by bolus s.c. injections. Concentrations of Fc-endostatin were corrected for the Fc contribution. Consequently, all indicated concentrations refer to concentrations of endostatin in Fc-endostatin. After experiments were completed, tumors were excised and fixed in either 4% paraformaldehyde or were snap frozen. Ten mice were treated with each dose of endostatin.

Unless otherwise specified, antitumor studies were done with injection doses delivered every 6 days. The dose amounts were converted into mg/kg/d to compare with our previous published data for endostatin alone (no Fc).

Immunohistology. Melanomas (A2058) were removed and fixed with 4% paraformaldehyde for 2 h and then incubated in 30% sucrose in PBS overnight. Tumors were embedded in ornithine carbamyl transferase medium (Tissue-Tek). Sections were treated with proteinase K (20 μg/mL) for 20 min before staining. hFc-endostatin was detected by FITC-labeled polyclonal antibody against human Fc fragment (Sigma). Blood vessels were visualized with monoclonal antibody against CD-31 (BD PharMingen). The primary antibody was detected by biotin-labeled goat anti-rat antibody (Vector) followed by Alexa 594–labeled streptavidin (Molecular Probes). The sections were imaged by confocal microscopy (model DM IRE2; Leica).

Terminal deoxynucleotidyltransferase–mediated dUTP nick end labeling assay. Apoptosis was examined by use of the terminal deoxynucleotidyltransferase–mediated dUTP nick end labeling (TUNEL) assay (18). To detect apoptotic cells *in vivo*, frozen tumor sections were treated with proteinase K (20 μg/mL) for 20 min, and the slides were stained by manufacturer's protocol (Promega). Hoescht 33258 (Molecular Probes) was used as a counter stain. Quantitative results were expressed as the number of apoptotic cells per total cells at magnification ×200.

Statistical method. Data are expressed as mean ± SD. Statistical significance was assessed by using the Student's t test.

Results

Pharmacokinetics of Fc-endostatin versus endostatin alone is significantly different. We used mouse endostatin, human endostatin, and their Fc counterparts to investigate their pharmacokinetics. Immunocompetent mice received a single

injection s.c. and they were bled at indicated time intervals. The concentration of endostatin in serum was detected by ELISA. The data in Fig. 1A show that in contrast to human endostatin alone (*blue*), which has a half-life of 1 to 2 h, the half-life of hFc-endostatin (*red*) is at least a week and a half and possibly longer; a phenomenon known for Fc containing proteins and antibodies (19, 20). The maximum endostatin concentration is 329 ng/mL and decreases to 187 ng/mL by day 7. Similar data were obtained for mouse endostatin and mFc-endostatin (Fig. 1B). In the case of murine endostatin, the highest endostatin concentration was 595 ng/mL, which decreased to 385 ng/mL by day 12. Mouse endostatin concentrations have been corrected for the baseline value of 20 to 60 ng/mL.

Antitumor activity of hFc-endostatin in a melanoma cancer model requires much less protein and shows a U-shaped curve. Human melanoma cells (A2058) were injected into SCID mice, and the animals were treated with hFc-endostatin at doses delivered once every 6 days. We show here that smaller doses administered at longer intervals resulted in optimum antitumor activity. The tumor volumes as a function of endostatin dosage are presented in Fig. 2A. The optimum antitumor effect is observed at 0.67 mg/kg/d [100 μg of endostatin per mouse every 6 days; treated versus control (T/C) = 0.52; P = 0.0006]. In Fig. 2B, the data are presented as a histogram at the completion of the experiment (8). Anti-VEGF monoclonal Avastin and clinical grade endostatin were used for comparison in Fig. 2B. The T/C for Avastin is 0.35 at the dose of 0.67 mg/kg/d. In Fig. 2C, the same data are shown by a U-shaped curve. The antitumor efficacy drops below and above the optimum concentration; consistent with a biphasic curve of efficacy.

For comparison of endostatin levels in the circulation corresponding to different doses of recombinant hFc-endostatin, we carried out an ELISA analysis (Fig. 2D). The optimum concentration (1.192 ng/mL) is a function of endostatin concentration of the dose and the frequency.

Treatment of mice bearing pancreatic tumor cell line ASPC-1 with hFc-endostatin yields similar results to those of melanoma-bearing mice. For a second tumor model, we used a human pancreatic cancer cell line ASPC-1. The cells were injected into the dorsa of SCID mice. After tumors reached a mean volume of ~100 mm^3, the mice were treated with hFc-endostatin (Fig. 3). The optimum antitumor activity was achieved with a dose of 0.67 mg/kg/d (100 μg of endostatin per mouse every 6 days; Fig. 3A). In Fig. 3B, the tumor sizes are plotted as a function of endostatin doses (8). The U-shaped curve for these data are presented in Fig. 3C.

We conclude that the U-shaped curve is a property of endostatin in a number of tumor models, based on our data presented here, our previous data, and those generated by another group of investigators in our laboratory (14, 15).

Histidine and arginine mutations in hFc-endostatin affect antitumor activity of endostatin. We previously reported that the antitumor activity of endostatin is mimicked by a 25-amino-acid peptide corresponding to the NH_2 terminus of the molecule (8). Substitution of histidines 1 and 3 by alanines in this peptide eliminated its antitumor activity. This result showed that zinc binding of endostatin is required for its activity. The zinc binding requirement has been controversial and has been reviewed by us (8). Boehm et. al. (21) reported the first evidence for the criticality of zinc binding for the antitumor activity of endostatin. For antitumor activity, the authors used an *Escherichia coli* suspension of endostatin that was poorly soluble. The data showed that zinc binding was necessary for antiangiogenic and antitumor activity but did not include comparison to a soluble form of endostatin.

In the construct reported here, we have substituted alanines for the two crucial histidine residues essential for zinc binding (H1A and H3A). The antitumor activity of this mutant in the ASPC-1 tumor model is shown in Fig. 3 (A and B). Consistent with our previous data, we conclude that zinc binding of endostatin is critical for its antitumor activity. Substitution for the two histidine residues reduces this activity from 50% to 20%.

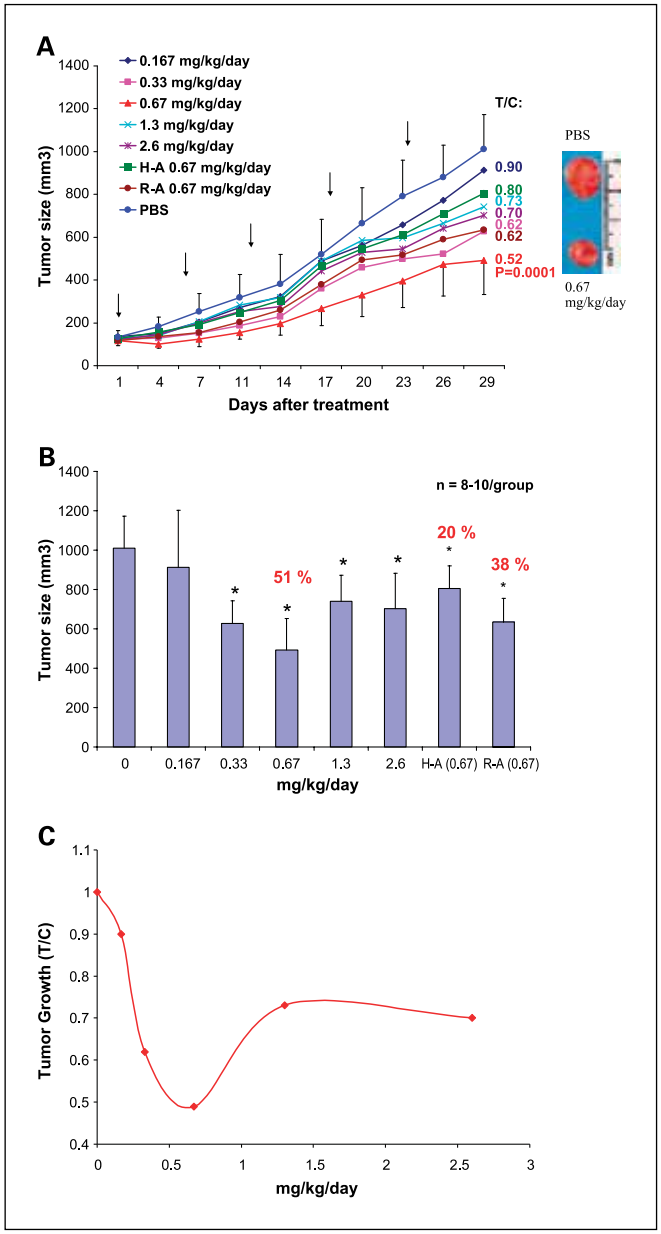

Fig. 3. Treatment of mice bearing human pancreatic tumors (ASPC-1) with hFc-endostatin. The protocol was identical to that in Fig. 2 except a different tumor cell line was used. H-A, endostatin mutants H1A and H3A; R-A, endostatin mutants R27A and R139A.

The U-shaped curve of ASPC-1 is not as symmetrical as that of melanoma (compare Figs. 2C and 3C). The antitumor activity of the mutant endostatin resembles the nonoptimum doses of the wild-type molecule. Based on these data, in addition to the zinc binding contribution to the antitumor activity, other constituents of the endostatin molecule may play a smaller role in such an activity.

The heparin binding domain of endostatin is clustered on the protein surface (which cannot be mimicked by a linear peptide). We prepared a mutant of endostatin lacking heparin binding (R27A and R139A) in the context of hFc-endostatin as described previously (17). Mutation of these two arginines eliminates the heparin binding property of endostatin (22). Antitumor activity of this mutant, using ASPC-1 tumor cells, is shown in Fig. 3A and B. We observed 38% tumor inhibition for mice treated with endostatin (deficient for heparin binding), in contrast to 50% tumor inhibition for mice treated with wild-type endostatin. Both zinc-binding and heparin-binding mutant Fc-endostatin will need to be tested in a number of tumor models to reach a more definite conclusion.

Clinical grade yeast–expressed endostatin shows a doublet on PAGE with ~50% of endostatin having reduced antitumor activity. It has been reported that the endostatin protein used in clinical trials showed a doublet on PAGE (7). Based on their animal studies, the authors concluded that deletion of four amino acids from the NH_2 terminus (HSHR), which included two zinc-binding histidines in endostatin, did not affect its antitumor activity. In this study, it was found that histidine-deleted endostatin bound two atoms of zinc, whereas wild-type endostatin bound 10 atoms of zinc. However, the zinc binding data are inconsistent with the crystal structure of human endostatin and our zinc measurements of native endostatin where one atom of zinc is bound to the endostatin molecule (9). We conclude that the reported high zinc-binding endostatin was probably the result of nonspecific interactions between zinc and endostatin. This artifact occurs under certain conditions during the reconstitution of endostatin with zinc. For example, during reconstitution of zinc with endostatin, the protein should be dialyzed against a large volume of buffer containing low zinc concentration to allow a gradual addition of the metal ion to the protein.

We previously reported that endostatin antitumor activity requires zinc binding (8, 21). In Fig. 4, clinical grade endostatin and hFc-endostatin are subjected to PAGE. The faster migrating protein in endostatin (*lane 2*) lacks four amino acids HSHR (data not shown). Based on PAGE, we speculate that the antiangiogenic and antitumor activity of recombinant endostatin used in clinical trials may have been reduced by at least 30%. This is because ~50% of the final endostatin product lacked zinc. In contrast, hFc-endostatin seems to show a single protein band under the same conditions (*lane 3*).

hFc-endostatin accumulates in tumor vessels. To verify the location of exogenous hFc-endostatin, histologic sections of melanoma were incubated with FITC-labeled anti-human Fc fragment antibody (*green*) and anti-mouse CD31 antibody (*red*). The FITC-labeled antibody reacted with the histologic sections of tumors from mice treated with endostatin but not with the histologic sections of tumors treated only with PBS (Fig. 5A). We conclude that the injected hFc-endostatin is selectively localized in tumor vessels.

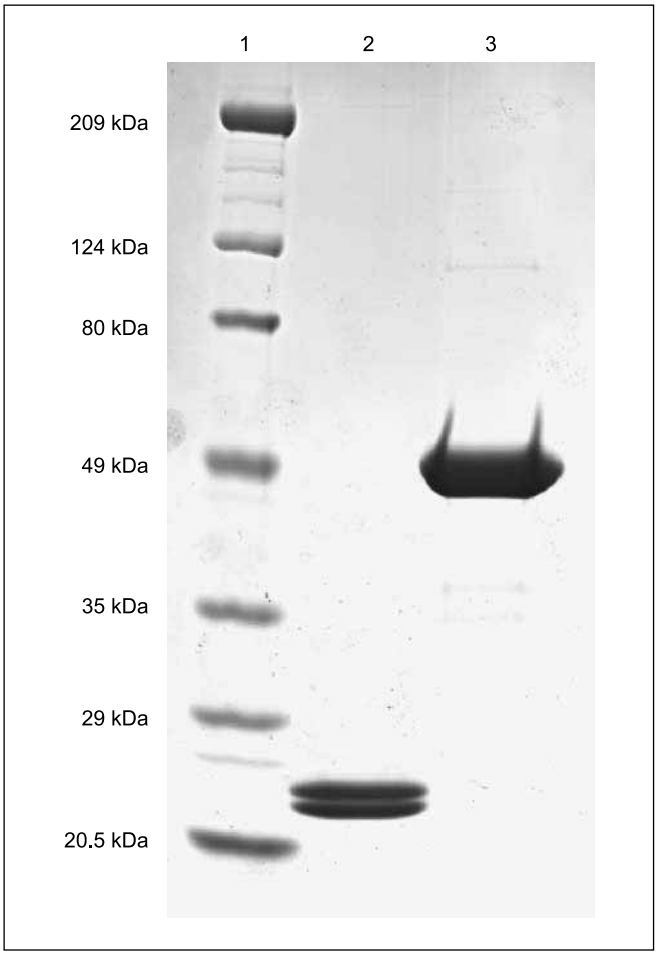

Fig. 4. Electrophoretic analysis of the clinical grade endostatin, 4-20% gradient PAGE. Lane 1, molecular weight markers. Lane 2, clinical grade endostatin. Lane 3, hFc-endostatin.

TUNEL-positive apoptotic cells are increased after hFc-endostatin treatment. To confirm the role of hFc-endostatin as an apoptosis inducer, we did TUNEL analysis on histologic sections of melanoma (Fig. 5B). TUNEL-positive apoptotic cells were increased in hFc-endostatin–treated sections. The mean percentage of apoptotic tumor cells was 34.7% ± 6.82% in the histologic sections of the hFc-endostatin–treated (0.67 mg/kg/d) mice but was only 8.77% ± 0.87% in PBS-treated tumor sections (Fig. 5C).

Discussion

A major problem observed with clinical grade recombinant human endostatin produced in yeast has been its short half-life. Forty-two patients with advanced neuroendocrine tumors who had failed conventional therapy were treated with daily self-administered subcutaneous injections of recombinant human endostatin (from yeast) in a phase II study at a dose of 90 mg/m^2 day (~2.5 mg/kg/d; ref. 23). There was minimal or no toxicity, and the disease remained stable in 80% of patients. Four patients had stable disease for >3.5 years of uninterrupted therapy. However, there was no partial response to therapy (i.e., 50% tumor regression), as defined by WHO criteria.

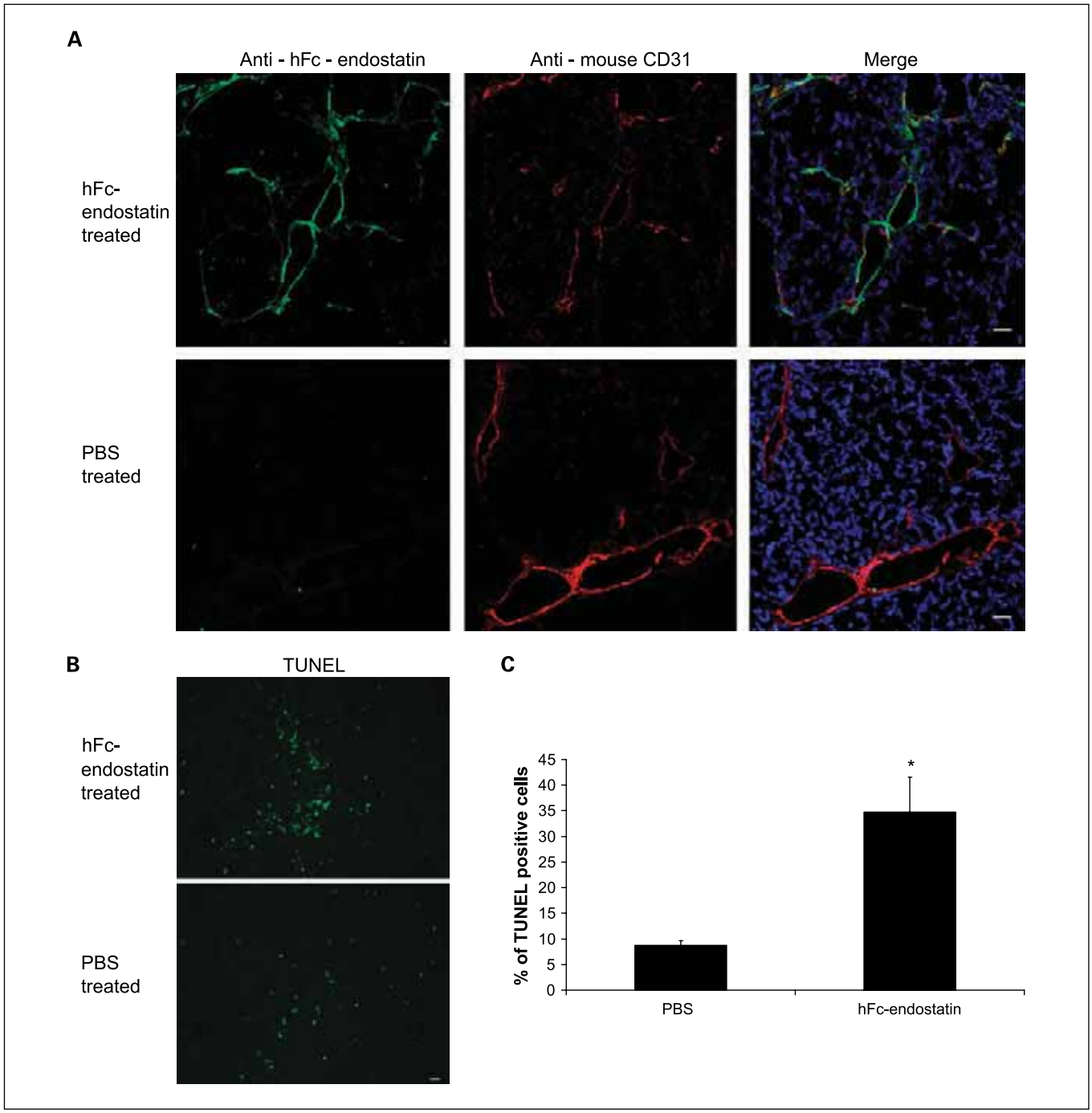

Fig. 5. Immunohistochemistry and TUNEL assay. *A,* immunohistochemistry results for one of the mice treated at 0.67 mg/kg/d and a control mouse. *B* and *C,* TUNEL assay (scale, 20 μm).

The median steady-state trough serum level after dose escalation was 331 ng/mL. The fact that only half of the endostatin bound zinc (deletion of four amino acids at the NH_2 terminus) suggests that the actual median protein concentration of active endostatin was ~200 ng/mL. This estimate is based on the assumption that the ELISA detects both intact and deleted endostatin equally well. The level of endogenous endostatin was reported to be 61 ng/mL. We conclude that the measured median steady-state trough in serum was only 3.3-fold higher than the baseline value.

In contrast, when Avastin (anti-VEGF monoclonal antibody) was administered to cancer patients at a dose of 0.1 to 10 mg/kg, the maximum concentration of circulating antibody was determined to be linear with a range of 2.8 to 284 μg/mL and with a half-life of 3 weeks (11, 24). The dose of antibody administered to patients with colorectal cancer was 5 mg/kg. This translates to 140 μg/mL for maximum circulating antibody. The long half-life of Avastin is mainly due to the presence of the Fc domain. Of interest is that Lucentis, a Fab fragment derived from Avastin, has a half-life of only a few hours (13).

Although the modes of actions of endostatin and Avastin are different, and the requirements for the two drugs are not equivalent, we believe that the poor pharmacokinetics of recombinant endostatin from yeast may be a critical basis for its lack of robust response in patients. Therefore, we have formulated *Fc-endostatin*, in the event that this construct will increase the serum concentration of endostatin in patients by at least 100-fold compared with endostatin lacking the Fc domain. From our experimental results in tumor-bearing mice, we predict that the half-life of Fc-endostatin in humans may be ~2 to 3 weeks, in contrast to hours for endostatin lacking the Fc-fragment. In other words, Fc-endostatin would be expected to have a similar half-life in the circulation as Avastin or VEGF-Trap.

For VEGF-Trap, treatment of patients with 0.8 mg/kg of the protein resulted in a maximum concentration of ~14 μg/mL with a half-life of 25 days (16). Based on the observed linear pharmacodynamics for Avastin in patients (11), at a dose of 0.8 mg/kg of the antibody, the maximum circulating antibody is calculated to be 22 μg/mL with a half-life of ~3 weeks. We conclude that the concentration of endostatin in the serum of cancer patients may have to reach 10 to 100 μg/mL with a 2- to 3-week half-life to achieve antitumor efficacy for endostatin. hFc-endostatin is potentially capable of achieving such a level.

We also report here that the antitumor activity of endostatin is biphasic and reveals a U-shaped curve for efficacy. Other proteins that regulate angiogenesis have also been reported to show similar biphasic curves of antitumor efficacy. These include IFN-α (25), rosiglitazone (26), and thrombospondin (27). In our study of hFc-endostatin in mice, we determined that maximum antitumor activity was achieved by administration of ~0.7 mg/kg/d for the two tumor models. We compared Fc-endostatin from this study with clinical endostatin in the tumor models ASPC-1 and BxPC-3 (15). Maximum antitumor activity was achieved with Fc-endostatin at 0.67 mg/kg/d. In contrast, maximum antitumor activity for endostatin lacking the Fc-fragment was achieved at ~100 mg/kg/d for BxPC-3 and 500 mg/kg/d for ASPC-1. Thus, the optimum antitumor dose for Fc-endostatin is 150- to 700-fold lower than the optimum antitumor dose for endostatin that lacks the Fc-fusion domain. However, when the clinical grade recombinant lacking the Fc-domain (from yeast) was used in tumor-bearing animals, the authors reported 90% inhibition of tumor growth. We observed ~55% inhibition of tumor growth in mice given recombinant Fc-endostatin and 65% inhibition of tumor growth in mice treated with Avastin.

In conclusion, the new data presented here: (*a*) provide a molecular explanation for why the limited clinical trials of endostatin did not achieve the full potential expected for this broad-spectrum, endogenous antiangiogenic protein (2); (*b*) show that the antitumor potency of human endostatin can be increased at least by 100 fold by fusing an Fc domain to the NH_2 terminus, thus increasing the half-life of the protein, stabilizing the terminal histidines, and conserving the zinc affinity of endostatin; (*c*) reveal a biphasic U-shaped curve of antitumor activity for Fc-endostatin, as we previously reported for endostatin lacking the Fc-domain; and (*d*) make a compelling case for initiation of clinical trials of recombinant hFc-endostatin.

Acknowledgments

We thank Sarah Short for her critical reading of the manuscript and for making many helpful suggestions and Catherine Butterfield for technical help.

References

1. O'Reilly MS, Boehm T, Shing Y, et al. Endostatin: an endogenous inhibitor of angiogenesis and tumor growth. Cell 1997;88:277–85.
2. Folkman J. Antiangiogenesis in cancer therapy-endostatin and its mechanisms of action. Exp Cell Res 2006;312:594–607.
3. Wickstrom SA, Alitalo K, Keski-Oja J. Endostatin associates with integrin $\alpha_5\beta_1$ and caveolin-1, and activates Src via a tyrosyl phosphatase-dependent pathway in human endothelial cells. Cancer Res 2002;62:5580–9.
4. Teodoro JG, Parker AE, Zhu X, Green MR. p53-mediated inhibition of angiogenesis through up-regulation of a collagen prolyl hydroxylase. Science 2006;313:968–71.
5. Folkman J. Tumor suppression by p53 is mediated in part by the antiangiogenic activity of endostatin and tumstatin. Sci STKE 2006;354:pe35.
6. Thomas JP, Arzoomanian RZ, Alberti D, et al. Phase I pharmacokinetic and pharmacodynamic study of recombinant human endostatin in patients with advanced solid tumors. J Clin Oncol 2003;21:223–31.
7. Sim BK, Fogler WE, Zhou XH, et al. Zinc ligand-disrupted recombinant human endostatin: potent inhibition of tumor growth, safety and pharmacokinetic profile. Angiogenesis 1999;3:41–51.
8. Tjin Tham Sjin RM, Satchi-Fainaro R, Birsner AE, Sadagopa Ramanujam VM, Folkkman J, Javaherian K. A 27-amino-acid synthetic peptide corresponding to the NH_2-terminal zinc-binding domain of endostatin is responsible for its antitumor Activity. Cancer Res 2005;65:3656–63.
9. Ding Y-H, Javaherian K, Lo K-M, et al. Zinc-dependent dimers observed in crystals of human endostatin. Proc Natl Acad Sci U S A 1998;95:10443–8.
10. Bergers G, Javaherian K, Lo K-M, Folkman J, Hanahan D. Effects of angiogenesis inhibitors on multistage carcinogenesis in mice. Science 1999;284:808–12.
11. Gordon MS, Margolin K, Talpaz M, et al. Phase I safety and pharmacokinetic study of recombinant human anti-vascular endothelial growth factor in patients with advanced cancer. J Clin Oncol 2001;19:843–50.
12. Holash J, Davis S, Papadopoulos N, et al. VEGF-Trap: a VEGF blocker with potent antitumor effects. Proc Natl Acad Sci U S A 2002;99:11393–8.
13. Stone EM. A very effective treatment for neovascular macular degeneration. N Engl J Med 2006;355:1493–5.
14. Tjin Tham Sjin RM, Naspinski J, Birsner AE, et al. Endostatin therapy reveals a U-shaped curve for antitumor activity. Cancer Gene Ther 2006;13:619–27.
15. Celik I, Sürücü O, Dietz C, et al. Therapeutic efficacy of endostatin exhibits a biphasic dose-response curve. Cancer Res 2005;65:11044–50.
16. Dupont J, Schwartz L, Koutcher J, et al. Phase I and pharmacokinetic study of VEGF Trap administered subcutaneously (sc) to patients (pts) with advanced solid malignancies [abstract]. J Clin Oncol 2004;22:14s.
17. Javaherian K, Park SY, Pickl WF, et al. Laminin modulates morphogenic properties of the collagen XVIII endostatin domain. J Biol Chem 2002;277:45211–8.
18. Gavrieli Y, Sherman Y, Ben-Sasson SA. Identification of programmed cell death *in situ* via specific labeling of nuclear DNA fragmentation. J Cell Biol 1992;119:493–501.
19. Capon DJ, Chamow SM, Mordenti J, et al. Designing CD4 immunoadhesins for AIDS therapy. Nature 1989;337:525–31.
20. Lo K-M, Sudo Y, Chen J, et al. High level expression and secretion of Fc-X fusion proteins in mammalian cells. Protein Eng 1998;11:495–500.
21. Boehm T, O'Reilly MS, Keough K, Shiloach J, Shapiro R, Folkman J. Zinc-binding of endostatin is essential for its antiangiogenic activity. Biochem Biophys Res Commun 1998;252:190–4.
22. Sasaki T, Larsson H, Kreuger J, et al. Structural basis and potential role of heparin/heparan sulfate binding to the angiogenesis inhibitor endostatin. EMBO J 1999;18:6240–8.
23. Kulke MH, Bergsland EK, Ryan DP, et al. Phase II study of recombinant human endostatin in patients with advanced neuroendocrine tumors. J Clin Oncol 2006;24:3555–61.
24. Motl S. Bevacizumab in combination chemotherapy for colorectal and other cancers. Am J Health Syst Pharm 2005;62:1021–32.
25. Slaton JW, Perrotte P, Inoue K, Dinney C, Fidler IJ. Interferon-mediated down-regulation of angiogenesis-related genes and therapy of bladder cancer are dependent on optimization of biological dose and schedule. Clin Cancer Res 1999;5:2726–34.
26. Panigrahy D, Singer S, Shen LQ, et al. PPARγ ligands inhibit primary tumor growth and metastasis by inhibiting angiogenesis. J Clin Invest 2002;110:923–32.
27. Motegi K, Harada K, Pazouki S, Baillie R, Schor AM. Evidence of a bi-phasic effect of thrombospondin-1 on angiogenesis. Histochem J 2002;34:411–21.

Doxycycline inhibits vascular leakage and prevents ovarian hyperstimulation syndrome in a murine model

Ofer Fainaru, M.D., Ph.D.,[a,b] *Mark D. Hornstein, M.D.,*[b] *and Judah Folkman, M.D.*[a]

[a] Department of Surgery, Vascular Biology Program, Children's Hospital; and [b] Department of Obstetrics and Gynecology, Brigham and Women's Hospital, both at Harvard Medical School, Boston, Massachusetts

Objective: To determine whether doxycycline would inhibit the development of ovarian hyperstimulation syndrome (OHSS) in a murine model.
Design: Testing the effect of oral doxycycline treatment on gonadotropin-induced peritoneal capillary leakage in mice.
Setting: Animal research facility.
Animal(s): Four-week-old female C57Bl/6 mice.
Intervention(s): Ovarian hyperstimulation syndrome was induced in mice by administering gonadotropins for 3 days followed by human chorionic gonadotropin. Peritoneal vascular leakage was quantified using the Miles vascular permeability assay. Mice were treated with daily oral doxycycline or vehicle.
Main Outcome Measure(s): The concentration of dye in abdominal fluid extracted by peritoneal lavage was measured spectrophotometrically. Ascites volume was determined using dye dilution.
Result(s): Doxycycline inhibited peritoneal vascular leakage and ascites accumulation in the hormonally stimulated mice. Doxycycline treatment did not inhibit ovarian stimulation or ovulation when compared with controls, as indicated by similar ovarian morphology, ovarian weights, and corpora lutea counts. Importantly, vessel density within the corpora lutea was similar in the two groups.
Conclusion(s): Doxycycline prevents OHSS in a murine model without compromising ovarian stimulation. This effect is caused by inhibition of vascular leakage. Doxycycline's potential in preventing human OHSS is promising and warrants further studies. (Fertil Steril® 2008;■:■–■. ©2008 by American Society for Reproductive Medicine.)

Key words: Ovarian hyperstimulation syndrome, angiogenesis, doxycycline

The female ovary is one of the few known sites where physiologic programmed angiogenesis occurs in a cyclic fashion (1). The cyclic pulsatile secretion of gonadotropins is responsible for follicle growth, ovulation, and the formation and regression of a highly vascularized structure, the corpus luteum. Therefore, the angiogenic cyclicity is most likely coordinated by gonadotropins and/or locally produced sex steroids. Exaggerated gonadotropin stimulation and angiogenesis results in the ovarian hyperstimulation syndrome (OHSS), a known iatrogenic complication of ovulation induction for infertility (2). During ovulation induction a large number of follicles and ultimately corpora lutea are formed. In OHSS, these highly vascularized structures are characterized by vascular leakage and extravasation of protein-rich fluid out of the vascular space, which account for the manifestations of the syndrome.

Vascular endothelial growth factor (VEGF), first described as vascular permeability factor (VPF), is a cytokine secreted by tumor cells that rapidly increases microvascular permeability (3). It was later found to be a powerful promoter of angiogenesis that stimulates microvessel sprouting from existing blood vessels (4). In contrast to other proangiogenic cytokines, VPF/VEGF is also a potent vascular permeabilizing factor, and it has been known for some time that tumors and other forms of pathologic angiogenesis are preceded and/or accompanied by enhanced vascular permeability (5). Blood VEGF levels have been reported to correlate with the severity of OHSS (6), and recombinant VEGF led to OHSS symptoms that were reversed by specific antibodies (7, 8). Hence, the inhibition of vascular permeability appears to be an attractive and novel therapeutic approach to preventing and treating OHSS.

Tetracyclines are potent inhibitors of the matrix metalloproteinase protein family and have been used to reduce tissue degradation in arthritis and periodontal disease (9). Doxycycline, a tetracycline derivative, has been shown to inhibit angiogenesis both in human (10) and in animal models (11). We have recently demonstrated that oral doxycycline prevents

Received May 30, 2008; revised August 25, 2008; accepted August 26, 2008.
O.F. has nothing to disclose. M.D.H. has nothing to disclose. J.F. has nothing to disclose.
Supported by Rothschild, Fulbright, and the European Molecular Biology Organization (EMBO) postdoctoral fellowships (O.F.), Department of Defense Congressional Award, #W81XWH-05-1-0115, and Breast Cancer Research Foundation 81090-07 (J.F.).
Presented in part at the 63rd Annual Meeting of the American Society of Reproductive Medicine, which was held in Washington, DC, October 13–17, 2007.
Reprint requests: Ofer Fainaru, M.D., Ph.D., Vascular Biology Program, Children's Hospital Boston, Harvard Medical School, 300 Longwood Avenue, Boston, MA 02115 (FAX: 617-730-0232; E-mail: Ofer.Fainaru@childrens.harvard.edu).

VEGF-induced vascular permeability, interleukin-2-induced pulmonary edema, delayed-type hypersensitivity reactions, and tumor vessel hyperpermeability in mice (12). We therefore hypothesized that doxycycline would also suppress VEGF-induced vascular hyperpermeability caused by gonadotropin stimulation and thus prevent OHSS.

To test this hypothesis, we induced OHSS in mice by administering postmenopausal mare serum gonadotropins (PMSG) followed by human chorionic gonadotropin (hCG). The magnitude of peritoneal vessel permeability was estimated by quantifying protein leakage into the peritoneal cavity and by measuring the accumulation of ascites.

MATERIALS AND METHODS

Animal Studies

Study animals were 4-week-old female C57BL/6 mice (Jackson Laboratories, Bar Harbor, ME). Mice were housed in groups of five mice per cage with free access to water and chow. Before inclusion into the study, mice were acclimated for a week. All animal studies were conducted according to protocols approved by the Institutional Animal Care and Use Committee of Children's Hospital, Boston, MA, which strictly observe federal, local, and institutional guidelines. All procedures besides injections and oral gavages were performed under general anesthesia after intraperitoneal injection of 2.5% Avertin (Sigma-Aldrich, St. Louis, MO). Procedures were done at room temperature.

Murine OHSS Model

Pregnant mare serum gonadotropin (Sigma-Aldrich) was administered intraperitoneally (20 IU/day) for 3 days and on day 4, hCG (Sigma-Aldrich) (5 IU) was injected to induce ovulation. Vascular permeability was quantified using the modified Miles vascular permeability assay (13). Mice were anesthetized 48 hours after hCG, and 0.1 mL of 5 mM Evan's blue dye was injected intravenously. Evan's blue dye binds to plasma proteins and leaks with them at sites of vessel permeability. After 30 minutes, 2 mL of sterile saline were injected intraperitoneally. The fluid was then carefully massaged throughout the abdomen for 1 minute, after which the abdominal cavity was opened in the midline. One milliliter of fluid was removed, pipetted into a 96-well ELISA plate (eBioscience, San Diego, CA), and absorbance was read at 620 nm.

Designated groups of mice were treated during hormone stimulation (days 1–4) with daily oral doxycycline (0–80 mg/kg/day) by gavage (100 μL in water). Control mice were given equal volumes of water. In all experiments four to five mice were used per treatment group. Of note, it has been previously shown (14) that a doxycycline dose of 100 mg/kg/day in mice achieved a mean plasma concentration similar to the plasma levels of human patients taking the commonly used dose of 200 mg/day. We therefore chose a similar dosing range in all our experiments.

Ascites volume was determined 48 hours after hCG, using Evans blue dye dilution. Mice were anesthetized and 2 mL of 0.01% Evans blue in saline was injected intraperitoneally. The fluid was then retrieved as described above and the concentration of diluted dye was determined at 620 nm. The volume of peritoneal fluid was calculated as:

$$\text{Volume } [\mu\text{L}] = [(\text{OD 620 nm injected}/\text{OD 620 nm retrieved}) \times 2000] - 2000.$$

Histology and Immunohistochemistry

To investigate the effect of doxycycline treatment on follicular development, we counted the number of corpora lutea per ovary as an indicator of recent ovulation. Formalin fixed ovaries were embedded in paraffin, sectioned (4–6 μm), and stained with Harris' hematoxylin and eosin (Fisher Scientific, Pittsburgh, PA). The number of corpora lutea/ovary (largest diameter section) were counted.

Ovarian sections were also stained with rat antimouse anti-CD31 (BD Biosciences PharMingen, San Jose, CA) for the visualization of blood vessels, using the Vectastain Elite ABC kit (Vector Laboratories, Burlingame, CA).

Data Analysis

Peritoneal fluid volume, mouse and ovarian weights, corpora lutea counts, and the concentration of Evans blue dye in the peritoneum (OD 620 nm) data were reported as mean $\pm$ SD for each group. After verifying equal variances within the different groups of mice using the Levene test, the differences between groups were compared using analysis of variance (ANOVA). A value of $P<.05$ was considered statistically significant. Subsequent pairwise comparisons between groups were performed using Tukey-Kramer HSD test. All statistical analysis was performed using Microsoft Excel datasheets and JMP 7.01 software.

RESULTS

Doxycycline Prevents Generalized Edema and Ascites Accumulation

We first tested the effect of doxycycline treatment on generalized edema and ascites formation in gonadotropin-stimulated mice. As demonstrated in Figure 1A, untreated mice gained ~15% in weight during the course of the experiment. Gonadotropin treatment led to a twofold increase in weight compared with the untreated mice. This weight gain may be attributed to the expected generalized edema caused by gonadotropin treatment leading to OHSS. Doxycycline treatment decreased significantly this weight gain in a dose-dependent fashion (Fig. 1A). Importantly, control mice treated with high-dose doxycylcline (80 mg/kg/day) for similar time periods did not lose weight, nor did they show other

FIGURE 1

Doxycycline prevents edema and ascites accumulation caused by gonadotropin stimulation. (**A**) Ovarian hyperstimulation syndrome was induced in female mice (n = 5/group). Designated groups of mice were treated with oral doxycycline (0–40 mg/kg/day) as of day 1 of gonadotropin stimulation. The percentage of weight increase over baseline values is presented (ANOVA, $P=.02$; Tukey-Kramer HSD, $^*P<.05$). (**B**) In another experiment (n = 5/group) mice were treated with doxycycline (80 mg/kg/day) or vehicle and the volume of peritoneal fluid was determined by Evans blue dye dilution (ANOVA, $P=.045$; Tukey-Kramer HSD, $^*P<.05$).

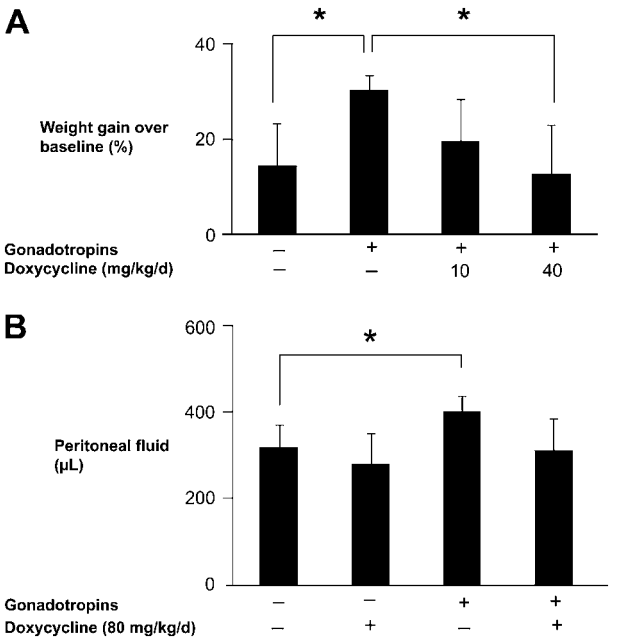

Fainaru. Doxycycline and ovarian hyperstimulation. Fertil Steril 2008.

signs of toxicity when compared with vehicle-treated mice (data not shown).

We next tested whether doxycycline affected intraperitoneal ascites accumulation (Fig. 1B). As hypothesized, gonadotropin stimulation led to a significant increase of peritoneal fluid volume when compared with vehicle-treated controls. Note that similar to its effect on general weight gain, doxycycline treatment decreased ascites accumulation caused by gonadotropin administration.

Doxycycline Prevents Peritoneal Vessel Leakage

We next tested the hypothesis that doxycycline administration leads to decreased peritoneal vascular leakage. OHSS was induced in mice and 48 hours after hCG we performed a modified Miles assay (13). Gonadotropin treatment led to an approximate twofold increase in protein leakage into the abdominal cavity when compared with nonstimulated mice (Fig. 2A). When mice were treated with doxycycline, a dose-dependent decrease in peritoneal vascular leakage was observed. Gonadotropin treatment led to an increase in ovarian weight (Fig. 2B). Importantly, doxycycline did not affect the increase in ovarian weight observed in gonadotropin-stimulated mice.

Doxycycline Does Not Inhibit Ovarian Stimulation

We next tested whether the observed doxycycline-induced inhibition of vascular hyperpermeability results from disturbed ovarian stimulation. Histologic sections were prepared from ovaries harvested 48 hours after hCG from mice that were or were not treated by doxycycline (80 mg/kg/day) (Fig. 3A). The general morphology of stimulated ovaries from both groups showed similar features; the number of corpora lutea observed in both groups was similar (Fig. 3B). We next sought to determine whether the antiangiogenic properties of doxycycline would affect vascular development within the corpus luteum. Histologic sections, in which endothelial cells were specifically stained with anti-CD31 antibodies, showed no difference in microvascular density in the corpora

FIGURE 2

Doxycycline prevents peritoneal vessel leakage. Ovarian hyperstimulation syndrome was induced in female mice (n = 5 mice/group). Designated groups of mice were treated with oral doxycycline (0–40 mg/kg/day) as of day 1 of gonadotropin stimulation. (**A**) Forty-eight hours after hCG administration, Evans blue was injected intravenously. Vascular leakage in the abdominal cavity was analyzed by measuring spectrophotometrically the dye concentration in the fluid retrieved by peritoneal lavage (ANOVA, $P=.0072$; Tukey-Kramer HSD, $^*P<.05$). (**B**) Ovarian weight from the same mice (ANOVA, $P<.0001$; Tukey-Kramer HSD, $^*P<.05$).

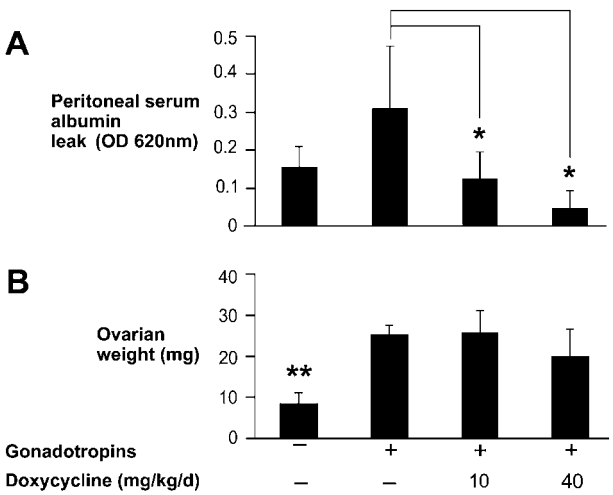

Fainaru. Doxycycline and ovarian hyperstimulation. Fertil Steril 2008.

FIGURE 3

Doxycycline does not affect ovarian stimulation or angiogenesis. Ovarian hyperstimulation syndrome was induced in female mice (n = 4 mice/group). Designated groups of mice were treated with oral doxycycline (80 mg/kg/day) as of day 1 of gonadotropin stimulation. Histologic sections were prepared from ovaries harvested 48 hours after hCG and stained with H&E; bar = 500 μm (**A**). The number of corpora lutea (examples designated by red disturbed circle) in ovarian sections with the largest diameter was determined (Student's *t* test; *P*=NS) (**B**). Endothelial cells within the corpora lutea were specifically stained with anti-CD31 antibodies (**C**). Note the similar microvessel density in both sections; bar = 100 μm.

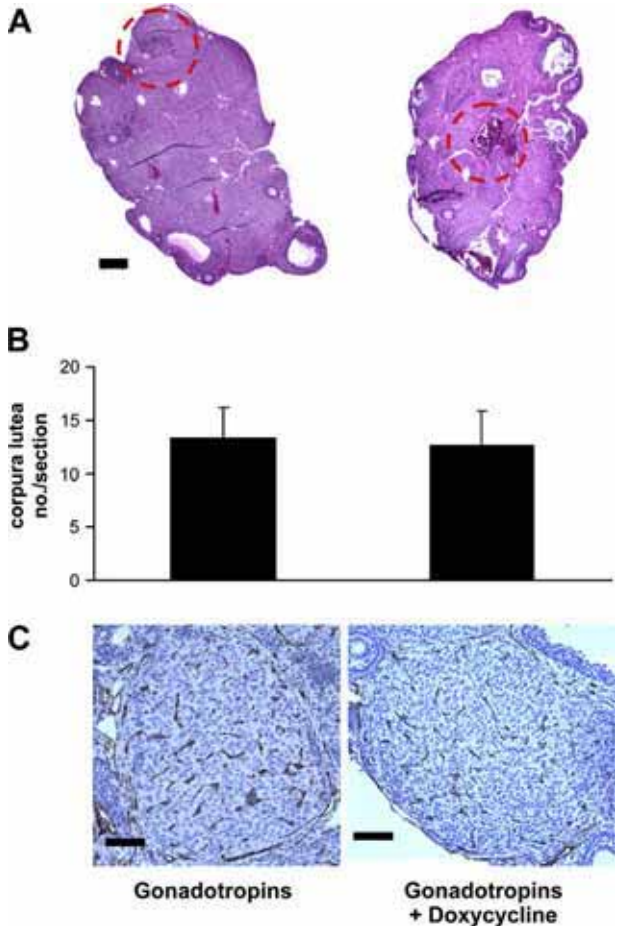

Fainaru. Doxycycline and ovarian hyperstimulation. Fertil Steril 2008.

lutea between ovaries derived from doxycycline-treated or -untreated mice (Fig. 3C).

DISCUSSION

Ovarian hyperstimulation syndrome is an iatrogenic disorder associated with marked morbidity and cost. Proposed methods for avoiding OHSS include lowering the gonadotropin stimulation doses, cancellation of in vitro fertilization (IVF) cycles (withholding hCG), or freezing and postponing the transfer of the embryos rather than transferring them at their fresh state (15). These methods result in lower success rates in achieving pregnancy, patient frustration, and higher cost. Yet to date there are no therapies that directly target the underlying pathophysiology of OHSS, namely vascular hyperpermeability. Therefore, direct inhibition of vascular permeability may be an attractive new therapeutic option for patients undergoing controlled ovarian hyperstimulation when signs and symptoms of OHSS develop or when highly elevated hormone levels precede these symptoms.

We have recently demonstrated that oral doxycycline prevents vascular permeability in several mouse models of disease (12). To test the potential of doxycycline in treating vascular hyperpermeability caused by gonadotropin stimulation, we used a mouse model of OHSS based on the rat experimental model reported by Ujioka et al. (16), in which gonadotropin treatment led to increased vascular permeability in the ovaries. Administration of high doses of the postmenopausal gonadotrophins PMSG and hCG resulted in increased ovarian weight, vascular permeability, expression of VEGF and its receptors, and production of sex steroids such as progesterone, estradiol, androstenedione, testosterone, and DHEA-S (17), mimicking human OHSS. Treatment with gonadotropin releasing hormone agonists (GnRH-a) in the rat OHSS model has been shown to reduce ovarian weight, sex steroid hormone production, and vascular permeability (18). The latter may be related to a decrease in expression of VEGF and/or its receptors. However, controlled ovarian hyperstimulation in IVF treatment protocols using GnRH-a in humans have been disappointing in the prevention of OHSS (19).

We now show that the drug, doxycycline, directly inhibits vascular hyperpermeability in a mouse model of OHSS in a dose-dependent manner. Doxycycline decreased the gonadotropin-induced general edema formation (as demonstrated by reduced body weight gain), the development of ascites, and the direct permeability of peritoneal blood vessels (as determined by Evans blue leakage). The long elimination half life of doxycycline (12–25 hours) (20), necessitates at least 3–5 days of treatment to achieve steady state plasma levels. Nevertheless, we have now performed VEGF induced vascular permeability assays (using classical Miles Assays) (13) and have observed a significant anti vascular permeability effect as soon as 24 hours after doxycycline treatment (data not shown). We can therefore speculate that doxycycline treatment can be started later on the course of gonadotropin treatment and will still be effective in preventing vascular leakage. The antivascular leakage in gonadotropin-treated mice was achieved without compromising ovarian stimulation as demonstrated by similar ovarian weight increases, histologic features, and corpus luteum formation. Importantly, doxycycline did not affect angiogenesis in the corpus luteum, but rather the vascular hyperpermeability effect caused by the gonadotropin induced proangiogenic milieu. This may explain the

normal development of corpora lutea in the presence of doxycycline, as angiogenesis is central in the development of these highly vascularized structures.

Doxycycline treatment has been incorporated into several IVF programs, and the safety of extended therapy has also been reported (21). Doxycycline may help in treating occult tubal and endometrial inflammation caused by chlamydia or other bacteria, which may impair the development of the preimplantation embryo (21). Our findings suggest that doxycycline therapy, given during the course of gonadotropin stimulation, may also prevent vascular hyperpermeability and the development of OHSS if given prophylactically to high risk patients from the beginning of gonadotropin stimulation. This promising new potential of doxycycline warrants clinical trials.

Acknowledgments: We thank Dr. Donald Ingber for critically reviewing the manuscript, Lauren Bazinet for technical assistance, and Kristin Johnson for graphic work.

REFERENCES

1. Geva E, Jaffe RB. Role of vascular endothelial growth factor in ovarian physiology and pathology. Fertil Steril 2000;74:429–38.
2. Navot D, Margalioth EJ, Laufer N, Birkenfeld A, Relou A, Rosler A, et al. Direct correlation between plasma renin activity and severity of the ovarian hyperstimulation syndrome. Fertil Steril 1987;48:57–61.
3. Senger DR, Galli SJ, Dvorak AM, Perruzzi CA, Harvey VS, Dvorak HF. Tumor cells secrete a vascular permeability factor that promotes accumulation of ascites fluid. Science 1983;219:983–5.
4. Folkman J. Angiogenesis: an organizing principle for drug discovery? Nat Rev Drug Discov 2007;6:273–86.
5. Dvorak HF. Vascular permeability factor/vascular endothelial growth factor: a critical cytokine in tumor angiogenesis and a potential target for diagnosis and therapy. J Clin Oncol 2002;20:4368–80.
6. Levin ER, Rosen GF, Cassidenti DL, Yee B, Meldrum D, Wisot A, et al. Role of vascular endothelial cell growth factor in Ovarian Hyperstimulation Syndrome. J Clin Invest 1998;102:1978–85.
7. McClure N, Healy DL, Rogers PA, Sullivan J, Beaton L, Haning RV Jr, et al. Vascular endothelial growth factor as capillary permeability agent in ovarian hyperstimulation syndrome. Lancet 1994;344:235–6.
8. Neulen J, Yan Z, Raczek S, Weindel K, Keck C, Weich HA, et al. Human chorionic gonadotropin-dependent expression of vascular endothelial growth factor/vascular permeability factor in human granulosa cells: importance in ovarian hyperstimulation syndrome. J Clin Endocrinol Metab 1995;80:1967–71.
9. Golub LM, Lee HM, Ryan ME, Giannobile WV, Payne J, Sorsa T. Tetracyclines inhibit connective tissue breakdown by multiple non-antimicrobial mechanisms. Adv Dent Res 1998;12:12–26.
10. Moses MA, Harper J, Folkman J. Doxycycline treatment for lymphangioleiomyomatosis with urinary monitoring for MMPs. N Engl J Med 2006;354:2621–2.
11. Suomalainen K, Sorsa T, Golub LM, Ramamurthy N, Lee HM, Uitto VJ, et al. Specificity of the anticollagenase action of tetracyclines: relevance to their anti-inflammatory potential. Antimicrob Agents Chemother 1992;36:227–9.
12. Fainaru O, Adini I, Benny O, Bazinet L, Pravda E, D'Amato R, et al. Doxycycline induces membrane expression of VE-cadherin on endothelial cells and prevents vascular hyperpermeability. FASEB J 2008.
13. Miles AA, Miles EM. Vascular reactions to histamine, histamine-liberator and leukotaxine in the skin of guinea-pigs. J Physiol 1952;118:228–57.
14. Prall AK, Longo GM, Mayhan WG, Waltke EA, Fleckten B, Thompson RW, et al. Doxycycline in patients with abdominal aortic aneurysms and in mice: comparison of serum levels and effect on aneurysm growth in mice. J Vasc Surg 2002;35:923–9.
15. Mathur R, Kailasam C, Jenkins J. Review of the evidence base of strategies to prevent ovarian hyperstimulation syndrome. Hum Fertil (Camb) 2007;10:75–85.
16. Ujioka T, Matsuura K, Kawano T, Okamura H. Role of progesterone in capillary permeability in hyperstimulated rats. Hum Reprod 1997;12:1629–34.
17. Gomez R, Simon C, Remohi J, Pellicer A. Administration of moderate and high doses of gonadotropins to female rats increases ovarian vascular endothelial growth factor (VEGF) and VEGF receptor-2 expression that is associated to vascular hyperpermeability. Biol Reprod 2003;68:2164–71.
18. Kitajima Y, Endo T, Manase K, Nishikawa A, Shibuya M, Kudo R. Gonadotropin-releasing hormone agonist administration reduced vascular endothelial growth factor (VEGF), VEGF receptors, and vascular permeability of the ovaries of hyperstimulated rats. Fertil Steril 2004;81(Suppl 1):842–9.
19. Rizk B, Smitz J. Ovarian hyperstimulation syndrome after superovulation using GnRH agonists for IVF and related procedures. Hum Reprod 1992;7:320–7.
20. Agwuh KN, MacGowan A. Pharmacokinetics and pharmacodynamics of the tetracyclines including glycylcyclines. J Antimicrob Chemother 2006;58:256–65.
21. Hurst BS, Tucker KE, Awoniyi CA, Schlaff WD. Hydrosalpinx treated with extended doxycycline does not compromise the success of in vitro fertilization. Fertil Steril 2001;75:1017–9.

The FASEB Journal • Research Communication

Doxycycline induces membrane expression of VE-cadherin on endothelial cells and prevents vascular hyperpermeability

Ofer Fainaru,*[,1,2] Irit Adini,[†,1] Ofra Benny,* Lauren Bazinet,* Elke Pravda,* Robert D'Amato,*[,†] and Judah Folkman*

*Vascular Biology Program at Children's Hospital Boston, Department of Surgery, and [†]Department of Ophthalmology, Harvard Medical School, Boston, Massachusetts, USA

ABSTRACT **The endothelium lining blood vessels serves as a barrier against vascular hyperpermeability, and its maintenance is critical to organ health. Inflammatory mediators evoke tissue edema by disrupting the expression of membrane junctional proteins, which mediate binding between endothelial cell membranes. Endothelial cell-cell junctions form a diffusion barrier between the intravascular and interstitial space. To prevent the morbidity and mortality caused by exaggerated vascular permeability associated with pathological states (*e.g.*, inflammatory and hypersensitivity disorders, pulmonary edema, traumatic lung injury, cerebral edema resulting from stroke, and others), it is important to develop therapeutic approaches to stabilize these interendothelial junctions. Vascular endothelial growth factor (VEGF), a potent proangiogenic cytokine, was first described as vascular permeability factor (VPF). Doxycycline, a tetracycline derivative, has been shown to inhibit angiogenesis in both humans and animal models. We now report that oral doxycycline prevents VPF/VEGF-induced vascular permeability, interleukin-2-induced pulmonary edema, and delayed-type hypersensitivity (DTH) in mice. Remarkably, doxycycline also inhibits tumor growth and tumor-associated vascular hyperpermeability. Finally, we show that doxycycline targets the adherens junction in vascular endothelial cells by inducing the total amount of VE-cadherin expression while decreasing the degree of its phosphorylation. The potential of doxycycline as a therapeutic inhibitor of vascular hyperpermeability in human clinical conditions is promising and warrants further studies.—Fainaru, O., Adini, I., Benny, O., Bazinet, L., Pravda, E., D'Amato, R., Folkman. J. Doxycycline induces membrane expression of VE-cadherin on endothelial cells and prevents vascular hyperpermeability. *FASEB J.* 22, 3728–3735 (2008)**

Key Words: pulmonary edema · angiogenesis · delayed-type hypersensitivity

Vascular endothelial growth factor (VEGF) was first described as vascular permeability factor (VPF), a cytokine secreted by tumor cells that rapidly increases microvascular permeability (1). It was then found to be a powerful promoter of angiogenesis, which stimulates microvessel sprouting from existing blood vessels (2). These actions are complementary, as tumor angiogenesis and other forms of pathological angiogenesis are preceded and/or accompanied by enhanced vascular permeability (3). The integrity of the endothelium lining blood vessel walls serves as a barrier against vascular hyperpermeability, and its maintenance is critical for tissue homeostasis. Enhanced vascular permeability due to disruption, loss, or disorganization of the interendothelial junctions—a hallmark of inflammation that can be triggered by various inflammatory mediators [*e.g.*, interleukin (IL) -2, lipopolysacharide] induced by different inciting events (*e.g.*, pathogens, trauma, *etc.*) (4)—is associated with intercellular leakage of large molecular solutes and associated fluid flux across the vascular endothelium, which can lead to tissue edema and organ failure. Conditions in which exaggerated vascular permeability leads to morbidity and mortality include pulmonary edema secondary to traumatic lung injury, stroke-induced cerebral edema, and various inflammatory and hypersensitivity disorders. Yet no therapies exist to prevent or restore junctional integrity in endothelium.

Tetracyclines, potent inhibitors of the matrix metalloproteinase (MMP) proteins, have been used to reduce tissue degradation in arthritis and periodontal disease (5). Doxycycline, a tetracycline derivative, has been shown to inhibit angiogenesis in both humans (6) and animal models (7); however, its antiangiogenic effect is MMP independent *in vitro* (8). We now report that oral doxycycline prevents VPF/VEGF-induced vascular permeability, IL-2-induced pulmonary edema, and delayed-type hypersensitivity (DTH) in mice. We further show that doxycycline prevents tumor vessel hyperpermeability and suppresses tumor growth. Fi-

[1] These authors contributed equally to this work.

[2] Correspondence: Vascular Biology Program, Children's Hospital Boston, Harvard Medical School, 300 Longwood Ave., Boston, MA 02115, USA. E-mail: ofer.fainaru@childrens.harvard.edu

doi: 10.1096/fj.08-110494

0892-6638/08/0022-3728 © FASEB

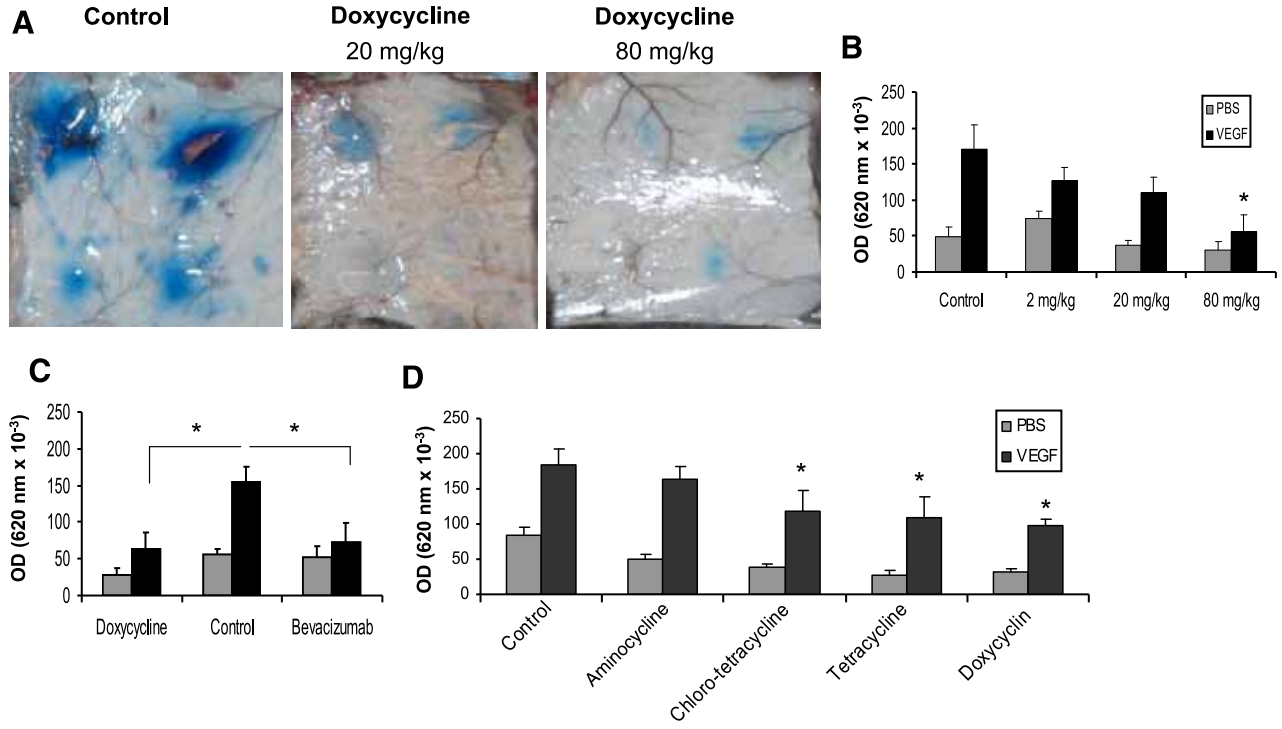

Figure 1. Doxycycline inhibits vascular leakage in dermal vessels. Dermal vessel permeability was determined by the Miles assay. Mice (n=5/group) were pretreated with oral doxycycline (80, 20, and 2 mg/kg/day) or vehicle for 5 days, anesthetized, and administered with i.v. Evans blue. After 10 min, PBS (50 μl) and VEGF (50 ng in 50 μl) were injected into the back skin, and after 20 min mice were sacrificed. *A*) Diminished dye leakage is observed in mice treated with doxycycline. Top: VEGF; bottom: PBS. *B*) Skin was excised, and extracted dye content was quantified by measurement of absorbance at 620 nm (P=0.03; ANOVA). *C*) Pretreatment with a single dose of i.p. bevacizumab (100 μg/mouse) or oral doxycycline (80 mg/kg/day for 5 days) resulted in similar inhibition of vascular leak when compared to control mice (P=0.0002; ANOVA). *D*) To compare the relative potency of different tetracycline analogues on VEGF-induced vascular permeability, mice (n=5/group) were pretreated with i.p. minocycline, chloro-tetracycline, tetracycline, doxycycline (all 80 mg/kg/day) or vehicle for 3 days. On day 4 a Miles assay was performed. Note that the i.p. route of administration was chosen to control for the different oral availability of these drugs (P<0.0001; ANOVA); Data are expressed as means ± SE. *$P < 0.05$ *vs.* control; *post hoc* Tukey-Kramer HSD test.

nally, we show that a possible mechanism for these effects is the specific targeting of adherens junctions by doxycycline, inducing the expression of VE-cadherin and decreasing its phosphorylation on the membranes of endothelial cells.

MATERIALS AND METHODS

Materials

IL-2 was a gift from Dr. Steven A. Rosenberg (National Cancer Institute, Bethesda, MD, USA). $VEGF_{165}$ was a gift from the National Institute of Health (Bethesda, MD, USA). Doxycycline was obtained from American Pharmaceutical Partners (Schaumburg, IL, USA) and from Sigma (St. Louis, MO, USA). Tetracycline, chloro-tetracycline, minocycline, bovine serum albumin, formamide, Evans blue, histamine, platelet activating factor, and oxazolone (4-ethoxymethylene-2-phenyloxazolone) were from Sigma. Avastin (bevacizumab) was provided by Genentech Inc. (South San Francisco, CA, USA). Isoflurane was purchased from Baxter Healthcare Corporation (New Providence, NJ, USA) and Avertin was from Fisher (Pittsburgh, PA, USA). Antibodies: VE-cadherin (Santa Cruz Biotechnology Inc., Santa Cruz, CA, USA), VE-cadherin (Tyr 685)-phospho specific (ECM Biosciences, Versailles, KY, USA), β-catenin (Sigma), β-tubulin (Sigma), β-actin (Sigma), ZO-1 (Zymed, South San Francisco, CA, USA).

Mice

C57Bl/6J mice (6–8 wk) were purchased from Jackson Laboratories (Bar Harbor, ME, USA). All animal procedures were performed in compliance with Boston Children's Hospital guidelines, and protocols were approved by the Institutional Animal Care and Use Committee.

Miles vascular permeability assay

C57Bl/6J mice were treated with oral doxycycline (intragastric gavage) at the specified doses or vehicle for 3–5 days before the Miles assay was performed (9–11). Of note, as it has been previously shown (12), a doxycycline dose of 100 mg/kg/day achieved a mean plasma concentration similar to plasma levels of human patients taking the recommended dose of 200 mg/day. We therefore used a similar dosing range in all our *in vivo* experiments. For the Miles assay, Evans blue dye (100 μl of a 1% solution in 0.9% NaCl) was injected intravenously into mice. Evan's blue dye binds to plasma proteins and leaks with them at sites of vessel permeability. After 10 min, 50 μl of human $VEGF_{165}$ (1 ng/μl), platelet activating factor (PAF; 100 μM), histamine (1.2 μg/ml), or PBS was injected intradermally into the preshaved back skin.

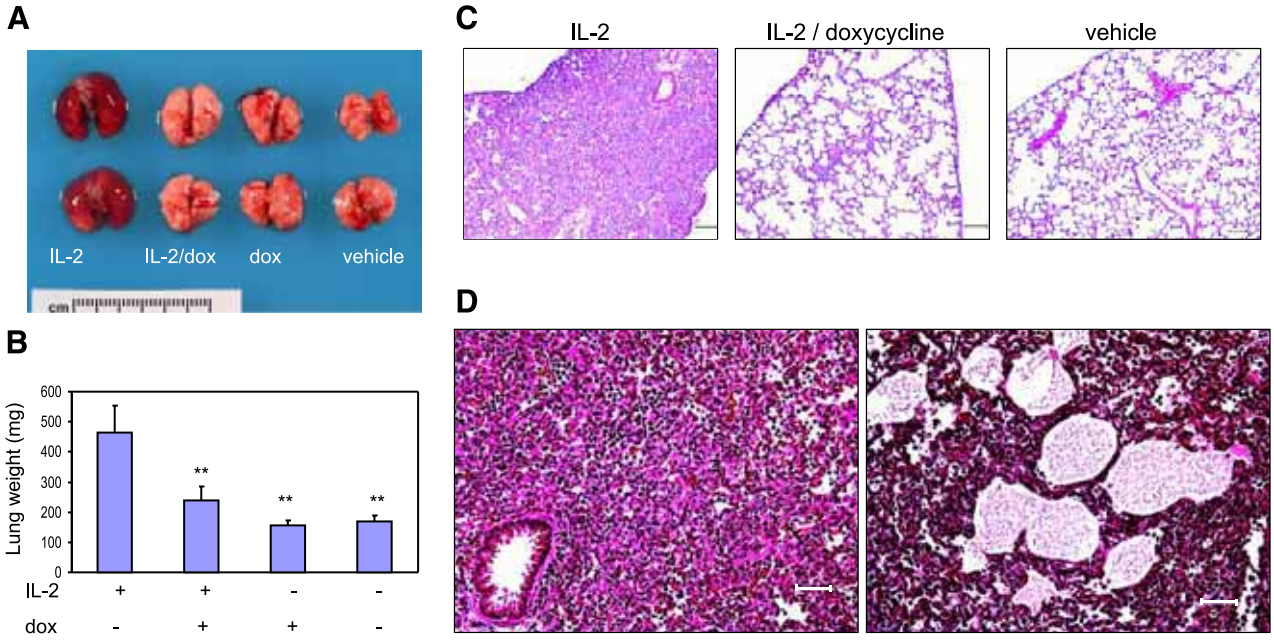

Figure 2. Doxycycline prevents IL-2-induced pulmonary edema. Mice pretreated with oral doxycycline (80 mg/kg/day) or vehicle for 4 days were injected with i.p. IL-2 (1.2×10^6 IU, 3×/day) for 5 days. Doxycycline was continued through the course of IL-2 injections. *A*, *B*) Lungs from sacrificed mice were dissected (*A*) and weighed (*B*). Data are expressed as mean ± SD; n = 5 mice/group. $^{**}P < 0.001$. *C*) IL-2-induced pulmonary edema led to massive thickening of the alveolar wall by cellular infiltration. *D*) At higher magnification, interstitial fibrin deposition and proteinacious fluid accumulation is observed in the alveoli of IL-2 treated mice., Scale bars = 100 μm (*C*); 50 μm (*D*).

After 20 min the animals were sacrificed, and an area of skin that included the entire injection site was removed. Evans blue dye was extracted from the skin by incubation with formamide for 5 days at room temperature, and the absorbance of extracted dye was measured at 620 nm.

Tumor vascular permeability

Mice were inoculated with subcutaneous 1×10^6 Lewis lung carcinoma cells. When tumors reached a volume of ~150 mm^3, mice were treated with doxycycline (80 mg/kg/day) for 9 days. Evans blue dye was then injected intravenously, and dye was extracted from the tumors and assessed as above. The results were normalized to tumor weight.

DTH reactions

DTH reactions were induced in the ears of 8-wk-old C57Bl/6J male mice (n=5) as described previously (13). Mice were sensitized by topical application of 2% oxazolone solution in vehicle (acetone:olive oil, 4:1 v/v), to the shaved abdomen (50 μl). Mice were treated with oral doxycyline (80 mg/kg/day) for 5 days beginning on day 3, and after 5 days the right ears were challenged by topical application of 10 μl of a 1% oxazolone solution; the left ears were treated with vehicle alone. Ear thickness was then measured daily as a measure of inflammation intensity (14). Some mice from each experimental group were sacrificed 24 h after oxazolone challenge. Their ears were fixed in 10% formalin and processed for H&E-stained paraffin sections.

IL-2-associated pulmonary edema

Mice were pretreated with oral doxycycline (80 mg/kg/day) or vehicle for 5 days. On the sixth day, mice received an i.p. injection with IL-2 (1.2×10^6 U/100 μl) or saline 3×/day for 5 days. Doxycycline or vehicle treatment was continued through the course of IL-2 injections. At termination, mice were sacrificed and lungs were dissected, weighed, fixed, and processed for H&E staining.

Permeability of endothelial monolayers

Endothelial permeability was analyzed *in vitro* by the diffusion of 2000 kDa fluorescein isothiocyanate (FITC) -dextran (Sigma) through the endothelial monolayer (15). Human microvascular endothelial cells (HMVECs) were grown on Transwell inserts (Costar, Cambridge, MA, USA) up to confluence. The cells were pretreated with doxycycline (20 μM) for 16 h. Medium containing 2.5 mg/ml 2000 kDa FITC-dextran was then loaded in the upper compartment of the Transwell. The amount of FITC-dextran diffused through the endothelial monolayer into the lower compartment was measured by a microplate reader (Vactor^3, PerkinElmer, Waltham, MA, USA).

Cell culture and confocal microscopy

Primary human dermal microvascular endothelial cells were grown in 131 complete medium (Cascade Biologics Inc., Portland, OR, USA), treated at passage 4–6, and used for further studies. In some experiments, cells were grown on coverslips precoated with collagen in 131 complete medium. After reaching confluence, the cells were starved overnight (0.5% BSA in 131 medium) with or without doxycycline (0–30 μM) and then treated with 50 ng/ml VEGF for 10 min. The concentration range of doxycycline used in all the *in vitro* experiments (0–30 μM) corresponds to human serum levels, which were reported to reach up to 160 μM (16).

The cells were fixed with 4% paraformaldehyde for 10 min,

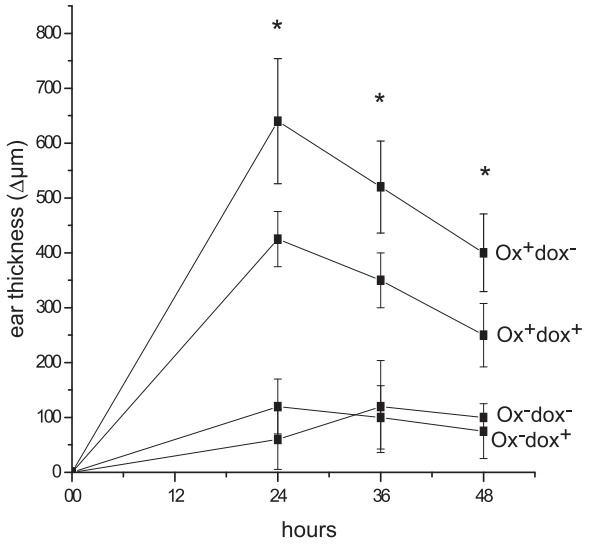

Figure 3. Doxycycline decreases skin edema in a contact sensitivity model. Contact sensitivity (DTH reaction) was induced in the ears of mice (n=5/group) using oxazolone challenge. Ear swelling is expressed as the increase ($\Delta\mu$m) over the original ear thickness (mean±SD). Mice treated with doxycycline showed a significantly decreased ear swelling 24, 36, and 48 h after challenge when compared to controls. Control ears challenged with vehicle alone showed no swelling. *$P < 0.05$. Ox, oxazolone; dox, doxycycline.

followed by incubation with 1% Triton X-100 for 10 min at room temperature and blocking with 3% BSA for 30 min at room temperature. The slips were incubated with the primary antibodies at 4°C overnight. After washing, the cells were incubated with appropriate fluorochrome-conjugated secondary antibodies. Coverslips were washed and mounted with Vectashield HardSet Mounting Media with DAPI (Vector Laboratories, Burlingame, CA, USA). Optical sections were scanned using a Leica TCS SP2 AOBS confocal system fitted to a DM IRE2 inverted microscope (Leica Microsystems, Wetzlar, Germany) with an ×40 objective and 488 nm argon, 543 nm HeNe, 633 nm HeNe, and 405 nm diode lasers. Images were scanned sequentially to avoid fluorescence crossover, and z stacks were produced by scanning optical sections every 366 nm.

Western blots

Cells were lysed in RIPA buffer [50 mM Tris HCl (pH 7.5), 150 mM NaCl, 1% Nonidet P-40, 0.5% sodium deoxycholate, 0.1% SDS, 0.2 mM PMSF, and 2 mM sodium orthovanadate] supplemented with protease inhibitor cocktail (Sigma). Protein was quantified, and 40 μg was run on 10% PAGE, blotted, and incubated with primary antibodies. Pierce detection reagents were used to visualize horseradish peroxidase-labeled secondary antibodies. Relative band intensity was quantified using Image J 1.37 v software (U.S. National Institutes of Health, Bethesda, MD, USA).

Data analysis

Tumor volume (mm^3) was calculated using the following formula: (tumor width)^2 × tumor length × 0.52. Statistical comparisons of continuous data were performed using Student's t test. Unpaired 2-tailed values of $P < 0.05$ were considered statistically significant. For multiple comparisons, the differences between groups were compared using analysis of variance (ANOVA); values of $P < 0.05$ were considered statistically significant. Subsequent pairwise comparisons between groups were performed using Tukey-Kramer HSD test. All statistical analyses were performed using Microsoft Excel datasheets (Microsoft, Redmond, WA, USA) and JMP 7.01 software (SAS Institute, Cary, NC, USA).

RESULTS

Doxycycline inhibits microvessel permeability

We used the Miles assay (10, 17) to determine the effect of doxycycline on VEGF-induced vascular permeability (**Fig. 1**). Doxycycline pretreatment decreased VEGF-induced extravasation of Evans Blue dye in a dose-dependent fashion (Fig. 1*A*, *B*). Bevacizumab, an antibody that recognizes all isoforms of VEGF-A, is known to block vascular permeability (18). When mice were pretreated with oral doxycycline (80 mg/kg) for 5 days or with a single injection of i.p. Bevacizumab (100 μg) before carrying out the assay, both doxycycline and bevacizumab inhibited vascular permeability (2.4- and 2.1-fold, respectively) when compared to controls (Fig. 1*C*). To determine the specificity of this effect, the

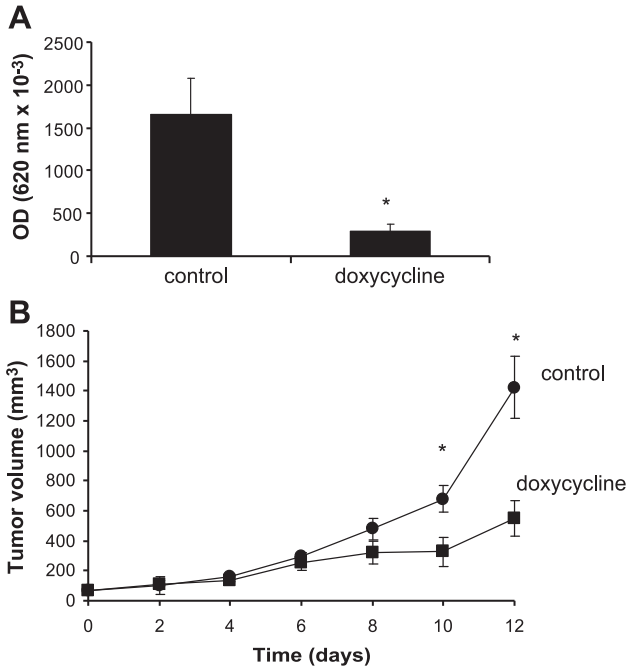

Figure 4. Doxycycline reduces tumor blood vessel permeability. Lewis lung carcinoma cells (10^6 cells) were injected subcutaneously on the flank skins of mice (n=3/group). At a tumor volume of ~150 mm^3, treatment with oral doxycycline (80 mg/kg/day) or vehicle was begun; after 9 days, mice were anesthetized and Evans blue was injected intravenously. After 10 min, the mice were sacrificed, and tumors were excised, weighed, and incubated in formamide for 5 days. *A*) Extravasated dye was measured at 620 nm, and the concentration was adjusted to tumor weight. *B*) In another experiment (n=5 mice/group), treatment was continued for 12 days; tumor volume was measured every 2 days during the course of treatment. Data are expressed as mean ± SE. *$P < 0.05$.

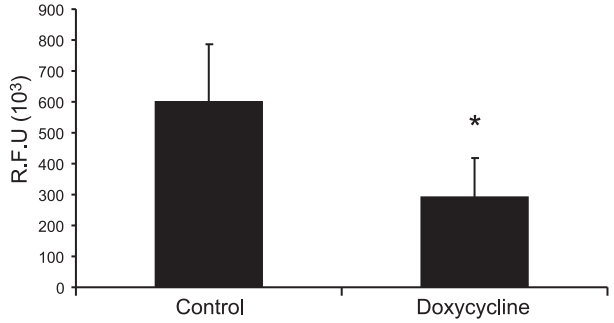

Figure 5. Doxycycline inhibits endothelial monolayer permeability. Endothelial permeability was measured by the diffusion of 2000 kDa FITC-dextran through the endothelial monolayer. HMVECs were grown on Transwell inserts to confluence. The cells were or were not treated overnight with doxycycline (20 μM). Medium containing 2000 kDa FITC-dextran was then loaded in the upper compartment of the Transwell. The amount of FITC-dextran diffused through the endothelial monolayer into the lower compartment was measured by a microplate reader. R.F.U., relative fluorescent units. $*P < 0.05$.

relative efficacy of various tetracycline analogues was compared with respect to their ability to prevent VEGF-induced vascular hyperpermeability following i.p. administration. Remarkably, when compared to minocycline, chloro-tetracycline, and tetracycline, doxycycline was the most effective in preventing Evan's blue dye leakage (Fig. 1*D*).

Doxycycline decreases IL-2-induced pulmonary edema

Treatment of patients with metastatic melanoma and renal cell carcinoma by i.v. administration of IL-2 is often limited by the development of a capillary leak syndrome, which, in turn, may cause life-threatening systemic edema (19). To explore the possibility that doxycycline may prevent this potentially lethal complication, mice were pretreated with oral doxycycline (80 mg/kg/day) or vehicle for 4 days before administering i.p. IL-2 for 5 days in the continued presence of drug. IL-2-treated mice developed severe pulmonary edema, as demonstrated by a 2.75-fold increase in wet lung weight when compared to vehicle-treated controls (**Fig. 2*A*, *B***), confirming previously published results (17). Histological sections of the lungs from control mice revealed severe congestion and edema with intra-alveolar fibrin deposition, as well as perivascular and peribronchial mononuclear cell infiltrates (Fig. 2*C*, *D*). Impressively, doxycycline almost completely inhibited the IL-2-induced increase in lung weight (Fig. 2*A*, *B*) and prevented tissue edema (Fig. 2*C*), without producing any evidence of systemic toxicity or weight loss.

Doxycycline decreases microvascular permeability in delayed type hypersensitivity

The DTH reaction is also characterized by enhanced vascular permeability and edema formation (20); thus, we tested whether doxycycline can inhibit this reaction in a mouse model of contact dermatitis. Mice were sensitized by applying the hapten oxazolone to their abdominal skin and then were treated either with oral doxycycline (80 mg/kg/day) or vehicle beginning on day 3 after sensitization. Six days after sensitization, we challenged the mice by application of oxazolone or vehicle to the right and left ears, respectively. Mice treated with doxycycline exhibited significantly reduced ($P<0.05$) erythema and ear swelling compared with vehicle-treated control mice at 24, 36, and 48 h (**Fig. 3**). Histological analysis demonstrated similar inflammatory mononuclear cell infiltration into the oxazolone challenged ear in both doxycycline-treated and untreated mice (not shown).

Doxycycline inhibits tumor blood vessel permeability and tumor growth

We next tested whether doxycycline would also prevent tumor vessel hyperpermeability. Mice bearing subcutaneous implants of Lewis lung carcinoma ~150 mm^3 in volume were treated with either oral doxycycline (80 mg/kg/day) or vehicle for 8 days, and on day 9 Evans blue was injected intravenously. Treatment with doxycycline reduced Evans Blue leakage from the tumor vasculature when compared to vehicle-treated mice (**Fig. 4*A***). Remarkably, doxycycline treatment for 12 days also resulted in a decrease in tumor volume by ~40% (Fig. 4*B*).

Doxycycline inhibits permeability of endothelial cell monolayers

We next tested the effect of doxycycline on endothelial permeability *in vitro* by quantifying the diffusion of 2000 kDa FITC-dextran through endothelial monolayers. HMVECs were grown to confluence on Transwell inserts. The cells were incubated overnight with doxycycline (20 μM). FITC-dextran was then loaded in the upper compartment of the Transwell. The amount of FITC-dextran diffused through the endothelial monolayer into the lower compartment was measured after 90 min. As depicted in **Fig. 5**, doxycycline pretreatment significantly inhibited vascular leakage when compared to control endothelial monolayers.

Doxycycline increases membrane expression of VE-cadherin and inhibits its phosphorylation in endothelial cells

We next sought to determine the mechanism by which doxycycline prevents vascular permeability in these mouse models. It is known that VEGF/VPF enhances endothelial cell permeability by promoting endocytosis of cell surface VE-cadherin (21). This effect disturbs the function of the adherens junction and leads to leakiness of the endothelial monolayer.

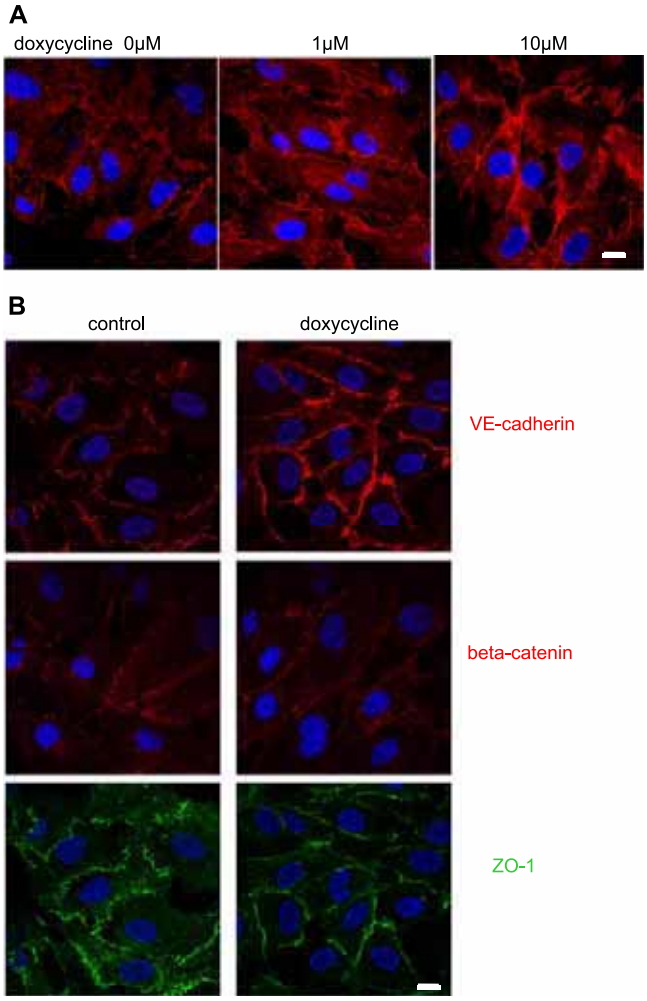

Figure 6. Doxycycline induces VE-cadherin expression at the cell junctions. *A*) HMVEC monolayers were serum starved for 16 h in the presence of doxycycline (0–10 μM) before stimulation with VEGF (10 min, 50 ng/ml). Cells were fixed, stained with anti VE-cadherin, and examined by confocal microscopy. *B*) Untreated endothelial cell monolayers (not subjected to starving or VEGF treatment) were subjected to doxycycline (30 μM) or vehicle for 16 h and were stained with anti-VE-cadherin, anti-β-catenin, ZO-1, and DAPI. Scale bars = 10 μm.

When serum-starved confluent human dermal microvascular endothelial cell monolayers were cultured overnight in the presence of doxycycline (0–30 μM) before stimulation with VEGF (10 min, 50 ng/ml), VE-cadherin staining was found to increase as the doxycycline concentration was raised when analyzed using both confocal immunofluorescence microscopy (**Fig. 6*A***) and Western blots (**Fig. 7*A***). Remarkably, doxycycline significantly inhibited the VEGF-induced decrease in VE-cadherin expression (Fig. 7*B*). This increase in VE-cadherin expression appeared to be a direct effect of doxycycline on endothelial cells, as a similar increase was observed in doxycycline-treated cells that were not starved or exposed to VEGF (Fig. 6*B*). In contrast, neither the expression of β-catenin, another adherens junction protein that colocalizes with VE-cadherin (22), nor the tight junction protein ZO-1 (23) was influenced by doxycycline treatment (Figs. 6*B* and 7*A*). As expected (24), VEGF treatment led to phosphorylation of VE-cadherin (Fig. 7*B*). Doxycycline pretreatment, however, reduced this phosphorylation. Taken together, these results suggest that doxycycline specifically targets the adherens junctions in endothelial cells by increasing membrane expression of VE-cadherin and inhibiting its phosphorylation.

DISCUSSION

Angiogenesis is a complex process that involves endothelial cell proliferation, migration, and pericyte recruitment. However, all forms of pathological angiogenesis, such as neovascularization induced by tumors and inflammation, are characterized by vascular hyperpermeability, usually caused by VEGF/VPF (25, 26). This increased permeability results in edema, clotting, and deposition of a provisional matrix that favors new vessel formation with mature stroma generation (27). Vascular hyperpermeability also contributes to the morbidity and mortality caused by fluid accumulation in body cavities (*e.g.*, pleura and peritoneum) and organs (*e.g.*, lung and brain) secondary to trauma or inflammation. Given that many angiogenesis inhibitors act by interfering with VEGF function, we tested the ability of the FDA-approved oral angiogenesis inhibitor, doxycycline, on vascular permeability in various mouse models of pathological angiogenesis and edema formation (6, 7).

We first demonstrated that doxycycline inhibited VPF/VEGF-induced vascular permeability in a dose-dependent manner using the *in vivo* vascular permeability (Miles) assay. We confirmed this effect of doxycycline on the vascular endothelium by showing its inhibition of FITC-dextran leakage through endothelial cell monolayers *in vitro*. Remarkably, the effect of doxycycline was comparable to that achieved by bevacizumab, a powerful inhibitor of VEGF action (18), in the Miles assay. When compared to tetracycline and other related compounds (*i.e.*, minocycline, chloro-tetracycline), doxycycline was the most effective at preventing Evan's blue dye leakage. The effect of doxycycline was not specific for VEGF/VPF, as it also prevented vascular leak induced by histamine but not that induced by PAF (data not shown). PAF was reported to modulate vascular permeability through inducing nitric oxide synthesis (28), which affects the integrity of the tight junction (29) rather than the adherens junction. Taken together with our immunostaining results, our findings suggest that doxycycline treatment specifically enhances the structural integrity of the adherens junction.

Of the molecular structures comprising the endothelial cell-cell contacts, the adherens junctions, composed of cadherins and catenins, are the primary adhesions between the cells and are essential for

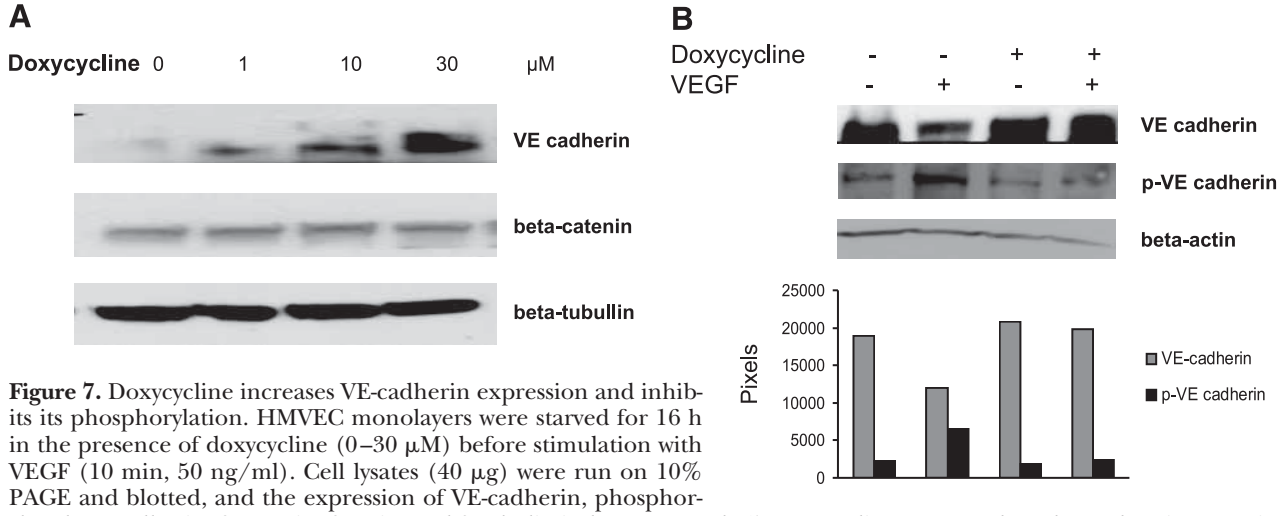

Figure 7. Doxycycline increases VE-cadherin expression and inhibits its phosphorylation. HMVEC monolayers were starved for 16 h in the presence of doxycycline (0–30 μM) before stimulation with VEGF (10 min, 50 ng/ml). Cell lysates (40 μg) were run on 10% PAGE and blotted, and the expression of VE-cadherin, phosphorylated-VE-cadherin, β-catenin, β-actin, and β-tubulin is demonstrated. *A*) Doxycycline causes a dose-dependent increase in expression of VE-cadherin. *B*) Doxycycline (20 μM) inhibits both the VEGF-induced decrease in VE-cadherin expression and the VEGF-induced VE-cadherin phosphorylation. Bottom panel shows relative band intensity. p-VE-cadherin, phosphorylated VE-cadherin.

barrier integrity (22). At the endothelial adherens junction, the key transmembrane protein is VE-cadherin (30, 31), which clusters together in these regions and mediates cell-cell adhesion through homophilic binding to other VE-cadherins expressed on adjacent endothelial cells. Paracellular permeability induced by inflammatory mediators, such as histamine and VEGF, is accompanied by phosphorylation of VE-cadherin (24), disruption of the VE-cadherin/catenin complex, and loss of cadherin from the cell borders (4, 21). In fact, disruption of cadherins within the adherens junction mediates the increase in permeability and lung edema that are induced by inflammatory stimuli (32, 33). Our results show that doxycycline treatment increases the expression of VE-cadherin at the intercellular junctions of human dermal endothelial cells *in vitro* without significantly altering the expression of β catenin or ZO-1. It has been suggested (34) that the phosphorylation of VE-cadherin leads to a decrease in cell contact integrity. We now show that doxycycline inhibits VEGF-induced phosphorylation of VE-cadherin. Taken together, these effects on VE-cadherin expression and phosphorylation may explain the potential of doxycycline to protect against VEGF-induced vascular hypermeability *in vivo*, as observed in the Miles assay.

In light of the ability of doxycycline to prevent vascular hyperpermeability, we tested mouse models of clinical conditions where vascular leak serves a major source of morbidity. Immunotherapy with IL-2 represents an important modality in the management of human metatstatic renal cell carcinoma and malignant melanoma. However, this effective treatment is often limited by myriad complications, mainly due to a vascular leak syndrome resulting in pulmonary edema (35, 36). Although it was shown previously (17) that treatment with i.v. administration of the experimental antiangiogenic agent TNP-470 can prevent this complication in mice, the present results show that IL-2-induced pulmonary edema may be effectively prevented by oral administration of the FDA-approved drug doxycycline. Furthermore, we show that this drug effectively inhibits edema caused by delayed type hypersensitivity reactions, and thus it may also prove to be of value in treating allergic conditions in humans. As mentioned above, all forms of pathological angiogenesis, including tumor vessel formation, are preceded by vascular leak and deposition of fibrin in the matrix (3). Doxycycline also prevented the permeability of these vessels in mouse tumors. It is tempting to speculate that this aspect of antiangiogenesis may be responsible for the decrease in tumor size observed in the doxycycline-treated mice, however, the contribution of the reduction in tumor edema to tumor volume was not assessed.

Taken together, our results indicate that doxycycline may prove useful as a potent oral antivascular permeability drug. The mechanism for this effect appears to be the up-regulation of total VE-cadherin at the adherens junctions while decreasing the degree of its phosphorylation, thereby enhancing intercellular adhesion and improving the barrier function of the endothelium. The potential use of this drug in the treatment of human conditions associated with increased vascular permeability warrants clinical trials. FJ

This research was supported by the Fulbright and Rothschild Foundations and the European Molecular Biology Organization (EMBO) Fellowship (O.F.), and Department of Defense award W81XWH-05–1-0115 (to J.F.). We thank Dr. Harold Dvorak for helpful discussions and pathological slide analysis, Dr. Donald Ingber for critically reviewing the manuscript, Kristin Johnson for photography and graphic art, and Steven A. Rosenberg for the generous gift of IL-2.

REFERENCES

1. Senger, D. R., Galli, S. J., Dvorak, A. M., Perruzzi, C. A., Harvey, V. S., and Dvorak, H. F. (1983) Tumor cells secrete a vascular permeability factor that promotes accumulation of ascites fluid. *Science* **219,** 983–985
2. Folkman, J. (2007) Angiogenesis: an organizing principle for drug discovery? *Nat. Rev. Drug Discov.* **6,** 273–286
3. Dvorak, H. F. (2002) Vascular permeability factor/vascular endothelial growth factor: a critical cytokine in tumor angiogenesis and a potential target for diagnosis and therapy. *J. Clin. Oncol.* **20,** 4368–4380
4. Leach, L. P. C., and Carden, D. (2005) Interendothelial junctions and barrier integrity. *Adv. Mol. Cell Biol.* **35,** 251–276
5. Golub, L. M., Lee, H. M., Ryan, M. E., Giannobile, W. V., Payne, J., and Sorsa, T. (1998) Tetracyclines inhibit connective tissue breakdown by multiple non-antimicrobial mechanisms. *Adv. Dent. Res.* **12,** 12–26
6. Moses, M. A., Harper, J., and Folkman, J. (2006) Doxycycline treatment for lymphangioleiomyomatosis with urinary monitoring for MMPs. *N. Engl. J. Med.* **354,** 2621–2622
7. Suomalainen, K., Sorsa, T., Golub, L. M., Ramamurthy, N., Lee, H. M., Uitto, V. J., Saari, H., and Konttinen, Y. T. (1992) Specificity of the anticollagenase action of tetracyclines: relevance to their anti-inflammatory potential. *Antimicrob. Agents Chemo.* **36,** 227–229
8. Gilbertson-Beadling, S., Powers, E. A., Stamp-Cole, M., Scott, P. S., Wallace, T. L., Copeland, J., Petzold, G., Mitchell, M., Ledbetter, S., and Poorman, R. (1995) The tetracycline analogs minocycline and doxycycline inhibit angiogenesis in vitro by a non-metalloproteinase-dependent mechanism. *Cancer Chemother. Pharmacol.* **36,** 418–424
9. Claffey, K. P., Brown, L. F., del Aguila, L. F., Tognazzi, K., Yeo, K. T., Manseau, E. J., and Dvorak, H. F. (1996) Expression of vascular permeability factor/vascular endothelial growth factor by melanoma cells increases tumor growth, angiogenesis, and experimental metastasis. *Cancer Res.* **56,** 172–181
10. Miles, A. A., and Miles, E. M. (1952) Vascular reactions to histamine, histamine-liberator and leukotaxine in the skin of guinea-pigs. *J. Physiol.* **118,** 228–257
11. Streit, M., Velasco, P., Riccardi, L., Spencer, L., Brown, L. F., Janes, L., Lange-Asschenfeldt, B., Yano, K., Hawighorst, T., Iruela-Arispe, L., and Detmar, M. (2000) Thrombospondin-1 suppresses wound healing and granulation tissue formation in the skin of transgenic mice. *EMBO J.* **19,** 3272–3282
12. Prall, A. K., Longo, G. M., Mayhan, W. G., Waltke, E. A., Fleckten, B., Thompson, R. W., and Baxter, B. T. (2002) Doxycycline in patients with abdominal aortic aneurysms and in mice: comparison of serum levels and effect on aneurysm growth in mice. *J. Vasc. Surg.* **35,** 923–929
13. Dvorak, A. M., Lett-Brown, M. A., Thueson, D. O., Pyne, K., Raghuprasad, P. K., Galli, S. J., and Grant, J. A. (1984) Histamine-releasing activity (HRA). III. HRA induces human basophil histamine release by provoking noncytotoxic granule exocytosis. *Clin. Immunol. Immunopathol.* **32,** 142–150
14. Gad, S. C., Dunn, B. J., Dobbs, D. W., Reilly, C., and Walsh, R. D. (1986) Development and validation of an alternative dermal sensitization test: the mouse ear swelling test (MEST). *Toxicol. Appl. Pharmacol.* **84,** 93–114
15. Chen, B., Pogue, B. W., Luna, J. M., Hardman, R. L., Hoopes, P. J., and Hasan, T. (2006) Tumor vascular permeabilization by vascular-targeting photosensitization: effects, mechanism, and therapeutic implications. *Clin. Cancer Res.* **12,** 917–923
16. Hoyt, J. C., Ballering, J., Numanami, H., Hayden, J. M., and Robbins, R. A. (2006) Doxycycline modulates nitric oxide production in murine lung epithelial cells. *J. Immunol.* **176,** 567–572
17. Satchi-Fainaro, R., Mamluk, R., Wang, L., Short, S. M., Nagy, J. A., Feng, D., Dvorak, A. M., Dvorak, H. F., Puder, M., Mukhopadhyay, D., and Folkman, J. (2005) Inhibition of vessel permeability by TNP-470 and its polymer conjugate, caplostatin. *Cancer Cell* **7,** 251–261
18. Wedam, S. B., Low, J. A., Yang, S. X., Chow, C. K., Choyke, P., Danforth, D., Hewitt, S. M., Berman, A., Steinberg, S. M., Liewehr, D. J., Plehn, J., Doshi, A., Thomasson, D., McCarthy, N., Koeppen, H., Sherman, M., Zujewski, J., Camphausen, K., Chen, H., and Swain, S. M. (2006) Antiangiogenic and antitumor effects of bevacizumab in patients with inflammatory and locally advanced breast cancer. *J. Clin. Oncol.* **24,** 769–777
19. Berthiaume, Y., Boiteau, P., Fick, G., Kloiber, R., Sinclair, G. D., Fong, C., Poon, M. C., and Lafreniere, R. (1995) Pulmonary edema during IL-2 therapy: combined effect of increased permeability and hydrostatic pressure. *Am. J. Respir. Crit. Care Med.* **152,** 329–335
20. Asherson, G. L., and Ptak, W. (1968) Contact and delayed hypersensitivity in the mouse. I. Active sensitization and passive transfer. *Immunology* **15,** 405–416
21. Gavard, J., and Gutkind, J. S. (2006) VEGF controls endothelial-cell permeability by promoting the beta-arrestin-dependent endocytosis of VE-cadherin. *Nat. Cell Biol.* **8,** 1223–1234
22. Lampugnani, M. G., and Dejana, E. (1997) Interendothelial junctions: structure, signalling and functional roles. *Curr. Opin. Cell Biol.* **9,** 674–682
23. Willott, E., Balda, M. S., Fanning, A. S., Jameson, B., Van Itallie, C., and Anderson, J. M. (1993) The tight junction protein ZO-1 is homologous to the Drosophila discs-large tumor suppressor protein of septate junctions. *Proc. Natl. Acad. Sci. U. S. A.* **90,** 7834–7838
24. Esser, S., Lampugnani, M. G., Corada, M., Dejana, E., and Risau, W. (1998) Vascular endothelial growth factor induces VE-cadherin tyrosine phosphorylation in endothelial cells. *J. Cell. Sci.* **111**(Pt. 13), 1853–1865
25. Carmeliet, P., and Collen, D. (2000) Molecular basis of angiogenesis. Role of VEGF and VE-cadherin. *Ann. N. Y. Acad. Sci.* **902,** 249–262; discussion 262–244
26. Matsumoto, T., and Claesson-Welsh, L. (2001) VEGF receptor signal transduction. *Sci. STKE* **2001,** RE21
27. Feng, D., Nagy, J. A., Dvorak, A. M., and Dvorak, H. F. (2000) Different pathways of macromolecule extravasation from hyperpermeable tumor vessels. *Microvasc. Res.* **59,** 24–37
28. Ramirez, M. M., Quardt, S. M., Kim, D., Oshiro, H., Minnicozzi, M., and Duran, W. N. (1995) Platelet activating factor modulates microvascular permeability through nitric oxide synthesis. *Microvasc. Res.* **50,** 223–234
29. Han, X., Fink, M. P., Uchiyama, T., Yang, R., and Delude, R. L. (2004) Increased iNOS activity is essential for pulmonary epithelial tight junction dysfunction in endotoxemic mice. *Am. J. Physiol. Lung Cell. Mol. Physiol.* **286,** L259–L267
30. Lampugnani, M. G., Resnati, M., Raiteri, M., Pigott, R., Pisacane, A., Houen, G., Ruco, L. P., and Dejana, E. (1992) A novel endothelial-specific membrane protein is a marker of cell-cell contacts. *J. Cell Biol.* **118,** 1511–1522
31. Gumbiner, B. M. (1996) Cell adhesion: the molecular basis of tissue architecture and morphogenesis. *Cell* **84,** 345–357
32. Zhao, X., Alexander, J. S., Zhang, S., Zhu, Y., Sieber, N. J., Aw, T. Y., and Carden, D. L. (2001) Redox regulation of endothelial barrier integrity. *Am. J. Physiol. Lung Cell. Mol. Physiol.* **281,** L879–L886
33. Lim, M. J., Chiang, E. T., Hechtman, H. B., and Shepro, D. (2001) Inflammation-induced subcellular redistribution of VE-cadherin, actin, and gamma-catenin in cultured human lung microvessel endothelial cells. *Microvasc. Res.* **62,** 366–382
34. Vestweber, D. (2008) VE-cadherin: the major endothelial adhesion molecule controlling cellular junctions and blood vessel formation. *Arterioscler. Thromb. Vasc. Biol.* **28,** 223–232
35. Rosenberg, S. A., and Lotze, M. T. (1986) Cancer immunotherapy using interleukin-2 and interleukin-2-activated lymphocytes. *Annu. Rev. Immunol.* **4,** 681–709
36. Mier, J. W., Aronson, F. R., Numerof, R. P., Vachino, G., and Atkins, M. B. (1988) Toxicity of immunotherapy with interleukin-2 and lymphokine-activated killer cells. *Pathol. Immunopathol. Res.* **7,** 459–476

Received for publication March 19, 2008.
Accepted for publication June 12, 2008.

nature biotechnology

An orally delivered small-molecule formulation with antiangiogenic and anticancer activity

Ofra Benny[1], Ofer Fainaru[1], Avner Adini[1], Flavia Cassiola[1], Lauren Bazinet[1], Irit Adini[1], Elke Pravda[1], Yaakov Nahmias[2], Samir Koirala[3], Gabriel Corfas[3], Robert J D'Amato[1,4] & Judah Folkman[1]

Targeting angiogenesis, the formation of blood vessels, is an important modality for cancer therapy. TNP-470, a fumagillin analog, is among the most potent and broad-spectrum angiogenesis inhibitors. However, a major clinical limitation is its poor oral availability and short half-life, necessitating frequent, continuous parenteral administration. We have addressed these issues and report an oral formulation of TNP-470, named Lodamin. TNP-470 was conjugated to monomethoxy-polyethylene glycol–polylactic acid to form nanopolymeric micelles. This conjugate can be absorbed by the intestine and selectively accumulates in tumors. Lodamin significantly inhibits tumor growth, without causing neurological impairment in tumor-bearing mice. Using the oral route of administration, it first reaches the liver, making it especially efficient in preventing the development of liver metastasis in mice. We show that Lodamin is an oral nontoxic antiangiogenic drug that can be chronically administered for cancer therapy or metastasis prevention.

Angiogenesis inhibition has become an important treatment modality for the suppression of tumor growth and metastasis progression[1,2]. TNP-470 is an analog of fumagillin, which was isolated from the fungus *Aspergillus fumigatus fresenius*[3] and is among the most potent inhibitors of angiogenesis. In animal models, TNP-470 showed a broad anticancer spectrum of activity[4]. TNP-470 inhibited the growth of primary and metastatic murine tumors and human xenografts such as breast cancer, neuroblastoma, ovarian cancer, prostate cancer, glioblastoma, neurofibrosarcoma and uterine sarcoma and led to a reduction in their vascularization[5–12]. The mechanism of the antiangiogenic activity of TNP-470 is still not completely clear, though proposed molecular mechanisms have suggested targeting methionine aminopeptidase (MetAP-2), affecting cell cycle through p53 activation, induction of p21(CIP/WAF) or preventing Rac1 activation[11,13–15].

TNP-470 was one of the first antiangiogenic drugs to undergo clinical trials[16]. It demonstrated its ability to slow tumor progression or cause durable complete regression[17] either given as a single agent, or in combination with other conventional chemotherapeutic drugs such as paclitaxel and carboplatin[17–23]. The dose-limiting toxicity was neural side-effects such as dizziness, decreased concentration, short-term memory loss, confusion and depression[23]. Successful elimination of these neurologic symptoms was achieved by the development of Caplostatin (formulated for injection)[24], in which TNP-470 was conjugated to a N-(2-hydroxypropyl)methacrylamide (HPLA) polymer to block penetration of the blood-brain barrier.

Nevertheless, a major clinical limitation of TNP-470 remained unresolved. The poor oral availability of TNP-470 coupled with its extremely short plasma half-life imposes a strict regime of prolonged parenteral administration[23,25]. TNP-470 needs to be administered frequently as continuous intravenous infusions (usually over 1 h, multiple times a week) in the clinic. Therefore, developing an oral formulation may considerably improve patient compliance and provide means for a long-term antiangiogenic therapy for cancer and other angiogenesis-dependent diseases.

In this work we report an oral antiangiogenic polymeric drug with potent antitumor and antimetastatic efficacy named Lodamin. We characterize the physicochemical properties and show that this formulation of TNP-470 overcomes the drug's limitations while retaining its antiangiogenic activity. Lodamin is produced by conjugation of TNP-470 to a di-block copolymer, monomethoxy-polyethyleneglycol–polylactic acid (mPEG-PLA). The amphiphilic nature of this polymeric drug enables self-assembly of micelles in an aqueous medium[26]. In this structure, the TNP-470 is located in the core, where it is protected from the acidic environment of the stomach, thus enabling oral availability. Furthermore, we take advantage of using biocompatible, commonly used and well-characterized polymers[27,28].

Our results indicate that Lodamin, administered orally, is effectively absorbed in the intestine and accumulates in tumor tissue. The drug significantly inhibits angiogenesis, as demonstrated by inhibition of human umbilical vein endothelial cell (HUVEC) proliferation, by the corneal micropocket assay and in mouse tumor models. Lodamin significantly inhibited primary tumor growth as demonstrated in models of melanoma and lung cancer. Notably, oral Lodamin successfully prevented liver metastasis of melanoma

[1]Vascular Biology Program and Department of Surgery, Children's Hospital Boston, Harvard Medical School, 1 Blackfan Circle, St. Karp Research Building, Boston, Massachusetts 02215, USA. [2]Center for Engineering in Medicine, Massachusetts General Hospital, Harvard Medical School, 114 16th Street, Charlestown, Massachusetts 02129, USA. [3]Department of Neurology, F.M. Kirby Neurobiology Center, Children's Hospital, Harvard Medical School, 300 Longwood Avenue, Boston, Massachusetts 02115, USA. [4]Department of Ophthalmology, Harvard Medical School, Children's Hospital Boston, 1 Blackfan Circle, St. Karp Research Building, Boston, Massachusetts 02215, USA. Correspondence should be addressed to O.B. (ofra.bennyratsaby@childrens.harvard.edu).

Received 11 January; accepted 3 June; published online 29 June 2008; doi:10.1038/nbt1415

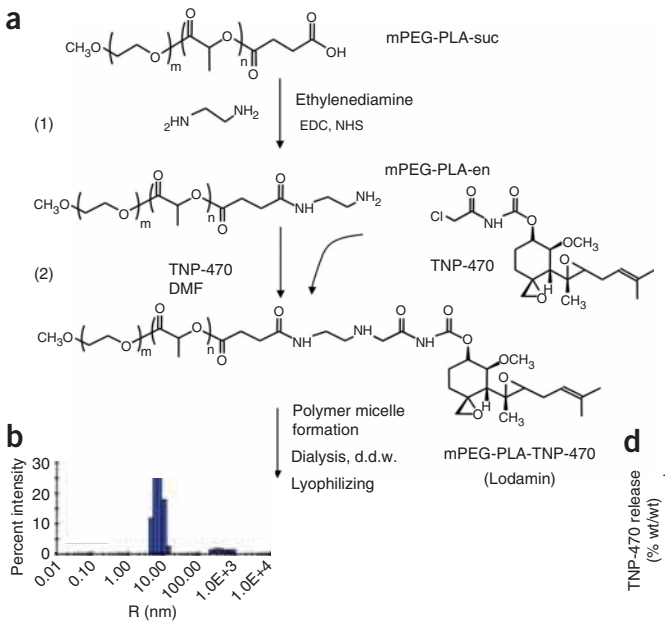

Figure 1 Lodamin synthesis and characterization. (**a**) Diagram of the conjugation reaction between TNP-470 and modified mPEG-PLA. 1. The reaction between succinated mPEG-PLA and ethylendiamine that results in an amine-terminated polymer. 2. The reaction between the amine-containing polymer and the terminal chlorine of TNP-470. The conjugate is then dialyzed against water in an excess of TNP-470 to form polymeric micelles. (**b**) A typical DLS measurement of Lodamin, the graph shows size distribution of the polymeric-micelles in water. (**c**) TEM images of Lodamin dispersed in water, the spherical structure of the micelles are shown at different time points after incubation in water. Scale bar, 10 nm. (**d**) TNP-470 release from Lodamin during a 30-d period as determined by HPLC; micelles were incubated in gastric fluid pH = 1.2 or PBS pH = 7.4 and analysis of the released TNP-470 was done in duplicate. The results are presented as means ± s.d. mPEG-PLA, methoxy-polyethylene glycol–polylactic acid; suc, succinated; EDC, ethyl(diethylaminopropyl) carbodiimide; NHS, *N*-hydroxysuccinimide; en, ethylenamine; d.d.w., double-distilled water; DMF, dimethylformamide.

tumor cells without causing liver toxicity or other side effects and prolonged mouse survival.

Unlike free TNP-470, Lodamin does not penetrate the blood-brain barrier and accordingly did not cause neurotoxicity in mice. These results suggest that Lodamin may be a good candidate for a safe maintenance drug with effective antitumor and antimetastatic properties.

RESULTS

Chemical and physical characterization of Lodamin

To predict the oral availability of TNP-470, we measured its hydrophobicity using the log-D parameter. The measured log-D values were 2.39 at pH = 2 and 2.57 at pH = 7.4. The high log-D values (>2) indicate very low solubility in water. This property

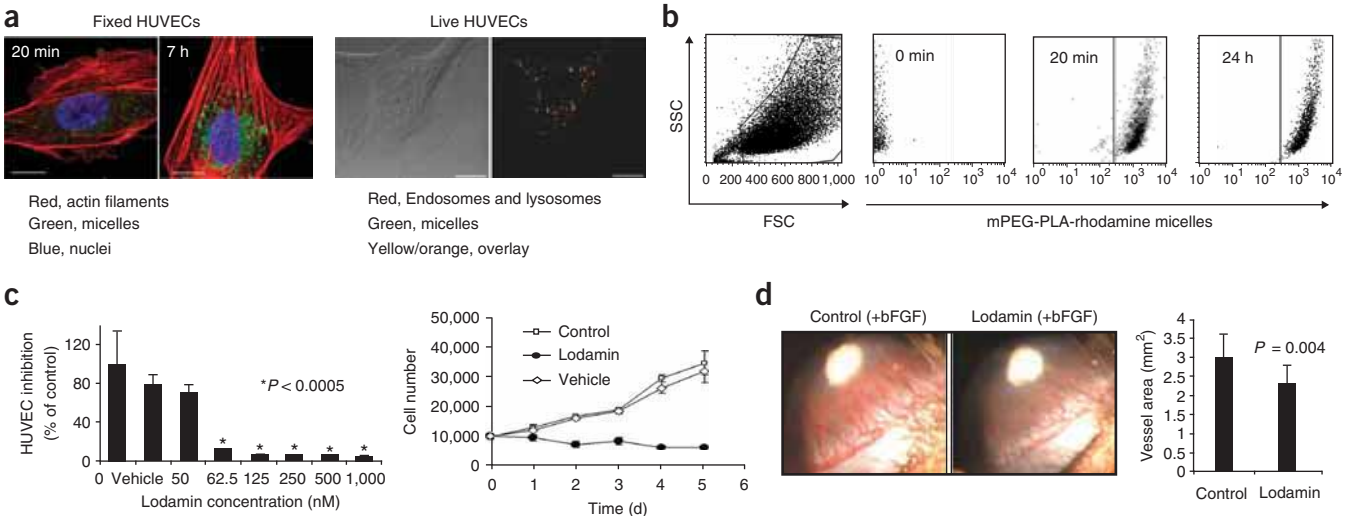

Figure 2 Effect of Lodamin on angiogenesis and cell uptake of the drug. (**a**) Left: Confocal images show HUVEC uptake of polymeric micelles labeled with 6-coumarin after 20 min and 7-h incubation time periods. Right: Live HUVECs imaged 1 h after the addition of labeled micelles to cell medium (15 μg/ml, in green). LysoTracker Red detecting endosomes and lysosomes is shown in red. Overlay between micelles and endosomes/lysosomes is represented in yellow/orange color. Scale bars, 5 μm. (**b**) Uptake of rhodamine-labeled mPEG-PLA micelles by HUVECs was evaluated by FACS analysis. A viable cell gate was established based on forward and side scatter (FSC and SSC), and another gate was set for SSC/$FL4_{high}$-measurement of HUVECs containing mPEG-PLA-rhodamine micelles. Graphs of 0 min, 20 min and 24 hr of incubation with micelles are shown. Incubation after 2, 4 and 7 h showed a similar pattern as after 24 h of incubation (not shown). (**c**) HUVEC growth and proliferation. Upper panel: inhibition of HUVEC proliferation by different concentrations of Lodamin 50–1,000 nM TNP-470 equivalent. Empty polymeric micelles were also added as a control ($n = 8$, $^*P < 0.0005$). Lower panel: HUVEC growth curve of cells treated every other day with Lodamin (60 nM TNP-470 equivalent), untreated cells and vehicle-treated cells. (**d**) Corneal micropocket assay: representative experiments of the corneal micropocket assay. Newly formed blood vessels are growing toward the bFGF pellet (in white); note the inhibition of angiogenesis in Lodamin-treated mouse (15 mg/kg per day) with respect to control. Lower panel shows the quantification of neovascularization area in the cornea ($n = 10$, mean ± s.d.).

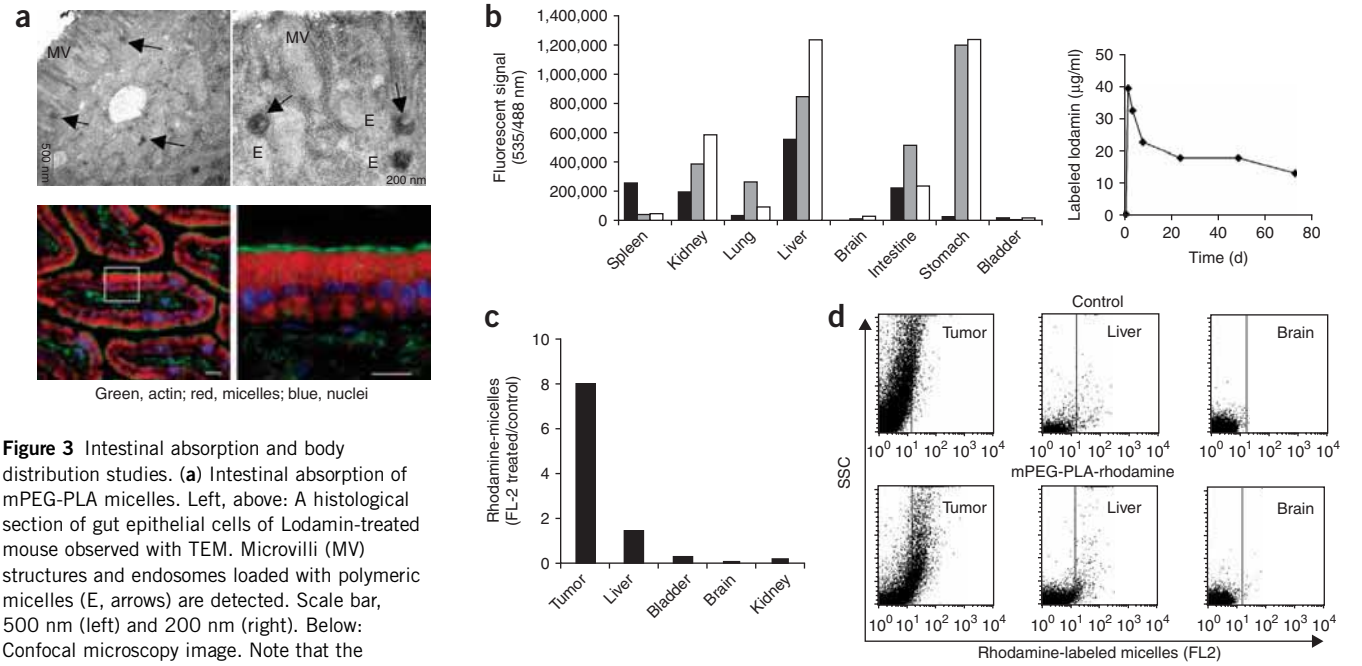

Figure 3 Intestinal absorption and body distribution studies. (**a**) Intestinal absorption of mPEG-PLA micelles. Left, above: A histological section of gut epithelial cells of Lodamin-treated mouse observed with TEM. Microvilli (MV) structures and endosomes loaded with polymeric micelles (E, arrows) are detected. Scale bar, 500 nm (left) and 200 nm (right). Below: Confocal microscopy image. Note that the polymeric micelles can be detected in the lamina propria in the vicinity of blood vessels. The actin filaments were stained with phalloidin-FITC (green), nuclei were labeled with DAPI (blue) and mPEG-PLA-rhodamine micelles were detected in red. Scale bars, 5 μm. (**b**) Fluorescent signal of tissue extracts and in serum. Mice ($n = 3$) were given a single dose of oral 6-coumarin–labeled polymeric micelles (150 μl, 30 mg/ml). Left: the graph shows the values of the three different mice, autofluorescence was omitted by subtracting the fluorescent signal of tissue extracts from an untreated mouse. The percent of labeled cells was measured for each organ. Right: levels of fluorescent signals in mouse serum as measured after different time points after oral administration. The results are presented as the concentration of micelles calculated by standard calibration curve. (**c**) The percentage of $FL2^{high}$-positive cells is shown as isolated from the designated organs (ratio of numbers $FL2^{high}$ cells of treated tumors to these of control mouse). (**d**) FACS analysis graphs of single-cell suspensions from three representative organs (tumor, liver, brain) taken from a mouse bearing Lewis lung carcinoma after controlled enzymatic degradation. The $FL2^{high}$ represents those cells that contain the mPEG-PLA-rhodamine micelles.

led us to design a formulation with improved solubility and oral availability.

We characterized the chemical and physical properties of Lodamin. We confirmed the binding of TNP-470 to mPEG-PLA by ^{3}H NMR (data not shown) and mass spectrometry showing an average m/z of 3,687 for mPEG-PLA-TNP-470. **Figure 1a** illustrates the preparation of Lodamin. Using an amine detection reagent, we determined the incorporation efficiency of ethylenediamine to mPEG-PLA as 65%, and in the second step TNP-470 was shown to be bound with an efficiency of >90%. Lodamin contained 0.8–1% (wt/wt) free TNP-470 as determined by high-performance liquid chromatography (HPLC). We determined the average size and size distribution of Lodamin by dynamic light scattering (DLS) spectroscopy (**Fig. 1b**) on the day of preparation and after 10 d of incubation in aqueous medium, to evaluate Lodamin stability ($n = 4$). The majority of micelles (90%) on the day of preparation were 7.8–8 nm in diameter, with a small population of larger particles (200–400 nm). The size remained almost unchanged after 10 d.

We characterized the morphology of Lodamin by transmission electron microscopy (TEM) (**Fig. 1c**). The images showed that the polymeric micelles had acquired a uniform spherical structure, which remained stable after 2 weeks of incubation in water at 37 °C. Because the drug is located in the PLA core of the micelle structure and PLA is spontaneously hydrolyzed in an aqueous environment, we studied the release kinetics of TNP-470 from Lodamin. A slow-release kinetic of TNP-470 was obtained after incubation in PBS (pH = 7.4) or in gastric liquid (pH = 1.2). The TNP-470 was released over a period of 28 d with an early peak burst of ~30% after the first day of incubation (**Fig. 1d**).

Endothelial cells take up Lodamin by endocytosis

We evaluated the uptake of polymeric micelles by HUVECs and the kinetics of their uptake. HUVECs were incubated with 6-coumarin labeled mPEG-PLA micelles for 20 min, 2, 4 and 7 h and were imaged by confocal microscopy (**Fig. 2a**). In as little as 20 min after incubation, micelles were taken up by the cells and located in their cytoplasm. After 2 h the uptake was maximal and after 4–7 h micelles were detected as defined aggregates inside the cytoplasm. Fluorescence-activated cell sorting (FACS) of HUVECs incubated with rhodamine-labeled polymeric micelles for the same incubation times confirmed a maximal uptake after 2 h (**Fig. 2b**), whereas no difference was observed between 2 and 24 h of incubation. In live-cell analysis, co-localization of Lyso-tracker staining with the micelles suggests endocytosis as the mechanism of uptake. Incubation of the micelles with HUVECs in cold conditions reduced micelle uptake by up to 55%, confirming that endocytosis is the most likely mechanism of uptake (data not shown).

Lodamin inhibits proliferation of endothelial cells

Next, we evaluated the effect of Lodamin on the proliferation of endothelial cells. After 48 h, Lodamin (62.5 nM–1,000 nM TNP-470 equivalent) inhibited HUVEC proliferation by 88–95% respectively (**Fig. 2c**). The growth of HUVECs treated with Lodamin (60 nM

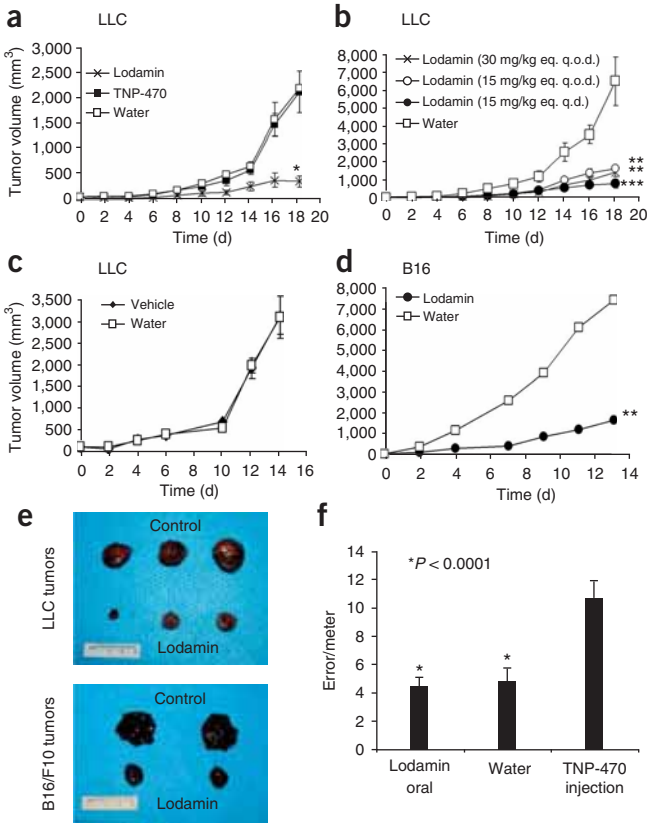

Figure 4 Lodamin inhibits primary tumor growth without causing neurotoxicity. (**a**) Effect of free or conjugated TNP-470 on established Lewis lung carcinoma tumors: effect of 30 mg/kg every other day of free TNP-470 given orally, compared to equivalent dose of Lodamin or water ($n = 5$ mice per group, $^*P < 0.05$). (**b**) Lewis lung carcinoma volume during 18 d of different frequencies and doses of Lodamin: 30 mg/kg every other day (q.o.d.), 15 mg/kg every other day, 15 mg/kg every day (q.d.) and water by gavage ($n = 5$ mice per group, $^*P < 0.05$. (**c**) Evaluation of the effect of the vehicle, empty mPEG-PLA micelles, on Lewis lung carcinoma ($n = 5$ mice per group, $^*P < 0.05$). (**d**) Effect of Lodamin given at a dose of 15 mg/kg every day on B16/F10 murine melanoma tumor in C57Bl/6J, water was given as control ($n = 5$ mice per group, $^*P < 0.05$). (**e**) Representative Lewis lung carcinoma and B16/F10 tumors removed from mice at day 18 after treatment with oral Lodamin at 30 mg/kg every other day and 15 mg/kg every day, respectively, and from control untreated mice. (**f**) Neurotoxicity evaluation of Lodamin-treated mice (10 d, 30 mg/kg every other day) compared to mice treated with subcutaneous (30 mg/kg every other day) free TNP-470 or water given by gavage. Balance beam test was quantified by foot-slip errors and the numbers of slips per meter are presented ($n = 4$–5 mice per group). $^*P < 0.05$, $^{**}P < 0.01$, $^{***}P < 0.0001$ (results are mean ± s.e.m.).

TNP-470 equivalent) was completely inhibited compared to untreated cells or cells treated by vehicle only. We observed no substantial cytotoxic effect (**Fig. 2c**).

Lodamin inhibits bFGF and VEGF-induced angiogenesis *in vivo*

The antiangiogenic properties of Lodamin were evaluated *in vivo* by the corneal micropocket angiogenesis assay[29]. Mice were treated with daily oral Lodamin (15 mg/kg per day) or vehicle for 6 d. **Figure 2d** shows the inhibition of basic fibroblast growth factor (bFGF)-induced angiogenesis in representative eyes of treated or untreated mice. Quantification of the angiogenesis area (**Fig. 2d**, lower panel) showed 31% inhibition of angiogenesis, compared to vehicle ($P = 0.00016$, $n = 10$). Similar results were obtained with 160 ng vascular endothelial growth factor $(VEGF)_{165}$-induced angiogenesis in the cornea (data not shown); in this case Lodamin treatment resulted in 40% inhibition of vessel area.

Polymeric micelles: absorption by the intestine

To study the intestinal absorption of the polymeric-micelles, we orally administered mPEG-PLA-rhodamine micelles to mice. After 2 h mice were euthanized and isolated segments of the small intestine were fixed and imaged using confocal microscopy. The polymeric micelles (detected in the red channel) were intensively taken up by columnar epithelium lining the luminal side of the small intestine (**Fig. 3a**). In a high magnification of small intestine villi, micelles are clearly detected in the lamina propria and in the vicinity of blood vessels, indicating transepithelial absorption. In high-resolution TEM images of single gut-epithelial cells, endosomes loaded with drug were readily detected (**Fig. 3a**, arrows). These endosomes differed in contrast and number when compared to those in the intestine of an untreated mouse. These data indicate that Lodamin is most likely taken up by intestinal villi through endocytosis.

Biodistribution, tumor accumulation and toxicity studies

The biodistribution and tissue uptake of orally administered labeled Lodamin was studied by treating mice with fluorescently labeled mPEG-PLA micelles for 3 d. After harvesting tissue, we quantified tissue drug concentration by dye extraction or by FACS. The results of the fluorescent dye extraction method (**Fig. 3b**) showed that a high concentration of fluorescent signal was present in the stomach and the small intestine, and the highest levels were present in the liver. Notably, the brain lacked fluorescent signal. In the serum, labeled micelles were already detected 1 h after oral administration, peaking after 2 h and were still detected at 72 h. In tumor-bearing mice, FACS analysis of enzymatically digested tissues (**Fig. 3c**,**d**) demonstrated a large uptake of labeled micelles by the liver, and no uptake by the brain. Notably, the highest uptake of micelles was detected in tumor cells (**Fig. 3c**). Taken together, these results indicate that the drug was concentrated mostly in the tumor and to a lesser extent in the gastrointestinal organs, and absent in the brain.

No tissue abnormalities were detected by histological analyses (H&E) of liver, intestine, lung and kidney in Lodamin-treated mice (15 mg/kg TNP-470 equivalent per day, for 20 d) compared to untreated mice (data not shown). In addition, no substantial differences were found between the mouse serum liver-enzyme profiles of Lodamin-treated and untreated mice. In the Lodamin-treated group the aspartate aminotransferase (AST) and alanine aminotransferase (ALT) concentrations were 41 ± 9 u/l and 120 ± 39 u/l, respectively, whereas in the untreated group they reached 37.5 ± 4 u/l and 152 ± 131 u/l, respectively.

Lodamin inhibits primary tumor growth

We evaluated the biological efficacy of Lodamin as an antiangiogenic anticancer agent in tumor-bearing mice. When mice received an oral dose of free TNP-470 (30 mg/kg every other day), we did not observe tumor growth inhibition in subcutaneous Lewis lung carcinomas (LLC) (**Fig. 4a**). The equivalent dose of Lodamin, however, resulted in substantial tumor growth inhibition (**Fig. 4a**). This inhibition was observed after 12 d of Lodamin treatment, and at day 18 tumor growth was inhibited by 83%. Different dosing regimens of Lodamin, 15 mg/kg every day, 30 mg/kg every other day and 15 mg/kg

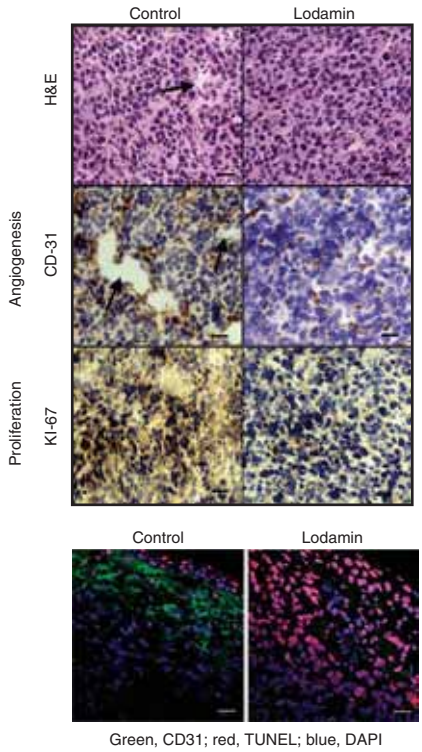

Figure 5 Lodamin effect on tumor structure, cell proliferation, angiogenesis and apoptosis. Lewis lung carcinoma (LLC) tumors were removed from Lodamin-treated or untreated mice and sectioned. Tissues were stained with H&E to detect tissue morphology. Immunostaining with anti-CD31 was used to detect microvessels and anti-Ki-67 nuclear antigen for cell proliferation. TUNEL staining was used for the detection of apoptotic cells in lower panels. Vessels are detected in green, apoptotic cells are detected in red by TUNEL and cell nuclei are in blue (DAPI). Sections were counterstained with eosin (nuclei). Arrows indicate vessel structures. Scale bars, 15 μm.

every other day, resulted in 87%, 77% and 74% inhibition of tumor volume, respectively (**Fig. 4b**). The vehicle (mPEG-PLA) showed no effect on tumor growth and was similar to untreated control mice (**Fig. 4c**).

In another tumor model, murine melanoma (B16/F10) subcutaneous tumor growth was also inhibited by oral Lodamin (15 mg/kg per day). This treatment was effective after 4 d of treatment, and after 13 d, 77% volume inhibition was obtained (**Fig. 4d**). No apparent side effects, including weight loss, were detected in either tumor model. Higher doses of Lodamin—30 mg/kg per day and 60 mg/kg every other day—showed substantial tumor inhibition; however, these higher doses were accompanied by weight loss (data not shown). **Figure 4e** shows representative tumors of treated or untreated LLC or B16/F10 tumors.

Lodamin does not cause neurotoxicity in mice

Because our biodistribution study indicated that Lodamin does not cross the blood-brain barrier, we tested whether the possible leaching of free drug into the brain might result in neurotoxicity and cerebellar dysfunction. We subjected mice to a sensitive test of motor coordination—crossing a narrow (4 mm) balance beam[30]. The performance of Lodamin-treated mice (30 mg/kg TNP-470 equivalent every other day for 14 d) was similar to that of control (water-treated) mice, whereas mice injected with the same dose of free TNP-470 committed over twice as many errors ($P < 0.0001$) (**Fig. 4f**). These results indicate that Lodamin treatment avoids the cerebellar neurotoxicity observed with unconjugated TNP-470 treatment.

Lodamin inhibits tumor angiogenesis and proliferation

We tested the effect of Lodamin on the histological structure of LLC tumors. Both treated and untreated tumors showed a dense cellular structure (**Fig. 5**). The tumors of untreated mice had a net organization of small and large vessels with an apparent lumen structure as demonstrated by CD-31 immunostaining. In contrast, Lodamin-treated tumors formed very small undeveloped vessels (**Fig. 5**). Lodamin-treated tumors showed less cellular proliferation than untreated tumors, as detected by the nuclear marker Ki-67. TdT-mediated dUTP nick end labelling (TUNEL) staining for the detection of apoptosis suggested enhanced apoptosis in Lodamin-treated tumors. Lodamin-treated tumors had fewer vessels (green) but high levels of apoptosis, predominantly in tumor cells (red). In the control

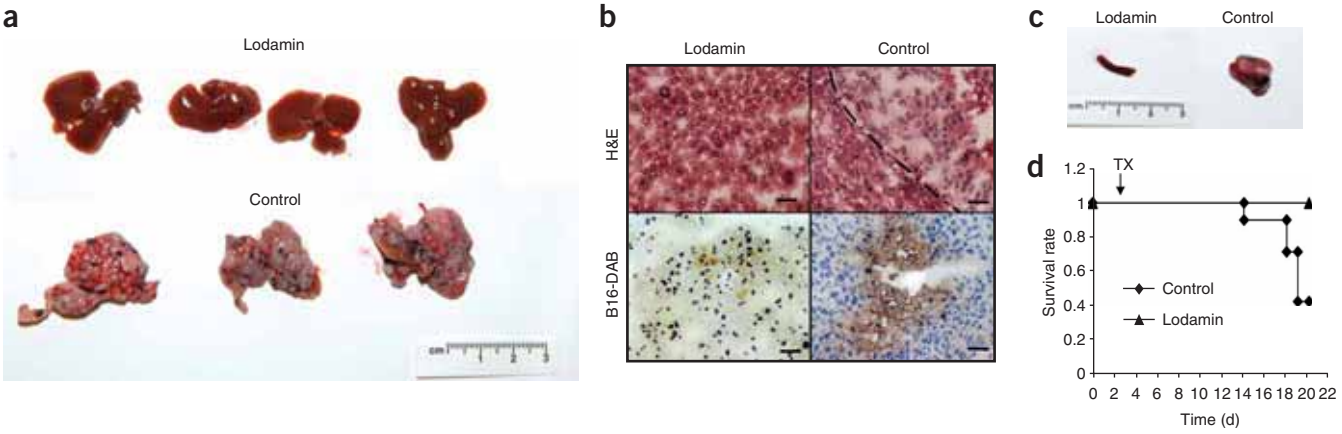

Figure 6 Lodamin inhibits liver metastasis in mice injected with B16/F10 cells into their spleen. (**a**) Livers removed from Lodamin-treated or untreated mice, 20 d after cell injection. Control livers were enlarged with widespread macroscopic malignant nodules and extensive cirrhosis. (**b**) Histology of liver tissues. Livers removed from Lodamin-treated or untreated mice stained with H&E (upper panel) or reacted with anti-mouse melanoma antibody (lower panel). B16/F10 melanoma cells are detected by positive DAB staining (brown). (**c**) Spleens removed from Lodamin-treated or untreated mice. Control spleens had large masses compared to treated mice with normal spleen morphology. (**d**) Survival curve of treated versus control mice ($n = 7$). Treatment started at day three (TX) after cell injection (arrow).

tumor tissue, apoptotic cells were mostly found in the capsule and less in the center.

Lodamin prevents development of liver metastasis

The effect of oral Lodamin administration on liver metastases was tested after injecting B16/F10 tumor cells into the spleen. Oral Lodamin treatment dramatically affected development of B16/F10 liver metastasis. After 18 d of treatment mice were autopsied. All untreated mice had ascites and their enlarged livers had macroscopic malignant nodules and extensive cirrhosis (**Fig. 6a**,**b**). In contrast, Lodamin-treated mice had no macroscopic metastases in the abdomen or in the liver (**Fig. 6a**,**b**). Their organs had a normal morphology and no weight loss or other apparent side effects were found. Immunohistology showed only a few sporadic B16/F10 cells in the liver that had not developed into lesions (**Fig. 6b**). Only one treated mouse out of seven had malignant nodules in its liver, but the liver was smaller than in the untreated control and had less cirrhosis. The spleens of all Lodamin-treated mice had a normal morphology compared to the congestion found in the enlarged spleens of control mice (**Fig. 6c**). Twenty days after B16/F10 cell injection into the spleen, four out of seven control mice had died whereas all treated mice survived (**Fig. 6d**).

DISCUSSION

In cancer patients, tumor- and micrometastasis can remain for prolonged periods of time in a dormant asymptotic state before diagnosis and development of disease[1,31]. Recent advances in identifying biomarkers of the "angiogenic switch"[2,32–34] may open new possibilities for early detection of dormant tumors. Dormancy highlights the need for chronic long-term therapy with nontoxic anticancer drugs preferentially administered orally.

In this study, we describe the development of a nontoxic oral formulation of TNP-470, named Lodamin, as an antitumor and antimetastatic drug. We chose this drug because TNP-470, a highly potent angiogenesis inhibitor, is a reasonable candidate for cancer maintenance therapy and metastasis prevention.

In the current study we devised a soluble formulation for TNP-470, a molecule with very poor oral availability as illustrated by its high log-D values, indicating low water solubility[35]. We made an oral formulation by conjugating TNP-470 with mPEG-PLA to form mPEG-PLA-TNP-470 polymeric micelles. Unlike TNP-470, which is only dissolvable in organic solvents, Lodamin can be suspended in water to form polymeric micelles thanks to the amphiphilic nature of PEG-PLA[26]. In this structure the drug is located in the core of the micelle, protecting it from the harsh gastrointestinal environment[36]. Polymer micelles have previously been used for the delivery of hydrophobic drugs[37,38] and gene delivery[39].

TEM indicated that Lodamin acquired a stable spherical morphology of nanomicelles. In addition, PLA, a biodegradable and biocompatible polymer, hydrolyzes in an aqueous environment and allows slow release of TNP-470. *In vitro* studies showed a continuous release of TNP-470 from Lodamin over almost a period of 1 month, with the majority of the drug releasing within the first 4 d (in both gastric and plasma pH conditions). Although an acidic environment is known to accelerate degradation of PLA, we observed only a minor effect on day 15. One possible explanation may be the masking effect of the PEG shell, which delays water penetration to the PLA core and slows diffusion-mediated release of the drug through this layer. In culture, Lodamin was rapidly taken up by endothelial cells via endocytosis and retained the original antiangiogenic activity of the free TNP-470 as demonstrated by the inhibition of HUVEC proliferation.

mPEG-PLA micelles penetrated the gut epithelial layer into the submucosa as shown by using fluorescent markers. The mechanism of Lodamin penetration to gut epithelial cells seems to be by endocytosis, as detected by high-resolution TEM. In serum, labeled micelles had a long blood circulation time of at least 72 h after administration, a significant increase compared to free drug, which was detected in mice sera up to 2 h after treatment[24]. Biodistribution showed relatively high concentrations in the liver, as oral administration directly delivers the drug from the intestine to the liver. However, no liver toxicity was observed by histology and by liver enzyme profiling after 20 d of daily Lodamin treatment.

Orally delivered Lodamin showed substantial antitumor effects (83% reduction), whereas orally administered free TNP-470 had no effect. The effect on LLC growth was dose dependent, as 30 mg/kg every other day was more effective than 15 mg/kg every other day, and a dose of 15 mg/kg daily was more effective than 30 mg/kg every other day (a double dose given every 2 d). A similar antitumor effect of Lodamin was observed with melanoma B16/F10 tumors, confirming the broad biological effect of Lodamin, very much like the original free TNP-470. Immunohistochemical studies carried out on LLC tumor tissues showed Lodamin-induced reduction of proliferation and angiogenesis. TUNEL staining indicated a high level of tumor cell apoptosis after treatment. These results suggest that the prevention of angiogenesis by Lodamin leads to tumor cell apoptosis.

One of the most important effects of oral Lodamin is the prevention of liver metastasis in mice. Liver metastasis is very common in many tumor types and is often associated with a poor prognosis and survival rate. We chose the intrasplenic model for induction of liver metastasis, in which the transition time of B16/F10 cells from the spleen to the liver microvasculature was found to be very fast (20% of the injected cells are located in the liver after 15 min)[40]. Mice injected in the spleen with B16/F10 cells had a low survival rate. They developed ascites, macroscopic malignant nodules and extensive cirrhosis in their livers 20 d after injection. However, all oral Lodamin–treated mice survived up to this point and had a normal liver and spleen morphology without any apparent side effects. This dramatic antitumor effect in the liver may be due to the oral route of administration in which Lodamin is absorbed in the gastrointestinal tract and concentrated in large quantities in the liver via the portal vein. These results suggest that Lodamin can prevent the development of metastasis in the liver. Importantly, this property of the polymeric micelles might be used for the development of other antiangiogenic or anticancer drugs that target liver metastasis.

In tumor-bearing mice, Lodamin showed preferential accumulation in the tumor rather than in other tissues. This accumulation may be due to the enhanced permeability and retention effect (EPR) caused by the 'leaky' discontinuous endothelium of the tumor vasculature[41]. The EPR effect plays a central role in nanoparticle targeting to tumor beds, as in the case of Caplostatin[24] and other conjugated drugs[42]. Furthermore, biodistribution studies showed that polymeric micelles do not penetrate the brain through the blood-brain barrier. Because TNP-470 was shown to cause neurotoxic side-effects in humans in clinical trials[23], we examined whether Lodamin treatment caused neurotoxicity and cerebellar dysfunction in treated mice. In the narrow beam test, mice injected with free TNP-470 showed a substantial increase in foot-slip errors, whereas Lodamin-treated mice performed like untreated control mice.

In summary, oral Lodamin shows promising therapeutic properties in the treatment of solid tumors and metastasis in mice. It retains the antiangiogenic properties of free TNP-470 while adding important advantages: oral availability, tumor accumulation, continued slow

release and fewer side effects. It may be useful for cancer patients as a long-term maintenance drug to prevent tumor recurrence. Furthermore, it may be used as a maintenance therapy for chronic angiogenic diseases such as age-related macular degeneration, endometriosis and rheumatoid arthritis.

METHODS

All animal procedures were performed in compliance with Boston Children's Hospital guidelines, and protocols were approved by the Institutional Animal Care and Use committee.

Log-D measurement for TNP-470. Aqueous solubility is one of the important chemical properties affecting oral absorption of a drug. In order to predict the intestinal absorption of TNP-470, we measured its log-D value which is a parameter of hydrophobicity determined by the ratio of drug concentration in octanol to that in water at 25 °C (Analiza). High log-D values (>2) indicate low water solubility and hence a poor oral availability of a drug. For this study log-D values of TNP-470 (30 mM) were measured at plasma and stomach pHs: pH = 7.4 and pH = 2, respectively.

Preparation of Lodamin: mPEG-PLA-TNP-470 polymeric micelles. TNP-470 (D. Figg) was conjugated to a diblock co-polymer using a two-step reaction (**Fig. 1**). In the first step succinated $mPEG_{2000}$-PLA_{1000} with free carboxic acid end-groups (Advanced Polymers Materials) was reacted with ethylenediamine (Sigma-Aldrich). Succinated mPEG-b-PLA-$OOCCH_2CH_2COOH$ (500 mg) was dissolved in DMSO and reacted with ethyl(diethylaminopropyl) carbodiimide (EDC) and a catalyst *N*-hydroxysuccinimide (NHS) in a molar ratio of 1:10:20 (Polymer:EDC:NHS, respectively). A fivefold molar excess of ethylendiamine was added and reacted for 4 h at 25 °C. The polymer solution was then dialyzed (MWCO 1000, Spectra/Por Biotech Regenerated Cellulose, VWR) against DMSO leading to a 65% reaction efficiency. In the second step, the amine-containing polymer was mixed with TNP-470 (350 g), dissolved in DMSO and the solution was stirred for 4 h at 25 °C. The polymeric micelles were formed by dialyzing the DMSO solution of the conjugate against double distilled water (d.d.w.) using a regenerated cellulose dialysis bag (MWCO 1000, Spectra/Por Biotech Regenerated Cellulose, VWR) to obtain micelles with high incorporation efficiency (>90%) and 0.8–1% free drug (wt/wt). The micelles were then lyophilized and stored at –20 °C in a dry environment until use.

Prepartion of fluorescently labeled mPEG-PLA micelle. Rhodamine-labeled polymeric-micelles were formed using a similar protocol. The mPEG-PLA was conjugated via the N-terminal amine group with lissamine rhodamine B sulfonyl chloride (Molecular Probes) in DMSO. For green fluorescent polymer micelles, a commonly used hydrophobic marker 6-coumarin (Sigma-Aldrich) at 0.1% wt/wt was added to the polymeric solution before the final dialysis step.

Characterization of conjugation. NMR spectrometer analysis (NERCE/BEID, Harvard Medical School) was conducted for each reaction step and mass spectrometry (Proteomic core, Harvard Medical School) was performed on the conjugate. To evaluate the efficiency of ethylendiamine binding to mPEG-PLA (first reaction step, **Fig. 1a**) and TNP-470 binding to the polymer by the amine (second step, **Fig. 1a**), we used the colorimetric amine detection reagent: 2,4, 6-trinitrobenozene sulfonic acid (TNBSA) (Pierce). TNBSA reacts with primary amines to produce a yellow product whose intensity was measured at 450 nm. To calculate amine concentration in the polymer a linear calibration curve of amino acid was used. To measure TNP-470 loading into polymeric micelles, we incubated 10 mg/ml Lodamin in 500 µl NaOH (0.1 N) to accelerate PLA degradation. After an overnight incubation with shaking (100 r.p.m) at 37 °C, we added acetonitrile to the samples (1:1 NaOH:acetonitrile) and analyzed for TNP-470 concentration. TNP-470 concentration was measured using HPLC (System Gold Microbore, Beckman Coulter). A 20-µl portion of each sample was injected into a Nova-pak C_{18} column (3.9 mm × 150 mm i.d.; Waters) and analyzed using a calibration curve of TNP-470. TNP-470 binding to amine was also measured using TNBSA reagent and was confirmed by subtracting the nonbound drug from the total drug added to the reaction.

Lodamin size, morphology and *in vitro* TNP-470 release. The particle size distribution of Lodamin was measured by Dynamic Light Scattering (DLS, DynaPro, Wyatt Technology). The measurements were done at 25 °C using Dynamic V6 software. Lodamin (1.5 mg/ml) dispersed in d.d.w. was measured in 20 successive readings of the DLS.

To study the morphology of Lodamin, TEM images were taken on the day of preparation and 1 week after preparation. Polymer micelles dispersed in d.d.w. were imaged with cryo-TEM (JEOL 2100 TEM, Harvard University—CNS). To study the kinetic release of TNP-470 (without its chlorine), Lodamin (20 mg) was incubated with either 1 ml PBS pH = 7.4 or simulated gastric fluid (HCL:d.d.w. pH = 1.2). Every few days, supernatant was taken and analyzed for TNP-470 concentration and a cumulative release graph of TNP-470 was determined. TNP-470 concentration was measured using HPLC. TNP-470 was detected as a peak at 6 min with 50% acetonitrile in water at the mobile phase. The flow rate was 1 ml/min, and the detection was monitored at 210-nm wavelength.

Cell culture. Murine LLC and B16/F10 melanoma cells were obtained from American Type Culture Collection. HUVECs were purchased from Cambrex. The cells were grown and maintained in medium as recommended by the manufacturers. Dulbecco's Modified Eagle's Medium with 10% FBS was used for tumor cells and EMB-2 (Cambrex Bio Science) containing 2% FBS and EGM-2 supplements was used for HUVECs.

Uptake of polymeric micelles by HUVECs and their localization in cells. To evaluate the uptake of polymeric micelles by HUVEC, we used 6-coumarin-labeled mPEG-PLA micelles or rhodamine conjugated to mPEG-PLA. HUVECs were seeded in a 24-well plate (2×10^4 per well) in EGM-2 medium (Cambrex) and were allowed to attach overnight. Fluorescent-labeled micelles (10 mg/ml) were suspended over a bath sonicator for 5 min, and 20 µl of the suspension was added to the cultured cells. After the designated time points (20 min, 2, 4, 7 and 24 h), the cells were washed three times with PBS and analyzed by FACS or alternatively fixed with 4% parformaldehyde. For confocal microscopy, cells were mounted using DAPI containing Vectashild (Vector Laboratories). Optical sections were scanned using Leica TCS SP2 AOBS, a ×40 objective equipped with 488-nm argon, 543-nm HeNe and 405-nm diode lasers. To study Lodamin internalization into endothelial cells, we used confocal microscopy to co-localize 6-coumarin–labeled polymeric micelles with endo-lysozome. Live HUVECs were imaged in different time points after addition of labeled micelles to cell medium (15 µg/ml) up to 1 h. At this point, LysoTracker Red (Molecular Probes) was added to the medium for the detection of acidic intracellular vesicles: endosomes and lysosomes. After 20 min of incubation, cells were imaged by confocal microscopy using optical sections with 488-nm argon, 543-nm HeNe and 405-nm diode lasers.

To further verify that Lodamin internalization occurs through endocytosis, we measured cell uptake in cold conditions (4 °C) in comparison to cell uptake at 37 °C. HUVECs were plated in a concentration of 15,000 cells/ml in two 24-well plates for 24 h. Fluorescence-labeled polymeric micelles (15 µg/ml) were added and incubated at different time points: 20, 30, 40 and 60 min ($n = 3$) in 4 °C and in 37 °C. After the designated time points, the cells were washed three times with PBS and lysed with 100 µl lysis buffer (BD Biosciences). Cell extracts were measured for fluorescent signal in a Wallac 1420 VICTOR plate-reader (Perkin-Elmer Life Sciences) with excitation/emission at 488 nm/530 nm.

HUVEC growth and proliferation. HUVECs were exposed to different concentrations of Lodamin equivalent to 50–1,000 nM free TNP-470 (0.12–2.4 mg/ml micelles) and incubated in a low serum medium for 48 h at 37 °C. To rule out a possible cytotoxic effect of the carrier, empty micelles were added to HUVECs at the same concentration as the control (4.8 mg/ml). A WST-1 proliferation assay (Roche Diagnostics) was used. Cell viability was calculated as the percentage of formazan absorbance at 450 nm of treated versus untreated cells. Data were derived from quadruplicate samples in two separate experiments. The effect of Lodamin (60 nM TNP-470 equivalent every other day) on HUVEC growth rate was evaluated by daily counting of HUVECs up to 5 d and comparing this to the number of untreated cells or cells treated with vehicle (same concentration as Lodamin).

Corneal micropocket assay. To evaluate the antiangiogenic properties of Lodamin, the corneal micropocket angiogenesis assay was performed as previously detailed[29]. Pellets containing 80 ng carrier-free recombinant human bFGF or 160 ng VEGF (R&D Systems) were implanted into micropockets created in the cornea of anesthetized mice. Mice were treated daily with 15 mg/kg TNP-470 equivalent of Lodamin for 6 d, and then the vascular growth area was measured using a slit lamp. The area of neovascularization was calculated as vessel area by the product of vessel length measured from the limbus and clock hours around the cornea, using the following equation: vessel area (mm^2) = (π × clock hours × vessel length (mm) × 0.2 mm).

Body distribution, intestinal absorption and toxicity of Lodamin. For all biodistribution studies we used a fluorescent marker for tracking Lodamin. Mice were administered 6-coumarin–labeled mPEG-PLA by oral gavage for 3 d (100 µl of 1.5 mg/ml). On the third day of treatment, after 8 h of fasting, animals were killed and spleen, kidney, brain, lungs, liver, intestine, stomach and bladder were collected. The fluorescent 6-coumarin was extracted from the tissues by incubation with formamide for 48 h at 25 °C. Samples were centrifuged and signal intensity of fluorescence of supernatants was detected with a Wallac 1420 VICTOR plate-reader (Perkin-Elmer Life Sciences) with excitation/emission at 488 nm/530 nm. The results were normalized to protein levels in the corresponding tissues. Tissue autofluoresence was corrected by subtracting the fluorescent signal of nontreated mouse organs from the respective readings in treated mice. Similarly, levels of fluorescent signal in mouse sera were measured at different time points (1, 2, 4, 8, 24, 48 and 72 h) using excitation/emission readings at 488 nm/530 nm.

To analyze cell uptake in the different tissues in tumor-bearing mice, we administered orally mPEG-PLA-rhodamine micelles (100 µl of 1.5 mg/ml) or water to C57Bl/6J mice bearing LLC tumors (200 mm^3) for 3 d. Organs were removed, incubated for 50 min in collagenase (Liberase Blendzyme 3; Roche Diagnostics) in 37 °C to obtain a single-cell suspension. These suspensions were analyzed by FACS to quantify the uptake of micelles into different tissue cells when compared to those in the untreated mouse.

To evaluate intestinal absorption, mPEG-PLA-rhodamine micelles were orally administered to C57Bl/6J mice after 8 h of fasting. After 2 h mice were killed and 2.5-cm segments of the small intestine were removed, washed and analyzed by histology and confocal microscopy. The rhodamine-labeled polymeric micelles were detected by confocal microscopy (Leica TCS SP2 AOBS) with a 488-nm argon laser line. Actin filaments were stained with phalloidin-FITC (Sigma) and nuclei were stained by DAPI (Sigma). To further study the uptake of Lodamin in the intestine, high-resolution images were made with cryo-TEM. Intestines from treated (as above) and untreated mice were excised and immersed immediately in a freshly prepared 4% paraformaldehyde in PBS pH 7.4 for 2 h at 25 °C. The samples were washed in PBS, transferred to a 30% sucrose solution overnight at 4 °C and embedded in OCT and kept at –80 °C until processing. Fifteen sections, each 10 µm thick, were prepared and processed for confocal microscopy or TEM. Four TEM samples were fixed for 30 min in freshly prepared 2% paraformaldehyde, 2.5% glutaraldehyde, 0.025% CaCl2 in 0.1 M sodium cacodylate buffer, pH 7.4 and subsequently postfixed for 30 min in 1% osmium tetroxide in 0.1 M sym collidine buffer, pH 7.4 at 25 °C, stained *en bloc* in 2% uranyl acetate, dehydrated and embedded under inverted plastic capsules. Samples were snapped free of the glass coverslips by a cycle of rapid freezing and thawing. Thin sections were cut *en face* with diamond knives using a LEICA UCT Ultramicrotome. Specimens were examined using a JEOL 2100 TEM.

To exclude tissue toxicity, histological analysis (H&E) of liver, intestine, lung and kidneys was conducted (Beth-Israel pathology department). To further exclude liver toxicity, we analyzed serum levels of the liver enzymes AST and ALT (done at Shriners Burns Hospital). These studies were performed on mice treated with Lodamin for 20 d (15 mg/kg TNP-470 equivalent per day) and compared to untreated mice (n = 3–4).

Oral administration of Lodamin *in vivo* and primary tumor experiments. Animal procedures were performed in the animal facility at Children's Hospital Boston using 8-week-old C57Bl/6J male mice (Jackson Laboratories).

For tumor experiments: LLC cells (1×10^6) or B16/F10 melanoma cells (1×10^6) were implanted subcutaneously in 8-week-old C57Bl/6J male mice. Oral availability of free TNP-470 was compared to that of Lodamin. A dose of 30 mg/kg every other day of free TNP-470 and an equivalent dose of Lodamin (Lodamin, 6 mg in 100 µl/d per mouse) were administered to LLC tumor-bearing mice (~100 mm^3) and tumor growth was followed for 18 d. Free drug was given as a suspension in d.d.w. and freshly prepared before each dose. Additionally, we compared different doses and frequencies of Lodamin treatment: 15 mg/kg every day, 15 mg/kg every other day and 30 mg/kg every other day. To eliminate any possible effect of the vehicle (polymer without drug), we gave one group of mice micelles without drug and tumor progression was compared to water-treated mice.

For the melanoma tumor experiment, a daily dose of 15 mg/kg Lodamin was administered to B16/F10 melanoma-bearing mice. In all experiments, tumor size and animal weight were monitored every 2 d. Tumor volume was measured with calipers in two diameters as follows: $(\text{width})^2 \times (\text{length}) \times 0.52$. Note that all the above Lodamin doses are presented as TNP-470 equivalent.

Oral administration of Lodamin and liver metastasis experiments. To examine the effect of oral Lodamin treatment on metastasis development and prevention, liver metastases were generated by spleen injection. C57Bl/6J mice (n = 14) were anaesthetized with isoflurane and prepared for surgery. A small abdominal incision was made in the left flank and the spleen was isolated. B16/F10 tumor cells in suspension (50 µl, 5×10^5 in DMEM medium without serum) were injected into the spleen with a 30-gauge needle, and the spleen was returned to the abdominal cavity. The wound was closed with stitches and metal clips. After 2 d mice were divided into two groups: one was treated daily with oral Lodamin (15 mg/kg) using gavage and the second group was administered water by gavage. After 20 d, we terminated the experiment. Mice were killed and autopsied, livers and spleens were removed by surgical dissection, imaged and histology was carried out. Liver and spleen tissues were stained with H&E to evaluate tissue morphology and detect metastasis. Immunohistochemistry was carried out to specifically detect B16/F10 cells in the liver using anti-mouse melanoma antibody (HMB45, abCAM) and using DAB staining.

Evaluation of neurotoxicity with balance beam motor coordination test. A slightly modified balance beam motor coordination test[30] was performed on three groups of mice: oral Lodamin–treated mice (30 mg/kg eq. every other day), free TNP-470 (30 mg/kg every other day) subcutaneously injected mice and water-treated mice (administered by gavage). The mice were pretreated for 14 d (n = 4–5 per group) and then the mice were allowed to acclimate to the procedure room for 1 h, after which they were trained in three trials to cross a wide (20 mm width × 1 m length) balance beam. All the mice crossed the wide beam without making foot-slip errors. The mice were then trained on a narrow (4 mm width × 1 m length) beam for three trials. At the end of the training trials, no freezing behavior was observed, and the mice would start to walk within 4 s of being placed on the beam. The mice were then videotaped as they performed in three test trials of three beam crossings each—a total of nine crossings per mouse. The three trials were separated by at least 1 h to avoid fatigue of the mice. Videotaped crossings were scored for number of foot-slip errors and time to cross. All experiments and scoring of the different groups were performed by a blinded investigator.

Lodamin effect on angiogenesis, proliferation and apoptosis in tumor tissues. Histologic evaluation of tissue was performed on 8-µm thick frozen sections of LLC tumors that were removed from two random Lodamin-treated or untreated mice 14 d after treatment (15 mg/kg every day. TNP-470 equivalent). Tumors were sectioned and analyzed for cell markers, 20 microscope fields (×400) were imaged.

Tissues were stained with H&E to detect tissue morphology. Immunohistochemistry was carried out using Vectastain Elite ABC kit (Vector Laboratories). Primary antibodies included CD31 (BD Biosciences) for microvessel staining and anti-Ki-67 (DAKO) for proliferating cell. Detection was carried out using a 3,3′-diaminobenzidine chromogen, which results in a positive brown staining. Apoptotic cells were detected by reacting the tissues with TUNEL using a kit (Roche) following the company's protocol. Vessels were detected in the same tissues by anti-CD31 and secondary FITC anti-mouse antibody (Jackson ImmunoResearch) conjugated antibody (green) and nuclei were detected by DAPI (blue).

Statistics. *In-vitro* data are presented as mean ± s.d., whereas *in vivo* data are presented as mean ± s.e.m. Differences between groups were assessed using unpaired two-tailed Student's *t*-test, and $P < 0.05$ was considered statistically significant.

ACKNOWLEDGMENTS

We thank Donald Ingber for his support and encouragement of this work, Daniela Prox and Jenny Mu for their assistance with animal studies and chemical analysis, Kristin Johnson for the graphic work, Chun Wang (University of Minnesota) for fruitful discussions. We thank D. Figg, National Cancer Institute, for TNP-470. This work is supported in part by a Department of Defense Congressional Award W81XWH-05-1-0115 (to J.F.). The submission of this paper was completed before Folkman passed away in January and is dedicated to him for his support and mentorship.

AUTHOR CONTRIBUTIONS

O.B. designed and developed Lodamin formulation, designed experiments, performed tissue culture, *in vivo* studies and histology, analyzed data and wrote the manuscript; O.F. conducted intrasplenic injections, assisted with editing the manuscript; A.A. and I.A. assisted with cell assays and histology; F.C. conducted TEM imaging and analysis; L.B. assisted with animal studies and conducted corneal assays; E.P. performed confocal microscope imaging; Y.N. performed liver toxicity assays; S.K. and G.C. designed, conducted and analyzed neurotoxicity tests in mice; R.J.D. advised, edited the revisited manuscript and supervised corneal assays. J.F. supervised the entire study, designed experiments, analyzed data and edited the manuscript.

COMPETING INTERESTS STATEMENT

The authors declare competing financial interests: details accompany the full-text HTML version of the paper at http://www.nature.com/naturebiotechnology/.

Published online at http://www.nature.com/naturebiotechnology/
Reprints and permissions information is available online at http://npg.nature.com/reprintsandpermissions/

1. Holmgren, L., O'Reilly, M. & Folkman, J. Dormancy of micrometastases: balanced proliferation and apoptosis in the presence of angiogenesis suppression. *Nat. Med.* **1**, 149–153 (1995).
2. Naumov, G. & Folkman, J. Strategies to prolong the nonangiogenic dormant state of human cancer. in *Antiangiogenic cancer therapy* Edn. 1. (ed. Darren, W., Herbst, R.S., Abbruzzese, J.L.) 3–23 (CRS Press, Boca Raton, FL, Taylor and Francis, 2007).
3. Ingber, D. *et al.* Synthetic analogue of fumagillin that inhibit angiogenesis and suppress tumour growth. *Nature* **348**, 555–557 (1990).
4. Folkman, J. & Kalluri, R. Tumor angiogenesis. in *Cancer Medicine* Vol. 1. (ed. Kufe, D. *et al.*) 161–194 (B.C. Decker Inc., Hamilton, Ontario, 2003).
5. Yamaoka, M., Yamamoto, T., Ikeyama, S., Sudo, K. & Fujita, T. Angiogenesis inhibitor TNP-470 (AGM-1470) potently inhibits the tumor growth of hormone-independent human breast and prostate carcinoma cell lines. *Cancer Res.* **53**, 5233–5236 (1993).
6. Shusterman, S. *et al.* The angiogenesis inhibitor tnp-470 effectively inhibits human neuroblastoma xenograft growth, especially in the setting of subclinical disease. *Clin. Cancer Res.* **7**, 977–984 (2001).
7. Yanase, T., Tamura, M., Fujita, K., Kodama, S. & Tanaka, K. Inhibitory effect of angiogenesis inhibitor TNP-470 on tumor growth and metastasis of human cell lines in vitro and in vivo. *Cancer Res.* **53**, 2566–2570 (1993).
8. Takamiya, Y., Brem, H., Ojeifo, J., Mineta, T. & Martuza, R. AGM-1470 inhibits the growth of human glioblastoma cells in vitro and in vivo. *Neurosurgery* **34**, 869–875 (1994).
9. Takamiya, Y., Friedlander, R.M., Brem, H. & Malick, A. Martuza, RL Inhibition of angiogenesis and growth of human nerve-sheath tumors by AGM-1470. *J. Neurosurg.* **78**, 470–476 (1993).
10. Emoto, M., Tachibana, K., Iwasaki, H. & Kawarabayashi, T. Antitumor effect of TNP-470, an angiogenesis inhibitor, combined with ultrasound irradiation for human uterine sarcoma xenografts evaluated using contrast color Doppler ultrasound. *Cancer Sci.* **98**, 929–935 (2007).
11. Nahari, D. *et al.* Tumor cytotoxicity and endothelial Rac inhibition induced by TNP-470 in anaplastic thyroid cancer. *Mol. Cancer Ther.* **6**, 1329–1337 (2007).
12. Kanamori, M., Yasuda, T., Ohmori, K., Nogami, S. & Aoki, M. Genetic analysis of high-metastatic clone of RCT sarcoma in mice, and its growth regression in vivo in response to angiogenesis inhibitor TNP-470. *J. Exp. Clin. Cancer Res.* **26**, 101–107 (2007).
13. Sin, N. *et al.* The anti-angiogenic agent fumagillin covalently binds and inhibits the methionine aminopeptidase, MetAP-2. *Proc. Natl. Acad. Sci. USA* **94**, 6099–6103 (1997).
14. Zhang, Y., Griffith, E., Sage, J., Jacks, T. & Liu, J. Cell cycle inhibition by the anti-angiogenic agent TNP-470 is mediated by p53 and p21WAF1/CIP1. *Proc. Natl. Acad. Sci. USA* **97**, 6427–6432 (2000).
15. Mauriz, J. *et al.* Cell-cycle inhibition by TNP-470 in an in vivo model of hepatocarcinoma is mediated by a p53 and p21WAF1/CIP1 mechanism. *Transl. Res.* **149**, 46–53 (2007).
16. Kruger, E. & Figg, W.D. TNP-470: an angiogenesis inhibitor in clinical development for cancer. *Expert Opin. Investig. Drugs* **9**, 1383–1396 (2000).
17. Kudelka, A., Verschraegen, C. & Loyer, E. Complete remission of metastatic cervical cancer with the angiogenesis inhibitor TNP-470. *N. Engl. J. Med.* **338**, 991–992 (1998).
18. Tran, H. *et al.* Clinical and pharmacokinetic study of TNP-470, an angiogenesis inhibitor, in combination with paclitaxel and carboplatin in patients with solid tumors. *Cancer Chemother. Pharmacol.* **54**, 308–314 (2004).
19. Kudelka, A. *et al.* A phase I study of TNP-470 administered to patients with advanced squamous cell cancer of the cervix. *Clin. Cancer Res.* **3**, 1501–1505 (1997).
20. Herbst, R. *et al.* Safety and pharmacokinetic effects of TNP-470, an angiogenesis inhibitor, combined with paclitaxel in patients with solid tumors: evidence for activity in non-small-cell lung cancer. *J. Clin. Oncol.* **20**, 4440–4447 (2002).
21. Stadler, W. *et al.* Multi-institutional study of the angiogenesis inhibitor TNP-470 in metastatic renal carcinoma. *J. Clin. Oncol.* **17**, 2541–2545 (1999).
22. Logothetis, C. *et al.* Phase I trial of the angiogenesis inhibitor TNP-470 for progressive androgen-independent prostate cancer. *Clin. Cancer Res.* **7**, 1198–1203 (2001).
23. Bhargava, P. *et al.* A phase I and pharmacokinetic study of TNP-470 administered weekly to patients with advanced cancer. *Clin. Cancer Res.* **5**, 1989–1995 (1999).
24. Satchi-Fainaro, R. *et al.* Targeting angiogenesis with a conjugate of HPMA copolymer and TNP-470. *Nat. Med.* **10**, 255–261 (2004).
25. Cretton-Scott, E., Placidi, L., McClure, H., Anderson, D. & Sommadossi, J. Pharmacokinetics and metabolism of O-(chloroacetyl-carbamoyl) fumagillol (TNP-470, AGM-1470) in rhesus monkeys. *Cancer Chemother. Pharmacol.* **38**, 117–122 (1996).
26. Kataoka, K., Harada, A. & Nagasaki, Y. Block copolymer micelles for drug delivery: design, characterization and biological significance. *Adv. Drug Deliv. Rev.* **47**, 113–131 (2001).
27. Harris, J. & Chess, R. Effect of pegylation on pharmaceuticals. *Nat. Rev. Drug Discov.* **2**, 214–221 (2003).
28. Edlund, U. & Albertsson, A. Degradable polymer microspheres for controlled drug delivery. *Adv. Polym. Sci.* **157**, 67–112 (2001).
29. Rogers, M., Birsner, A. & D'Amato, R. The mouse cornea micropocket angiogenesis assay. *Nat. Protoc.* **2**, 2545–2550 (2007).
30. Carter, R., Morton, A. & Dunnett, S. Motor coordination and balance in rodents. in *Current Protocols in Neuroscience* Vol. 8.12. (ed. Taylor G.), 1–8 (John Wiley & Sons, Inc, New York, 2001).
31. Almog, N. *et al.* Prolonged dormancy of human liposarcoma is associated with impaired tumor angiogenesis. *FASEB J.* **20**, 947–949 (2006).
32. Marler, J. *et al.* Increased expression of urinary matrix metalloproteinases parallels the extent and activity of vascular anomalies. *Pediatrics* **116**, 38–45 (2005).
33. Folkman, J. & Klement, G. Platelet biomarkers for the detection of disease. *US and International Patent 20060204951* (2006).
34. Cervi, D. *et al.* Platelet-associated PF-4 as a biomarker of early tumor growth. *Blood* (2007).
35. Kwon, Y. *Handbook of Essential Pharmacokinetics, Pharmacodynamics and Drug Metabolism for Industrial Scientists.* (Plenum, New York, 2001).
36. Pierri, E. & Avgoustakis, K. Poly(lactide)-poly(ethylene glycol) micelles as a carrier for griseofulvin. *J. Biomed. Mater. Res. A* **75**, 639–647 (2005).
37. Kakizawa, Y. & Kataoka, K. Block copolymer micelles for delivery of gene and related compounds. *Adv. Drug Deliv. Rev.* **54**, 203–222 (2002).
38. Torchilin, V. Targeted polymeric micelles for delivery of poorly soluble drugs. *Cell. Mol. Life Sci.* **61**, 2549–2559 (2004).
39. Nishiyama, N. & Kataoka, K. Current state, achievements, and future prospects of polymeric micelles as nanocarriers for drug and gene delivery. *Pharmacol. Ther.* **112**, 630–648 (2006).
40. Barbera-Guillem, E., Smith, I. & Weiss, L. Cancer-cell traffic in the liver. I. Growth kinetics of cancer cells after portal-vein delivery. *Int. J. Cancer* **52**, 974–977 (1992).
41. Greish, K. Enhanced permeability and retention of macromolecular drugs in solid tumors: a royal gate for targeted anticancer nanomedicines. *J. Drug Target.* **15**, 457–464 (2007).
42. Duncan, R. Polymer conjugates as anticancer nanomedicines. *Nat. Rev. Cancer* **6**, 688–701 (2006).

BLOOD, *in press*
Accepted May 7, 2009

Title page:

Title:
Angiostatin regulates the expression of antiangiogenic and pro-apoptotic pathways via targeted inhibition of mitochondrial proteins.

Short title:
Mechanism of anti-tumor activity of angiostatin

Authors:
Tong-Young Lee[1], Stefan Muschal[2], Elke A. Pravda[1], Judah Folkman[1], Amir Abdollahi[1,2,3], and Kashi Javaherian[1*]

[1]Vascular Biology Program, Department of Surgery, Children's Hospital Boston and Harvard Medical School, Boston, MA, USA; [2]Department of Radiation Oncology, German Cancer Research Center (DKFZ) and University of Heidelberg Medical School, Heidelberg 69120, Germany; [3]Center of Cancer Systems Biology, Department of Medicine, Caritas St. Elizabeth's Medical Center, Tufts Univ. School of Medicine, Boston, MA, USA.

*Correspondence should be addressed to Kashi Javaherian
(Kashi.Javaherian@childrens.harvard.edu)
1 Blackfan Circle
Karp Research Bldg.
Boston, MA 02115
TEL: 617-919-2392
FAX: 617-730-0002

Abstract

Angiostatin, a proteolytic fragment of plasminogen, is a potent endogenous antiangiogenic agent. The molecular mechanisms governing angiostatin's antiangiogenic and anti-tumor effects are not well understood. Here, we report the identification of mitochondrial compartment as the ultimate target of angiostatin. Following internalization of angiostatin into the cell, at least two proteins within the mitochondria bind this molecule: malate dehydrogenase, a member of Krebs cycle and ATP synthase. *In vitro* and *in vivo* studies revealed differential regulation of key pro-survival and angiogenesis related proteins in angiostatin treated tumors and tumor-endothelium. Angiostatin induced apoptosis via downregulation of mitochondrial BCL-2. Angiostatin treatment led to downregulation of c-Myc and elevated levels of another key antiangiogenic protein, thrombospondin-1, reinforcing its anti-tumor and antiangiogenic effects. Further evidence is provided for reduced recruitment and infiltration of bone marrow-derived macrophages in angiostatin treated tumors. The observed effects of angiostatin were restricted to the tumor site and were not observed in other major organs of the mice, indicating unique tumor specific bioavailability. Together, our data suggests mitochondria as a novel target for antiangiogenic therapy and provides mechanistic insights to the antiangiogenic and anti-tumor effects of angiostatin.

Introduction

Human plasminogen is an abundant protein in blood circulation. Its plasma concentration is approximately 200 μg/L. It is a glycoprotein with a molecular mass of 92 KDa, containing 2 % carbohydrate and consisting of 5 kringles with a total of 24 disulfide bonds[1].

In 1994, it was reported that a proteolytic fragment of this protein, generated endogenously, demonstrated potent antiangiogenic activity in mice[2]. It was called angiostatin and consisted of kringles 1-4 of plasminogen. It is reasonable to assume that angiostatin has properties distinct from plasminogen. Presumably, removal of a segment of plasminogen introduces a conformational change in the molecule which confers unique binding properties compared to the plasminogen.

In order to understand the mechanism of action of angiostatin, a search for receptors and binding proteins was initiated by several laboratories. Annexin[3], angiomotin[4], integrin $\alpha v\beta 3$[5] and c-met[6] have been identified as some of the prominent candidates on the cell surface for binding angiostatin. However, some of these proteins appear also to bind plasminogen, thus failing to describe the distinct properties of angiostatin compared to its abundant precursor protein; plasminogen (for a review see ref. 7).

F_1F_0 ATP synthase has been reported to be a surface binding receptor on endothelial cells that selectively binds angiostatin but not plasminogen[8-11]. ATP synthase is a

multicomponent enzyme with mechanochemical properties[12]. It couples ATP synthesis to rotation of the molecule, generating a pumping mechanism for protons. Depending on the clockwise or counterclockwise rotation of the molecule, ATP and ADP are interconverted and protons are pumped in or out. Despite the controversies on localization of the ATP synthase on endothelial cell surface, in addition to mitochondria, recent evidence from other laboratories confirmed this observation[13,14].

In order to investigate angiostatin's mechanism of action, we used protein affinity purification to identify potential angiostatin binding partner. We have now discovered mitochondrial malate dehyrogenase (MDH2), a member of Krebs cycle, as an angiostatin binding protein.

Energy production in the cells depends on two pathways; one is glycolysis which originally in evolution was an anaerobic process. The second pathway is the more efficient oxidative phosphorylation (Krebs cycle). The glycolytic pathway, although less efficient in terms of overall ATP production, is used by a large number of tumor cells for processing glucose to ATP and lactate. On the other hand, malignant cells produce large amounts of lactate dehydrogenase A (LDH-A). It has been shown that the ability of tumor cells to metabolize glucose was compromised by reducing LDH, limiting their proliferation under hypoxia conditions and stimulating mitochondrial respiration[15].

More recently, genetic analysis in patients with brain tumor (glioblastoma multiforme) identified a mutation in the active site of the enzyme isocitrate dehydrogenase, a member of Krebs cycle[16].

We identified cell type specific actions of angiostatin by demonstrating selective inhibition of c-Myc while a key antiangiogenic protein, thrombospondin was upregulated in endothelial cells. We confirmed this data *in vivo* in a human melanoma tumor xenograft model. We found reduced levels of mitochondrial antiapoptotic protein BCL-2 and increased apoptosis in angiostatin treated tumors. Further, decreased c-Myc protein levels and elevated thrombospondin-1 expression correlated with impaired angiogenesis and reduced infiltration of bone marrow derived macrophages in angiostatin treated tumors.

Materials and methods

Cell lines and cell culture. Human tumor cell lines: A2058 (melanoma), BxPC-3 (pancreatic) were cultured in DMEM or RPMI 1640 with L-glutamine, respectively, and supplemented with 10% FCS and antibiotics. HUVECs and HMVECs (Lonza, Switzerland) were maintained in EGM endothelial growth media and EGM Bullet Kit or EGM-2MV microvascular growth media (Lonza, Switzerland) with antibiotics.

Human FcAS and mouse FcAS expression and purification. Construction, expression and purification of human Fc-angiostatin (hFcAS) and mouse Fc-angiostatin (mFcAS) have been described previously[17]. The recombinant constructs were prepared by placing the Fc regions at the N-terminus of angiostatin. Stable cell lines of these constructs were produced in NS/0 murine myeloma cells. The proteins were expressed and secreted into the media. Protein A was used for purification of the recombinant proteins (at least 90 % purity). We obtained approximately 50 mg/liter of Fc-AS by employing fermentors of 10-18 liter capacity.

Animal and tumor models. All animal procedures were carried out in compliance with Children's Hospital Boston guidelines. Protocols were approved by the Institutional Animal Care and Use Committee. Eight-week-old male (24-27g) SCID mice (Massachusetts General Hospital, Boston, MA) were used. Mice were acclimated, caged in groups of five in a barrier care facility, and fed animal chow and water *ad libitum*. Animals were euthanized by CO_2 inhalation. Human melanoma cell line A2058 was used for animal studies. Mice were shaved and the dorsal skin was cleaned with ethanol before cell injection. A suspension of $5x10^6$ tumor cells in 0.1 ml of PBS was injected s.c. into the dorsa of mice at the proximal midline. Mice were weighed and tumors were monitored twice a week in two diameters with digital calipers. Tumor volumes were determined using a^2 x b x 0.52 (where a is the shortest and b is the longest diameter). Tumors were allowed to grow to ~100 mm^3 and mice were randomized. Treatment was by bolus s.c. injections. Concentrations of hFcAS were corrected for the Fc contribution. Consequently, all indicated concentrations refer to concentrations of angiostatin in Fc-Angiostatin. After experiments were completed, tumors and organs were excised and fixed in either 4 % paraformaldehyde or were snap frozen. Ten mice were treated with each dose of Angiostatin. Unless specified otherwise, anti-tumor studies were performed with injection doses delivered every six days. The dose amounts were converted into mg/kg/day in order to compare with our previously published data for angiostatin alone (without Fc)[2].

ELISA determination of hFcAS. Mouse serum samples were obtained by retro-orbital puncture with non-heparinized capillary tubes under anesthesia. Serum was collected after centrifugation at 10,000 rpm for 10 min and human IgG concentrations were determined by sandwich ELISA (GenWay, San Diego, CA) following the manufacturer's protocol.

TUNEL assay. Apoptosis was examined by use of the terminal deoxynucleotidyltransferase-mediated deoxyuridine triphosphate nick end labeling (TUNEL) assay[18] through the manufacturer's protocol (Promega, Madison, WI).

Western blotting analysis. *In vivo,* tumor masses were homogenized with RIPA buffer (Boston Bioproducts, Worcester, MA) containing a mixture of protease inhibitors (Roche, Germany). *In vitro*, cells were starved overnight and treated with hFcAS (10 μg/ml) or hFc in starvation medium for 6 hrs and 16 hrs and lysed by the same buffer. Equal amount of total protein was fractionated by SDS–PAGE and then blotted onto nitrocellulose membrane. The protein blot was hybridized with TSP-1, c-Myc, BCL-2, Bax and beta-actin antibodies and then with secondary antibody, followed by detection with Renaissance chemiluminescence reagent (ThermoFisher).

Flow-cytometry analysis of hFcAS binding on cell-surface. All operations were performed at 4° C. Cells were trypsinized and resuspended in PBS (2 % BSA) for 30 min followed by 1 h incubation with 1 and 10 μg/ml hFcAS or hFc. Cells were centrifuged and washed by cold PBS, and then incubated with FITC-labeled secondary antibodies (Sigma, St. Louis, MO) against human Fc fragment and analyzed by BD Biosciences FACS Calibur flow cytometer.

Immunocytochemistry. HUVECs and A2058 cells were plated on cover slips and fixed by 4 % paraformaldehyde for surface staining (non-permeabilized; NP) or methanol, acetone mixture buffer (1:1 ratio) for intracellular staining (permeabilized; P). Cells were incubated with hFcAS for 2h and detected by Alexa 488 anti-human IgG. The cells were

double-stained by anti-ATP synthase beta subunit antibody, mitochondria marker (Mito-tracker) or actin staining (phalloidin) and detected by Alexa Fluor 594 antibody and imaged by confocal-microscopy (model DM IRE2; Leica). DAPI counterstaining of nuclei is shown in blue.

Tumors and organs were embedded in OCT medium (EMS, Hatfield, PA). Sections were rinsed by cold PBS and fixed with 4 % paraformaldehyde for 10 min with before staining. Human Fc-Angiostatin was detected by Alexa 488 anti-human IgG. Antibodies toTSP-1 (Thermo Fisher, Fremont, CA), CD31 (BD Pharmingen, San Jose, CA) and von Willebrand Factor (Dako, Carpinteria, CA) were used for staining. Antibodies to CD11b (AbD serotec, UK), CD45 (BD Pharmingen) and F4/80 (abcam, Cambridge, MA) were used to detect host leukocytes including monocytes and macrophages. The primary antibodies were detected by Alexa 488, 568, 594 and 647-labeled secondary antibodies (Molecular Probes, Eugene, OR). The sections were imaged by confocal-microscopy (model DM IRE2; Leica). A F4/80 marker was considered positive if the fluorescent pixel was present on or around it.

RNA interference and MDH2 transfection. HUVECs or A2058 cells were seeded in 6 cm dishes at a density of 1.5×10^5 per dish and transfected at 50 % confluency with 20 nM control nonspecific siRNA or ATP synthase alpha, beta specific siRNA (Dhamacon, Chicago, IL) using Silentfect (Bio-Rad, Hercules, CA) according to the manufacturer's instructions. Seventy-two hours after transfection, cells were fixed or lysed for immunostaining or immunoblotting. The MDH2 clone was provided by Harvard Plasmid Repository (http://plasmid.med.harvard.edu/PLASMID). The MDH2 insert was cloned into a GFP destination vector (pcDNA-DEST47, Invitrogen). The vector expresses MDH2-GFP fusion protein under CMV promoter and provides Ampicillin and Neomycin resistance for selection. The cloning and plasmid preparation procedure were performed by recombination according to the manufacturers' protocol (Invitrogen). The integrity of the MDH2 insert was confirmed by sequence analysis (GATC, Konstanz, Germany). 1.6 µg GFP-MDH2 plasmid was used for transfection assay through the protocol of the manufacturer.

Internalization assay. HUVECs were plated and grown to about 70 % confluence on cover slips. Cells were incubated with 10 µg/ml hFcAS, hFc or plasminogen for 30 min or 120 min at 37°C and then fixed by permeable condition. The slips were incubated in the blocking buffer (2 % BSA PBS) for 30 min, and then incubated with Alexa 488 anti-human IgG and imaged by confocal-microscopy.

Isolation of MDH-2 by affinity chromatography.

Mouse livers were homogenized in PBS + 50 mM octyl β-D glucoside followed by centrifugation and filteration. It was passed over a 10 ml column of Fc-Sepharose. The flow through was subjected to a second affinity column containing Fc-angiostatin-Sepharose. The affinity columns were prepared according to the protocol provided by Pharmacia (GE Healthcare) using activated-CNBr sepharose and purified mFc and mFcAS. Prior to application of the samples, both columns were equilibrated with 10 mM Hepes, 150 mM NaCl, 2mM Mg, 2mM Ca, pH 7.4. For elution, 90 mM Citrate, 2M NaCl, pH 3 was employed. After dialysis overnight, the sample was concentrated.

ATP generation by bioluminescent luciferase assay. Confluence HUVECs and A2058 cells in 48-well plates were incubated with 10 or 50 µg/ml hFcAS or hFc with fresh medium for 30, 120 and 360 min in 37°C. Aliquots of cellular supernatants from cell

surface ATP and cell lysis buffer (100 mM Tris, 4 mM EDTA, pH 7.75) from intracellular ATP were analyzed by using the ATP bioluminescence assay kit (Roche, Germany).

Statistical method: Data are expressed as mean ± SD. Statistical significance was assessed by using the Student's *t* test.

Results

In Vivo Efficacy and Bioavailability of Angiostatin

In order to examine the anti-tumor properties of angiostatin, SCID mice received subcutaneous injections of cultured tumor cells (human melanoma A2058). Animals were given a dose of 100 micrograms of hFcAS/mouse once every six days (s.c). An approximate 50 % reduction of tumor volume was observed as a result of treatment with angiostatin (Fig.1A). The distribution of exogenous angiostatin, using antibody to Fc, is shown in Fig. 1B. The concentration of exogenous angiostatin in the liver, heart, and kidney was found to be below the detection level in treated mice. In contrast, angiostatin was highly enriched in tumor, in particular in surrounding tumor vessels. This phenomenon is likely due to leaky tumor vasculature[19].

We also determined the concentration of exogenous angiostatin in the plasma of SCID mice. Since endogenous plasminogen interferes with a direct assay, we used the human Fc-tag of the exogenous angiostatin (hFcAS) and performed ELISA to measure the protein concentration. The circulating angiostatin (FcAS) concentration was found to be approximately 50 μg/ml (at the stated dose) (Fig. 1C). The level for control mice treated with the same amount of Fc was 25 μg/ml.

Angiostatin Induces Apoptosis Via Downregulation of BCL-2 Protein

In order to detect the extent of apoptosis in angiostatin treated tumors, TUNEL assay was performed[18]. TUNEL-positive apoptotic cells were increased as a result of angiostatin treatment (Fig.1D). Histologic sections of tumors revealed the mean percentage of apoptotic tumor cells to be 34.46 ± 4.31 % with 10.16 ± 2.22 % in PBS treated tumor sections.

The family of BCL related proteins are located in the mitochondria of mammalian cells and considered key regulators of the programmed cell death[20]. Two members of this family, called BAX and BAD, are pro-apoptotic, whereas BCL-2 exerts anti-apoptotic effects. We examined the expression levels of these proteins in tumor samples by Western blot analysis (Fig. 2A). We found no differences in BAX expression after angiostatin treatment. Likewise, BAD expression level remains unchanged after angiostatin therapy (data not shown). In contrast, the amount of the anti-apoptotic BCL-2 protein was reduced in the angiostatin treated tumors compared to sham-treated control tumors. Thus, inhibition of BCL-2 survival signaling might be a mechanism by which angiostatin induced apoptosis in our tumor model *in vivo*.

Angiostatin Upregulates Thrombospondin-1 Protein and Downregulates c-Myc

Thromsbospondin is a suppressor of angiogenesis. Downregulation of thrombospondin follows activation of oncogenes[21]. TSPs reduce tumor growth by a number of mechanisms, including interactions with VEGF, inhibition of MMP-9 and inhibition of endothelial cell migration[22]. On the other hand, c-Myc has been identified as a major promoter of tumor growth[23]. Western blot analysis for the expression of TSP-1 and c-

Myc is shown in Fig. 2A. Angiostatin treatment increased TSP-1 level by 1.6-fold and reduced c-Myc expression by 2.3-fold (Fig. 2B).

A dramatic increase in TSP-1 expression was observed in tumor vessels after treatment with angiostatin (Fig. 2C), a novel observation for angiostatin. Increase in TSP-1 expression following treatment with angiostatin is consistent with a number of previous reports, demonstrating up-regulation of TSP-1 expression in tumor vessels as an anti-angiogenic response[24,25]. Similar IF data is shown for different mouse organs (Fig. 2D). The increase in TSP-1 is mainly confined to the tumor vessels.

In vitro assay employing tumor cells and HUVECs provides strong evidence that following treatment of these cells by angiostatin, TSP-1 is up-regulated in endothelial cells and not in the tumor cells (Fig. 3A). TSP-1 was secreted into cell culture medium (Fig. 3B). The major receptor of TSP-1, CD36, was expressed on A2058 melanoma tumor cell surface (Fig. 3C). Melanoma cells showed lower proliferation and higher apoptosis rates after treatment with recombinant TSP-1 (rTSP-1) (Fig. 3D, E). c-Myc protein level of tumor cells decreased following treatment with TSP-1 rich HUVEC culture conditional medium (CM) or serum free medium (SF) plus rTSP-1 (Fig. 3F). No change in c-Myc was observed when cells were treated with angiostatin in serum-free media (Fig. 3F). We conclude that certain factors present in CM contribute to the increase of TSP in media. Overall, these data indicate that an increase in TSP-1 is associated with a decrease of c-Myc in tumors, consistent with previous published reports[26,27] (Fig. 2A).

Angiostatin Inhibits Migration of Host Macrophages to the Tumor

Bone marrow-derived cells (BMDCs) that infiltrate tumors and differentiate into macrophages are called TAMs (tumor-associated macrophages). Migration and infiltration of macrophages are hallmarks of tumor growth[28-30]. TAMs release a number of angiogenic factors, including MMP-9, VEGF, IL-8.

Our data for the presence of macrophages and their infiltration into the tumors is shown in Fig. 4 (A-C). We utilized 3 markers for identification of macrophages: CD11b, CD 45 and F4/80 were employed. Immunohistochemical analysis of mouse tumors showed reduced macrophage infiltration in angiostatin-treated mice relative to sham-treated controls (Fig. 4D).

Flow Cytometry and Immunofluorescence Studies Demonstrate that Angiostatin Targets Mitochondria

Flow cytometry was employed to monitor the binding of angiostatin to the cell surfaces of human umbilical vein endothelial cells (HUVECs), human dermal microvascular endothelial cells (HMVECs) and two tumor cell lines (pancreatic BxPC-3 and melanoma A2058) (Fig. 5A). Two concentrations of angiostatin were used and angiostatin was shown to bind to the cell surface.

Immunofluorescence (IF) analysis of some of these cell lines under permeable and nonpermeable conditions is presented in Fig. 5B. Angiostatin appears to be clustered on the cell surface under nonpermeabilized conditions. Under permeable conditions, angiostatin location resembles mitochondria (Fig. 5C). ATP synthase, in addition to being a mitochondrial protein, has been reported to bind angiostatin on endothelial cell surface[12,13]. We employed a monoclonal antibody directed to the β subunit of ATP synthase. Co-localization of angiostatin and ATP synthase in mitochondria are observed (Fig. 5C, 1st row). Confocal 3D image showed the distributions of angiostatin and ATP synthase in mitochondria of the endothelial cell (Supplementary 1). Both human Fc and

plasminogen failed to be located in mitochondria. Images in the fourth column in Fig. 4D were obtained by merging of the previous two columns.

MitoTracker, a small molecule, which passively diffuses across plasma membrane and accumulates in active mitochondria and Phalloidin (directed to actin) probes, were also employed. The data are shown in Fig. 5D. MitoTracker and angiostatin have similar patterns and overlap (Fig. 5D, 2nd row). In contrast, Phalloidin which binds actin, has a distinct distribution compared with angiostatin (Fig. 5D, 3rd row).

Immunostaining of angiostatin treated tumors showed localization of angiostatin to mitochondria in both endothelial cells and tumor cells *in vivo* (Supplementary 2).

Angiostatin Targeting to Mitochondria is Achieved by Internalization

Endothelial cells were incubated in the presence of angiostatin at different intervals and IF measurements were carried out. Following internalization of angiostatin by the cell, angiostatin was detected in the mitochondria (Fig. 6A). No internalization of plasminogen was observed. Similar results were obtained by removing Fc and treating the cells with angiostatin alone (data not shown).

Expression of ATP synthase α and β subunits was diminished by treatment with interfering RNA (Fig. 6B). Inhibition of either subunit by siRNA reduced the presence of angiostatin in mitochondria (Fig. 6A). Thus, reduced angiostatin staining in mitochondria may be the result of ATP synthase knockdown on the cell surface and/or in the inner mitochondrial membrane. IF analysis of HUVECs under nonpermeable and permeable conditions, following siRNA treatment of the β subunit, is shown in Fig. 6C. A marked reduction in expression of the β subunit is observed on the surface and in the mitochondria. Flow cytometry data show that ATP synthase accounts for approximately 9% of total binding of angiostatin to the cell surface, consistent with the observation that angiostatin binds to a number of cell surface proteins including ATP synthase (Fig. 6D).

Angiostatin binds to malate dehydrogenase in mitochondria

In order to identify the cellular proteins binding to angiostatin, we adopted a simple affinity purification protocol of the mouse liver homogenate preparation. Two affinity columns were employed and the liver homogenate was first passed through mFc-Sepharose. The flow through was subsequently applied to a mouse Fc-angiostatin affinity column (mouse Fc and mouse angiostatin). Proteins bound to the second column were eluted and sequenced (Fig. 7A). The most intense band was identified as mitochondria malate dehydrogenase (mt MDH or MDH-2), based on the sequence results (data not shown). Mitochondrial MDH, a member of the Krebs cycle, is a dimer composed of two identical subunits each with a molecular mass of 34kDa[31]. Subsequently, binding assay (ELISA) of the two types of MDH (cytoplasmic and mitochondrial) using a small number of ligands was undertaken. Only MDH-2 bound angiostatin (Fig. 7B). No binding was observed between angiostatin and cytoplasmic MDH (data not shown).

Both angiostatin and plasminogen bind MDH-2 at the indicated concentrations (Fig. 7B). However, as we showed earlier, angiostatin is capable of being internalized by the cell, whereas plasminogen entry is blocked (Fig. 6A). Furthermore, the binding of plasminogen to mitochondria is reduced considerably in comparison with angiostatin in immunostaining using the same concentration of both proteins (Fig. 5C).

Initially, we tested commercial monoclonal antibody and polyclonal antibodies against MDH-2 in immunofluorescence. The monoclonal antibody showed very weak staining in IF. The results for polyclonal antibodies were not highly specific. In order to overcome

this problem, a GFP-MDH-2 DNA plasmid was constructed (Methods). A2058 tumor cells were transfected with this plasmid and IF was undertaken (Fig.7C). The efficiency of transfection was approximately 40 %. Transfection of endothelial cells with GFP-MDH DNA construct caused toxicity (data not shown).
Staining with antibodies to ATP synthase β and angiostatin is presented for cells after treatment with Fc-angiostatin (top panel, Fig. 7C). Three proteins, namely ATP synthase, MDH-2 and angiostatin, show colocalization. Upon treatment of the cells with ATP synthase β siRNA, colocalization of angiostatin and MDH-2 remains intact, even though the signal for ATP synthase β has disappeared (lower panel, Fig. 7C).

ATP Generation of Cells is Reduced Following Treatment with Angiostatin

We hypothesized that angiostatin inhibits production of ATP by targeting two critical mitochondrial proteins MDH-2 and ATP synthase. To answer this question, we measured intracellular and extracellular ATP in HUVECS using a bioluminescence assay (Fig. 7D). ATP concentration was reduced by approximately 20 % (extracellular) and 80 % (intracellularl) after 90 minutes incubation with 10 μg/ml angiostatin. Similar data were obtained with A2058 tumor cells (data not shown). Analogous ATP inhibition in HUVECs was previously reported upon treatment with angiostatin[9].
In a separate experiment, HUVECs were treated with siRNAs of ATP synthase and MDH-2 for 72 hrs. Approximately, 20 % reduction of ATP was observed (data not shown). Apparently, the cells may compensate for ATP reduction by other mechanisms, after a period of time, consistent with the data of Fig. 7D where IntraC level of ATP increases after 6 hrs.

Discussion

The anti-tumor mechanism of angiostatin is poorly understood. There is a general consensus about the following properties of angiostatin; 1) angiostatin binds to a variety of cell surface proteins. Some of these binding proteins are shared by plasminogen. It is not clear which of these sites play a major role in determining its antitumor activity[7]. 2) The antitumor activity of angiostatin has been demonstrated to reside in kringles 1-3, kringles 1-4, kringle 1-4.5 and kringle 5[7,32]. 3) A number of mitochondrial inner membrane proteins are also present on the endothelial cell plasma membrane, a phenomenon requiring more investigation[7].
Here, we present strong evidence that angiostatin targets mitochondria and at least binds to two mitochondrial proteins: ATP synthase and MDH-2. It has been reported that ATP synthase on endothelial cell surface is a selective receptor for angiostatin[8,9]. However, the same group of investigators have also reported that angiostatin blocks the binding of plasminogen to CD26 in human prostate tumor cells[33]. We show that knock-down of alpha or beta subunits of ATP synthase results in reduced angiostatin signals in mitochondria. We also show that the binding of angiostatin to cell surface is reduced only by 9% as a result of knocking out the ATP synthase (Fig. 6D). Thus, ATP synthase seems to be at least in part involved in angiostatin internalization. However, other cell surface receptors and mechanisms for angiostatin internalization could not be excluded. Clearly, angiostatin is capable to bind to a number cell surface proteins and the contribution of these proteins in facilitating angiostatin internalization remains to be elucidated.

Glycolysis, the main pathway for utilizing glucose by tumor cells, has been extensively studied for decades. Angiostatin appears to impact Krebs cycle. Both cycles use glucose under aerobic conditions to produce ATP. Comparing the two pathways, glycolysis is more efficient in terms of ATP production in a short time but less efficient in overall ATP production. Tumor cells use more glucose through glycolysis to generate ATP.

Lactate dehydrogenase has been shown to play an important role in regulating glycolysis in tumor growth (Warburg's effect)[15,34]. Interestingly, it has been found that malate dehydrogenase from the extremely *halophilic archaebacterium Haloarcula Marismortui* has more sequence homology to LDH than to other MDHs[35]. Apparently, there has been an overlap between the two families of the enzymes in early evolution before divergence to later MDHs.

Involvement of enzymes of Krebs cycle in tumorigenesis is not unprecedented. Krebs cycle associated metabolites released from tissues, in the presence of insufficient oxygen, have been shown to be proangiogenic[36]. Under these conditions, Krebs cycle intermediates accumulate in a process independent of HIF-1α[37].

On the other hand, succinate dehydrogenase (SDH) and fumarase (FH) have been shown to be tumor suppressors, since mutations in the genes of these enzymes have been shown to promote cancer growth[38-40]. Apparently, as a result of mutations in these genes, degradation of HIF-1α is inhibited. Evidence has been presented showing that stabilization of hypoxia-inducible factor (HIF-1α) results in upregulation of important angiogenesis genes, such as VEGF and MMP-9[41]. We have not observed any changes in HIF expression following analysis of the angiostatin treated tumors discussed in this paper (data not shown).

Genetic analysis of patients with glioblastoma revealed the presence of a single mutation in the active site of isocitrate dehydrogenase, one of the major enzymes in the Krebs cycle[16]. These data clearly imply the importance of targeting anti-cancer drugs to mitochondria.

We have analyzed protein levels of different important markers in tumors obtained from PBS and angiostatin-treated mice. A decrease in BCL-2 expression is consistent with observed higher apoptosis. However, as previously pointed out, we did not detect changes in protein levels for BAK and BAD, two pro-apoptotic proteins belonging to the BCL-2 family. It is possible that the observed decrease in BCL-2 correlates with tumor size and does not relate to interactions of angiostatin with mitochondria.

An important finding in this paper relates to the increase in TSP-1 expression observed in angiostatin-treated mice. The role of microenvironment in cancer has been a major focus of researchers since the mid-1990s[42]. The extracellular matrix embodies a large number of factors, which play an important role in tumor growth and angiogenesis. Migration of macrophages to tumor sites is associated with providing a series of enzymes required for tumor survival and formation of blood vessels. Angiostatin has been reported to be an anti-inflammatory factor by inhibiting leukocyte recruitment[43]. It has been shown that inhibition of plaque neovascularization by angiostatin reduces macrophage accumulation and progression of advanced atherosclerosis[44]. Angiostatin inhibits migration of macrophages by disruption of their actin cytoskeleton[45]. Macrophages secrete metalloelastase, which is responsible for generation of angiostatin in Lewis lung carcinoma (LLC)[46].

We have observed three novel features in angiostatin-treated SCID mice, which are known to be important components of tumor regulation; a decrease in c-Myc, an increase in TSP-1 and a decrease in macrophage recruitment. Available evidence indicates that the mechanism of action of these three are related. Upon c-Myc inactivation, an increase of either p53 or TSP-1 is required in order to maintain tumor regression[26,27,47]. Our data indicates that TSP-1 is secreted by endothelial cells and not tumor cells. On the other hand, we have observed an elevated level of TSP-1 in tumor cells of treated mice, while showing a decline in infiltrating macrophages. The role of c-Myc is not limited to an increase in TSP-1 or p53. It has been shown to transactivate LDH, an important enzyme in glycolysis[48].

The fact that anti-tumor properties of angiostatin is independent of the length of the kringles, raise the possibility that any one kringle is capable of eliciting anti-tumor response. We propose that a single disulfide bonded kringle is an important component for binding to the diverse cell surface proteins reported for angiostatin. Additional support for this hypothesis comes from binding of angiostatin to c-met, a receptor for HGF, another kringle- shaped ligand[6]. Furthermore, for a kringle to be active, it may require to have a basic isoelectric point. Examination of all 5 kringles of plasminogen confirms that indeed all 5 kringles are positively charged. Therefore, it is interesting to point out to a report from Philip Leder's laboratory where a small positively charged molecule, called F16, accumulated in mitochondria and showed inhibition of tumor growth[49].

We have attempted to include the data addressed in this publication in a diagram containing both endothelial cells and tumor cells. Angiostatin targets mitochondria in endothelial cells. At least two proteins, ATP synthase and MDH-2 in mitochondria bind angiostatin. ATP production is reduced, TSP-1 is increased. TSP-1 is secreted and binds to corresponding receptors on the tumor cells (for example CD36). Consequently, BCL-2 and c-Myc are downregulated (Fig. 7E).

Finally, an interesting finding reported in this paper is the selective tumor uptake of angiostatin while most examined organs were spared from angiostatin treatment. This phenomenon has been reported to be a consequence of enhanced permeability and retention (EPR)[19]. Previously, other investigators in our laboratory reported a similar observation with TNP-40, an antiangiogenic drug, conjugated to HPMA- polymer[50]. If this specificity for angiostatin is confirmed in other tumor models, angiostatin has the potential for use in the conjugation of small molecular size drugs directed to tumors[51].

Acknowledgments

This article is dedicated to the memory of Dr. Judah Folkman, a great mentor and the leading pioneer of the field of angiogenesis research. We are grateful to Professors Yussef Hatefi, Douglas Hanahan, Lena Claesson-Welsh and Bruce Zetter, for reading the manuscript and making helpful suggestions. We also thank Sandra Ryeom, Taturo Udagawa, Diane Bielenberg, Randy Watnik, Carmen Barnes, Sarah Short and Han-Chung Wu, for their comments on the manuscript. We are indebted to Dr. Kim-Ming Lo of Merck Serono for constructing Fc-Angiostatin. Special thanks to Pauline Breen, Melissa Herman for proofreading the manuscript and Kristin Johnson for preparing the figures. This work was supported by NIH grants R01-CA064481 (JF), NIH P01-CA45548 (JF), NASA grant NNJ04HJ12G (AA, JF), DFG grant SPP1190 (AA),

Department of Defense Grant W81XWH-05-1-0115 (JF) and a grant from The Breast Cancer Research Foundation (JF).

Author contributions

T.Y.L., K.J. designed, performed, analyzed experiments and prepared manuscript. T.Y.L., S.M., E.A.P. and K.M.L. prepared experiments. A.A. and J.F. designed experiments and prepared manuscript. The authors have no conflicts of interest to disclose.

Abbreviations used

hFcAS: human Fc-human angiostatin
mFcAS: murine Fc-murine angiostatin
hFcES : human Fc-human endostatin
mFcES : murine Fc-murine endostatin
TSP: Thrombospondin
IF : Immunofluroescence
Plgn : human plasminogen

References:

1. Collen D, Lijnen HR, Verstraete M. Blood Principles and Practice of Hematology (ed Hardin, R.I., Lux, S. and Stossel, T.P). J.B. Lippincott Company, Philadelphia. 1995; 1261-1288.
2. O'Reilly MS, Holmgren L, Shing Y, et al. Angiostatin: a novel angiogenesis inhibitor that mediates the suppression of metastases by a Lewis lung carcinoma. Cell. 1994; 79: 315–328.
3. Tuszynski GP, Sharma MR, Rothman VL, Sharma MC. Angiostatin binds to tyrosine kinase substrate annexin II through the lysine-binding domain in endothelial cells. Microvasc Res. 2002; 64: 448-462.
4. Troyanovsky B, Levchenko T, Mansson G, Matvijenko O, Holmgren L. Angiomotin: An angiostatin binding protein that regulates endothelial cell migration and tube formation. J Cell Biol. 2001; 152: 1247–1254.
5. Tarui T, Miles LA, Takada Y. Specific interaction of angiostatin with integrin αvb3 in endothelial cells. J Biol Chem. 2001; 276: 39562–39568.
6. Wajih N, Sane DC. Angiostatin selectively inhibits signaling by hepatocyte growth factor in endothelial and smooth muscle cells. Blood. 2003; 101: 1857-1862.
7. Wahl ML, Kenan DJ, Gonzalez-Gronow M, Pizzo SV. Angiostatin's Molecular Mechanism: Aspects of Specificity and Regulation Elucidated. J Cell Biochem. 2005; 96: 242-261.
8. Moser TL, Stack M, Asplin I, et al. Angiostatin binds ATP synthase on the surface of human endothelial cells. Proc Natl Acad Sci USA. 1999; 96: 2811–2816.
9. Moser TL, Kenan DJ, Ashley TA, et al. Endothelial cell surface F1-Fo ATP synthase is active in ATP synthesis and is inhibited by angiostatin. Proc Natl Acad Sci USA. 2001; 98: 6656–6661.

10. Wahl ML, Grant DS. Effects of microenvironmental extracellular pH and extracellular matrix proteins on angiostatin activity and on intracellular pH. J Gen Pharm (Vascular). 2002; 35:1-10.

11. Arakaki N, Nagao T, Niki R, et al. Possible role of cell surface H^+ATP synthase in the extracellular ATP synthase and proliferation of human umbilical vein endothelail cells (HUVECs). Mol Cancer Res. 2003; 1:931-939.
12. Boyer PD. The ATP synthase-A splendid molecular machine. Annu Rev Biochem**.** 1997; 66: 717-749.
13. Das B, Mondragon MO, Sadeghian M, Hatcher VB, Norin AJ. A novel ligand in lymphocyte-mediated cytotoxicity: Expression on the subunit of H+ transporting ATP sythase on the surface of tumor cell lines. J Exp Med. 1994; 180: 273–281.
14. Soltys BJ, Gupta RS. Mitochondrial-matrix proteins at unexpected locations: Are they exported? Trends Biochem. Sci. 1999; 24: 174–177.
15. Fantin VR, St-Pierre J, Leder P. Attenuation of LDH-A expression uncovers a link between glycolysis, mitochondrial physiology, and tumor maintenance. Cancer Cell. 2006; 9: 425-434.
16. Parsons DW, Jones S, Zhang X. et al. An integrated genomic analysis of human glioblastoma multiforme. Science. 2008; 321: 1807-1812.
17. Bergers G, Javaherian K, Lo K-M, Folkman J, Hanahan D. Effects of angiogenesis inhibitors on multistage carcinogenesis in mice. Science. 1999; 284: 808-812.
18. Gavrieli Y, Sherman Y, Ben-Sasson SA. Identification of programmed cell death in situ via specific labeling of nuclear DNA fragmentation. J Cell Biol. 1992; 119: 493-501.
19. Dvorak HF, Nagy JA, Dvorak JT, Dvorak AM. Identification and characterization of the blood vessels of solid tumors that are leaky to circulating macromolecules. Am J Pathol. 1998; 133: 95-109.
20. Danial NN, Korsmeyer SJ. Cell Death: Critical Control Points. Cell. 2004; 116: 205-219.
21. Lawler J, Detmar M. Tumor progression: the effects of thrombosondin-1 and –2. Inter J Biochem Cell Biol. 2004; 36: 1038-1045.
22. Rodríguez-Manzaneque JC, Lane TF, Ortega MA, Hynes RO, Lawler J, Iruela-Arispe ML. Thrombospondin-1 suppresses spontaneous tumor growth and inhibits activation of matrix metalloproteinase-9 and mobilization of vascular endothelial growth factor. Proc Natl Acad Sci USA. 2001; 98: 12485-12490.
23. Hahn WC, Weinberg RA. Rules for making human tumor cells. N Engl J Med. 2002; 347: 1593-1604.
24. Dameron KM, Volpert OV, Tainsky MA, Bouck N. Control of angiogenesis in fibroblasts by p53 regulation of thrombospondin-1. Science. 1994; 265: 1582-1584.
25. Lawler J. Thrombospondin-1 as an endogenous inhibitor of angiogenesis and tumor growth. J Cell Mol Med. 2002; 6: 1-12.
26. Tikhonenko AT, Black DJ, Linial ML. Viral Myc oncoproteins in infected fibroblasts down-modulate thrombospondin-1, a possible tumor suppressor gene. J Biol Chem. 1996; 271: 30741-30747.

27. Watnick RS, Cheng YN, Rangarjan A, Ince TA, Weinberg RA. Ras modulates Myc activity to repress thrombospondin-1 expression and increase tumor angiogenesis. Cancer Cell. 2003; 3: 219-31.
28. Hanahan D, Weinberg RA. The hallmarks of cancer. Cell. 2000; 100: 57-70.
29. Condeelis J, Pollard JW. Macrophages: obligate partners for tumor cell migration, invasion, and metastasis. Cell. 2006; 124: 263-266.
30. Coussens LM, Werb Z. Inflammation and cancer. Nature. 2002; 420: 860-867.
29. Musrati RA, Kollárová M, Mernik N, Mikulášová D. Malate dehydrogenase: distribution, function and properties. Gen Physiol Biophys. 1998; 17: 193-210.
30. Christofk HR, Vander Heiden KG, Harris MH, et al. The M2 splice isoform of pyruvate kinase is important for cancer metabolism and tumor growth. Nature. 2008; 452: 230-233.
31. Musrati RA, Kollárová M, Mernik N, Mikulášová D. Malate dehydrogenase: distribution, function and properties. Gen Physiol Biophys. 1998; 17: 193-210.
32. Chen Y-H, Wu H-L, Li C, et al. Anti-angiogenesis mediated by angiostatin K1-3, K1-4 and K1-4.5. Thromb Haemost. 2006; 95: 668-677.
33. Gonzalez-Gronow M, Grenett HE, Gawdi G, Pizzo SV. Angiostatin directly inhibits human human prostate tumor cell invasion by blocking plasminogen binding to its cellular receptor, CD26. Exp Cell Res. 2005; 303: 22-31.
34. Christofk HR, Vander Heiden KG, Harris MH, et al. The M2 splice isoform of pyruvate kinase is important for cancer metabolism and tumor growth. Nature. 2008; 452: 230-233.
35. Cendrin F, Chroboczek J, Zaccai G, Eisenberg H, Mevarech M. Cloning, sequencing, and expression in E. Coli of the gene coding for malate dehydrogenase of the extremely halophilic archaebacterium Haloarcula marismortui. Biochem. 1993; 32: 4308-4313.
36. Murray B, Wilson DJ. A study of metabolites as intermediate effectors in angiogenesis. Angiogenesis. 2001; 4: 71-77.
37. Sapieha P, Sirinyan M, Hamel D, et al. The Succinate receptor GPR91 in neurons has a major role in retinal angiogenesis. Nat. Med. 2008; 14: 1067-1076.
38. Selak MA, Armour SM, MacKenzie ED, et al. Succinate links TCA cycle dysfunction to oncogenesis by inhibiting HIF-1 α prolyl hydroxylase. Cancer Cell. 2005; 7: 77-85.
39. Gottlieb E, Tomlinson IPM. Mitochondrial tumor suppressors: a genetic and biochemical update. Nat Rev Cancer. 2005; 5: 857-865.
40. Pollard PJ, Spencer-Dene B, Shukla D, et al. Targeted inactivation of Fh1 causes proliferative renal cyst development and activation of the hypoxia pathway. Cancer Cell. 2007; 11: 311-319.
41. Du R, Lu KV, Petritsch C, et al. HIF1α induces the recruitment of Bone Marrow-Derived vascular modulatory cells to regulate tumor angiogenesis and invasion. Cancer Cell. 2008; 13: 206-220.
42. Marx J. All in the Stroma: Cancer's Cosa Nostra. Science. 2008; 320: 38-41.
43. Chavakis T, Athanasopoulos A, Rhee J-S, et al. Angiostatin is a novel anti-inflammatory factor by inhibiting leukocyte recruitment. Blood. 2005; 105: 1036-1043.

44. Moulton K, Vakili K, Zurakowski D, et al. Inhibition of plaque neovascularization reduces macrophage accumulation and progression of advanced atherosclerosis. Proc Natl Acad Sci USA. 2003; 100: 4736-4741.
45. Perri SR, Annabi B, Galipeau J. Angiostatin inhibits monocyte/macrophage migration via disruption of actin cytoskeleton. FASEB J. 2007; 21: 3928-3936.
46. Dong Z, Kumar R, Yang X, Fidler I. Macrophage-derived metalloelastase is responsible for the generation of angiostatin in Lewis lung carcinoma. Cell. 1997; 88: 801-810.
47. Giuriato S, Ryeom S, Fan AC, et al. Sustained regression of tumors upon MYC inactivation requires p53 or thrombospondin-1 to reverse the angiogenic switch. Proc Natl Acad Sci USA. 2006; 103: 16266-16271.
48. Shim H, Dolde C, Lewis BC, et al. c-Myc transactiavation of LDH-A: implications for tumor metabolism and growth. Proc Natl Acad Sci USA. 1997; 94: 6658-6663.
49. Fantin VR, Berardi MJ, Scorrano L, Korsmeyer SJ, Leder P. Cancer Cell. 2002; 2:29-42.
50. Ronit-Satchi F, Puder, M, Davies JW, et al. Targeting angiogenesis with a conjugate HPMA copolymer and TNP-470. Nat Med. 2004; 10: 255-261.
51. Lee TY, Lin CT, Kuo SY, Chang D-K, Wu HC. Peptide-mediated targeting to tumor blood vessels of lung cancer for drug delivery. Cancer Res. 2007; 67: 10958-10965.

Figure Legends

Fig 1. Treatment of mouse bearing human melanoma cancer cells (A2058) with hFc-angiostatin. (A) 10 tumor-bearing SCID mice in each group were s.c. treated with hFcAS, hFc (100 μg/mouse once every 6 days) or PBS. Treatment was stopped prior to the development of necrosis. Sites of injection were away from tumors. Tumor sizes and the ratio of treated/control (T/C) and P value are shown for hFcAS treated group. (B) Immunostaining shows that treated angiostatin (green) only bound in tumor masses but not in normal organs such as liver, heart and kidney. CD31 staining for vessels (red) and DAPI for nuclei (blue) (20X magnification) are also presented. (C) ELISA of circulating human IgG concentrations are shown four days after the last injection. (D) TUNEL assay shows more apoptosis cells in tumor area and no TUNEL positive cell in normal organs after the treatment (Bar, 20 μm).

Fig. 2. Angiostatin treatment of tumor-bearing mice affects the expression of a number of proteins. (A) Tumors reaching the sizes and weights of 0.1 to 0.8 g after treatment with angiostatin or PBS. Equal amounts of protein extracts from tumors were subjected to Western blot analysis with antibodies against TSP-1, c-MYC, BCL-2, BAX and Beta-actin. TSP-1 levels shown increased and c-Myc expressions decreased following angiostatin treatment. Relative amounts are indicated by the ratio of each protein to corresponding level of Beta-actin (B). The intensity of the protein bands were quantitated by densitometry and normalized against that of beta-actin. (C) Immunostaning of the above tumor sections after incubation with antibodies directed to TSP-1 and VWF, followed by Alexa 568 anti-rat and Alexa 647 anti-rabbit IgG. The

TSP-1 (red) was overexpressed in tumor vessels (pink). hFcAS (green) could be detected by Alexa 488 anti-human IgG (Bar, 20 μm). (D) Large scale sections showed that following treatment, TSP-1 is over-expressed only in tumor site but not in normal organs (Bar, 100 μm).

Fig. 3. TSP-1 over-expressed, induced by angiostatin, inhibits melanoma tumor cells growth. (A) HUVECs over-expressed TSP-1 by angiostatin treatment whereas tumor cells do not. (B) HUVECs secreted TSP-1 into cell culture medium (Sup). (C) FACS analysis showed that A2058 melanoma cells express CD36 on the surface. (D) Melanoma tumor cell proliferation was inhibited by 10 μg/ml recombinant TSP-1 treated. (E) TUNEL assay showed more apoptosis of tumor cells after rTSP-1 treatment. (F) c-Myc protein level of tumor cells was decreased after treatment with TSP-1 rich HUVEC culture conditional medium (CM) or serum free medium (SF).

Fig. 4. Angiostatin inhibits host macrophages recruitment to the tumors. Markers, CD11b, CD45 and F4/80 (A, B and C). Infiltration of the host bone marrow derived cells (BMDCs) decreased after hFcAS treatment. (D) Quantification of F4/80 positive area was counted by pixel numbers ($P<0.05$) (Bar, 100μm).

Fig. 5. Angiostatin binding activity and colocalization with ATP synthase in mitochondria. (A) Endothelial cell lines HUVEC, HMVEc and tumor cell lines AsPC-1, A2058 were subjected to FACS analyis using angiostatin concentrations of 1 (blue) and 10 μg/ml (green). The red area represents the control Fc binding. (B) IF analysis of HUVEC and A2058 under permeable (P) and nonpermeable (NP) conditions. No staining was observed with control Fc. (C) HUVECs and (D) A2058 cells, were fixed under permeabilized conditions and incubated with hFcAS (50 ng/ml) for 2 h and detected by Alexa Fluor 488 anti-human IgG (green). Those cells were also double stained by anti-ATP synthase β subunit antibody, mitochondria marker (MitoTracker) or actin staining Phalloidin and detected by Alexa Fluor 594 antibody (red). In merged (last column), hFcAS and ATP synthase β subunit or MitoTracker showed colocalization (yellow) in both endothelial and tumor cells by confocal microscopy. DAPI staining of nuclei is shown in blue (Bar, 20 μm).

Fig. 6. Angiostatin internalization and its migration to mitochondria.
(A) Endothelial cells were incubated with hFcAS (10 μg/ml) for 30 minutes and 120 minutes, then fixed and permeabilized and probed by Alexa 488 anti-human IgG. hFcAS, not plasminogen or hFc, could be internalized. Internalization was achieved at the indicated intervals after siRNA treatment for 72 hrs. Internalization of hFcAS was decreased in ATP synthase α or β subunits interfering RNA treated cells. Confirming that ATP synthase expression has been decreased after siRNA treated cells, (B) western blot and (C) immunostaining of β subunit after 72h treatment with siRNA (Bar, 20 μm). (D) HUVECs were subjected to FACS analysis using angiostatin concentration of 10 μg/ml and probed by Alexa 488 antihuman IgG. The red area represents the control Fc binding.

Fig. 7. Identification of MDH-2 as a binding protein to angiostatin. Mouse liver homogenate was first passed over a mFc-Sepharose column followed by mFc-

angiostatin-Sepharose step. PAGE analysis of the eluant is shown in A (arrow points to the major band identified as MDH-2) using Coomassie stain. ELISA(B) was performed by coating the plate with porcine heart mitochondria MDH (1 μg/ml). The ligands are indicated at the bottom (1μg/ml). (C) Either ATP synthase knocked down or wild type tumor cells were transfected with GFP-MDH2 plasmid (transfection efficiency was approximately 40 %). Cell were permeabilized and incubated with hFcAS and anti-ATP synthase β monoclonal antibody. Alexa 568 anti-human and 647 anti-mouse antibodies were used for detection. HFcAS (red) showed colocalization with ATP synthase (pink) in ATP synthase wild type cells and also with MDH2 (green) in ATP synthase knocked down cells (Bar, 20 μm). (D) ATP production in HUVECS was inhibited by hFcAS in both extracellular (ExtraC) and intracellular (IntraC) regions. The incubation times were 30, 90 and 360 minutes. (E) A diagram summarizing the identified pathways following angiostatin treatments *in vivo* and *in vitro*.

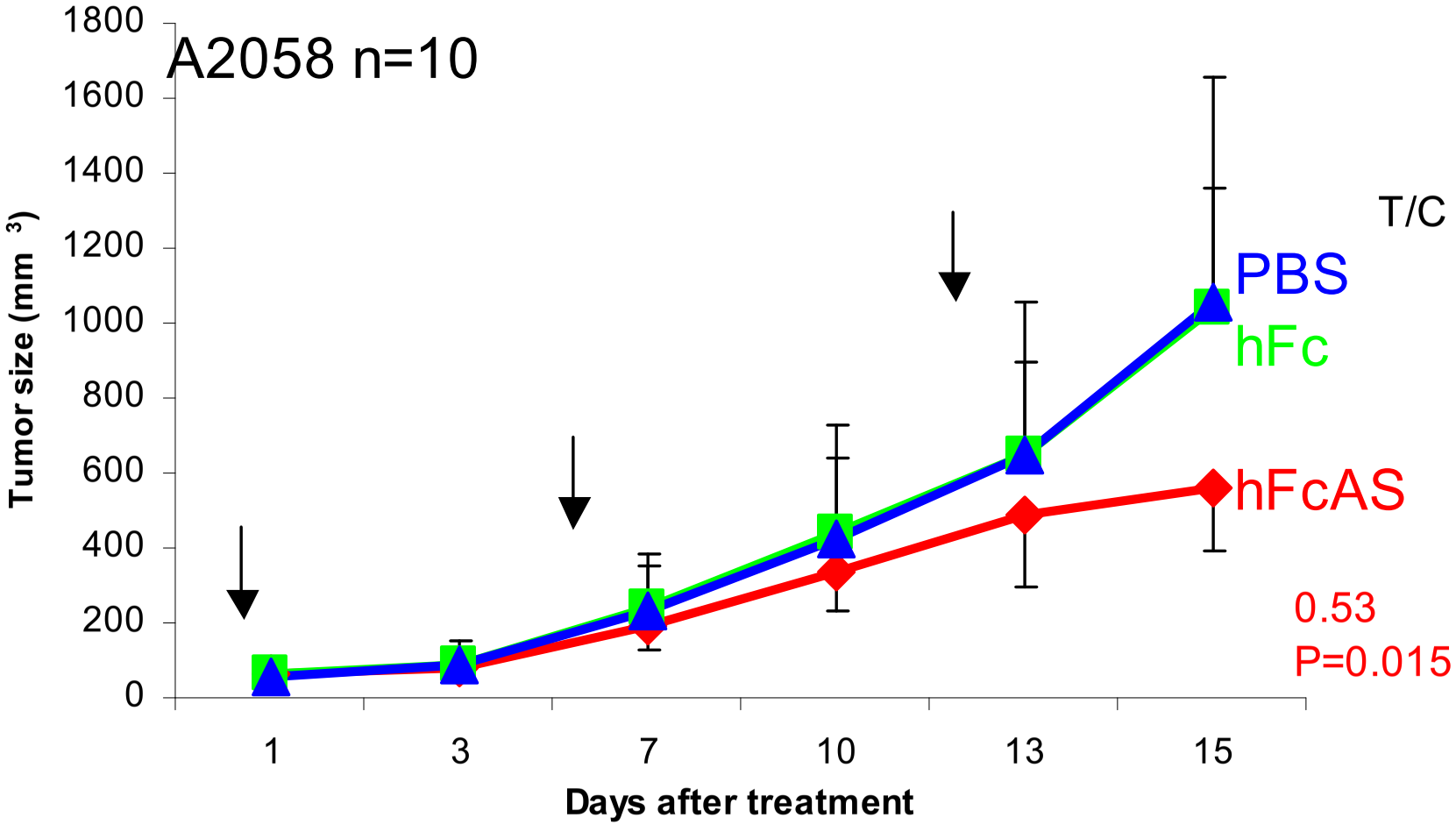
A2058 n=10
Tumor size (mm 3)
1800
1600
1400
1200
1000
800
600
400
200
0
1
3
7
10
13
15
Days after treatment
T/C
PBS
hFc
hFcAS
0.53
P=0.015

Blood/2008/197236-Javaherian Figure 1 B

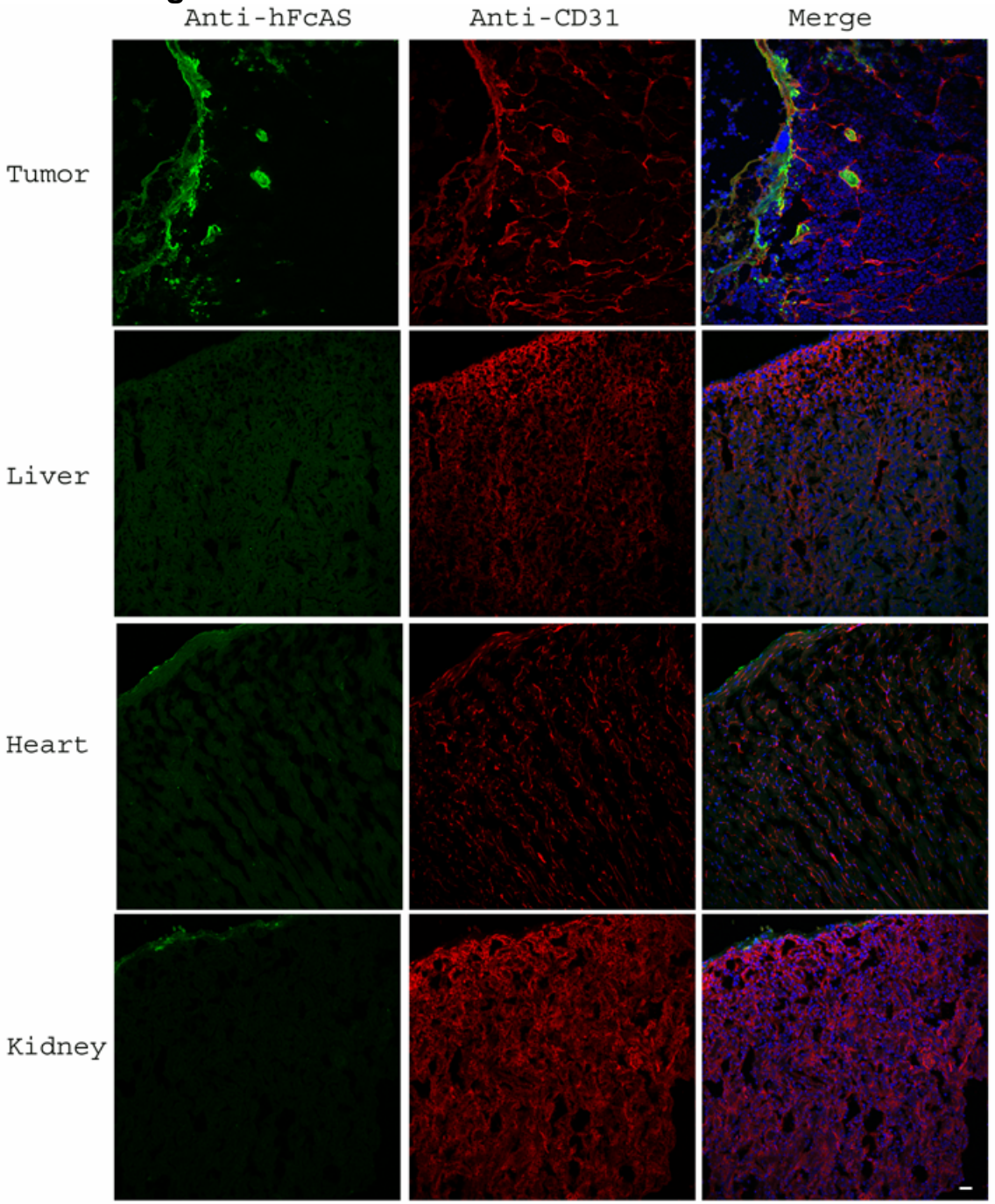

Blood/2008/197236-Javaherian Figure 1 C

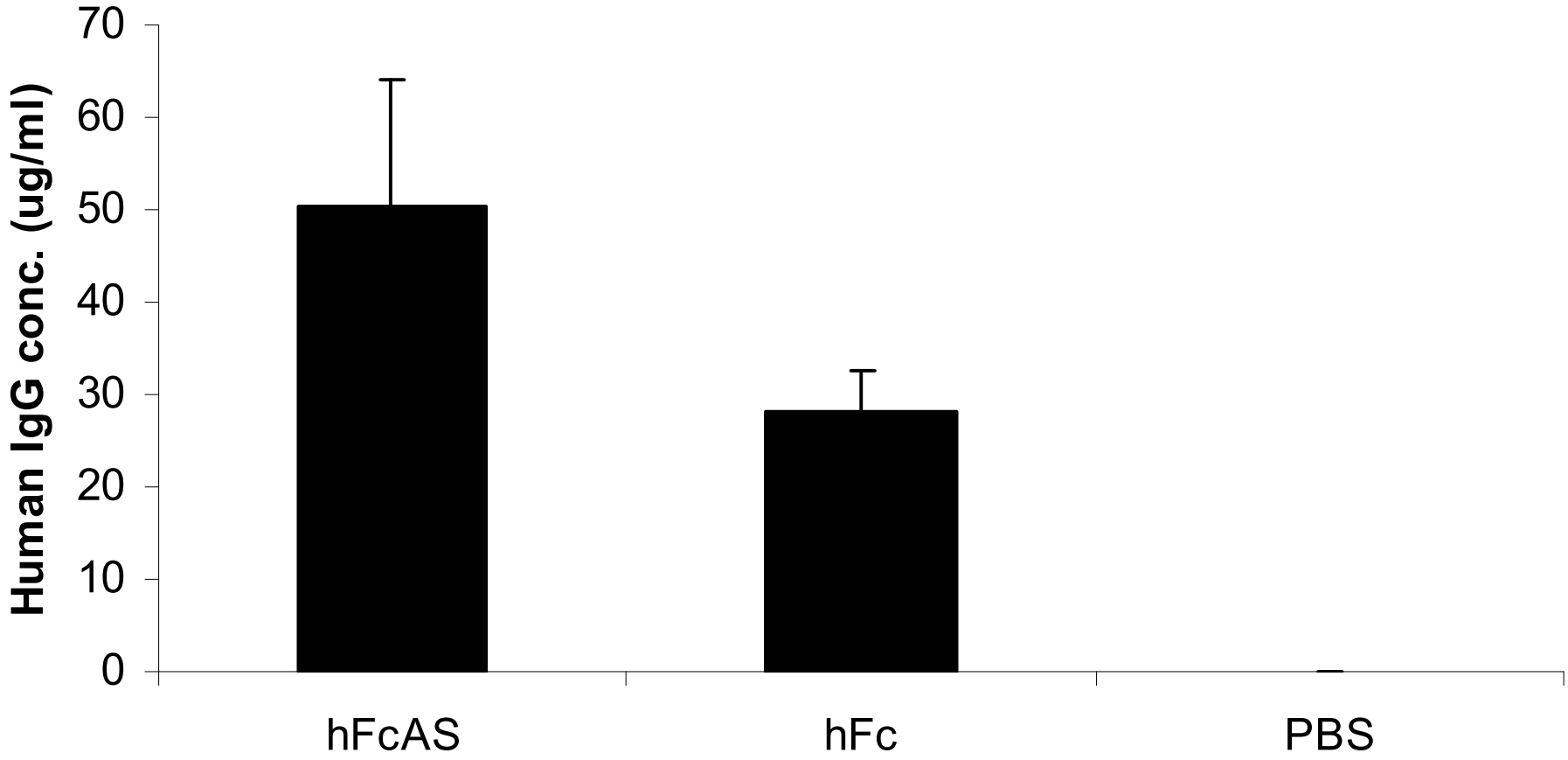

Blood/2008/197236-Javaherian Figure 1 D

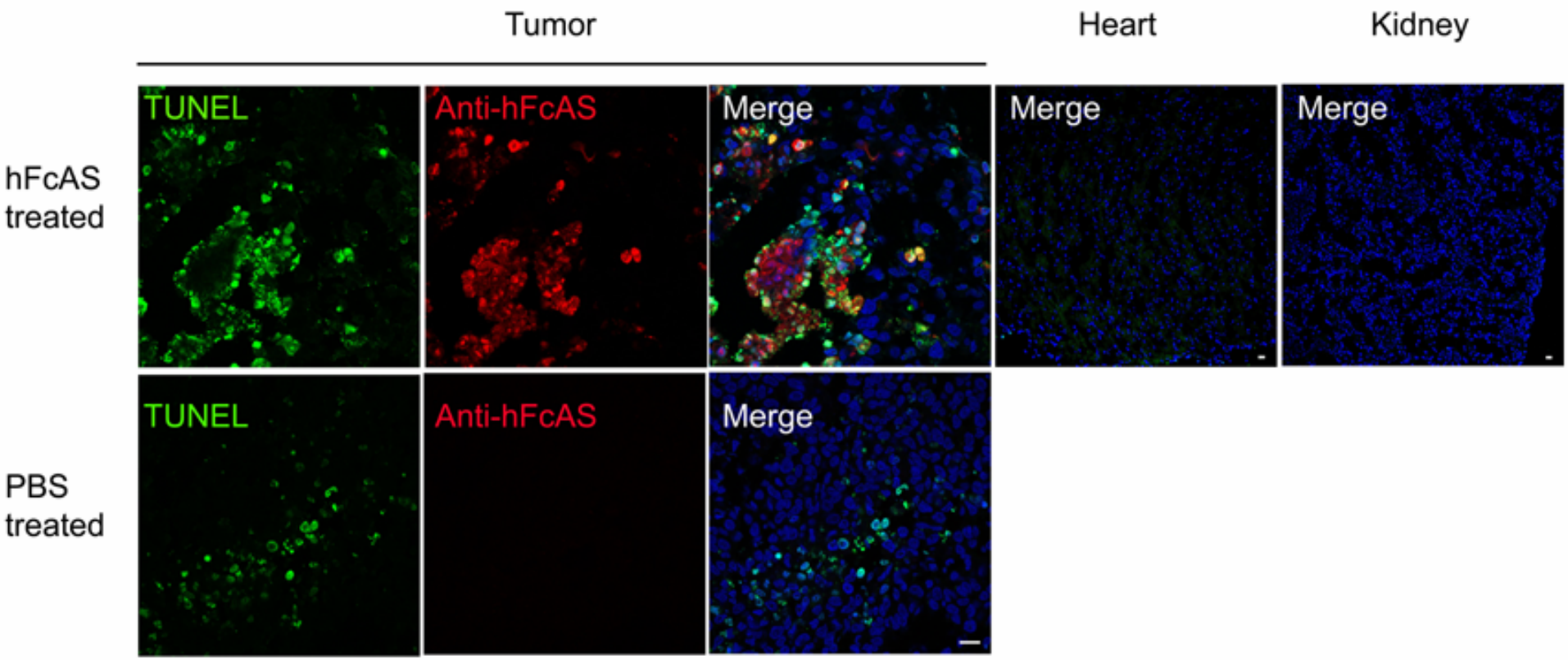

Blood/2008/197236-Javaherian Figure 2 A

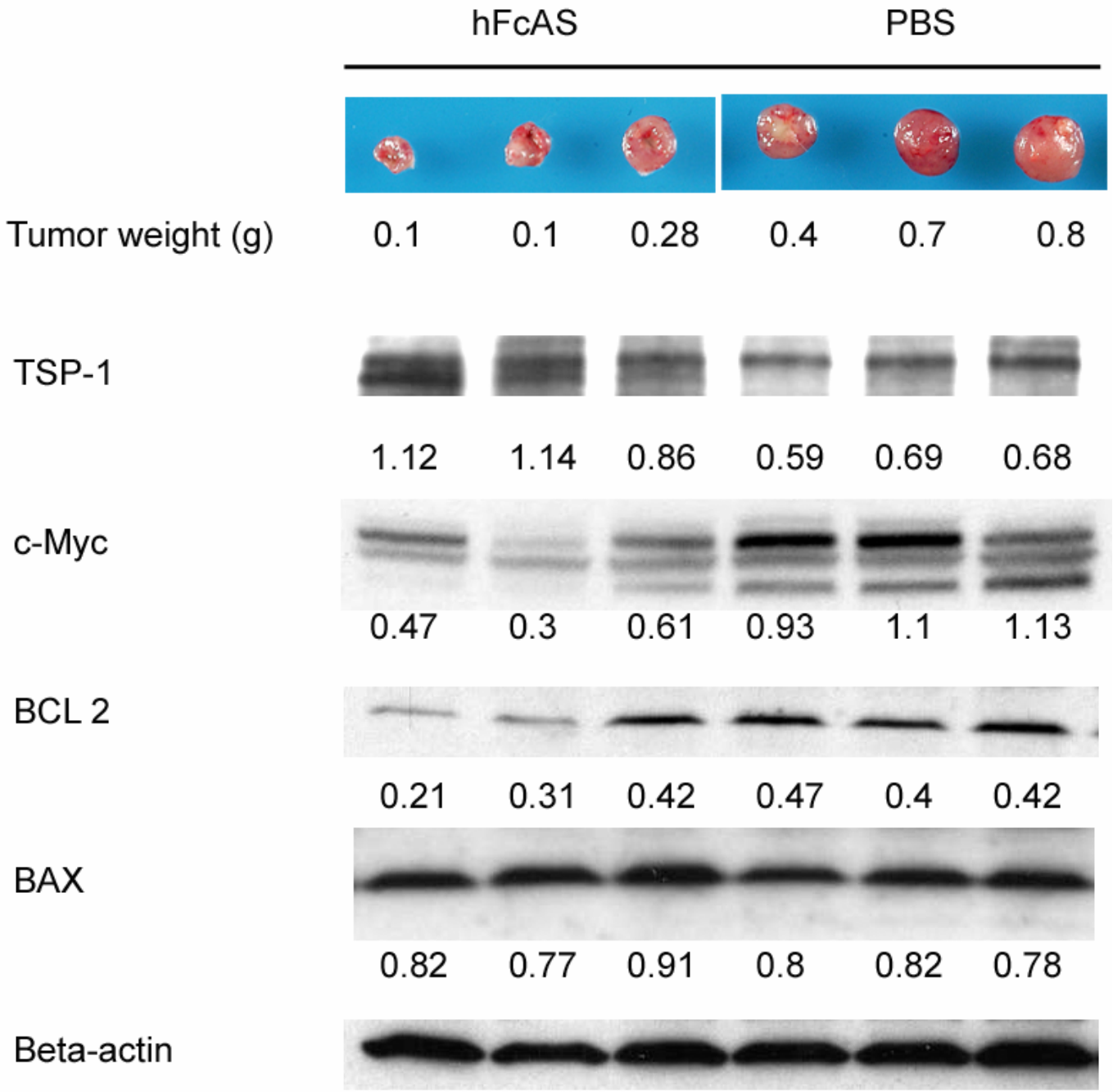

Blood/2008/197236-Javaherian Figure 2 B

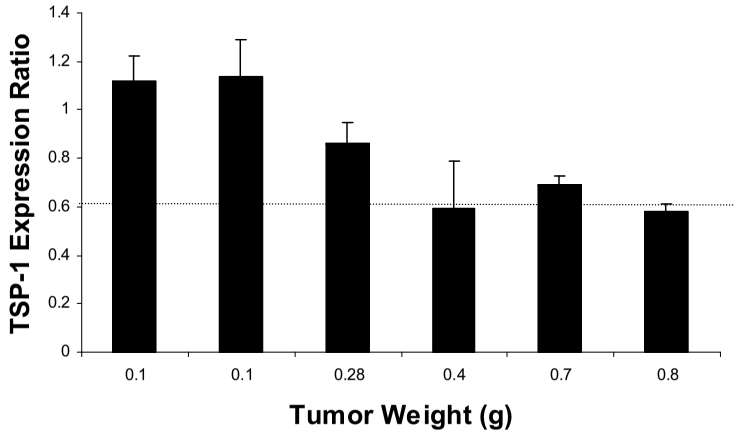

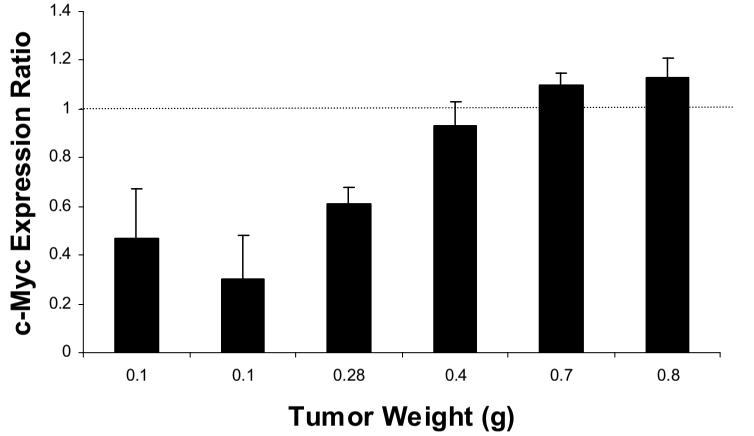

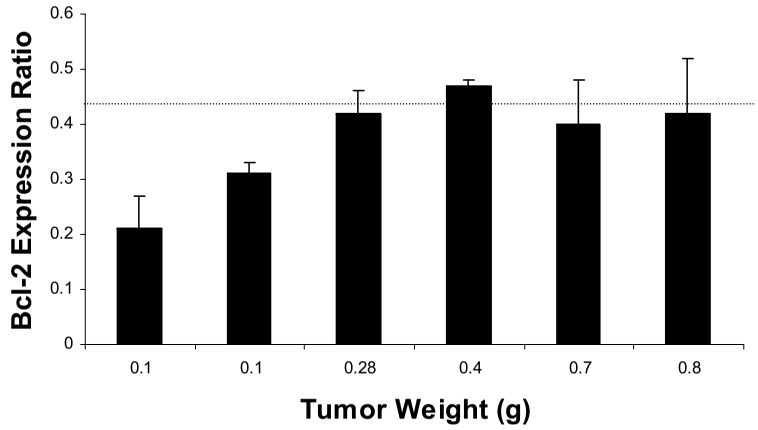

Blood/2008/197236-Javaherian Figure 2 C

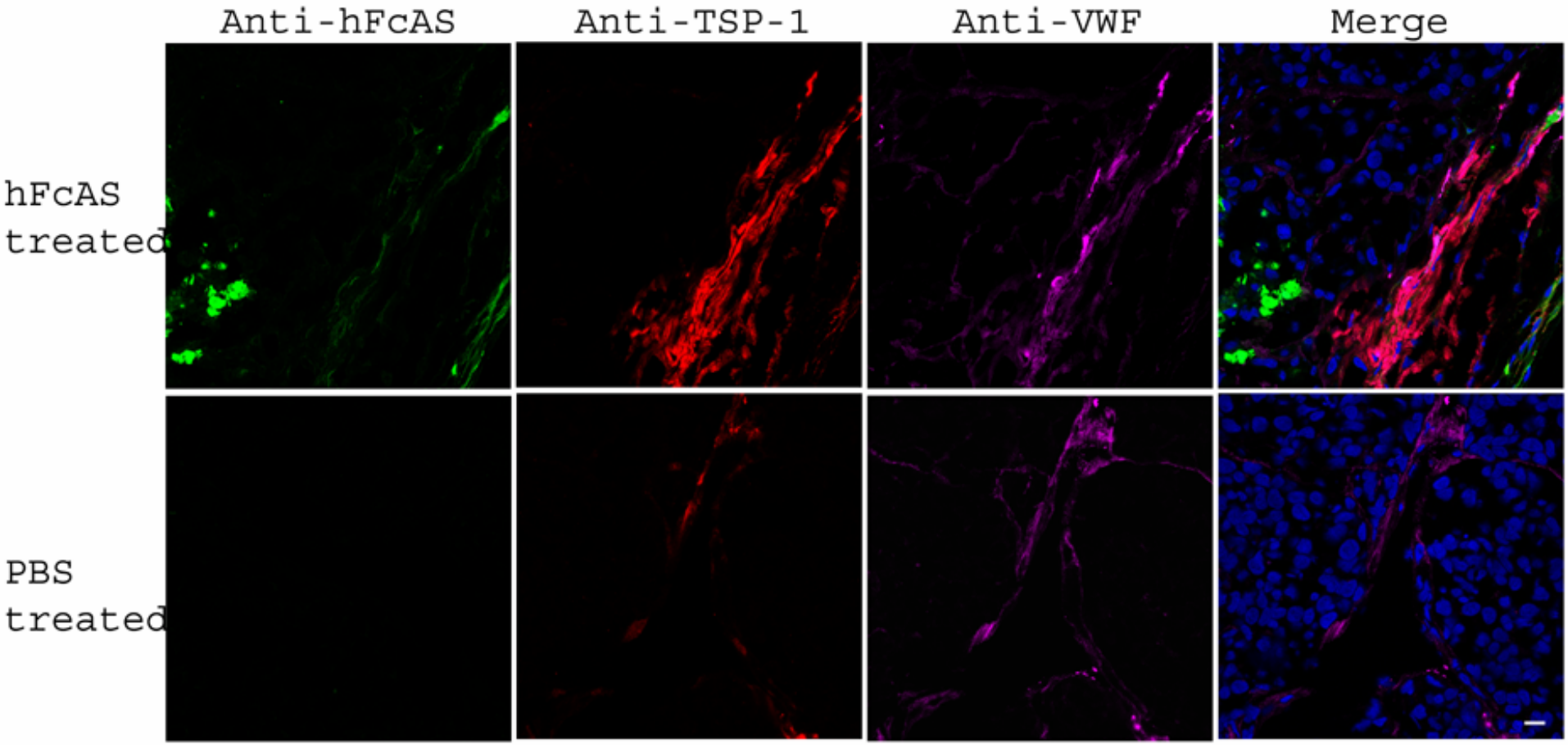

Blood/2008/197236-Javaherian Figure 2 D

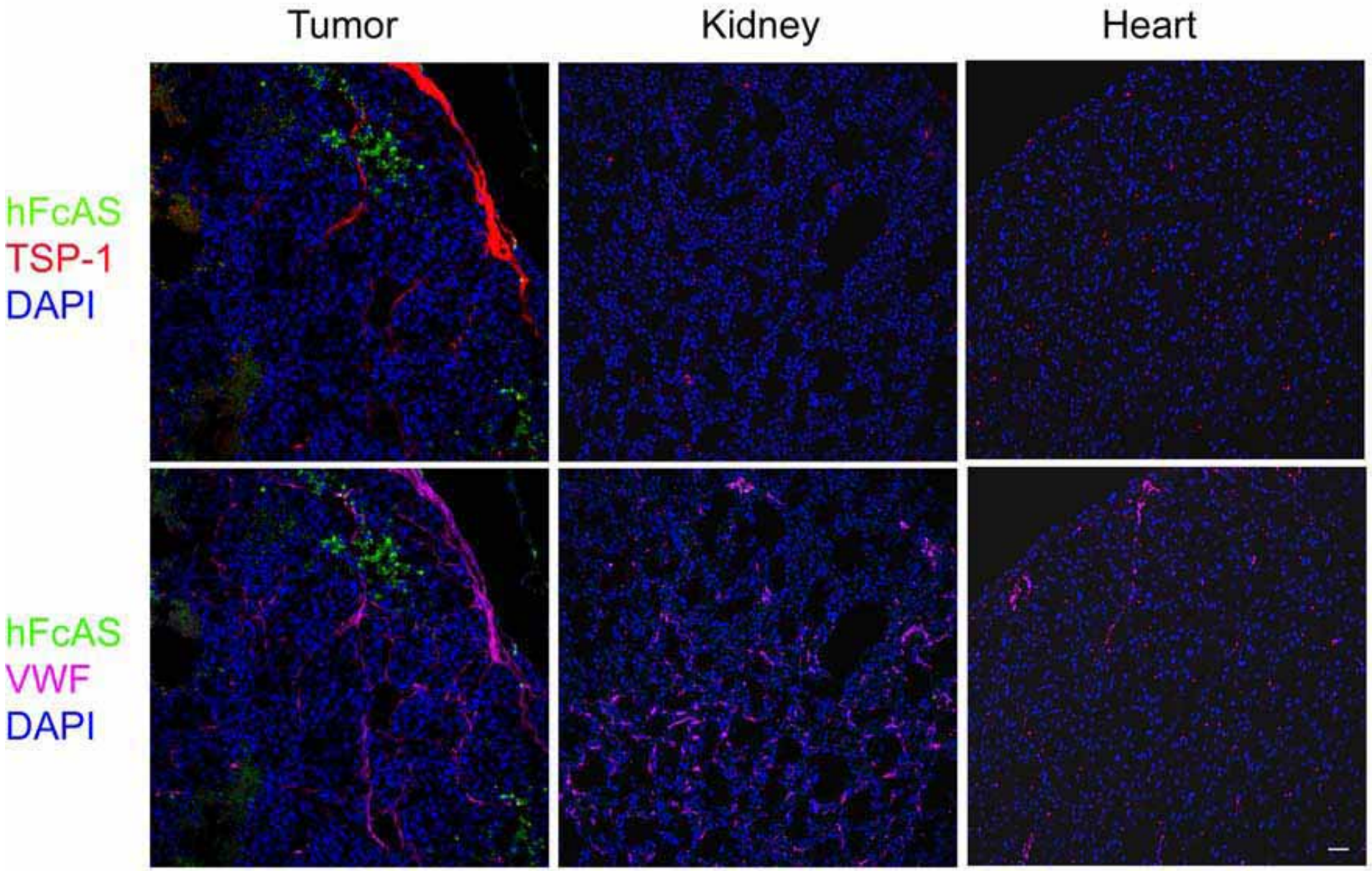

Blood/2008/197236-Javaherian Figure 3A

Blood/2008/197236-Javaherian Figure 3B

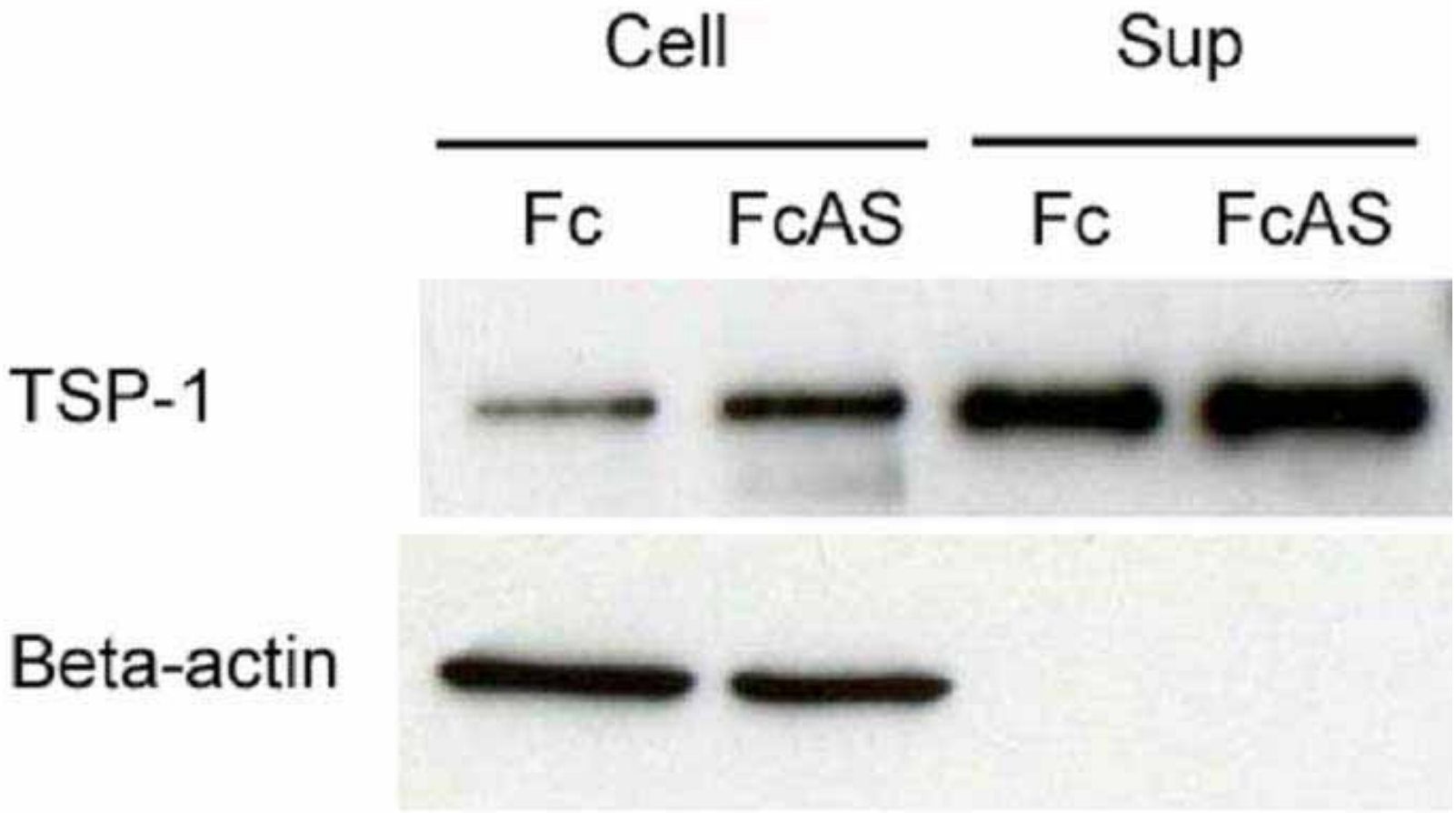

Blood/2008/197236-Javaherian Figure 3C

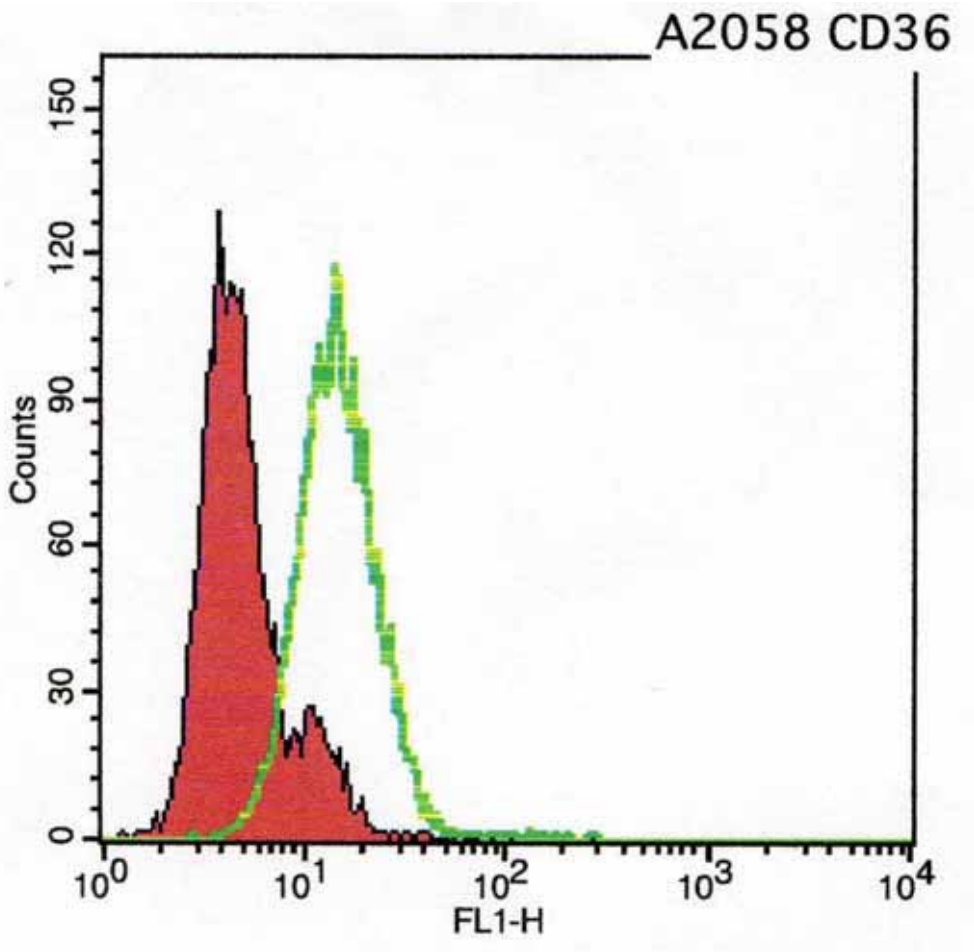

Blood/2008/197236-Javaherian Figure 3D

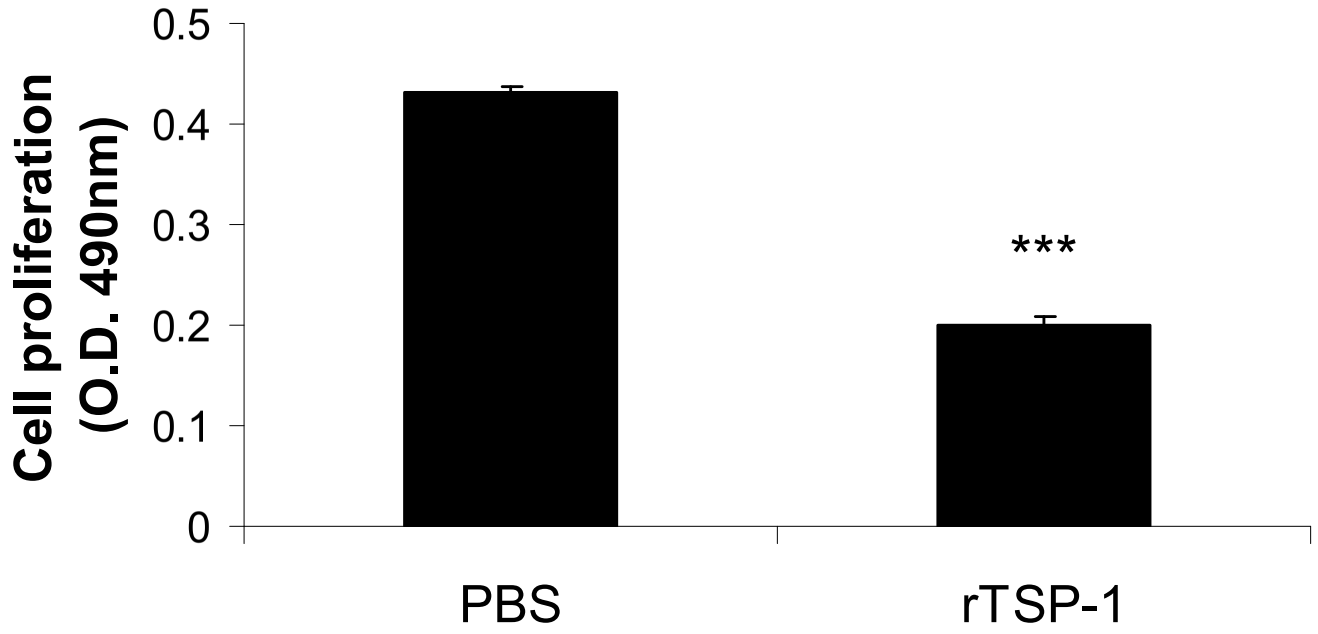

Blood/2008/197236-Javaherian Figure 3E

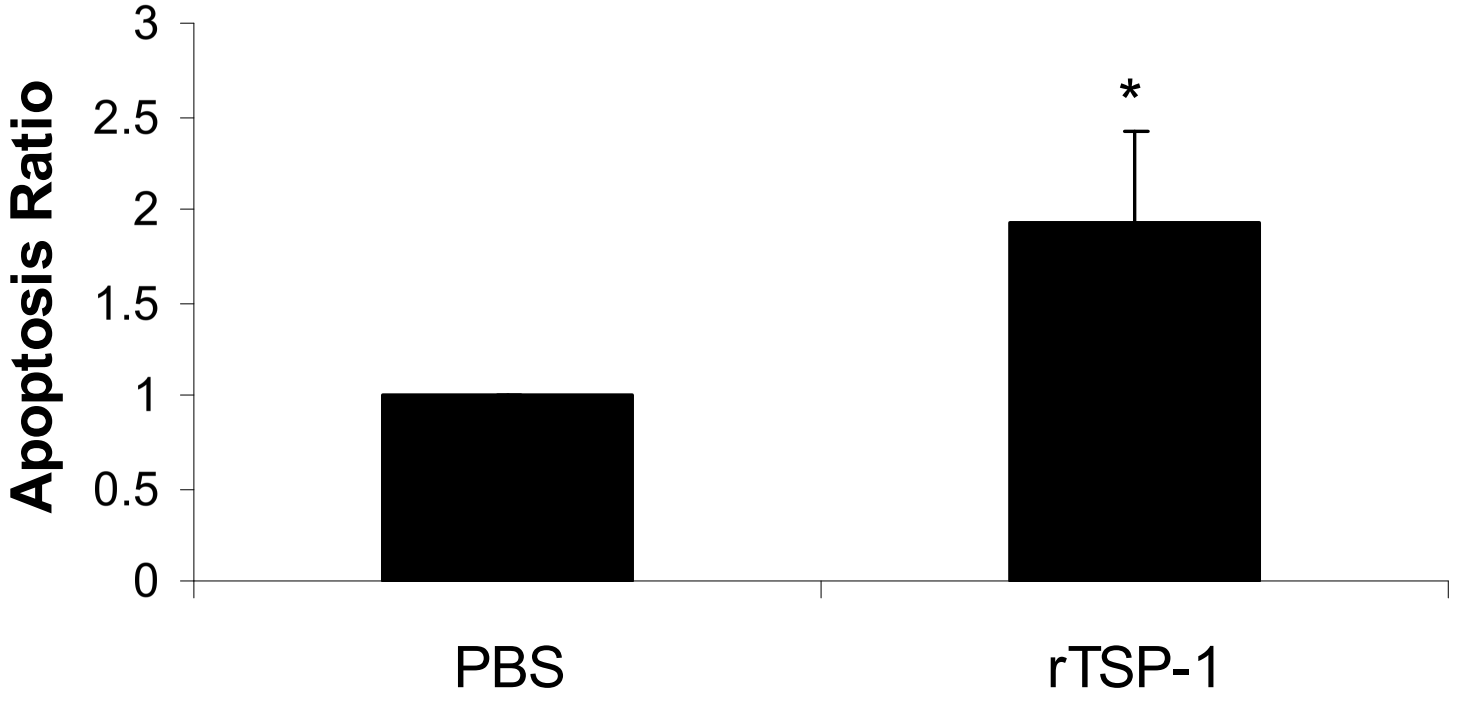

Blood/2008/197236-Javaherian Figure 3F

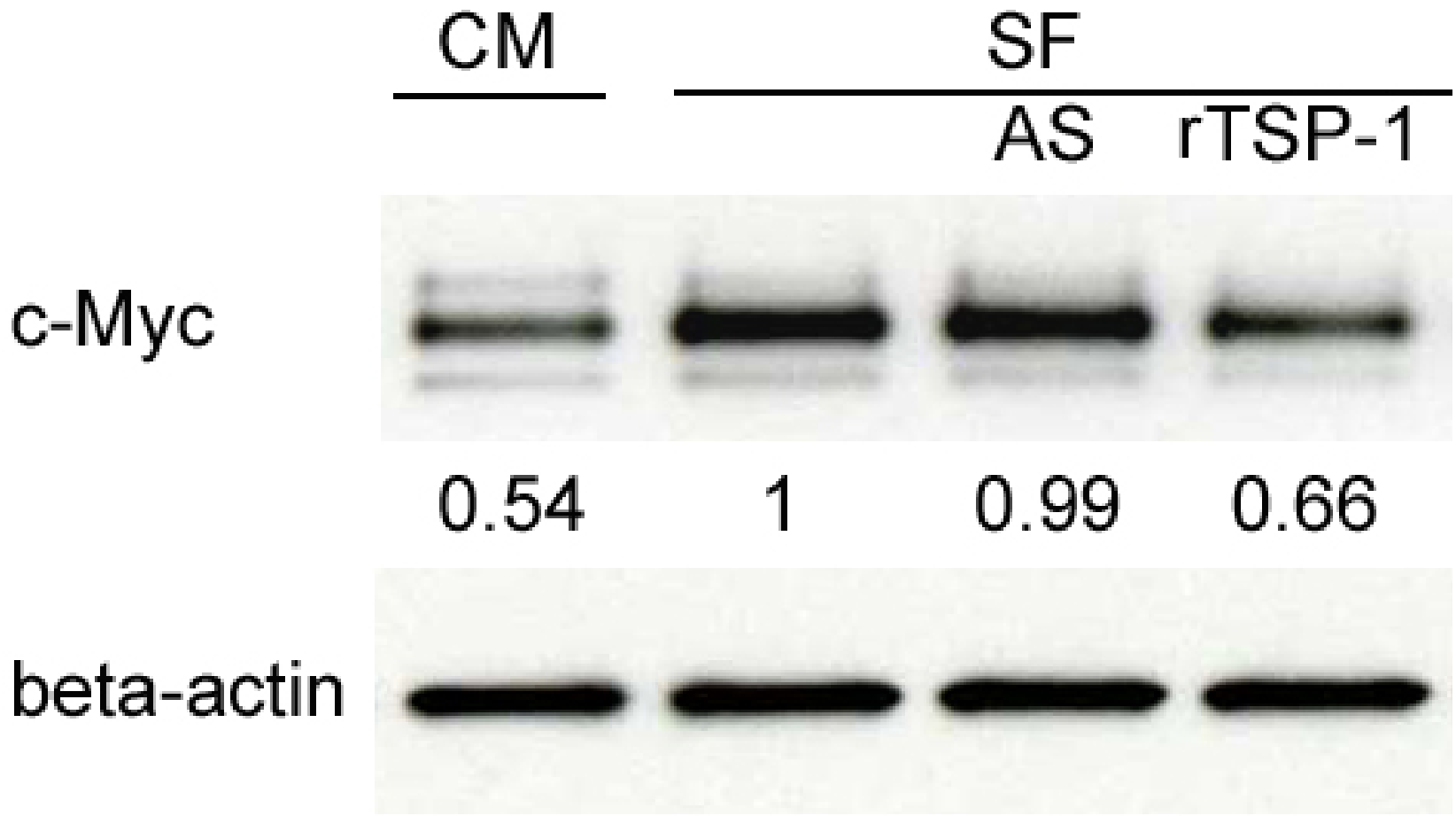

Blood/2008/197236-Javaherian Figure 4A

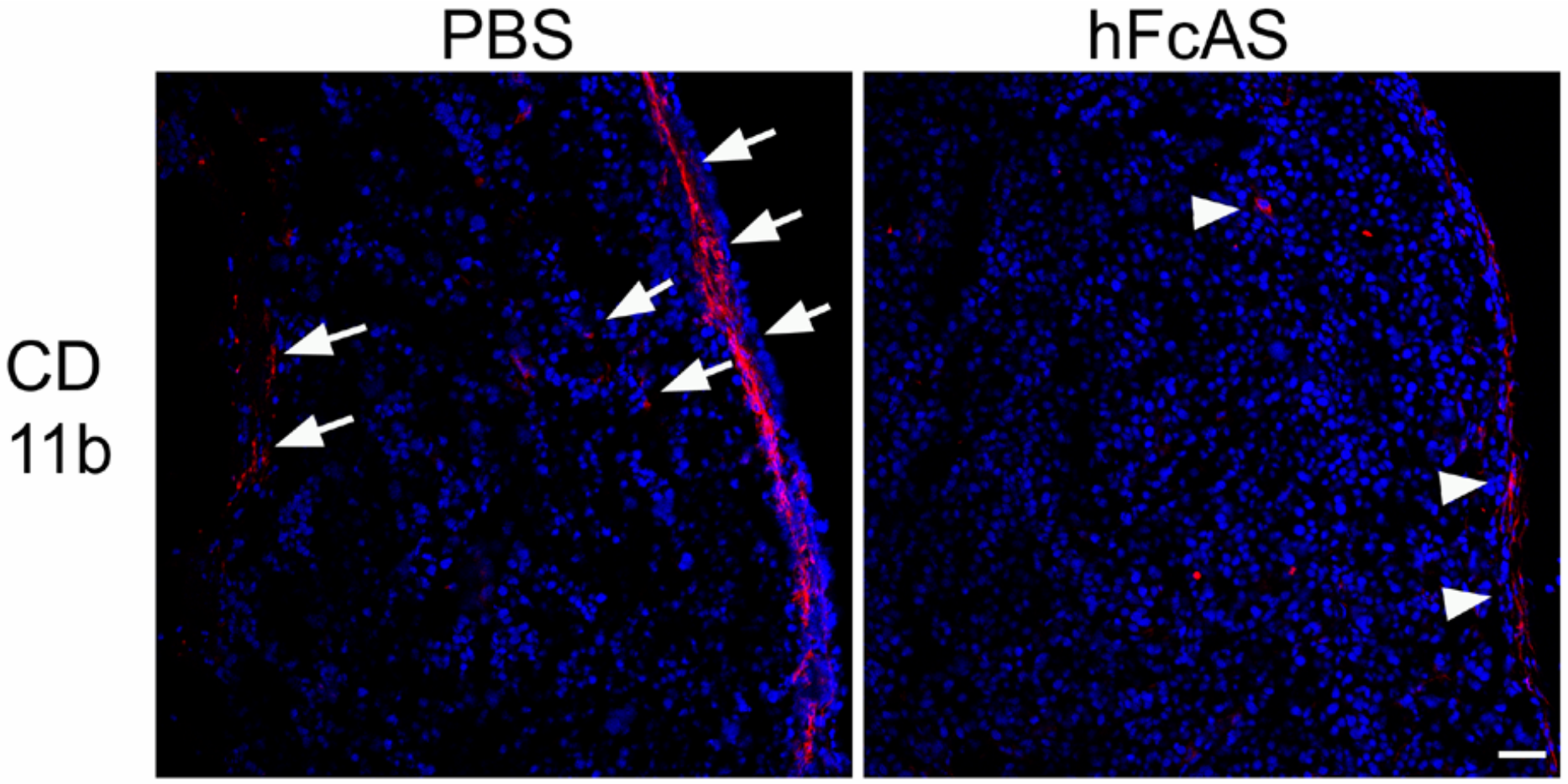

Blood/2008/197236-Javaherian Figure 4B

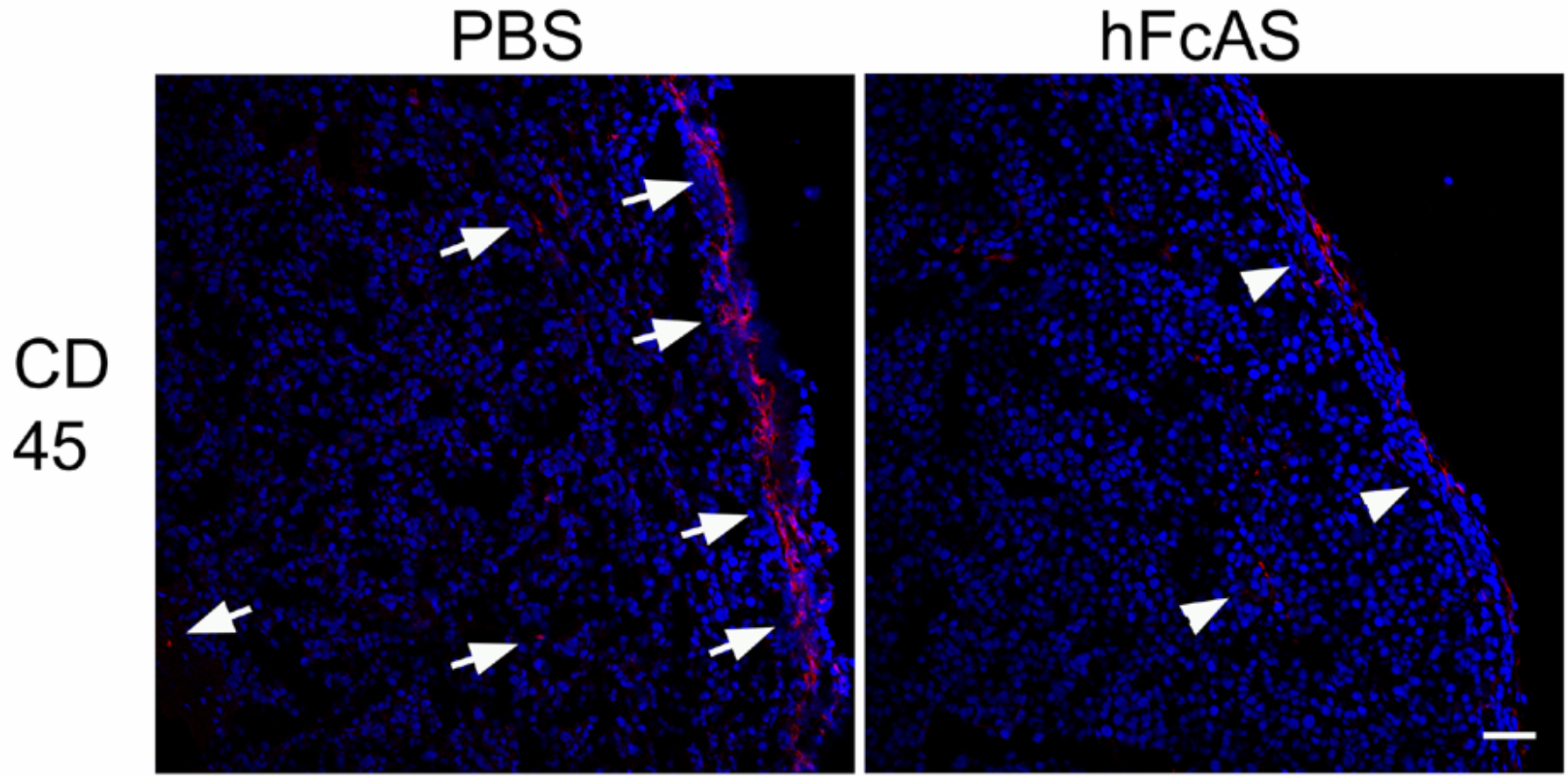

Blood/2008/197236-Javaherian Figure 4C

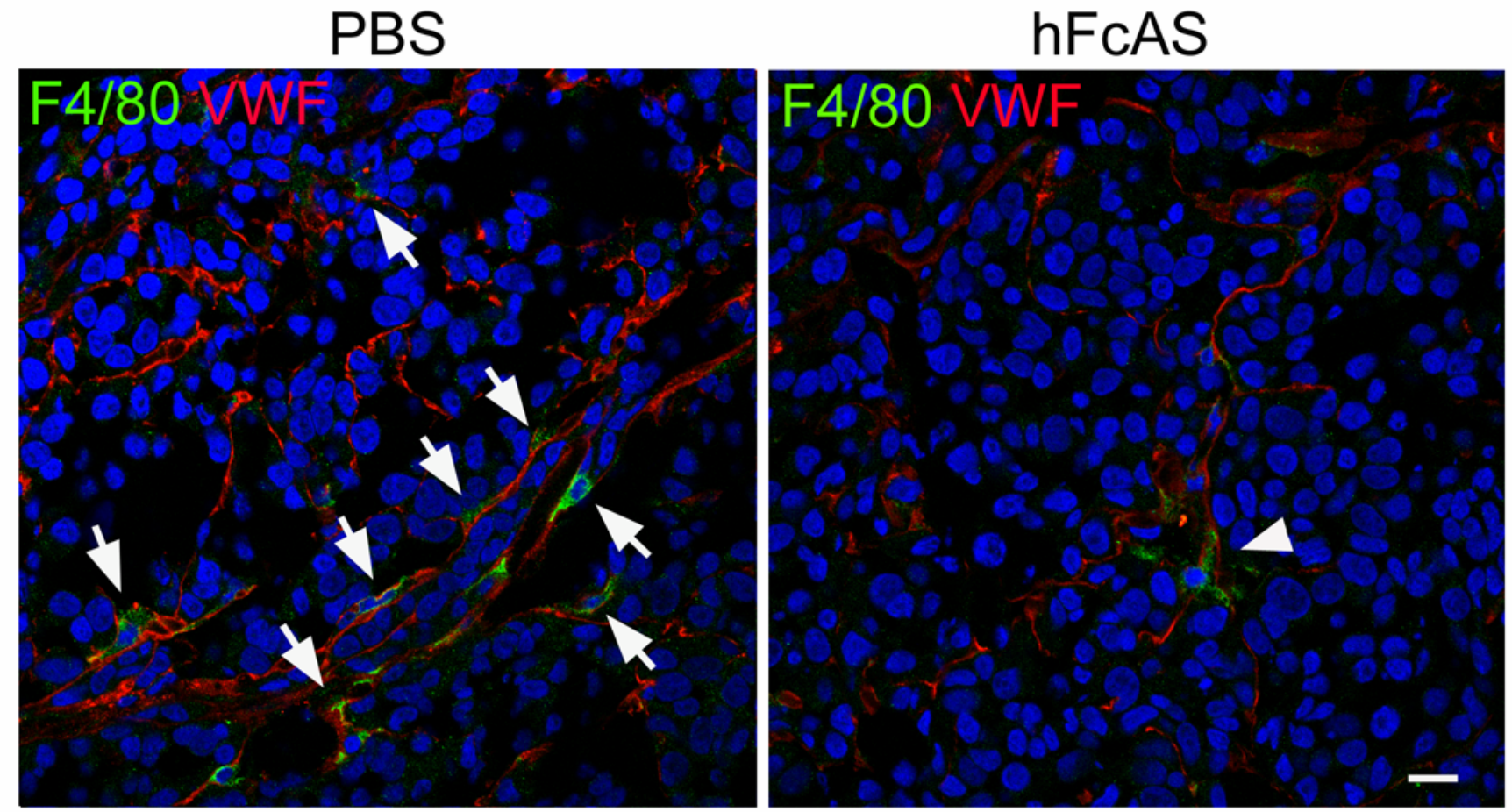

Blood/2008/197236-Javaherian Figure 4D

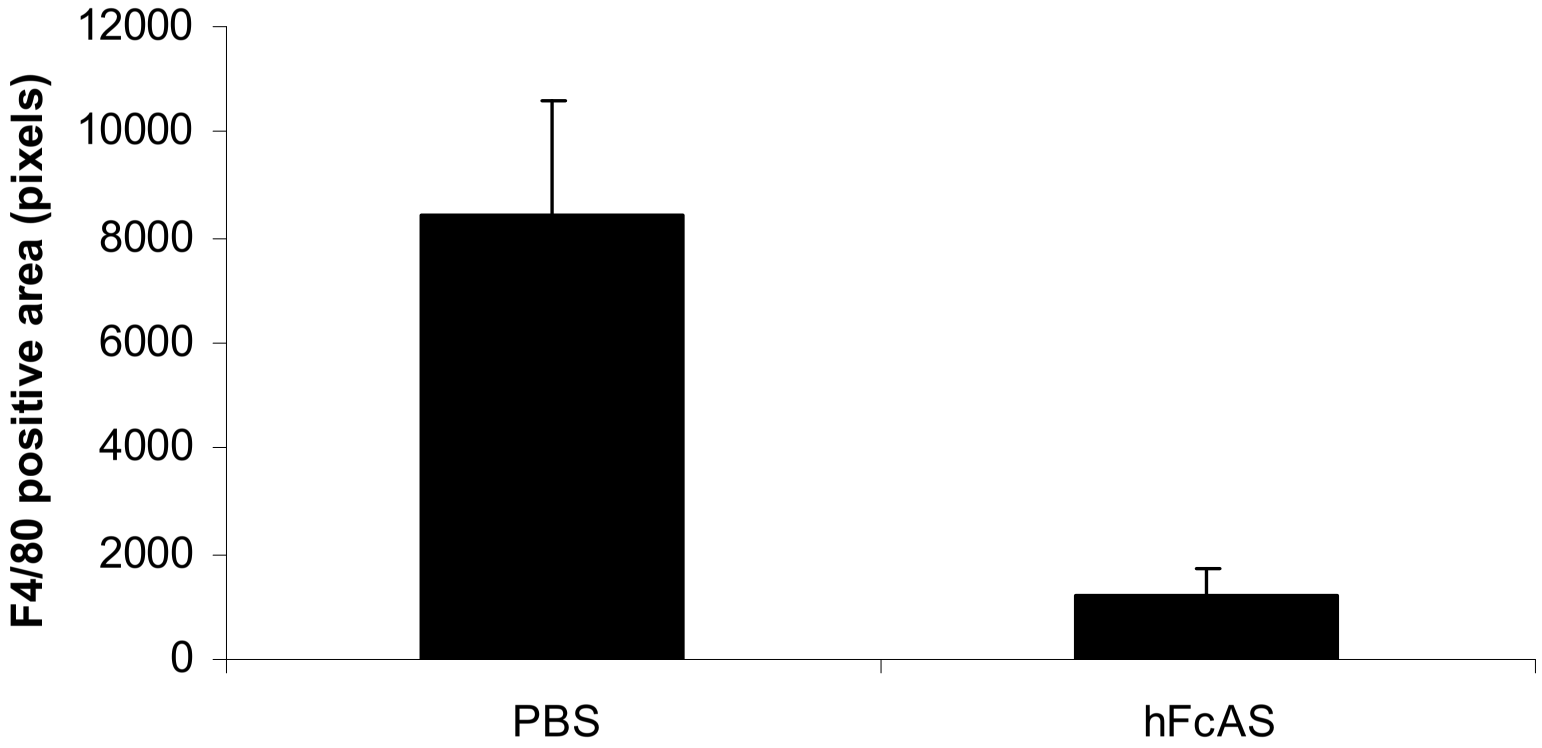

Blood/2008/197236-Javaherian Figure 5A

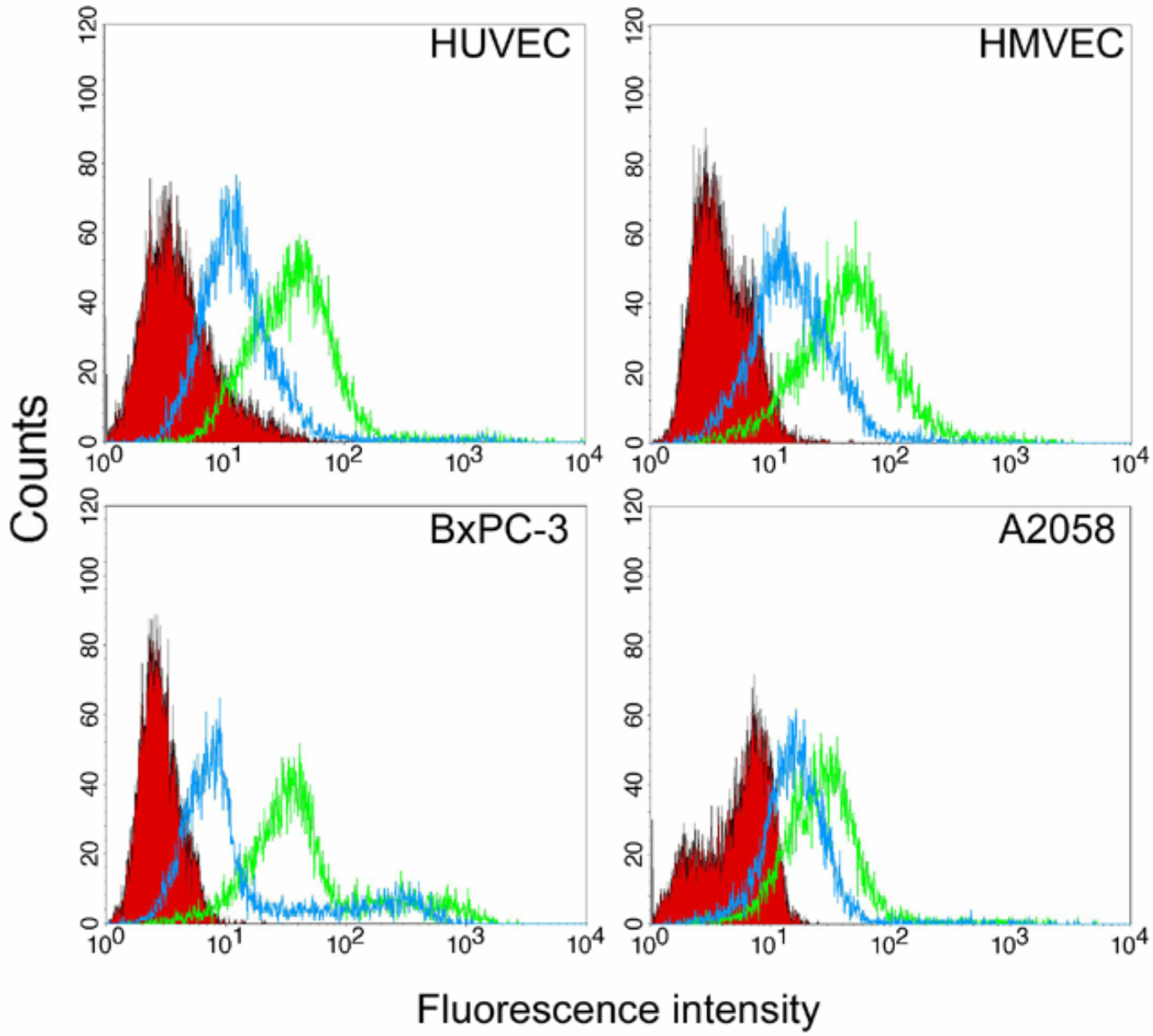

Blood/2008/197236-Javaherian Figure 5B

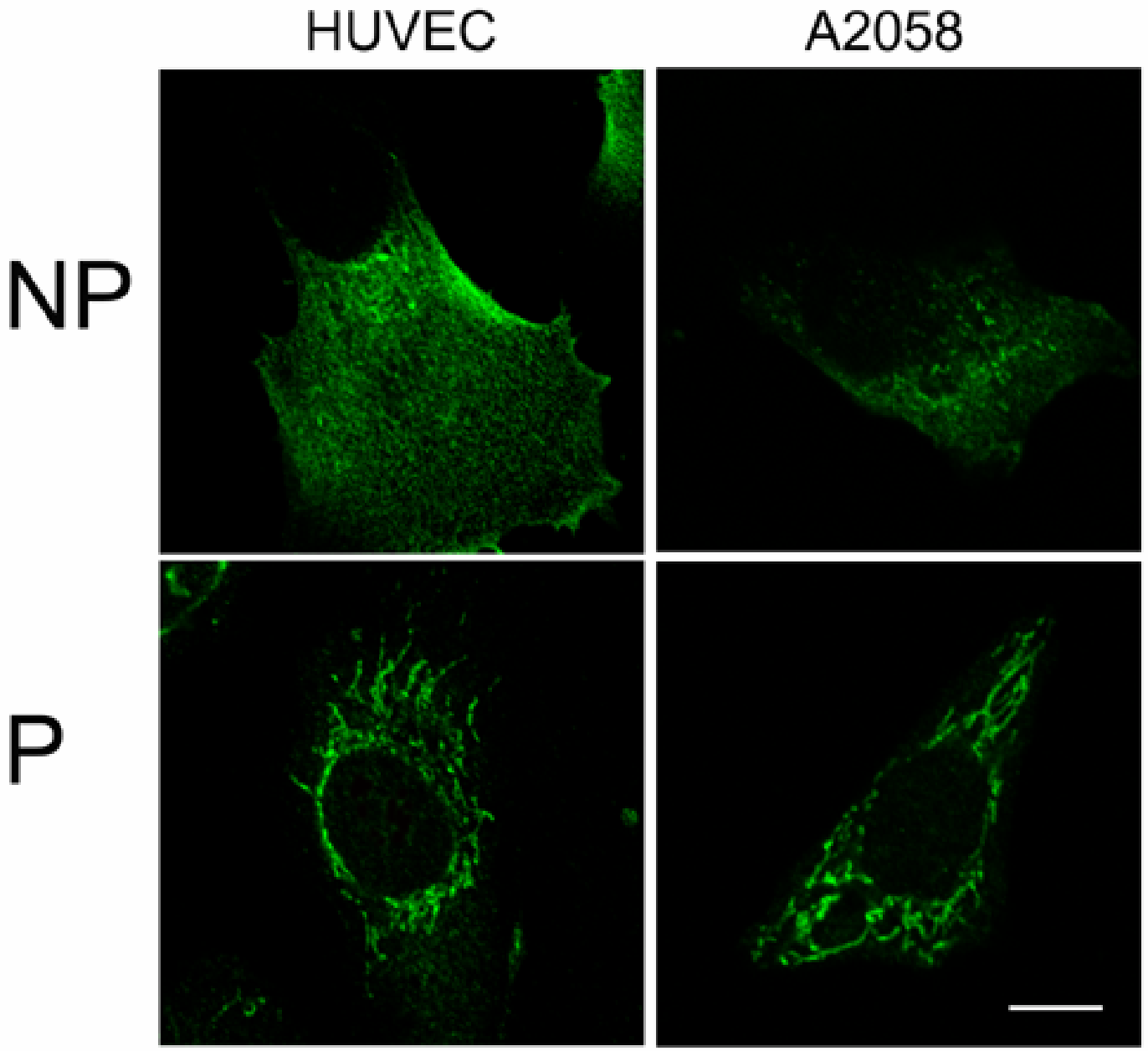

Blood/2008/197236-Javaherian Figure 5C

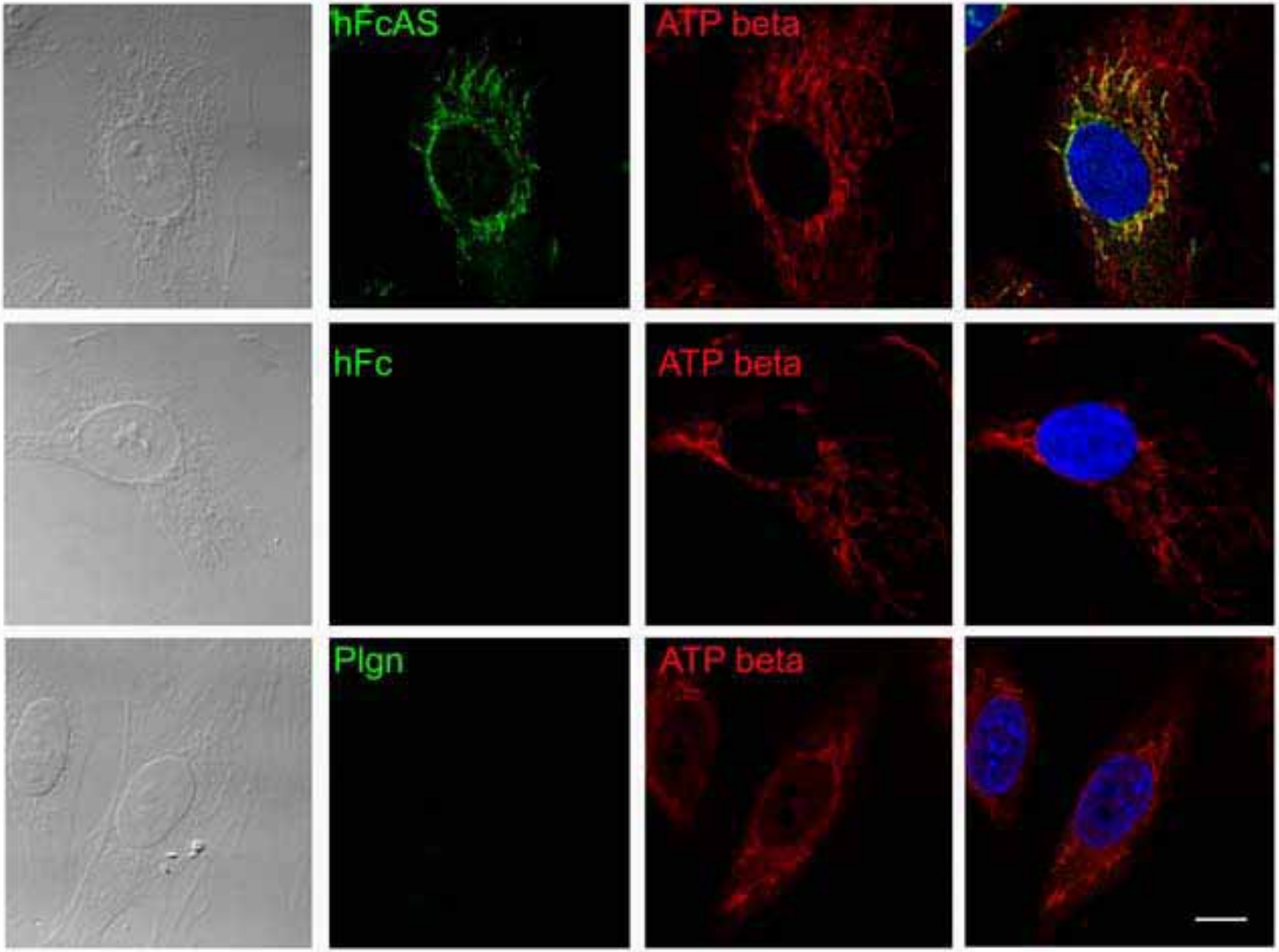

Blood/2008/197236-Javaherian Figure 5D

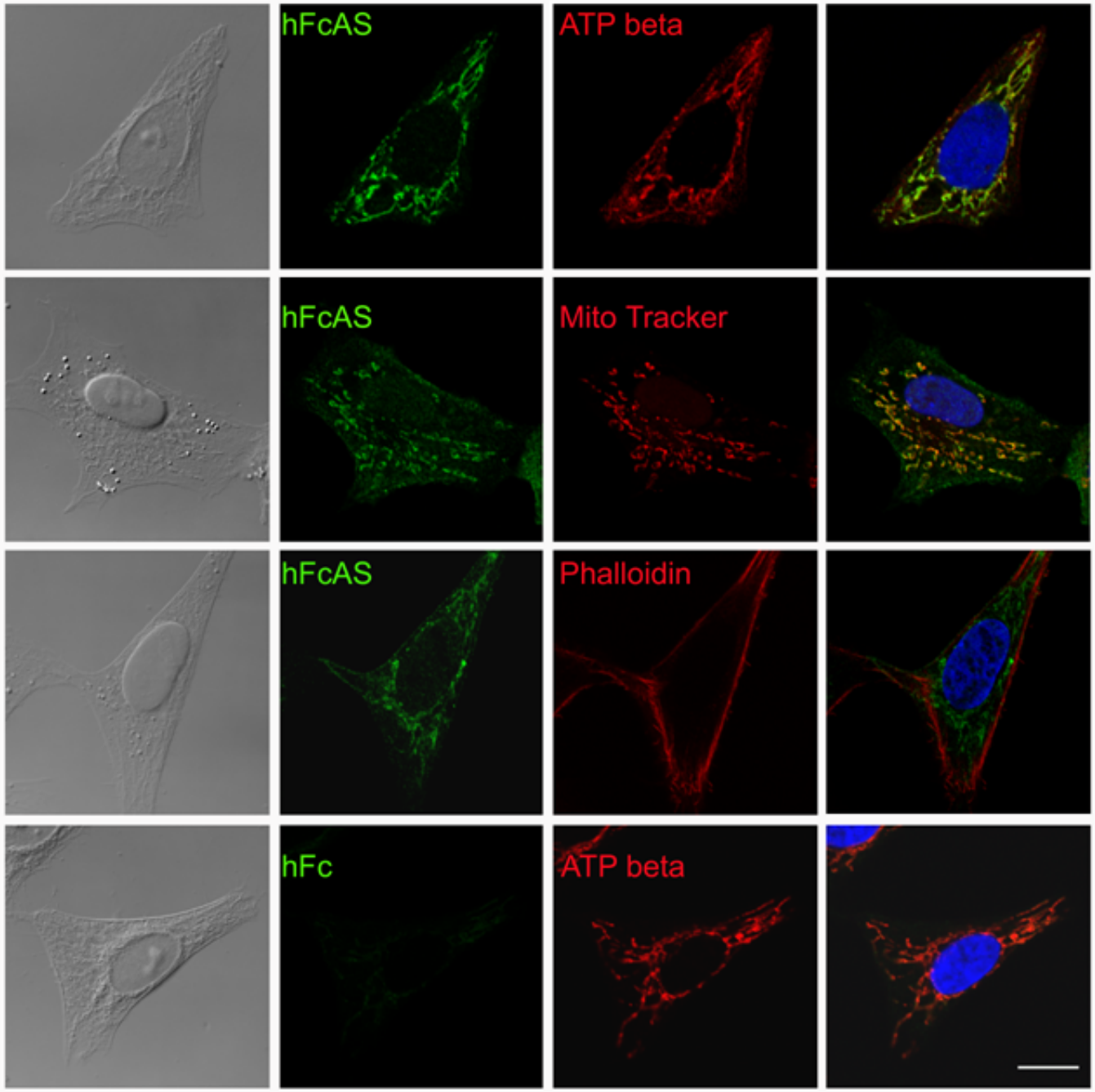

Blood/2008/197236-Javaherian Figure 6A

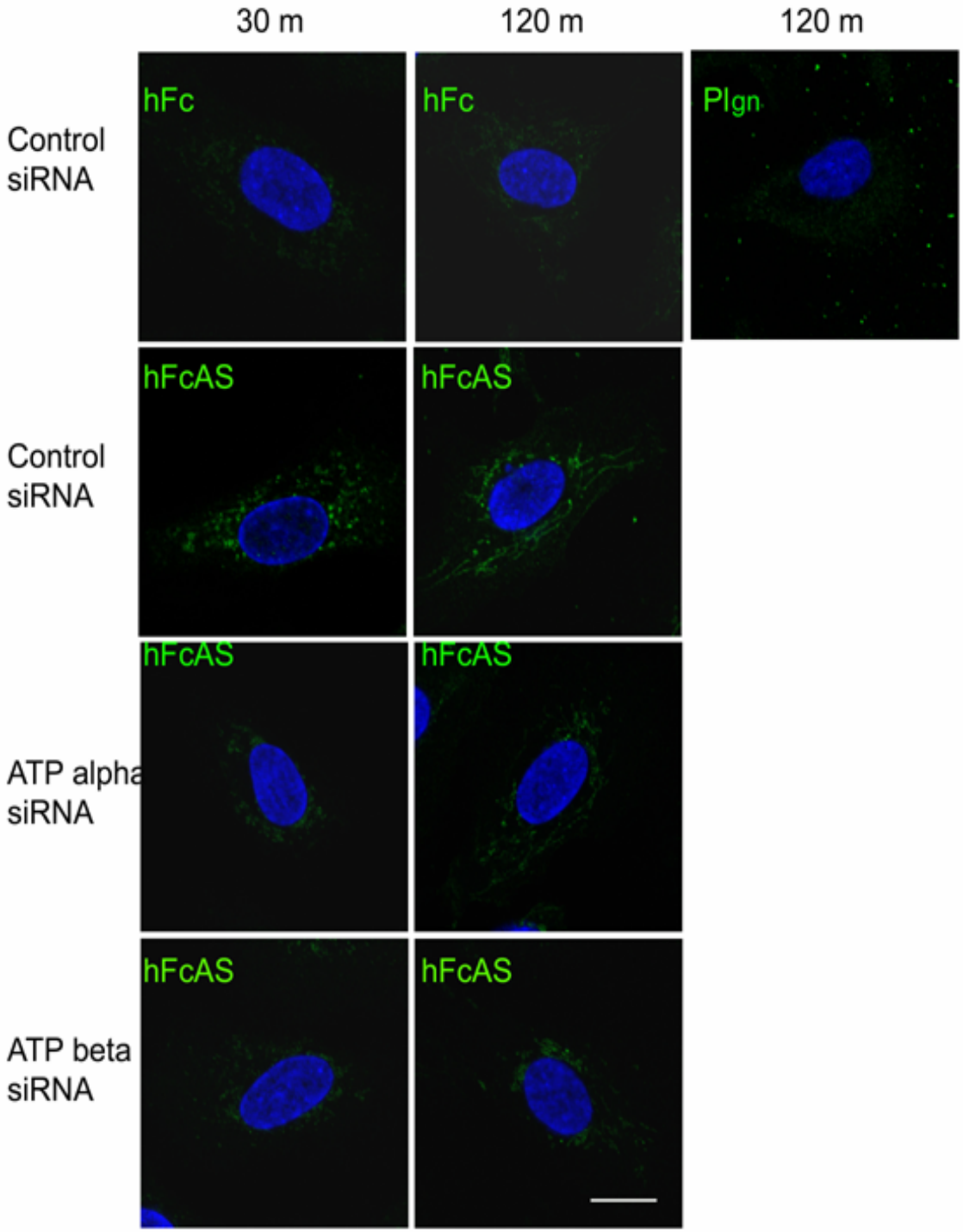

Blood/2008/197236-Javaherian Figure 6B

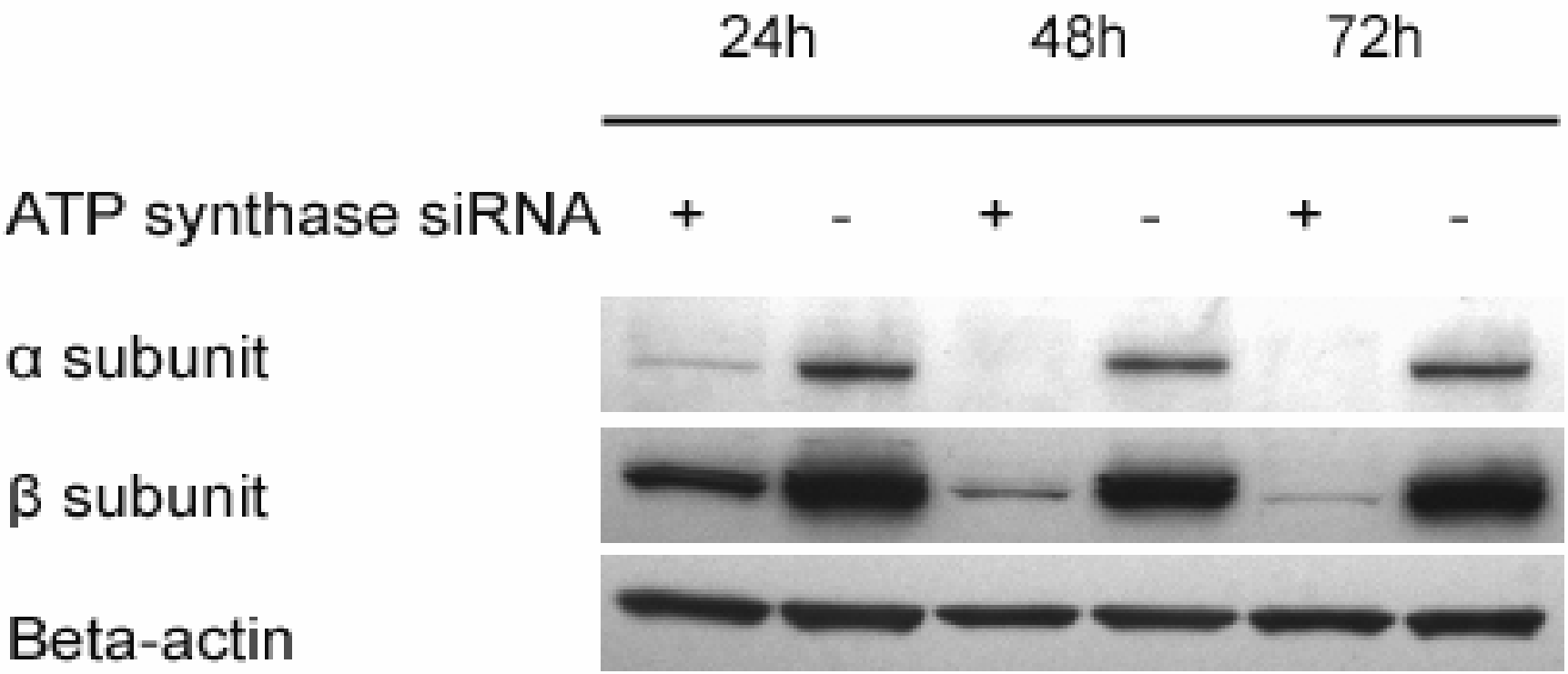

Blood/2008/197236-Javaherian Figure 6C

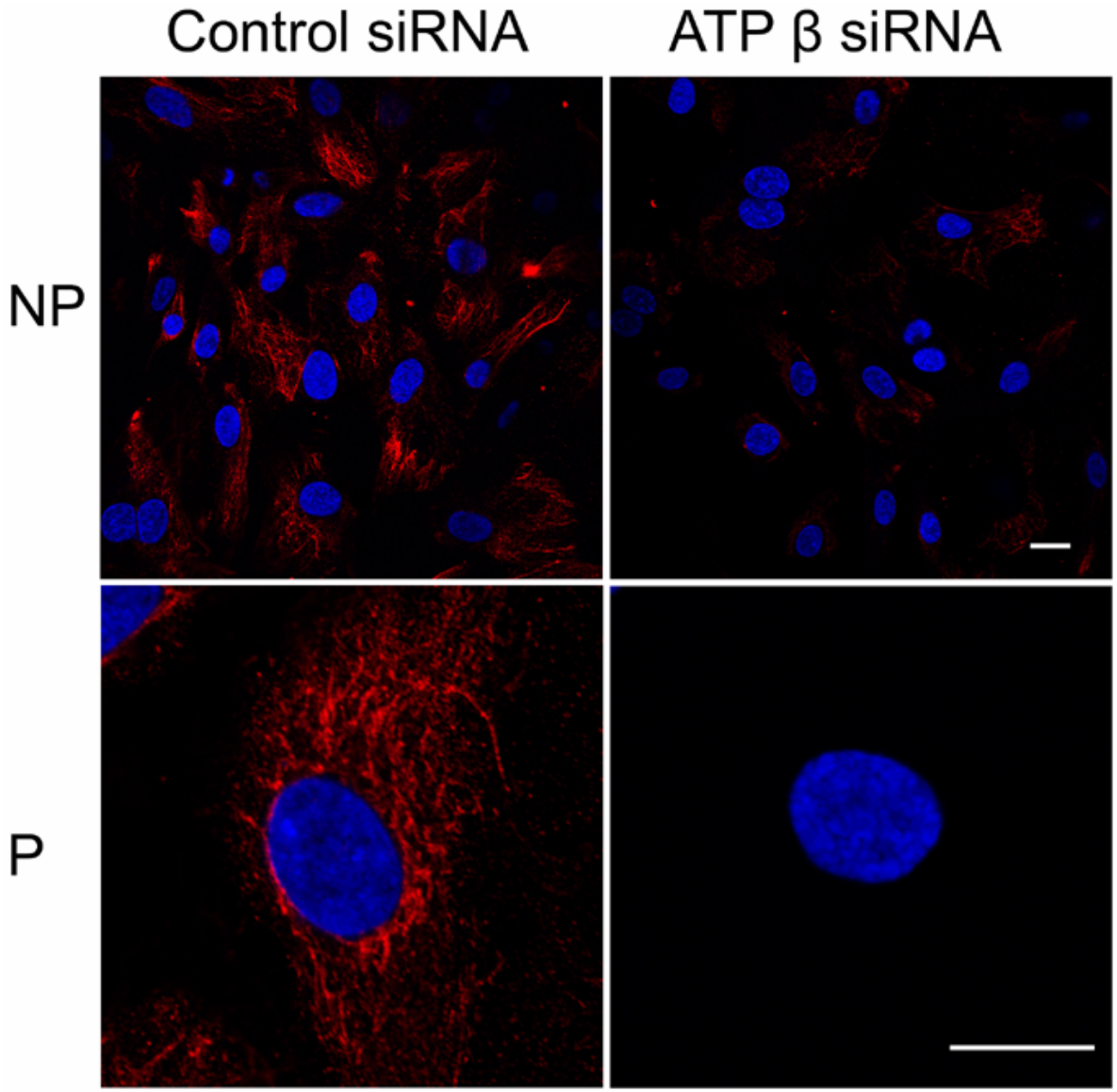

Blood/2008/197236-Javaherian Figure 6D

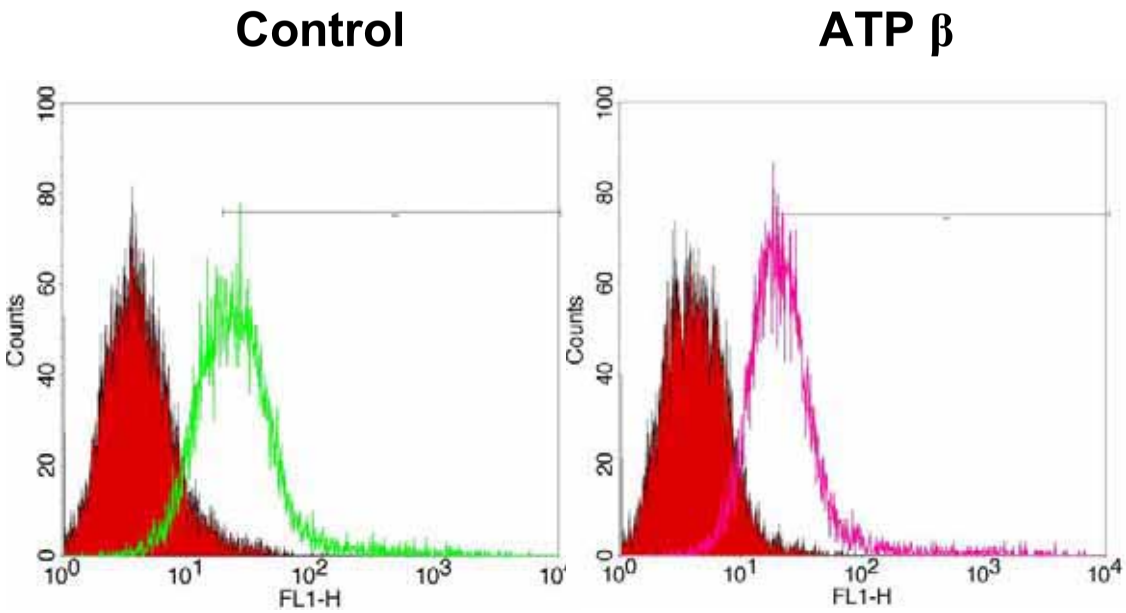

	Percent of hFcAS binding
Control si RNA	60.77 %
ATP synthase β si RNA	51.24 %

Blood/2008/197236-Javaherian Figure 7A B

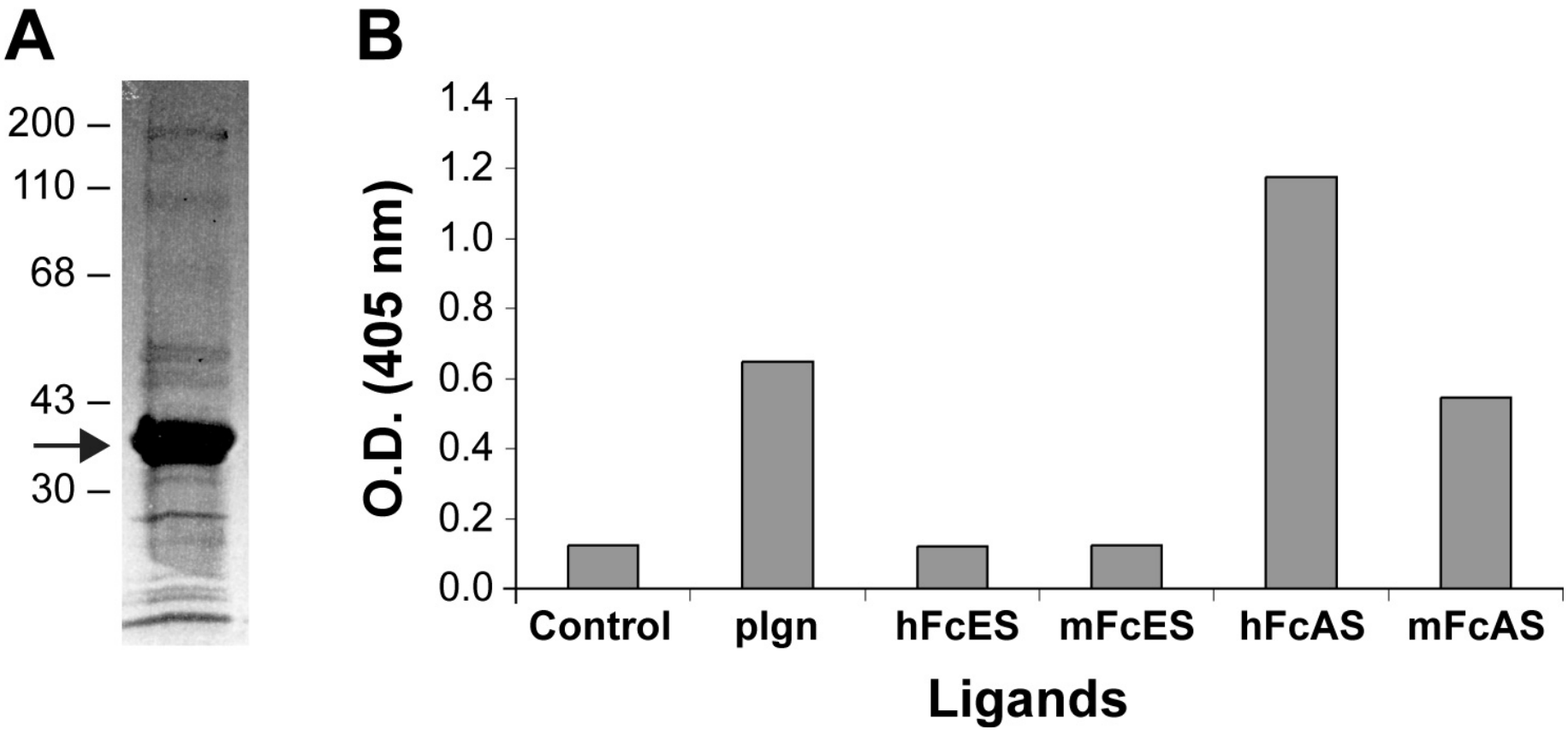

Blood/2008/197236-Javaherian Figure 7C

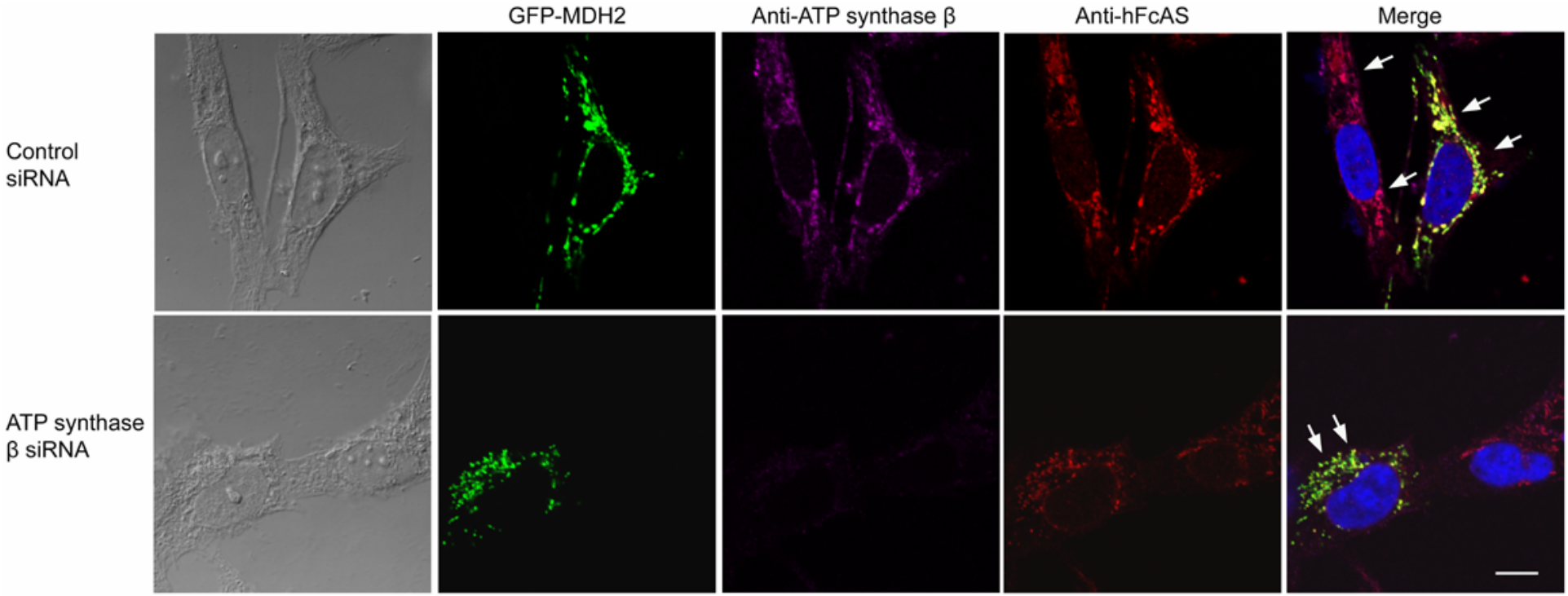

Blood/2008/197236-Javaherian Figure 7D

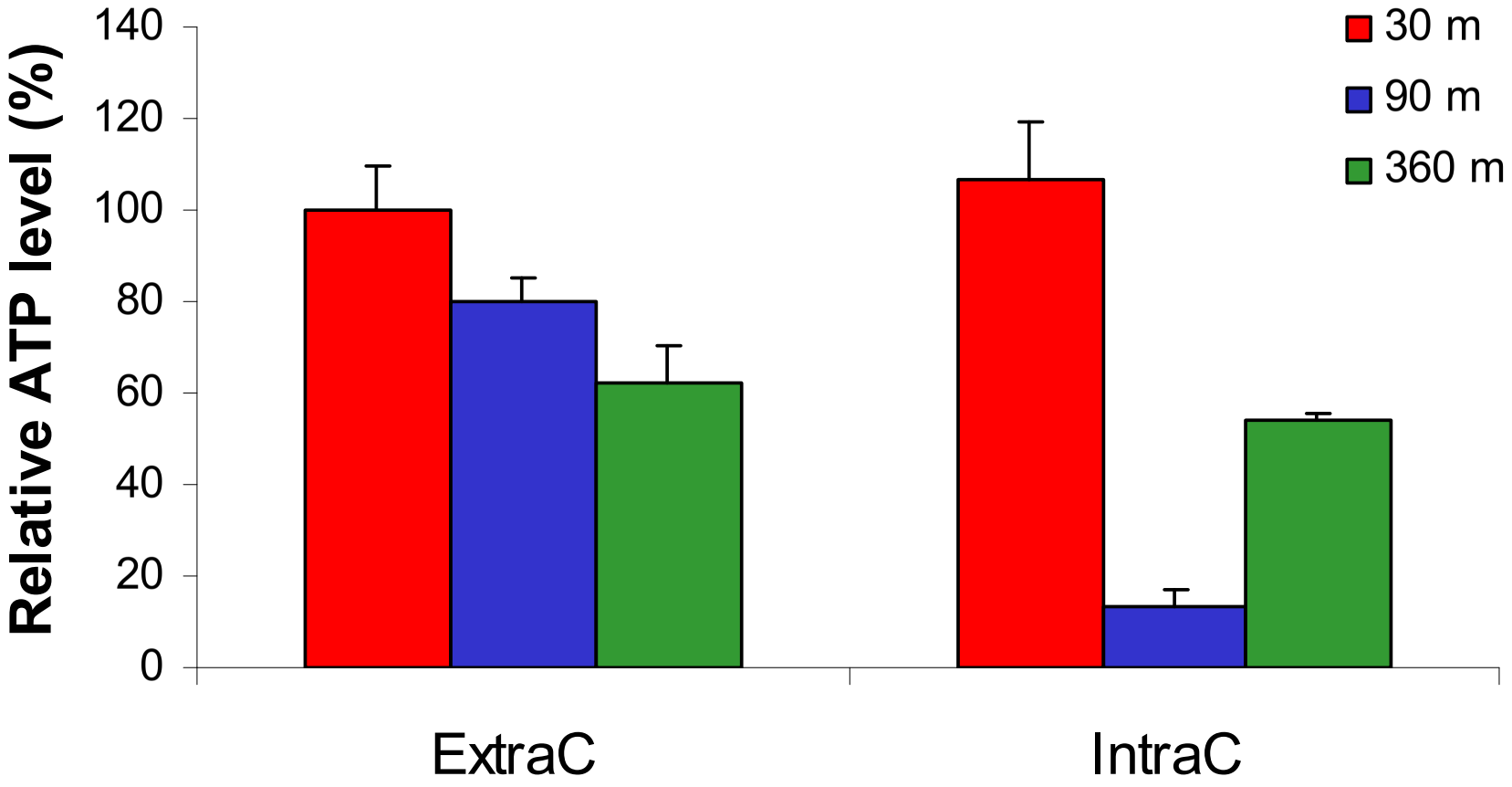

Blood/2008/197236-Javaherian Figure 7E

Figure 7E

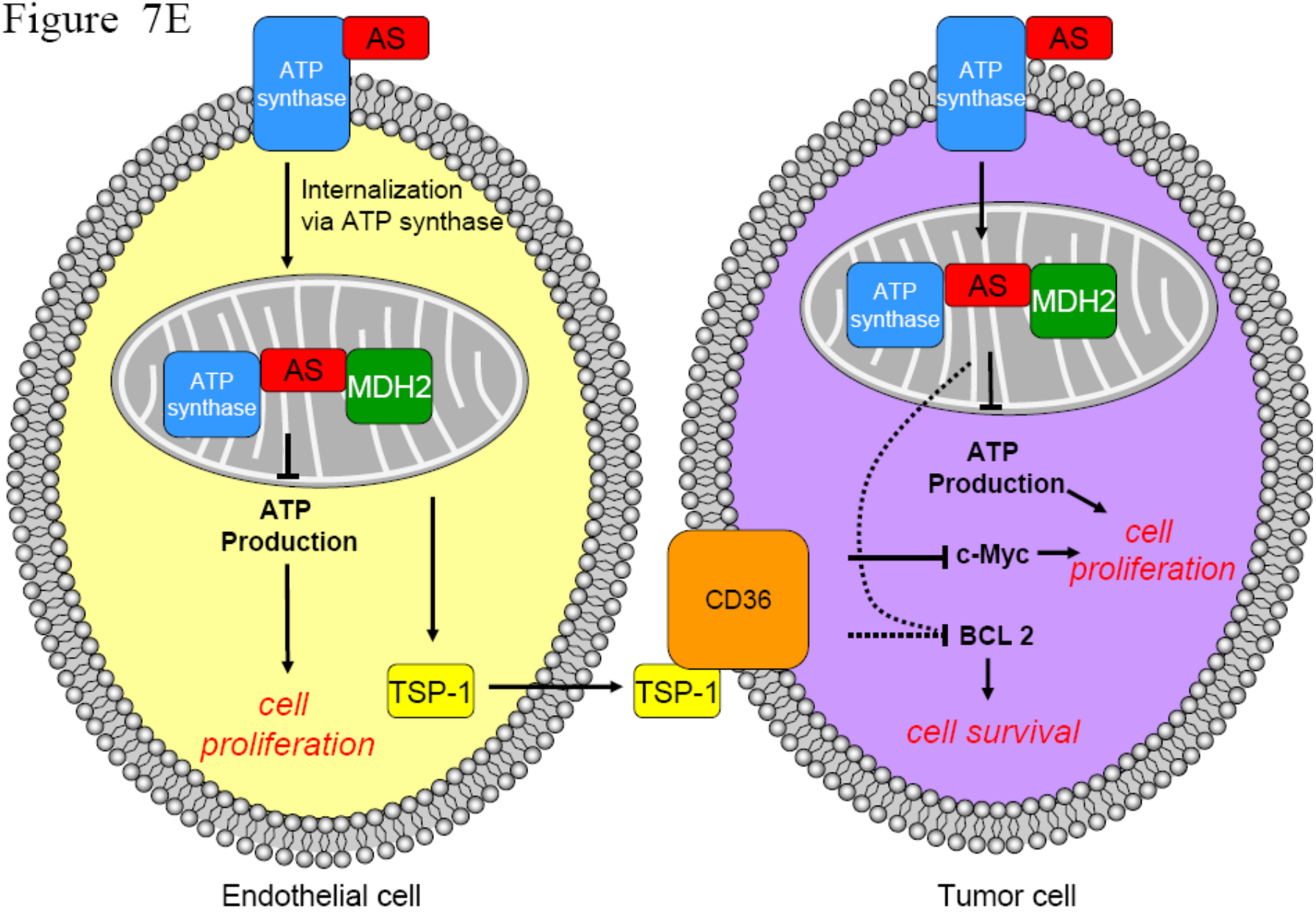

Lab on a Chip

Miniaturisation for chemistry, physics, biology, & bioengineering

www.rsc.org/loc

Volume 9 | Number 9 | 7 May 2009 | Pages 1153–1308

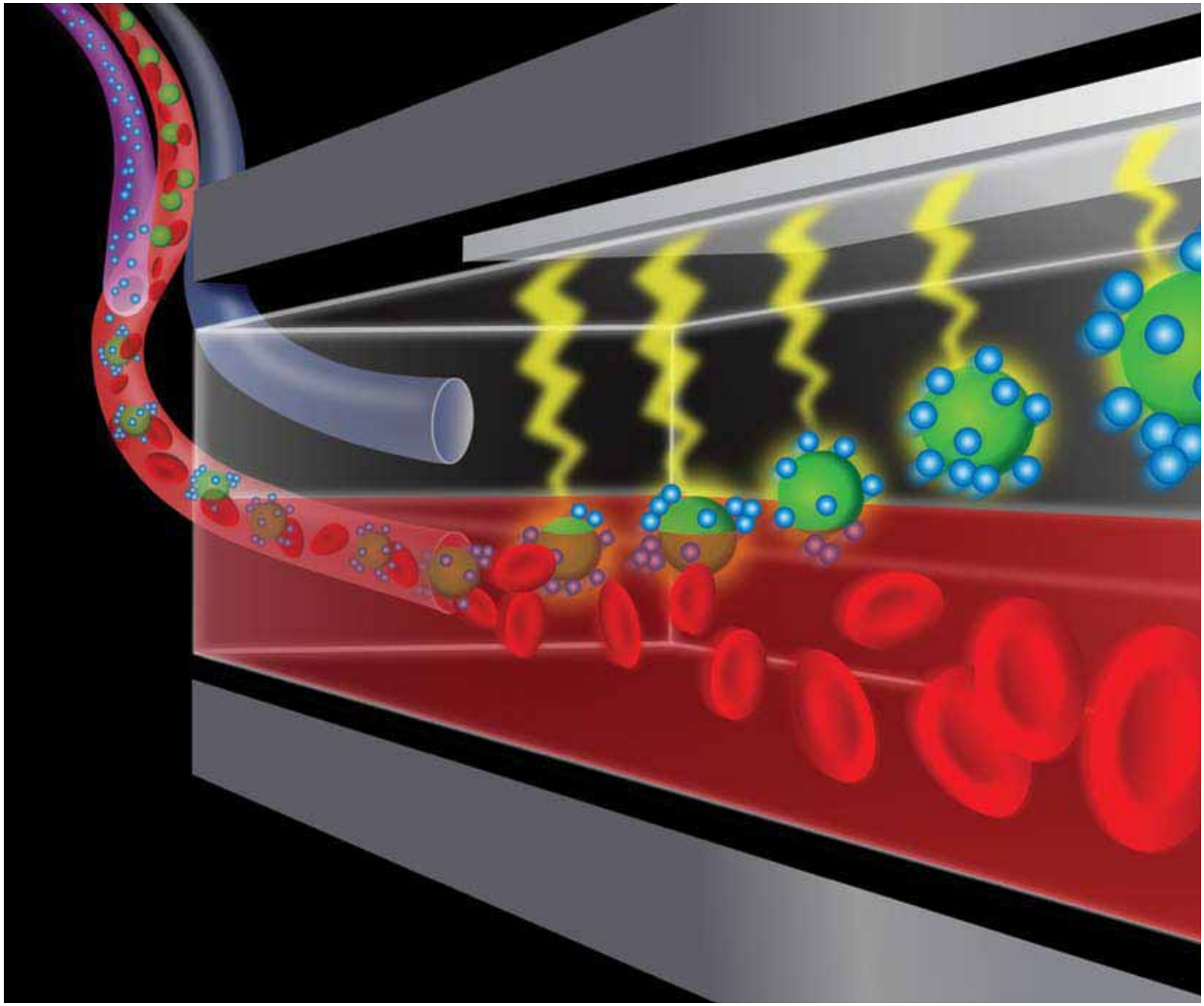

ISSN 1473-0197

RSC Publishing

1473-0197(2009)9:9;1-T

Micromagnetic–microfluidic blood cleansing device†

Chong Wing Yung,[a] Jason Fiering,[b] Andrew J. Mueller[b] and Donald E. Ingber*[ac]

Received 29th September 2008, Accepted 19th January 2009
First published as an Advance Article on the web 18th February 2009
DOI: 10.1039/b816986a

Sepsis is a lethal disease caused by a systemic microbial infection that spreads *via* the bloodstream to overwhelm the body's defenses. Current therapeutic approaches are often suboptimal, in part, because they do not fully eliminate the pathogen, and hence the source of deadly toxins. Here we describe an extracorporeal blood cleansing device to selectively remove pathogens from contaminated blood and thereby enhance the patient's response to antibiotic therapy. Immunomagnetic microbeads were modified to create magnetic opsonins that were used to cleanse flowing human whole blood of *Candida albicans* fungi, a leading cause of sepsis-related deaths. The micromagnetic–microfluidic blood cleansing device generates magnetic field gradients across vertically stacked channels to enable continuous and high throughput separation of fungi from flowing whole blood. A multiplexed version of the device containing four parallel channels achieved over 80% clearance of fungi from contaminated blood at a flow rate of 20 mL/h in a single pass, a rate 1000 times faster than a previously described prototype micromagnetic–microfluidic cell separation system. These results provide the first proof-of-principle that a multiplexed micromagnetic–microfluidic separation system can be used to cleanse pathogens from flowing human blood at a rate and separation efficiency that is relevant for clinical applications.

Introduction

Sepsis, a body's response to a systemic microbial infection, is the leading cause of death of immunocompromised patients, and is responsible for over 200,000 deaths per year in the United States.[1,2] The onset of sepsis occurs when rapidly growing infectious agents saturate the blood and overcome the body's immunological clearance mechanisms.[3] Most existing therapies are ineffective, and patients die because of clot formation, hypoperfusion, shock, and multiple organ failure.[4]

Current treatments for sepsis and septic shock include use of recombinant drugs, membrane filtration devices, antibiotics and blood transfusion with packed red blood cells, with the major focus being removal of inflammatory mediators that contribute to multi-organ system failure.[5–9] One form of recombinant therapy for sepsis is a human recombinant activated protein C (Xigris) used to restore dysfunctional anticoagulation, prevent microvascular thrombosis, and properly modulate the systemic inflammatory response.[10,11] However, this treatment can cause severe bleeding, deplete pro-inflammatory mediators necessary for proper immune function, and it has questionable efficacy.[11–15] Hemofiltration and hemadsorption devices, which are used to non-specifically remove blood proteins, can also remove many inflammatory cytokines that are required to fight infectious agents.[8,9] Interestingly, antibiotic therapies that simply act by reducing the pathogen load can be effective in some sepsis patients.[5,16] There are also clinical cases where the lives of septic infants were saved by performing whole body transfusions which removed pathogens from the blood.[17] Generalized use of these antibiotic therapies are unfortunately limited by dose toxicity and blood transfusions can deplete the patient of endogenous immune components and cells needed to fight the infection.[18] However, the success of these approaches indicate that a biomedical device that can selectively cleanse pathogens from a patient's blood without altering critical blood components can be an effective method for treating sepsis when used in conjunction with conventional therapies, such as fungicides.

Microfluidics technologies, such as the H-filter, offer a novel approach for selective separation of particulates from flowing liquids without the need for a filter membrane and they provide large interfacial surfaces to increase separation efficiency.[19–22] For example, microfluidic systems that utilize strong rare-earth magnets positioned adjacent to microfluidic channels have been developed to separate cells, magnetically-labeled cells and particles from a single sample stream.[23–26] But these devices have limited clearance capacity because captured species tend to accumulate near the magnet and obstruct flow over time. To address this limitation, we developed a prototype micromagnetic–microfluidic device that uses a collection fluid in a second laminar flow stream in direct contact with the flowing sample to continually carry away cells that are magnetically pulled across the flow stream boundary.[27] For targeted removal, magnetic opsonins (*i.e.* magnetic nano- or micro-beads coated with pathogen-specific antibodies) were used to selectively bind bacterial pathogens within a red blood cell solution at a rate of 20 μL/h.[27] Here we have developed a more clinically relevant

[a]*Vascular Biology Program, Department of Surgery and Pathology, Children's Hospital and Harvard Medical School, 300 Longwood Ave., KFRL 11.127, Boston, MA, 02115-5737, USA. E-mail: donald.ingber@childrens.harvard.edu; Fax: +617-730-0230; Tel: +617-919-2223*
[b]*Charles Stark Draper Laboratory, 555 Technology Square, Cambridge, MA, 02138, USA*
[c]*Wyss Institute for Biologically Inspired Engineering, School of Engineering & Applied Sciences, Harvard University, Cambridge, MA, 02139, USA*

† Electronic supplementary information (ESI) available: Fig. S1–S3. See DOI: 10.1039/b816986a

microfluidic device that employs a multiplexed design to achieve high separation efficiency of fungal pathogens from human whole blood (hWB) at a rate 1000 times faster than our initial prototype.

Experimental

Microdevice design and fabrication

The micromagnetic–microfluidic blood cleansing device (MMBCD) is composed of three major components: a polymeric microfluidic flow cell, a magnetic field concentrator, and a tunable external electromagnet (Fig. 1).[28] The microfluidic flow cell was created with standard microfabrication techniques and was assembled through plasma-bonding of four layers of molded polydimethylsiloxane (PDMS) cast from SU-8 masters (Fig. 2).

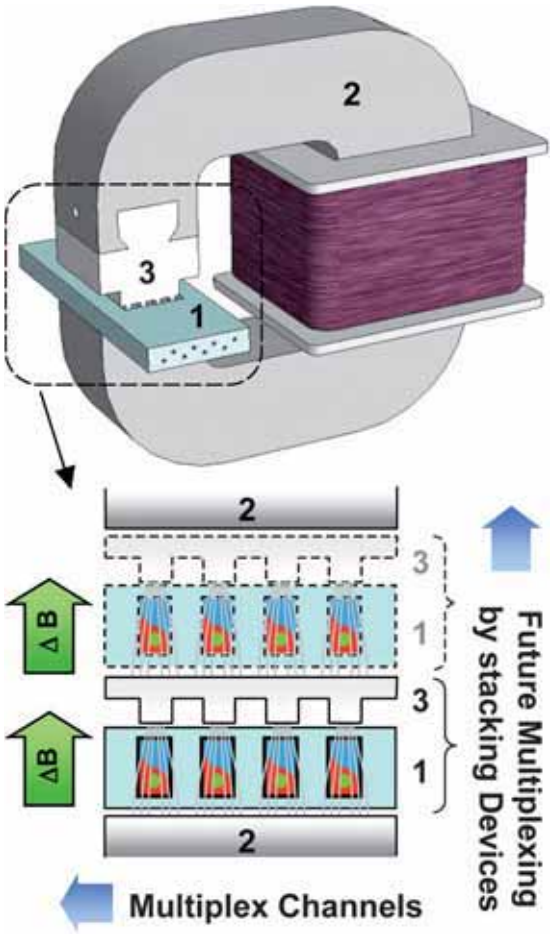

Fig. 1 Micromagnetic–microfluidic blood cleansing device (MMBCD) is assembled from three major components. The polymeric microfluidic flow cell (1) contains an array of channels where blood (bottom channel) and saline collection (top channel) fluids flow side-by-side under laminar conditions. A solenoid electromagnetic (2) generates magnetic fields that are conducted vertically across the microfluidic channels by a C-shaped steel core. (Inset) Strong magnetic field gradients directed vertically upwards (gray lines) are created by the ridged geometry of the magnetic field concentrator (3) and pull opsonized pathogens (green dots) from the blood into the collection fluid. Multiplexing was achieved by increasing the number of channels within each device, and in the future could be achieved by stacking up multiple concentrators and devices (dashed outlines).

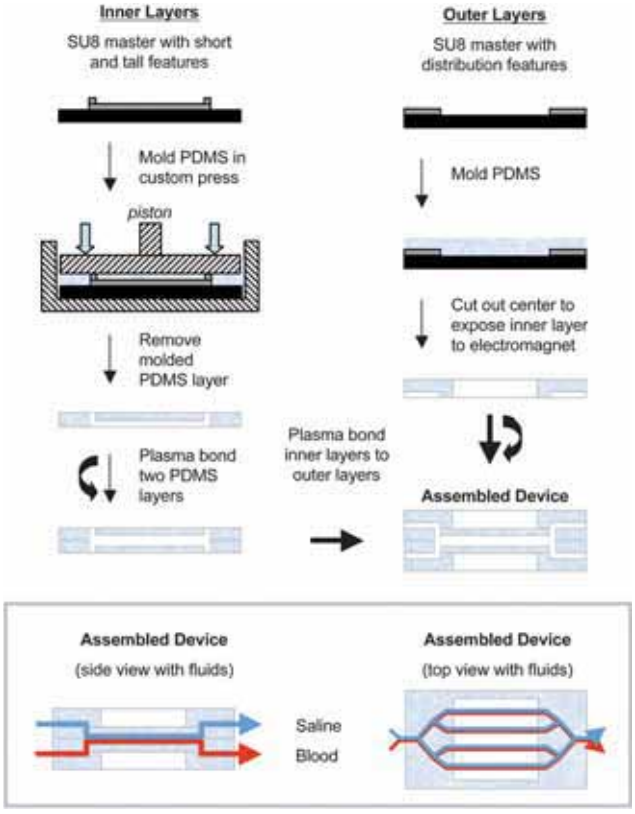

Fig. 2 Microfabrication approach used to create the microfluidic device. The polymeric microfluidic flow cell was fabricated by plasma-bonding four individually molded polydimethylsiloxane (PDMS) layers. The two inner layers were molded on a silicon wafer master (thick black line), which contains two levels of SU8 features (gray lines). The short features form channels for fluid flow, and the tall features form through-holes that connect to the outer layers and also act as a stop for the piston. The two outer layers are molded by standard polymer micromolding techniques and form channel features for fluid inlet, distribution and outlet.

The two inner layers contained wide channel features of (0.5 × 0.2 × 20 mm; w × h × l) that allowed direct contact between blood and collection flow streams, necessary for the magnetic separation. The two outer layers contained bifurcated channel manifolds that distributed fluid into the four inner separation channels. Thin inner PDMS layers (250 μm) were cast in order to position the channels in close proximity to the field concentrator and thereby maximize the magnetic field gradient within the separation chambers. Tubing connected from the side of the device allows for device stacking.

Our design has several advantages when compared to previous magnetic separation flow cells. It employs a separate metal field gradient concentrator layer with surface ridges that run directly above the entire length of each channel (inset of Fig. 1). Since this magnetic field concentrator is not placed within the PDMS layers as in past model systems,[27] multiple channels can be densely arrayed within a single polymeric device to increase throughput. Further multiplexing can also be achieved by stacking multiple devices vertically, interposed with multiple metal gradient concentrators that are placed between each PDMS layer inside a single electromagnet housing (Fig. 1). The electromagnet was constructed from a 1500 turn, 47 Ω solenoid and a C-shaped steel

core. The magnetic field concentrator, also machined from high magnetic permeability steel, has four individual ridges ($1 \times 1 \times 20$ mm; w × h × l), spaced 3 mm apart, and is attached to the top side of the C-shaped core. The total air gap between the top surface of the ridges and the opposing face of the magnet is 5.7 mm. The electromagnetic field strength of the concentrator was measured using a Teslameter (F.W. Bell 5080) and field gradient was quantified by measuring the change in the field strength at a distance of 0.25 mm normal to the surface of a ridge.

Cell culture

Candida albicans used for experiments were cultured in suspension in YPD media (BactoYeast 10 g/L, BactoPeptone 20 g/L, Dextrose 20 g/L) at 37 °C, shaking at 250 rpm overnight. The yeast form was harvested through centrifugation (1000*g*) and resuspended in phospate buffer saline (PBS) before use.

Preparation of magnetic opsonins

Super-paramagnetic beads (1 μm diameter, tosyl-coated; MyOne™ Dynabeads®, Invitrogen) were conjugated to biotinylated polyclonal antibodies (Abcam) against *C. albicans* fungi surface antigens. Beads were incubated with antibody (0.08 to 1.60 μg/μL) dissolved in carbonate buffer (Na_2CO_3 1.6 g/L, $NaHCO_3$ 0.93 g/L, pH = 9.4) overnight at 37 °C on a rotator, and then collected magnetically and washed twice in PBS (plus 0.5% Human Serum Albumin (HSA), 0.05% Tween20, 0.02% NaN_3) before rotating overnight at 37 °C. The beads were then washed again with PBS containing 0.1% HSA, 0.05% Tween20, and 0.02% NaN_3 and stored at 4 °C.

Fluorescence labeling and analysis

C. albicans cells were labeled using CellTracker™ Blue CMAC (353/466; 7-amino-4-chloromethylcoumarin; Molecular Probes) for bead binding assays. Cells were incubated with magnetic opsonins for 1 h at room temperature before bead-bound-fungi were removed with a permanent (Nd-Fe-B) magnet. The bead binding efficiency was indirectly quantified by measuring the remaining fluorescence after magnetic removal of the fungal cells (Victor3; PerkinElmer).

For cell binding assays performed in whole blood, a multi-fluorescence labeling strategy was used to distinguish beads from unbound and bead-bound-fungi (Fig. 3a). Beads conjugated with biotinylated antibodies were labeled with streptavidin-Alexa647-R-PE (496/668; Molecular Probes), and *C. albicans* cells were labeled with CellTracker™ Green CMFDA (491/517; 5-chloromethylfluorescein diacetate; Molecular Probes). Human whole blood samples that contained beads and fungi were incubated in a red blood cell (RBC) lysis buffer (FACS Lysing Solution, BD Biosciences) for 15 min at room temperature and assayed without washing in a four-color flow cytometer (FACS Calibur, BD Biosciences). Fluorescence-based gates were drawn around individual populations within dot plots to identify lone beads (only red fluorescence), lone fungi cells (only green fluorescence) and bead-bound-fungi (both red and green fluorescence) (Fig. 3b). CountBright™ counting beads (UV-635/385-800; Invitrogen) were used to simultaneously quantitate the absolute concentrations of all populations within one assay, thereby allowing accurate comparison among samples.

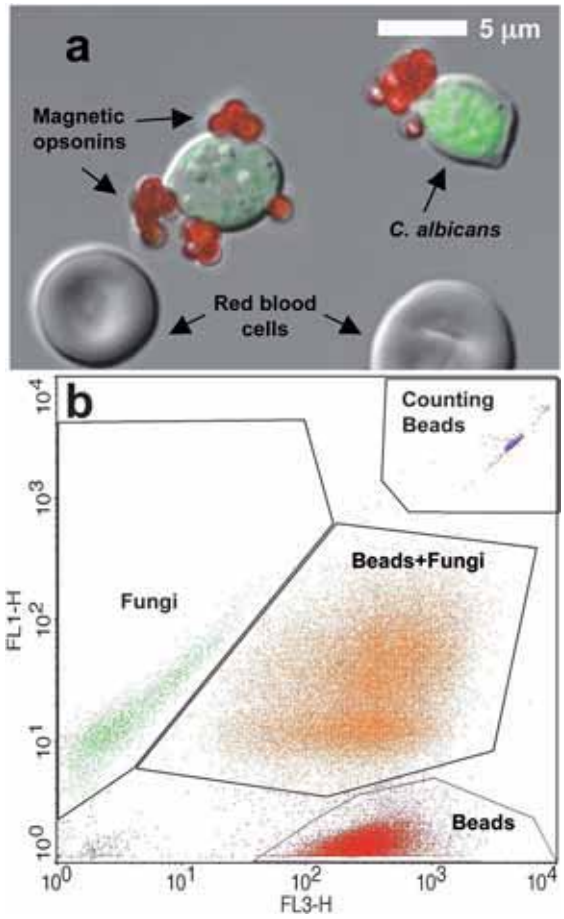

Fig. 3 Multi-fluorescence labeling and quantitation of magnetic opsonins and *C. albicans*. (a) Magnetic beads were conjugated with antibodies and Alexa647-R-PE (red) to create magnetic opsonins that selectively bound live *C. albicans* fungal pathogens stained with CMFDA CellTracker™ (Green) in human whole blood. (b) Magnetic opsonins (red) can be distinguished from bound (orange) and unbound pathogens (green) in RBC-lysed whole blood samples using a 4-color flow cytometer. Counting beads were added to blood sample to accurately quantitate the concentration of individual populations.

Quantitation of pathogen binding

Binding kinetics of fungi (*C. albicans*) and beads were first examined under batch conditions to optimize bead binding. *C. albicans* cells were suspended in PBS or hWB (from Children's Hospital Boston blood bank) at a concentration of 10^6 fungi/mL. Citrate–phosphate–dextrose–adenine (cpda-1) was used as a preservative and heparin (0.05 U/mL) was added as an anti-coagulant to maintain clot free flow (in microfluidic experiments). Bead binding saturation experiments were performed by varying the ratio of beads to fungi ($R_{b/p} = 20$ to 600) and samples were incubated in an end-over-end rotator (16 rpm) at 37 °C for 1 h. Kinetic binding experiments were performed over 4 h under similar incubation conditions. Flow cytometry was used to quantify the concentrations of bound fungi (positive for both

CMFD and Alexa647-R-PE fluorescence) and unbound fungi (positive for only CMFD) in order to determine the fraction of cells bound by beads (binding efficiency). Flow cytometry was also used to quantify the number of beads bound per fungi based on the increase of Alexa647-R-PE fluorescence between bead bound fungi and lone beads.

Pathogen clearance using the micromagnetic–microfluidic separator

To assess the cell separation efficiency of the multiplexed MMBCD, beads and fungi were pre-incubated in PBS to allow maximum binding before resuspending in heparinized hWB. The effects of varying electromagnet current on fungal separation efficiency were analyzed using bead-bound-fungi suspended in PBS. Two individual syringe pumps (New Era Pumps) were used to inject PBS or hWB samples into the bottom channels and PBS collection fluid into the top channels. To test how the viscosity of the collection fluid affected its hydrodynamic interaction with blood, medical grade dextran (40 kDa, Sigma) was used to vary the viscosity. Dextran was dissolved in PBS at 5, 10 and 20% to produce solutions with viscosities of 2, 3, 11 centipoise at room temperature, and all experiments were performed with a sample flow rate of 5 mL/h/channel. The 4-channel MMBCD, which was used to separate *C. albicans* fungal pathogens from heparinized hWB, had a total flow rate of 20 mL/h. The PBS collection fluid flow rate was 80 mL/h. Magnetic separation in hWB samples was achieved at a 10 V setting, which corresponds to a magnetic gradient of approximately 50 T/m. Fluid samples were collected from bottom-inlet, top-outlet, and bottom-outlet channels and analyzed by flow cytometry to assess the separation efficiency of beads and bead-bound fungi (Efficiency $= 1 - X_{\text{bottom-out}}/X_{\text{bottom-in}}$). Blood loss was quantified by measuring the OD_{600} of red blood cells (Loss $= OD_{\text{top-out}}/OD_{\text{bottom-out}}$).

Statistical analysis

All measured values are reported as an average of at least triplicate samples ± standard deviation (SD, as indicated by error bars in all graphs). Non-linear regressions of saturation and kinetic binding data were performed using Mathematica 6.0. The ANOVA *t*-test was used to determine *p*-values; $p < 0.05$ was considered statistically significant.

Results and discussion

Optimization of the bead–antibody conjugation

The optimal antibody concentration required for bead conjugation was assessed using a pathogen binding assay. The pathogen binding efficiency of the beads followed a first-order binding relationship, increasing with the concentration of conjugated antibodies and saturating at approximately 96 ± 1% at an antibody concentration of 1 μg/μL (Fig. 4). In contrast, only a low level of unspecific binding ($p < 8 \times 10^{-7}$) was detected when beads conjugated with anti-*E. coli* antibodies were mixed with *C. albicans* cells. Functionalized beads were also found to not bind blood cells based on visual examination under bright-field and fluorescence microscopy, as shown in Fig. 3.

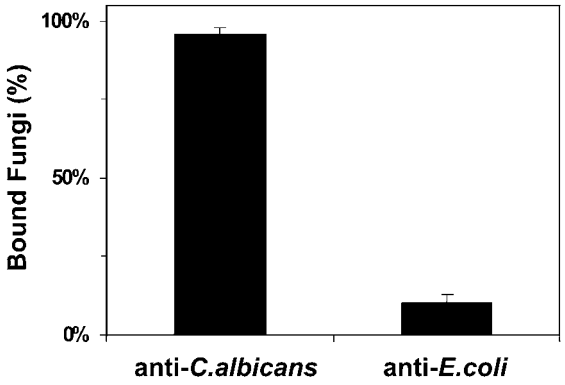

Fig. 4 Magnetic opsonins have high binding specificity and efficiency. Magnetic opsonins made from 1 μm magnetic beads conjugated with anti-*C. albicans* antibodies showed a high level of binding affinity for the fungal pathogens in PBS (96%). The high specificity of the magnetic opsonins was demonstrated by a low level of background binding when similar beads were conjugated with anti-*E. coli* antibodies.

Optimizing bead binding saturation and kinetics

The optimal amount of beads needed to bind fungal cells was determined by varying the bead : pathogen ratio ($R_{b/p}$) under batch conditions. The binding efficiency followed a Langmuir adsorption model with fungal cell binding increasing with bead concentration. A maximum binding efficiency of 80% was achieved at an $R_{b/p}$ of 120 in hWB (see ESI Fig. S1†). A cost-benefit analysis, based on minimizing the change in slope of the regression curve, indicated that an $R_{b/p}$ of 120 (beginning of the plateau) was the optimal concentration for binding fungal cells in hWB. The optimal incubation period required for magnetic microbead binding to fungi in blood was determined using a 4 h kinetic assay. Although maximum binding (85 to 90%) occurred between 30 to 60 minutes in whole blood, approximately half (48 ± 4%) of all pathogens were bound within the first 5 minutes of incubation (see ESI Fig. S2†). Thus, future devices may utilize the shorter incubation period but compensate by further multiplexing to maintain the same overall system efficiency to meet target clearance levels and process rates. Alternatively, a semi-batch process can be used where several small aliquots of blood can be drawn from a patient in stages that are staggered in time and premixed for continuous operation. Optimal binding conditions (1 h incubation at 37 °C and $R_{b/p}$ of 120) were used for all subsequent fungal cell binding experiments in whole blood. Under these optimized conditions, an average of 28 ± 15 beads was bound per fungal cell.

Fluid dynamics in microfluidic channels

Our design for the MMBCD contained channels that merged with a transverse velocity component (Fig. 5a); under these conditions the interface between the laminar streams of saline collection fluid and hWB rotated by ~90 degrees when the streams joined, resulting in the two streams flowing partially side-by-side along the length of the channel rather than being stacked vertically (Fig. 5b). This rotation of the laminar flow interface was predicted for a water–water interface in computational fluid dynamic modeling;[28] however, the model also predicted that the laminar streams would reflect when the channels

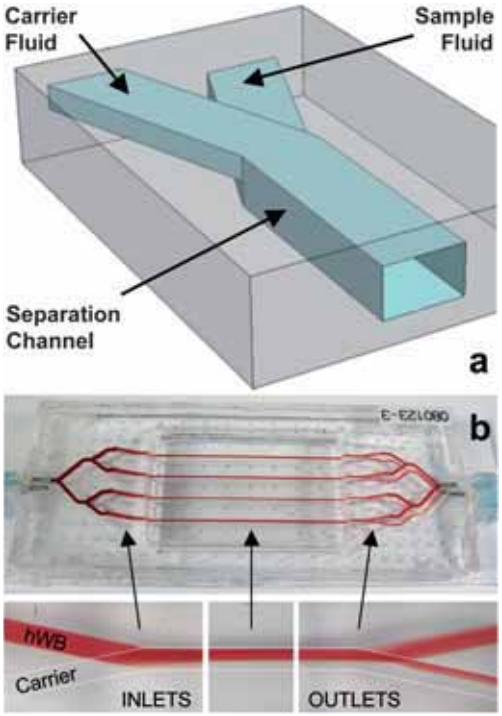

Fig. 5 Transverse merging of microfluidic channels in MMBCD caused rotation of inlet fluid streams. (a) The separation channel within the prototype MMBCD has inlets that merge from top and bottom layers of PDMS. As laminar streams of fluids from the inlets merged, the transverse angle of the inlets caused the fluids to rotate about the longitudinal axis of the separation channel. The rotation of a water–water interface at the inlets and reflection at the outlets was predicted by computational fluid dynamics modeling. (b) However, the predicted reflected rotation at the outlets did not occur in experiments that used human whole blood (hWB) and phosphate buffer saline (PBS) and this resulted in significant blood loss (50–60%). Replacement of PBS with a 6% Dextran solution, which has a similar viscosity as hWB, did little to reduce blood loss. Blood loss was significantly reduced to ~13% ($p < 0.01$) when the PBS to hWB flow ratio was increased by 4-fold (80 to 20 mL/h) in order to hydrodynamically confine the blood stream.

diverge at the outlets, so that separation of the blood and collection streams would be preserved. However, the rotated interface was not similarly reflected at the outlets in experiments that utilized hWB and PBS solutions, and this resulted in significant blood loss (50–60%) to the collection outlet, and comparable blood dilution at the blood outlet.

Attempts at matching the viscosity of the collection fluid and the apparent viscosity of blood, by replacing PBS with 6% Dextran solution (4 cp), did little to prevent blood loss. This is most likely because blood is a complex non-Newtonian fluid that exhibits both shear-thinning and viscoelastic properties and thus, its hydrodynamic behavior cannot be completely matched by a simple Newtonian fluid.[20,29,30] But we have found that it is possible to hydrodynamically confine blood to the bottom channel by increasing the flow rate and thus pressure of the collection fluid, as previously observed by others.[31] Utilizing a PBS : blood flow ratio of 4, blood loss was significantly reduced to ~13% ($p < 0.01$) with a similar level of dilution of the blood stream. Although the hematocrit level of diluted blood can be easily readjusted with conventional hemaconcentrators used in hemafiltration or renal dialysis machines, the increased saline flow may exert a momentum transfer into the blood phase, which can potentially impede the motion of magnetic particles and reduce separation efficiency.

Electromagnetic performance of microdevice

The magnetic field strength (B) that is directly normal to the surface of the concentrator increased linearly from 80 to 272 mT as the voltage supplied to the electromagnet was increased from 10 to 40 V (Fig. 6). The field strength began to saturate with settings beyond 40 V and reached a maximum of 295 mT at 50 V. The corresponding electromagnetic gradient (ΔB) varied from 50 T/m at 10 V up to a maximum of 200 T/m at 40 V. The efficiency of fungi separation utilizing a single-channel MMBCD was found to be tunable based on the voltage supplied to the electromagnet. Utilizing beads and fungi mixed in PBS, the separation efficiency increased linearly with the voltage up to 5 V, and began to plateau thereafter (see ESI Fig. S3†). A 90% separation efficiency was achieved at the maximum setting of 15 V; however, magnetic particles and microaggregates (which are normally present in blood-bank blood prior to filtration) were found to accumulate within the microfluidic channels when separations were performed in hWB. This was because beads and bead-bound-fungi were too strongly magnetized and were pulled tightly against the channel walls, which served as nucleation sites for further accumulation; but decreasing the voltage to 10 V prevented this accumulation.

The magnetic force ($\vec{F}_m$) exerted on a point-like magnetic dipole ($\vec{m}_b$) is proportional to the gradient ($\vec{\nabla}$) of an external magnetic field ($\vec{B}$):[32,33]

$$\vec{F}_m = (\vec{m}_b \cdot \vec{\nabla})\vec{B} \quad (1)$$

This equation can be simplified to calculate the total force on a number of beads (n) in one dimension (z) as:[34]

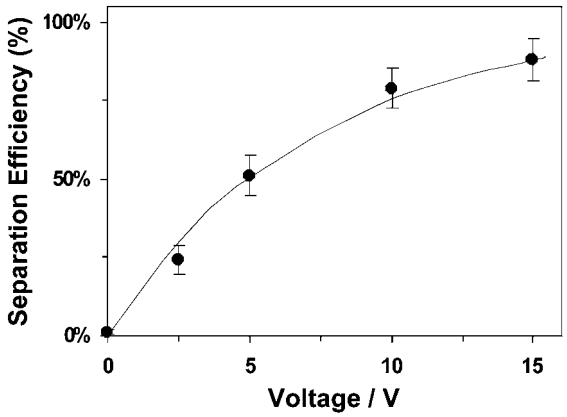

Fig. 6 Tunable electromagnetic cell separation was initially tested with pathogens in PBS. Initial studies to test the strength and tenability of electromagnetic separation in microfluidic experiments were performed with *C. albicans* in PBS. Fungal cell separation was found to be broadly tunable from 0–90% based on a voltage setting of 0–15 V. This demonstrated that our electromagnet had sufficient strength and sensitivity necessary for the further optimization of cell separation in whole blood samples.

$$F_m = nm_{sat}\frac{dB}{dz} \quad (2)$$

Based on eqn (2), a 10 V setting that generates a magnetic field gradient of 50 T/m would be able to exert 50 pN of force on each 1 μm bead, which has a saturated magnetic moment (m_{sat}) of 10^{-13} A m^2.[27] Because a minimum of 10 magnetic beads were bound to each opsonized fungi (average = 28 ± 15 beads/cell), at least 500 pN can be exerted on each cell. With this force, opsonized pathogens (5–10 μm diameter) would require 0.3–0.6 seconds to traverse the 100 μm height of the blood channel. Because blood was flowing at a rate of 5 mL/h and has a residence time of 0.7 seconds in the MMBCD, a 10 V setting would provide sufficient time to pull magnetic particles from the blood stream. Future systems used in the clinical setting, however, should integrate inline low-capacity, but ultra-high efficiency, magnetic traps to pull out any remaining magnetic particles in the blood before it is reintroduced into a human patient.

It is important to note that there is minimal undesired diffusion of blood proteins, such as albumins from blood into the saline using the flow conditions described here. Given that HSA has an approximate diffusion coefficient (D) of 6×10^{-7} cm^2/s,[35] the diffusion time scale ($t = L^2/2D$) across the height of the blood channel (L = 0.01 cm) is approximately 84 s, which is much longer than the time the blood and saline fluids were in direct contact (*i.e.*, residence time)..

Pathogen clearance from blood using microdevice

Utilizing the 4-channel multiplexed MMBCD, it was possible to clear 80% of bead-bound-fungi from a 10 mL volume of hWB within 30 min (Fig. 7). Excess beads not bound to fungal cells were also removed with relatively high efficiency (~82%). Accumulation of magnetic particles within the channels was not found under these conditions. These results demonstrate that a majority of fungi can be cleared upon a single pass through one 4-channel microfluidic system. The potential clinical value of this device is that multiple microfluidic cartridges can be positioned in parallel and in series, and it enables continual recirculation of contaminated blood, such that a patient's entire pathogen load can be further reduced over time through repeated passage through the device.

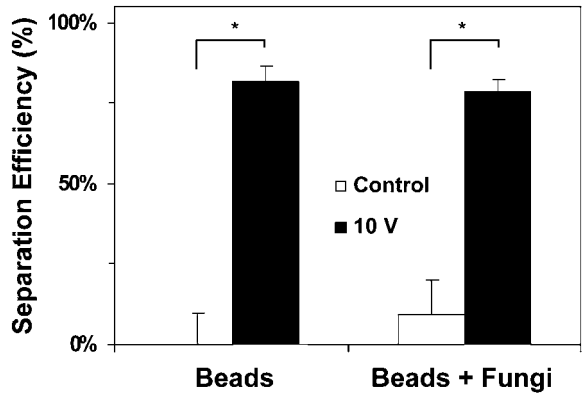

Fig. 7 Multiplexed MMBCD achieved high throughput separation of pathogens from hWB. The multiplexed 4-channel MMBCD was capable of cleansing 80% of all bead-bound-fungi from a 10 mL volume of hWB at a rate of 20 mL/h. Excess beads were also removed at a relatively high efficiency (~82%).

A simplified mathematical model, based on Monod kinetics,[36] to describe the systemic clearance of fungi in a recirculated system is defined by the differential equation:

$$\frac{dC_p}{dt} = \mu C_p - \frac{nF\varphi}{V}C_p \quad (3)$$

Where C_p is the concentration of pathogen in the patient, t is time, μ is the specific growth rate of the pathogen (0.7 h^{-1} under optimal conditions), n is the total number of microfluidic channels used in the multiplexed device, F is the blood flow rate per channel, φ is the separation efficiency per single pass, and V is the entire blood volume of the patient (500 mL in neonates). The systemic rate of pathogen clearance is thus determined by the rate of pathogen growth (1st term) minus the rate of magnetic separation (2nd term). Utilizing our current results, a multiplexed system that contains 100 channels will theoretically be able to reduce the total pathogen load by 90% in 3.6 h or 99% in 7.3 h. The respective clearance times can be further reduced to only 1.2 h and 2.3 h by doubling the number of channels.

Conclusion

Microfluidic devices have been used to separate molecules, particles and cells from small sample volumes at low flow rates (~μL/h) for various analytical applications.[37–39] However, this technology is rarely exploited for therapeutic applications or for high throughput processes (~mL/h) that utilize two fluid streams due to the challenges in multiplexing multiple pairs of channels while incorporating other separation features, such as magnetic field concentrators. We have demonstrated that this can be achieved by developing an array of vertically aligned channels that utilizes a separate magnetic field concentrator placed external to the microdevice. The advantage of this design is that it allows channels to be densely arrayed within each device. Additionally, in principle, multiple devices can be stacked with interposed magnetic field gradient concentrators, which ensure application of similar magnetic pulling forces across multiple interposed microfluidic systems, to achieve high throughput processing required for therapeutic applications. We successfully demonstrated proof-of-principle for this multiplexing concept by using a microfluidic device to cleanse 80% of living fungal pathogens from hWB flowing at a rate of 20 mL/h, which is 1,000 times faster than previously achieved in an earlier prototype microfluidic-micromagnetic separation device.[27] These results clearly demonstrate that the improved, multiplexed microfluidic–micromagnetic cell separation design provides much higher volume throughput while maintaining cell separation efficiencies, and thus, confirm its potential value for future clinical applications where it would provide a potentially exciting adjuvant to conventional antibiotic therapies.

Future design challenges include development of fully multiplexed arrays that can handle practical patient blood volumes, semi-batch mixing processes that will allow longer bead–pathogen incubation periods while maintaining continuous blood flow, as well as integration into conventional continuous veno–venous hemafiltration units, which have proven hemaconcentrators, blood warmers and oxygenation technologies.

Furthermore, additional safety features such as ultra-high-efficiency magnetic traps must also be developed to capture excess beads before such a prototype can be used clinically.

Acknowledgements

The authors kindly thank Dr. Julia R. Köhler of the Children's Hospital Boston for providing *C. albicans*. This research was provided by grant support (Award #07-057 to D.E.I.) and a Career Development award (to C.Y.) from the Center for Integration of Medicine and Innovative Technology (CIMIT). Microfabrication facilities for early-stage prototyping were provided by Harvard University's Center for Nanoscale Systems (CNS) and the National Nanotechnology Infrastructure Network (NNIN) initiative.

References

1 D. C. Angus, W. T. Linde-Zwirble, J. Lidicker, G. Clermont, J. Carcillo and M. R. Pinsky, *Crit. Care Med.*, 2001, **29**, 1303–1310.
2 R. S. Watson, J. A. Carcillo, W. T. Linde-Zwirble, G. Clermont, J. Lidicker and D. C. Angus, *Am. J. Respir. Crit. Care Med.*, 2003, **167**, 695–701.
3 R. S. Hotchkiss and I. E. Karl, *The New England Journal of Medicine*, 2003, **348**, 138–150.
4 J. Cohen, *Nature*, 2002, **420**, 885–891.
5 J. Garnacho-Montero, T. Aldabo-Pallas, C. Garnacho-Montero, A. Cayuela, R. Jimenez, S. Barroso and C. Ortiz-Leyba, *Critical Care (London, England)*, 2006, **10**, R111.
6 S. Trzeciak, R. P. Dellinger, J. E. Parrillo, M. Guglielmi, J. Bajaj, N. L. Abate, R. C. Arnold, S. Colilla, S. Zanotti and S. M. Hollenberg, *Ann. Emerg. Med.*, 2007, **49**, 88–98, 98 e81–82.
7 C. S. Bouman, H. M. Oudemans-van Straaten, M. J. Schultz and M. B. Vroom, *Journal of Critical Care*, 2007, **22**, 1–12.
8 C. Tetta, R. Bellomo, P. Inguaggiato, M. L. Wratten and C. Ronco, *Ther. Apher.*, 2002, **6**, 109–115.
9 R. Venkataraman, S. Subramanian and J. A. Kellum, *Crit. Care*, 2003, **7**, 139–145.
10 D. Nash, *P&T Journal*, 2002, **27**.
11 M. Levi, E. De Jonge and T. van der Poll, *International Journal of Clinical Practice*, 2002, **56**, 542–545.
12 P. Q. Eichacker, C. Natanson and R. L. Danner, *The New England Journal of Medicine*, 2006, **355**, 1640–1642.
13 P. C. Minneci, K. J. Deans, X. Cui, S. M. Banks, C. Natanson and P. Q. Eichacker, *Critical Care Medicine*, 2006, **34**, 538–541.
14 B. Gardlund, *Acta Anaesthesiologica Scandinavica*, 2006, **50**, 907–910.
15 B. Vangerow and M. A. Mignini, *Acta Anaesthesiologica Scandinavica*, 2007, **51**, 261–262.
16 C. M. Coopersmith, D. M. Amiot, 2nd, P. E. Stromberg, W. M. Dunne, C. G. Davis, D. F. Osborne, K. D. Husain, I. R. Turnbull, I. E. Karl, R. S. Hotchkiss and T. G. Buchman, *Shock (Augusta, Ga)*, 2003, **19**, 408–414.
17 Y. Asanuma, T. Takahashi, K. Koyama, T. Kato, S. Omokawa, A. Sueoka and J. Tanaka, *ASAIO transactions/American Society for Artificial Internal Organs*, 1989, **35**, 343–345.
18 D. P. Kontoyiannis, G. P. Bodey and C. S. Mantzoros, *Mycoses*, 2001, **44**, 125–135.
19 S. K. Sia and G. M. Whitesides, *Electrophoresis*, 2003, **24**, 3563–3576.
20 K. L. Helton and P. Yager, *Lab on a Chip*, 2007, **7**, 1581–1588.
21 M. S. Munson, C. R. Cabrera and P. Yager, *Electrophoresis*, 2002, **23**, 2642–2652.
22 A. E. Kamholz, B. H. Weigl, B. A. Finlayson and P. Yager, *Analytical Chemistry*, 1999, **71**, 5340–5347.
23 G. Blankenstein, *Microfabricated flow system for magnetic cell and particle separation*, Plenum Press, New York, 1997.
24 K. H. Han and A. B. Frazier, *Lab on a Chip*, 2006, **6**, 265–273.
25 K. H. Han, A. Han and A. B. Frazier, *Biosens. Bioelectron.*, 2006, **21**, 1907–1914.
26 N. Pamme and A. Manz, *Anal. Chem.*, 2004, **76**, 7250–7256.
27 N. Xia, T. P. Hunt, B. T. Mayers, E. Alsberg, G. M. Whitesides, R. M. Westervelt and D. E. Ingber, *Biomed. Microdevices*, 2006, **8**, 299–308.
28 J. Fiering, M. Varghese, C. W. Yung, K. M. Isaac and D. E. Ingber, in *MicroTAS*, San Diego, 2008.
29 G. B. Thurston, *Biorheology*, 1994, **31**, 179–192.
30 S. S. Shibeshi and W. E. Collins, *Appl. Rheol.*, 2005, **15**, 398–405.
31 B. Kuczenski, P. R. LeDuc and W. C. Messner, *Lab on a Chip*, 2007, **7**, 647–649.
32 R. J. S. Derks, A. Dietzel, R. Wimberger-Friedl and M. W. J. Prins, *Microfluid. Nanofluid.*, 2007, **3**, 141–149.
33 Q. A. Pankhurst, J. Connolly, S. K. Jones and J. Dobson, *J. Phys. D-Appl. Phys.*, 2003, **36**, R167–R181.
34 M. Berger, J. Castelino, R. Huang, M. Shah and R. H. Austin, *Electrophoresis*, 2001, **22**, 3883–3892.
35 B. Jachimska, M. Wasilewska and Z. Adamczyk, *Langmuir*, 2008, **24**, 6866–6872.
36 D. F. O. James Edward Bailey, *Biochemical Engineering Fundamentals*, McGraw-Hill, February 1986.
37 G. M. Whitesides, *Nature*, 2006, **442**, 368–373.
38 L. Kang, B. G. Chung, R. Langer and A. Khademhosseini, *Drug Discovery Today*, 2008, **13**, 1–13.
39 H. Becker, *Medical Device Technology*, 2008, **19**, 21–24.

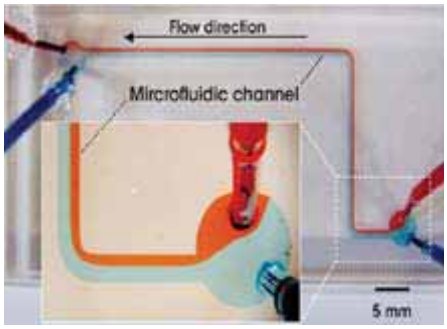

Septic Solution

Cleaning infected blood cells is set to be a breakthrough for treating patients with serious infections such as sepsis. With a new device purported to do just that, Chong Wing Yung and Donald E Ingber of the Children's Hospital Boston explain how their innovation could save lives and money.

Date: 01 Oct 2008

Sepsis is a lethal disease caused by a systemic microbial infection. This disease is a major killer of premature infants, immuno-compromised patients and citizens of many undeveloped nations. The overall death rate from this blood infection is over 25% in the US, and it is even higher internationally. The treatment of patients with sepsis also incurs a heavy economic burden: costs can be as high as $50,000 per patient and approximately $17bn is spent annually in the US to treat and manage patients with this disease.

The lethality of sepsis is triggered by an overload of the immune system due to rapidly growing pathogens that utilise the bloodstream to spread throughout the body. A 'tipping-point' is reached when the body's natural clearance mechanisms are overcome. This ignites widespread inflammatory responses and therapies are then no longer effective, as clot formation, hypoperfusion, shock, multiple organ failure and death ensue.

Treating sepsis

Patients with sepsis and septic shock are commonly treated with antibiotics, intravenous fluids, vasopressors, and, if necessary, packed red blood cells to restore blood pressure and oxygen saturation. Other therapies include anti-inflammatory and anti-thrombotic drugs or hemofiltration and hemadsorption treatments to remove inflammatory mediators (tumour necrosis factor, interleukin-1) with the goal of suppressing the damaging inflammatory cascade.

"A device that can rapidly cleanse the blood of pathogens could save the lives of many septic patients."

However, these methods do little to rid the patient of the living pathogens that are the primary source of toxins and continually activate this devastating inflammatory cascade. Excessive removal of pro-inflammatory mediators also can have a negative impact on patient outcome because many of these same mediators are required to combat the pathogens that still multiply within the body.

Because of the dominant focus on the systemic inflammatory response, most clinicians and investigators have essentially ignored the possibility that removal of pathogens from the blood could reverse the septic process. However, some patients with fulminant septicemia respond well to antibiotic therapy alone, which acts exclusively by reducing the pathogen load. Moreover, there have been anecdotal clinical cases in which septic neonates with documented infections of the blood have been saved by removing the patients' entire blood volume and replacing it with an equal volume of packed red blood cells.

Unfortunately, generalised use of whole blood transfusion is limited because removal of endogenous white cells, platelets, antibodies and other blood components leads to complications, including decreased immunoreactivity and an increased risk of infection (HIV, Hepatitis C). These observations suggest that a device that can rapidly cleanse the blood of pathogens without removing critical normal blood cells, proteins, fluids or electrolytes could save the lives of many septic patients.

Pathogen removal

Don Ingber, a professor at the Boston Children's Hospital, Harvard Medical School and Harvard School of Engineering and Applied Sciences, is the principal investigator of a translational research project that is focused on development of an extracorporeal blood-cleansing microdevice that rapidly clears blood of pathogens. This device uses microscopic 'magnetic opsonins' and a combined micromagnetic-microfluidic clearance technology, which functions like an 'artificial spleen' to capture and remove these bound microbes, restore homeostasis, and thereby make blood-borne infections responsive to conventional antibiotic therapy.

This ongoing research and development programme, which has been funded by the Center for Integration in Medicine and Innovative Technology (CIMIT), also involves Chong Yung at the Children's Hospital and the pair's collaborator, Jason Fiering at Draper Laboratory, as well as a team of experienced clinicians, engineers and

biomedical device developers.

This new cell-separation microdevice seamlessly integrates immunomagnetics and microfluidics. Immunomagnetic bead technology utilises nano- or micro-scale magnetic beads coated with antibodies or other specific ligands to bind targets of interest and confer magnetic mobility to those bound targets. Therefore, when pathogens lurking in the dense mixture of proteins and cells within whole blood are bound to these magnetic microparticles, they can be specifically removed by application of an external magnet field gradient. Microfluidics technology provides a means to carry out this magnetic separation in flowing blood.

At the microscopic scale of a single microfluidic channel, fluid flows are exclusively laminar, which means that when two different streams of fluid join together, the streams flow side by side without mixing, as if there were an invisible wall dividing them, as shown in Figure 1, p93. The blood cleansing device design, as in Figure 2, leverages this unique property of laminar flow. Whole blood is removed from the vein of a patient and mixed with magnetic microbeads coated with ligands (antibodies) that specifically bind to the pathogens. It is then flowed through a microfluidic channel next to a flowing isotonic saline collecting solution.

When a magnetic field gradient is applied perpendicularly to the flow, blood pathogens bound to the magnetic beads are pulled across the laminar stream into the flowing collection fluid, which is then discarded. This process cleanses the flowing blood, which is subsequently returned to another vein of the patient in a continuous flow system. It is analogous to existing clinical extracorporeal systems used for continuous veno-venous hemofiltration (CVVH) or extracorporeal membrane oxygenation (ECMO).

Micro-cleaners: cheap and robust

Because of their small size, multiple microfluidics devices of this type created with microfabrication techniques may be oriented in parallel, and in tandem, within a single integrated laminar flow network that can clear blood of pathogens at high throughput. Moreover, since the collected pathogens continuously flow out of the device, the capacity of this pathogen filter is unlimited. This micromagnetic-microfluidic separation technology can therefore potentially be used to create robust devices that may be mass produced and made available at low cost as point-of-care devices worldwide, including in underdeveloped nations.

"The device was able to achieve 80–90% clearance efficiency of *E.coli* bactera from a solution containing red blood cells."

The proof of principle for this approach was demonstrated in 2006 when a prototype blood cleansing device composed of a single microchannel created in polydimethylsiloxane polymer was developed that used a high gradient magnetic field concentrator integrated within the system during microfabrication to perform magnetic cell separations. Using 130nm superparamagnetic beads, the device was able to achieve 80–90% clearance efficiency of *E. coli* bacteria from an isotonic saline solution containing red blood cells at a density similar to blood when flowing at a rate of 25–30uL/hr in a single pass.

In more recent unpublished studies, this technique has been refined to cleanse human blood of pathogenic fungi. Fungal infections were targeted because conventional anti-fungal therapies are of limited use in treating sepsis due to dose-limited systemic toxicities. Preliminary in vitro results look extremely promising as the group has been able to demonstrate efficient clearance of living fungi (C. albicans) from whole human blood and to enhance throughput a thousand-fold in their newest versions of the device.

Innovative isolation technology

The goal is to develop a device containing multiplexed microfluidic and electromagnetic devices that will cleanse the entire blood volume of a human patient of deadly pathogens within a few hours. The same technology may provide a new platform to cleanse blood of patients with leukaemia who are undergoing 'blast crises', in which the level of tumour cells in the circulation is so high that infarcts can occur. It also may provide an efficient way to collect circulating stem cells for regenerative medicine applications.

This research has uncovered an exciting new platform technology for isolation of living cells from biological fluids. Soon the implications of sepsis and the increasingly fatal repercussions of the disease could be a thing of the past.

The following people contributed to this article:

- Chong Wing Yung, Postdoctoral, Children's Hospital Boston and Harvard Medical School
- Donald E Ingber, Professor, Children's Hospital Boston and Harvard Medical School

Engineering Robust and Functional Vascular Networks In Vivo With Human Adult and Cord Blood Derived Progenitor Cells

Juan M. Melero-Martin, Maria E. De Obaldia, Soo-Young Kang, Zia A. Khan, Lei Yuan, Peter Oettgen and Joyce Bischoff

Circ. Res. 2008;103;194-202; originally published online Jun 12, 2008;
DOI: 10.1161/CIRCRESAHA.108.178590
Circulation Research is published by the American Heart Association. 7272 Greenville Avenue, Dallas, TX 72514
 Print ISSN: 0009-7330. Online ISSN: 1524-4571

Engineering Robust and Functional Vascular Networks In Vivo With Human Adult and Cord Blood–Derived Progenitor Cells

Juan M. Melero-Martin, Maria E. De Obaldia, Soo-Young Kang, Zia A. Khan, Lei Yuan, Peter Oettgen, Joyce Bischoff

***Abstract*—**The success of therapeutic vascularization and tissue engineering will rely on our ability to create vascular networks using human cells that can be obtained readily, can be expanded safely ex vivo, and can produce robust vasculogenic activity in vivo. Here we describe the formation of functional microvascular beds in immunodeficient mice by coimplantation of human endothelial and mesenchymal progenitor cells isolated from blood and bone marrow. Evaluation of implants after 1 week revealed an extensive network of human blood vessels containing erythrocytes, indicating the rapid formation of functional anastomoses within the host vasculature. The implanted endothelial progenitor cells were restricted to the luminal aspect of the vessels; mesenchymal progenitor cells were adjacent to lumens, confirming their role as perivascular cells. Importantly, the engineered vascular networks remained patent at 4 weeks in vivo. This rapid formation of long-lasting microvascular networks by postnatal progenitor cells obtained from noninvasive sources constitutes an important step forward in the development of clinical strategies for tissue vascularization. **(*Circ Res*. 2008;103:194-202.)**

Key Words: vascular networks ■ endothelial progenitor cells ■ mesenchymal stem cells ■ mesenchymal progenitor cells ■ tissue engineering ■ regenerative medicine ■ vasculogenesis ■ angiogenesis

Engineered tissues must have the capacity to generate a vascular network that rapidly forms anastomoses with the host vasculature to guarantee adequate nutrients, gas exchange, and elimination of waste products.[1] Presently, there are no tissue-engineered (TE) constructs clinically available with an inherent microvascular bed, and therefore successes have been restricted to the replacement of relatively thin (skin) or avascular (cartilage) tissues, where postimplantation vascularization from the host is sufficient.

To overcome the problem of vascularization, strategies to promote ingrowth of microvessels by delivery of angiogenic molecules have been proposed.[2–5] However, rapid and complete vascularization of thick engineered tissues is likely to require an additional process of vasculogenesis.[1,6] Toward this goal, the feasibility of engineering microvascular networks in vivo has been shown using human umbilical vein endothelial cells and human microvascular endothelial cells[7–9]; however, such autologous tissue-derived endothelial cells (ECs) present problems for wide clinical use, because they are difficult to obtain in sufficient quantities. These limitations have instigated the search for other sources of ECs, such as those derived from embryonic and adult stem and progenitor cells.[6] For instance, ECs derived from embryonic stem cells (ESCs) have been used to form blood vessels and to enhance the vascularization of engineered skeletal muscle constructs in vivo.[10,11] However, the mechanisms controlling ESCs differentiation must be understood, and ethical issues surrounding their use must be resolved before their implementation in therapeutic strategies.

The identification of endothelial progenitor cells (EPCs) in blood presented an opportunity to noninvasively obtain ECs.[12–14] We and other authors have shown that adult and cord blood–derived EPCs have the required vasculogenic capacity to form functional vascular networks in vivo.[15–17] Importantly, these studies have also shown that to obtain stable and durable vascular networks, EPCs require coimplantation with perivascular cells. In our previous work, the role of perivascular cells was undertaken by smooth muscle cells (SMCs) isolated from human saphenous veins.[15] In the work by Au et al, the mouse embryonic cell line 10T1/2 served as the perivascular component of the vascular networks.[16] However, neither source is suitable for clinical utilization: harvesting SMCs from healthy vasculature would impose serious morbidity in patients and murine-derived cell lines will not be used in humans. Therefore, to exploit the full vasculogenic potential of EPCs, we set out to establish

Original received April 29, 2008; revision received May 29, 2008; accepted May 30, 2008.

From the Vascular Biology Program and Department of Surgery, Children's Hospital Boston (J.M.M.-M., M.E.D.O., S.-Y.K., Z.A.K., J.B.); and Division of Cardiology, Beth Israel Deaconess Medical Center (L.Y., P.O.), Harvard Medical School, Boston Mass.

Correspondence to Dr Joyce Bischoff, Vascular Biology Program and Department of Surgery, Children's Hospital Boston, Harvard Medical School, Boston, MA 02115. E-mail joyce.bischoff@childrens.harvard.edu

Circulation Research **is available at http://circres.ahajournals.org** **DOI: 10.1161/CIRCRESAHA.108.178590**

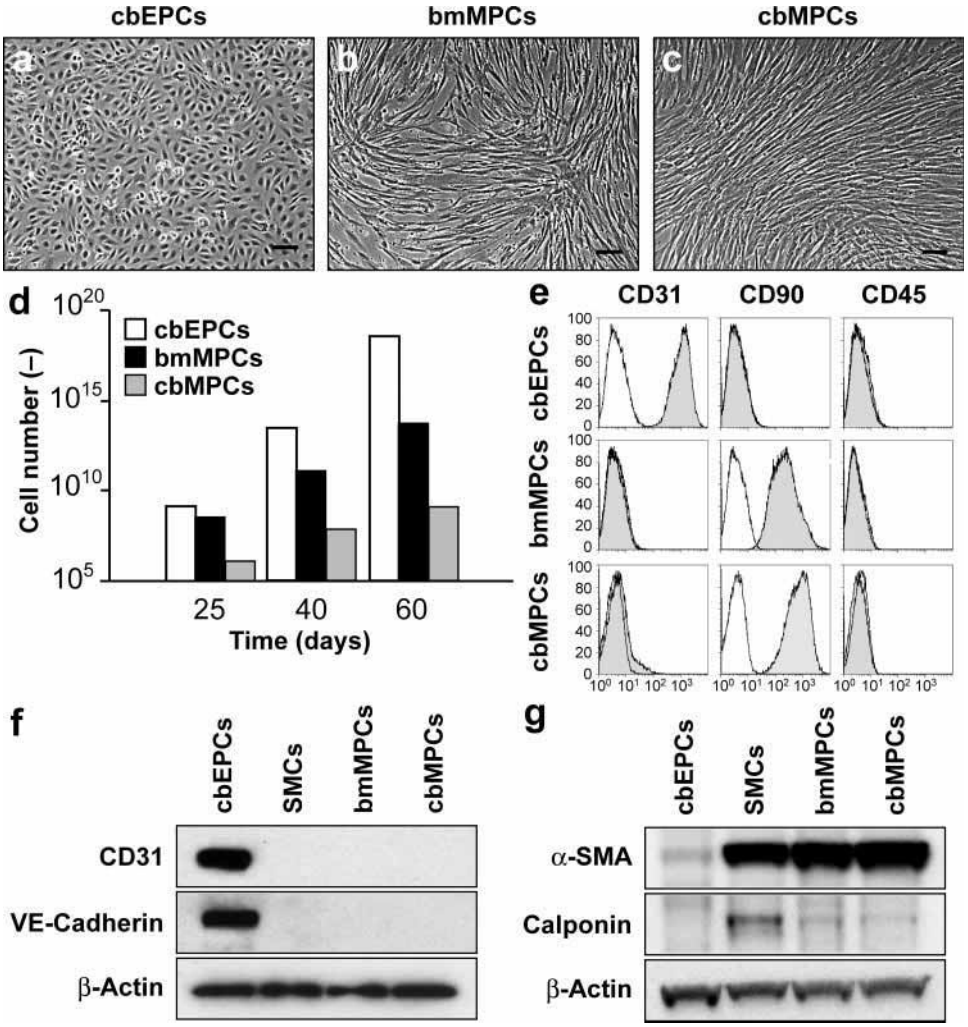

Figure 1. Phenotypic characterization of EPCs and MPCs. a through c, cbEPCs presented typical cobblestone morphology (a), whereas both bmMPCs (b) and cbMPCs (c) presented spindle morphology characteristic of mesenchymal cells in culture. Scale bars=100 μm. d, cbEPCs and MPCs were serially passaged and their in vitro expansion potential estimated by the accumulative cell numbers obtained from 25 mL of either cord blood or bone marrow samples. e, Flow cytometric analysis of cbEPCs, bmMPCs, and cbMPCs for the endothelial marker CD31, mesenchymal marker CD90, and hematopoietic marker CD45. Solid gray histograms represent cells stained with fluorescent antibodies. Isotype-matched controls are overlaid in a black line on each histogram. f and g, Western blot analyses of cbEPCs, bmMPCs, and cbMPCs for endothelial markers CD31 and VE-cadherin (f) and mesenchymal markers α-SMA and calponin (g). Expression of β-actin shows equal protein loading. SMCs isolated from human saphenous vein served as control.

clinically viable sources of perivascular cells. The ideal perivascular cells must present several key properties: (1) isolation with minimal donor site morbidity; (2) availability in sufficient quantities; and (3) immunologic compatibility with the recipients.[1] Mesenchymal stem/progenitor cells (herein referred to as MPCs)[18] meet these requirements. MPCs can be isolated by minimally invasive procedures from a diversity of human tissues, including bone marrow,[18] adult blood,[19] umbilical cord blood,[20–22] and adipose tissue.[23] Furthermore, MPCs undergo self-renewal and therefore can potentially be expanded to sufficient quantities for tissue and organ regeneration.[24]

Here, we demonstrate that MPCs obtained from both human adult bone marrow and human cord blood can serve as perivascular cells for in vivo vasculogenesis. Subcutaneous coimplantation of EPCs and MPCs, suspended as single cells in Matrigel, into immunodeficient mice resulted in the creation of extensive microvascular beds that rapidly formed anastomoses with the host vasculature. This study constitutes a step forward in the clinical development of therapeutic vasculogenesis by showing the feasibility of using human adult and cord blood–derived progenitor cells as the basic cellular building blocks to create functional vascular networks in vivo.

Materials and Methods

In Vivo Vasculogenesis Assay

The formation of vascular networks in vivo was evaluated using a xenograft model as described.[15] A total of 1.9×10^6 cells was resuspended in 200 μL of ice-cold Phenol Red-free Matrigel (BD Bioscience, San Jose, Calif), at ratios of 100:0, 80:20, 60:40, 40:60, 20:80, and 0:100 (EPCs:MPCs). The mixture was implanted on the back of a 6-week-old male athymic nu/nu mouse (Massachusetts General Hospital, Boston, Mass) by subcutaneous injection using a 25-gauge needle. Implants of Matrigel alone served as controls. One implant was injected per mouse. Each experimental condition was performed with 4 mice. Animal experiments were conducted under a protocol approved by the Institutional Animal Care and Use Committee at Children's Hospital Boston in an AAALAC-approved facility.

An expanded Materials and Methods section, available at http://circres.ahajournals.org, describes cell isolation and expansion, flow cytometry, Western blot analysis, differentiation assays, histology and immunohistochemistry, retroviral transduction, luciferase assay, microvessel density evaluation, and statistical analysis.

Results

Isolation of EPCs and MPCs

Cord blood–derived (cb)EPCs (Figure 1a) and adult blood (ab)EPCs were isolated from the mononuclear cells fraction of human blood samples and purified by CD31 selection as

described (see supplemental Figures I and XII in online the online data supplement for morphology of cbEPCs and abEPCs, respectively).[15] MPCs were isolated from the mononuclear cells fractions of human bone marrow samples (bmMPCs) and human cord blood samples (cbMPCs). bmMPCs adhered rapidly to the culture plates and proliferated until confluent, whereas cbMPCs emerged more slowly, forming mesenchymal-like colonies after one week (supplemental Figure I). cbMPC colonies were selected with cloning rings and expanded. Both bmMPCs (Figure 1b) and cbMPCs (Figure 1c) presented spindle morphology characteristic of mesenchymal cells in culture.[18]

cbEPCs and MPCs were grown in EPC medium and MPC medium, respectively, and their expansion potentials estimated by the cumulative cell numbers obtained from 25 mL of either cord blood or bone marrow samples after 25, 40, and 60 days in culture (Figure 1d). Remarkably, up to 10^{13} cbEPCs and 10^{11} bmMPCs were obtained after 40 days, consistent with previous studies.[13,15] The number of cells continued to increase so that at 60 days, there were an estimated 10^{18} cbEPCs and 10^{14} bmMPCs, respectively. In the case of cbMPCs, a longer culture period was necessary to obtain such numbers. The apparent decreased number of cbMPCs was likely attributable to the smaller number of MPCs in cord blood samples (typically 1 to 2 colonies per 25 mL; data not shown) as compared with bone marrow samples, where the majority of the adherent cells contributed to the final bmMPC population (supplemental Figure I).

The phenotype of the MPCs was confirmed by 3 methods. Flow cytometry (Figure 1e) showed that bmMPCs and cbMPCs uniformly expressed the mesenchymal marker CD90 and were negative for the endothelial marker CD31 and the hematopoietic marker CD45 (see further flow cytometric evaluations in supplemental Figure II). cbEPCs served as a control. Western blot analyses (Figure 1f and 1g) confirmed the mesenchymal phenotype of bmMPCs and cbMPCs (expression of α-smooth muscle actin [SMA] and calponin) and the endothelial phenotype of cbEPCs (expression of CD31 and VE-cadherin). These data were extended by indirect immunofluorescent staining (supplemental Figure III): bmMPCs and cbMPCs were shown to express the mesenchymal markers α-SMA, calponin, and NG_2 but not the EC markers CD31, VE-cadherin, and von Willebrand factor. Importantly, smooth muscle myosin heavy chain (smMHC), a specific marker of differentiated smooth muscle cells,[25,26] was found in mature SMCs but not in any of the MPCs.

The ability of MPCs to differentiate into multiple mesenchymal lineages was evaluated in vitro using well-established protocols.[18] Both bmMPCs and cbMPCs differentiated into osteocytes and chondrocytes, as shown by the expression of alkaline phosphatase (osteogenesis; Figure 2a and 2b) and glycosaminoglycan deposition in pellet cultures (chondrogenesis; Figure 2c and 2d), respectively (see also supplemental Figure IV). Adipogenesis was only evident with bmMPCs (Figure 2e) and not in cbMPCs (Figure 2f). This loss of adipogenic potential, reported for other mesenchymal cells in culture,[27,28] was attributed to the extensive expansion that these cells required because of their lower presence in cord

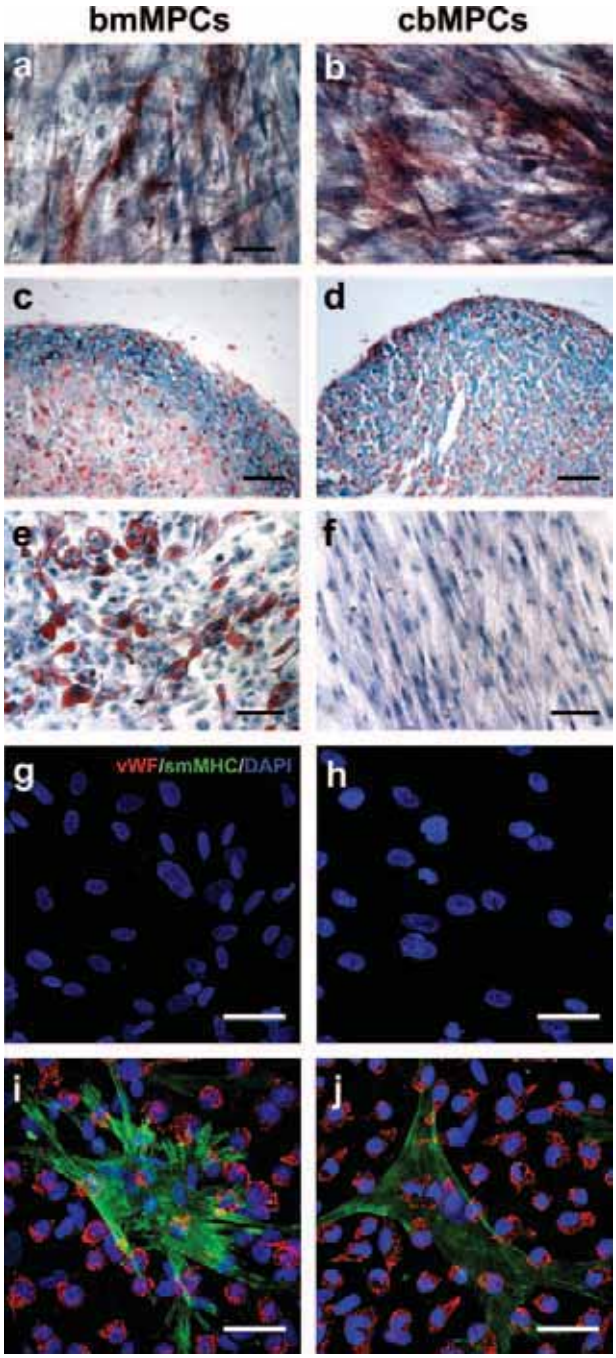

Figure 2. Multilineage differentiation of MPCs. a and b, bmMPC (a) and cbMPC (b) differentiation into osteocytes was revealed by alkaline phosphatase staining. c and d, bmMPC (c) and cbMPC (d) differentiation into chondrocytes was revealed by the presence of glycosaminoglycans, detected by Alcian blue staining. The presence of adipocytes was assessed by oil red O staining, and it was evident in bmMPCs (e) but absent in cbMPCs (f). Smooth muscle cell differentiation was evaluated by culturing MPCs in the absence or presence of cbEPCs (1:1 EPC-to-MPC ratio) for 7 days in EPC medium. Induction of SMC phenotype was assessed by the expression of smMHC. Immunofluorescence staining with anti–von Willebrand factor–Texas red and anti–smMHC-FITC, as well as nuclear staining with DAPI, revealed that smMHC was absent in both bmMPCs (g) and cbMPCs (h), but it was induced in MPCs when cocultured with cbEPCs (i and j). Scale bars correspond to 200 μm (e and f) and 50 μm (a through d and g through j).

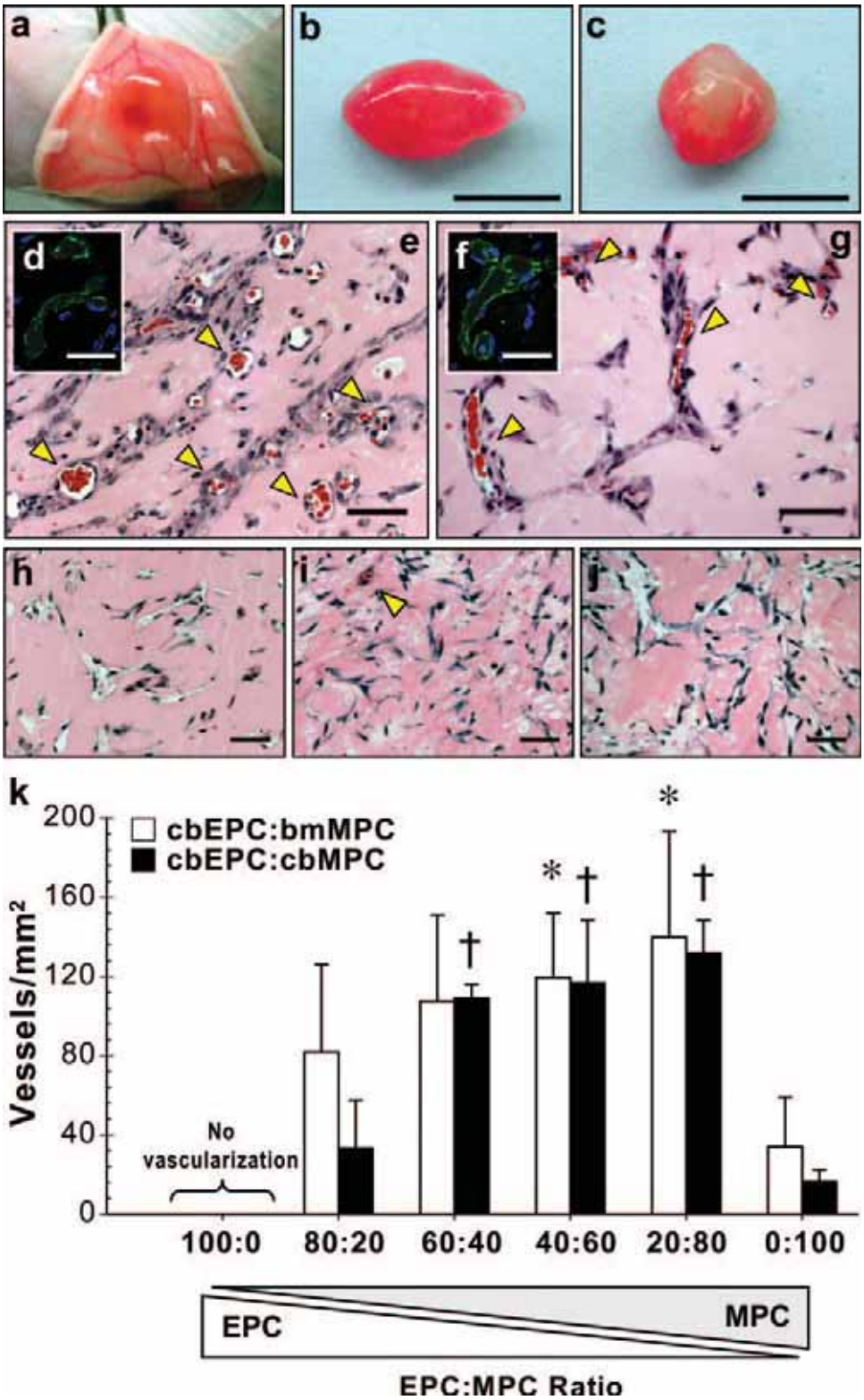

Figure 3. Formation of vascular networks in vivo with EPCs and MPCs. A total of 1.9×10^6 cells was resuspended in 200 μL of Matrigel using different ratios of cbEPCs and MPCs and implanted on the backs of 6-week-old nu/nu mice by subcutaneous injection. Implants were harvested after 7 days and stained with H&E. a through c, Macroscopic view of explanted Matrigel plugs seeded with 40% cbEPCs:60% bmMPCs (a and b) and 40% cbEPCs:60% cbMPCs (c). Scale bars=5 mm. e, g, and h through j, H&E staining revealed the presence of lumenal structures containing erythrocytes (yellow arrow heads) in implants where both cells types (cbEPCs and MPCs; 40:60) were used (e and g) but not in implants where cbEPCs (h), bmMPCs (i), and cbMPCs (j) were used alone. Scale bars=50 μm. d and f, Microvessels stained positive for human CD31. Scale bars=30 μm. Images are representative of implants harvested from at least 4 different mice. k, Quantification of microvessel density was performed by counting erythrocyte-filled vessels in implants with ratios of 100:0, 80:20, 60:40, 40:60, 20:80, and 0:100 (cbEPCs: MPCs; n≥4 each condition). Each bar represents the mean±SD (vessels/mm^2) obtained from vascularized implants. *$P<0.05$ compared with implants with bmMPCs alone (n=4); †$P<0.05$ compared with implants with cbMPCs alone (n=4).

blood samples (the earliest cbMPCs were tested for adipogenesis was at passage 5).

Because we intended to test MPCs as perivascular cells to engineer microvessel networks, we evaluated the ability of MPCs to differentiate toward a smooth muscle phenotype. As already shown, MPCs and mature SMCs shared a number of cellular markers including α-SMA, calponin, NG_2, and platelet-derived growth factor receptor-β (supplemental Figure V). Although the definitive smooth muscle cell marker smMHC was absent in MPCs (Figure 2g and 2h), both bmMPCs and cbMPCs were induced to express smMHC when directly cocultured with cbEPCs (Figure 2i and 2j). Importantly, induction did not occur when MPCs were indirectly cocultured with cbEPCs using a Transwell culture system (supple-

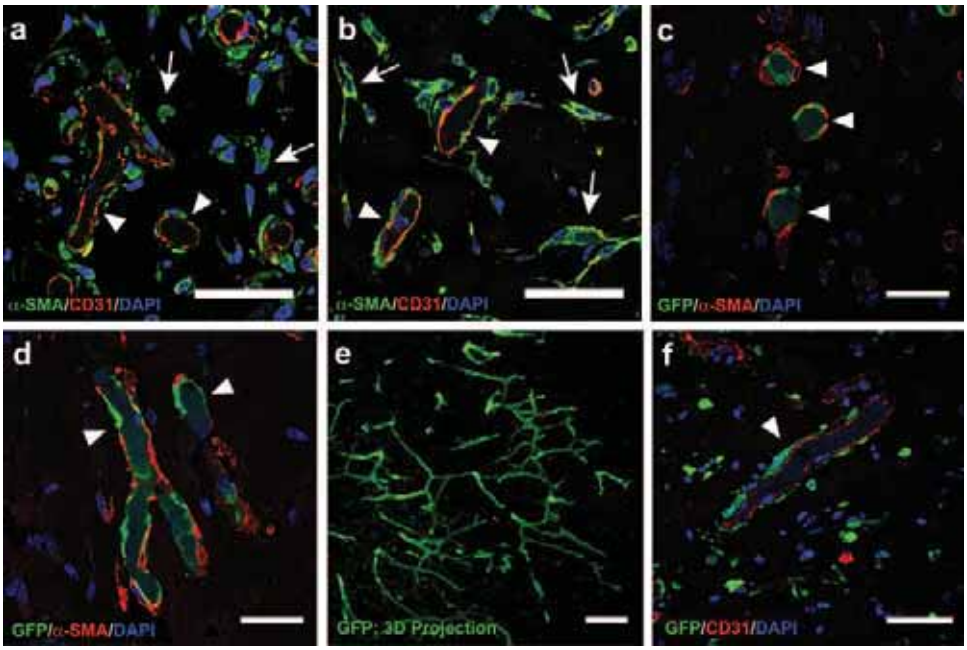

Figure 4. Specific location of EPCs and MPCs in the vascular bed. Matrigel implants containing cbEPCs and MPCs (40:60) were evaluated after 1 week. a and b, Implants with bmMPCs (a) and cbMPCs (b) produced lumenal structures that stained positive for human CD31, confirming that those lumens were formed by the implanted cells. In addition, α-SMA–expressing cells were detected both in the proximity (white arrows) and around the lumenal structures (white arrow heads). Scale bars=50 μm. c and d, Implants that used GFP-labeled cbEPC and either bmMPCs (c) or cbMPCs (d) produced GFP-positive lumenal structures (white arrow heads) covered by α-SMA–expressing perivascular cells, confirming that cbEPCs were restricted to the luminal aspect of the vessels. Scale bars=30 μm. e, Projections of whole-mount staining showed that the GFP-expressing cells formed extensive networks throughout the implants. Scale bar=100 μm. f, Implants that used GFP-labeled bmMPC and unlabeled cbEPCs resulted in human CD31-positive lumenal structures with GFP-expressing cells adjacent to lumens (white arrow heads), confirming the role of MPCs as perivascular cells. Scale bars=50 μm. Images are representative of implants harvested from 4 different mice.

mental Figure VI), consistent with previous reports that showed direct contact with ECs is required for mesenchymal cell differentiation into SMCs.[29,30]

In Vivo Formation of Human Vascular Networks

We have previously demonstrated the vasculogenic capacity of blood-derived EPCs both in vitro and in vivo.[15,31] In these studies, the presence of vascular smooth muscle cells was required for formation of vascular networks. To answer the question of whether MPCs could be used instead of SMCs, we implanted different combinations of cbEPCs and MPCs (either bmMPCs or cbMPCs) into nude mice for 1 week (Figure 3). A total of 1.9×10^6 cells was resuspended in 200 μL of Matrigel, using ratios of 100:0, 80:20, 60:40, 40:60, 20:80, and 0:100 (percentage of cbEPCs:percentage of MPCs) and injected subcutaneously. After harvesting the Matrigel implants (Figure 3a through 3c), hematoxylin/eosin (H&E) staining revealed numerous vessels containing erythrocytes in implants containing both cbEPCs and MPCs (Figure 3e and 3g). The structures stained positive for human CD31 (Figure 3d and 3f), confirming the lumens were lined by the implanted cells (the specificity of the antihuman CD31 antibody is shown in supplemental Figure IX). Implants of Matrigel alone were devoid of vessels (supplemental Figure VII), indicating the Matrigel itself was not responsible for the presence of vascular structures. As expected,[15] implants with cbEPCs alone (Figure 3h) failed to form microvessels. Implants with only MPCs (Figure 3i and 3j) presented infiltration of murine blood capillaries but no human microvessels (supplemental Figure IX). The ability of human MPCs to recruit murine vessels into Matrigel may be explained by the secretion of vascular endothelial growth factor (VEGF) from MPCs but not cbEPCs (supplemental Figure VIII).

Microvessel density was determined by quantification of lumens containing red blood cells (Figure 3k). The extent of the engineered vascular networks was influenced by the ratio of EPCs to MPCs (Figure 3k). A progressive increase in MPCs resulted in increased microvessel density and more consistent vascularization (supplemental Table I). When the ratio of EPC:MPC was 40:60, an average density of 119 ± 33 and 117 ± 32 vessels/mm^2 with bmMPCs or cbMPCs, respectively, was achieved in all implants. These densities were significantly higher ($P<0.05$) than those observed with MPCs alone, reaffirming the necessity of the endothelial component for the formation of human vessels in the implants.

Assembly of Endothelial and Mesenchymal Progenitor Cells in the Vascular Bed

In addition to the human CD31-positive lumenal structures, the engineered vessels were characterized by α-SMA staining of perivascular cells (Figure 4a and 4b). With bmMPCs or cbMPCs, α-SMA–positive cells were detected both in proximity and adjacent to lumenal structures, suggesting an ongoing process of perivascular cell recruitment during vessel maturation.[32–34] To determine more precisely the contribution of each cell type, we implanted green fluorescent protein (GFP)-labeled cbEPCs with unlabeled MPCs. Anti-GFP staining showed cbEPCs restricted to lumenal positions in the microvessel networks, whereas anti–α-SMA staining showed that the GFP-labeled vessels were covered by perivascular cells; this observation was valid with both sources of MPCs (Figure 4c and 4d). Projections of whole-mount staining showed that the GFP-expressing cells formed

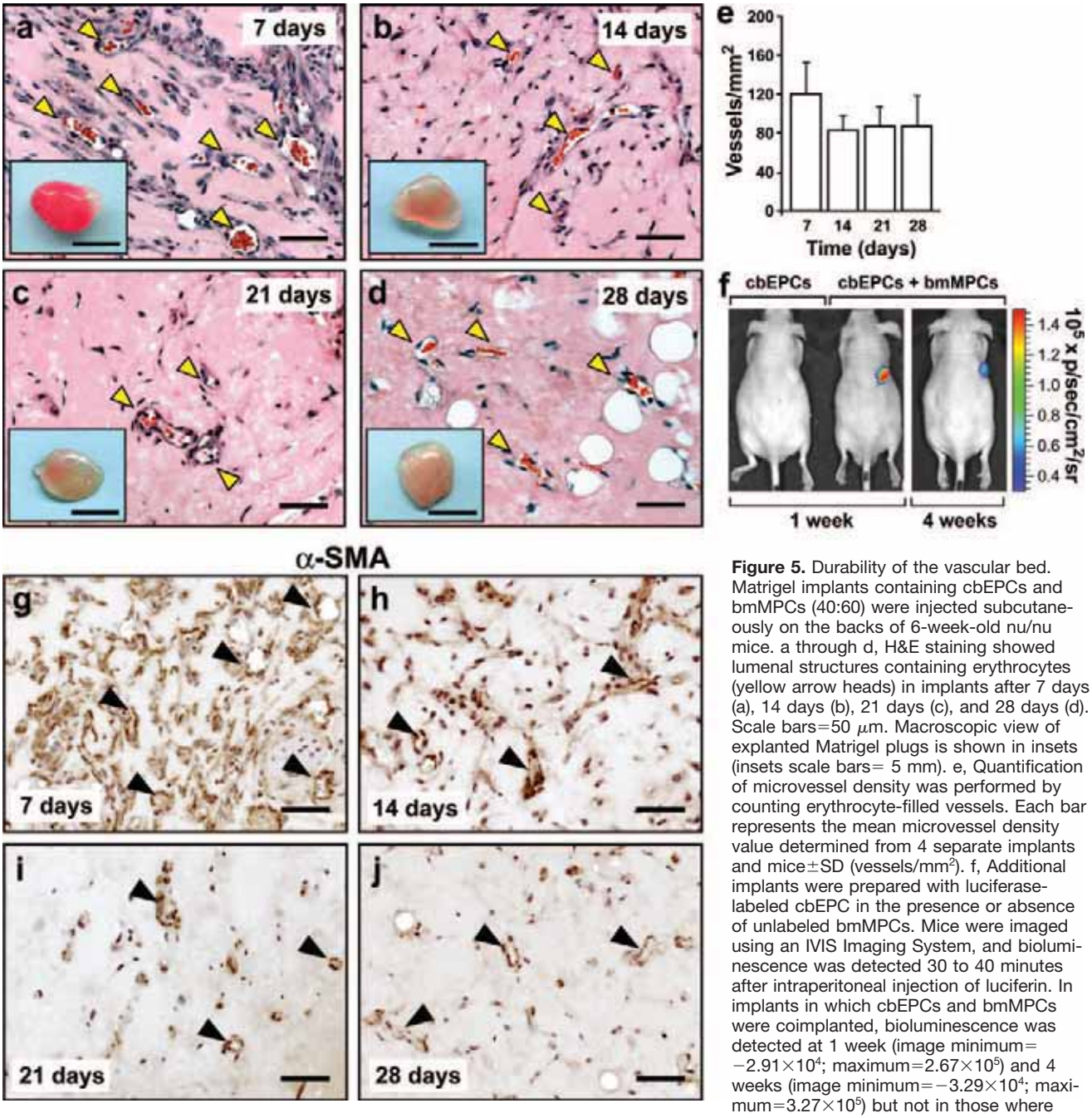

Figure 5. Durability of the vascular bed. Matrigel implants containing cbEPCs and bmMPCs (40:60) were injected subcutaneously on the backs of 6-week-old nu/nu mice. a through d, H&E staining showed lumenal structures containing erythrocytes (yellow arrow heads) in implants after 7 days (a), 14 days (b), 21 days (c), and 28 days (d). Scale bars=50 μm. Macroscopic view of explanted Matrigel plugs is shown in insets (insets scale bars= 5 mm). e, Quantification of microvessel density was performed by counting erythrocyte-filled vessels. Each bar represents the mean microvessel density value determined from 4 separate implants and mice±SD (vessels/mm^2). f, Additional implants were prepared with luciferase-labeled cbEPC in the presence or absence of unlabeled bmMPCs. Mice were imaged using an IVIS Imaging System, and bioluminescence was detected 30 to 40 minutes after intraperitoneal injection of luciferin. In implants in which cbEPCs and bmMPCs were coimplanted, bioluminescence was detected at 1 week (image minimum=-2.91×10^4; maximum=2.67×10^5) and 4 weeks (image minimum=-3.29×10^4; maximum=3.27×10^5) but not in those where cbEPCs were used alone. g through j, Immunohistochemical staining of α-SMA in implants after 7 days (g), 14 days (h), 21 days (i), and 28 days (j) revealed that α-SMA–expressing cells were progressively restricted to perivascular locations (black arrow heads). Scale bars=50 μm. Images are representative of implants harvested from 4 different mice.

extensive networks throughout the implants (Figure 4e). Conversely, we implanted GFP-labeled bmMPCs with unlabeled cbEPCs to identify input MPCs without relying on anti–α-SMA. Sections were stained with anti-GFP and anti-CD31 antibodies: GFP-expressing cells were detected as perivascular cells surrounding human CD31$^+$ lumens and as individual cells dispersed throughout the Matrigel implants (Figure 4f).

Durability of the Vascular Bed

To test the durability of the engineered vascular beds in vivo, we evaluated implants of cbEPCs/bmMPCs (40:60) at 7, 14, 21, and 28 days after xenografting (Figure 5). H&E staining revealed the presence of lumenal structures containing erythrocytes in all implants at each time point (Figure 5a through 5d). Microvessel quantification (Figure 5e) revealed an initial reduction (statistically nonsignificant; $P=0.105$) in the number of patent blood vessels from 119±33 vessels/mm^2 at day 7 to 83±16 vessels/mm^2 at day 14. Microvessel densities remained stable thereafter (87±21 and 87±32 vessels/mm^2 at days 21 and 28, respectively).

To further evaluate the engineered vascular bed, we used a luciferase-based imaging system to monitor perfusion of the Matrigel implants. cbEPCs were infected with lentivirus-associated vector encoding luciferase and implanted into

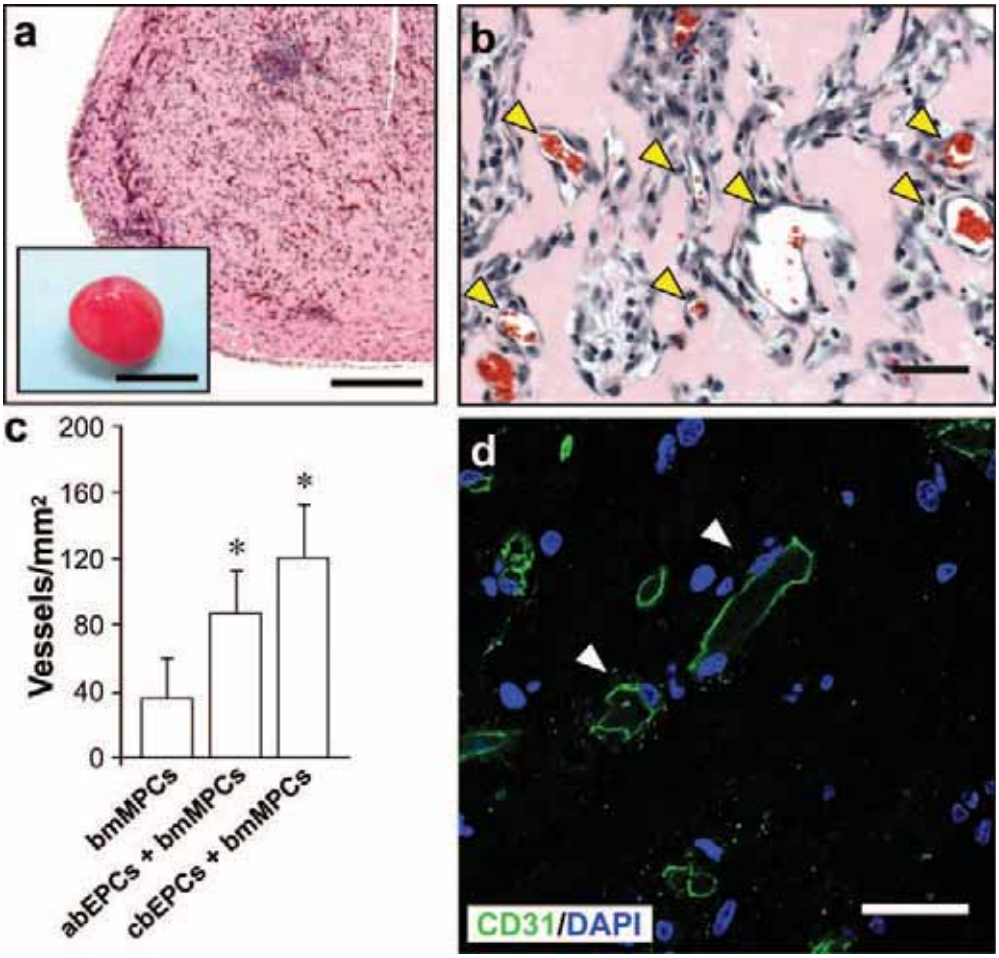

Figure 6. Vascular network formation using adult progenitor cells. Matrigel implants containing 40% abEPCs and 60% bmMPCs (obtained from human adult peripheral blood and adult bone marrow samples, respectively) were injected subcutaneously on the backs of 6-week-old nu/nu mice and evaluated after 1 week. a and b, H&E staining showed a uniform and extensive presence of lumenal structures containing erythrocytes (yellow arrowheads in b) throughout the implants. Scale bar in a, 500 μm; macroscopic view of explanted Matrigel plug is shown in the inset in a (scale bar=5 mm). Scale bar in b, 50 μm. c, Quantification of microvessel density was performed in implants seeded with bmMPCs in the absence or presence of either abEPCs or cbEPCs by counting erythrocyte-filled vessels. Each bar represents the mean microvessel density determined from 4 separate implants and mice±SD (vessels/mm^2). *$P<0.05$ compared with implants with bmMPCs alone (n=4). d, Microvessels from implants containing 40% abEPCs and 60% bmMPCs stained positive for human CD31 (white arrow heads), confirming that those lumens were formed by the implanted cells. Scale bar=30 μm. Images are representative of implants harvested from 4 different mice.

immunodeficient mice in the presence or absence of bmMPCs. At 1 and 4 weeks, mice were given the substrate luciferin by intraperitoneal injection (Figure 5f). No bioluminescence was detected in implants with luciferase-expressing cbEPCs alone, indicating that the substrate did not diffuse into the Matrigel. In contrast, a strong bioluminescent signal was detected in xenografts in which bmMPCs were coimplanted. This result, coupled with parallel histological data, confirmed that the presence of MPCs was crucial to achieve rapid perfusion of the implants. Importantly, the luciferase-dependent signal was still detected 4 weeks after implantation, a further indication of the long-lasting nature of the engineered vessels.

The cells within the Matrigel implants appeared to undergo a process of in vivo remodeling characterized by stabilization of total cellularity (supplemental Figure X) and progressive restriction of α-SMA–expressing cells to perivascular locations (Figure 5g through 5j), as expected in normal stabilized vasculature.[34] Finally, after 28 days in vivo, adipocytes were identified by staining with an anti-perilipin antibody (supplemental Figure XI), suggesting a process of integration between the implants and the surrounding murine adipose tissue.[35]

Vascular Network Formation Using Adult Progenitor Cells

We previously showed that adult peripheral blood–derived EPCs (abEPCs) combined with mature SMCs at a ratio of 4:1 (EPCs:SMCs) are vasculogenic in vivo, yet required higher seeding densities to achieve microvessel densities similar to that obtained with cbEPCs.[15] This apparently lower vasculogenic capacity of abEPCs has been suggested recently by others.[16] We hypothesized that the combination of adult bmMPCs and abEPCs at an "optimized ratio" (Figure 3k) would yield a high density vascular network. Indeed, there are no previous reports on adult human bmMPCs and abEPCs in the context of in vivo vasculogenesis. To evaluate this interaction, we isolated abEPCs as described[13–15] and confirmed their endothelial phenotype (supplemental Figure XII).

We implanted a total of 1.9×10^6 cells (40% abEPCs and 60% bmMPCs) in Matrigel by subcutaneous injection into immunodeficient mice (Figure 6). After harvesting the implants at 7 days (n=4), H&E staining consistently showed an extensive presence of blood vessels containing erythrocytes (Figure 6a and 6b). In addition, the lumenal structures stained positive for human CD31 (Figure 6d), confirming the lumens were formed by the implanted human abEPCs. Quantification of microvessel density (Figure 6c) revealed that the use of 40% abEPCs resulted in a statistically significant ($P<0.05$) increase in the number of blood vessels (86±26 vessels/mm^2) as compared with implants with bmMPCs alone (34±25 vessels/mm^2). Moreover, the difference between implants composed of abEPCs:bmMPCs and those of cbEPCs:

bmMPCs (119±33 vessels/mm^2) was not statistically significant (P=0.158), indicating that the presence of bmMPCs supported the vasculogenic properties of abEPCs to the same extent as was achieved with cbEPCs. These results show that a 2-cell system composed of human adult EPCs and MPCs exhibit the same robust in vivo vasculogenic activity as cbEPCs combined with adult bmMPCs, which is in contrast to conclusions drawn from experiments reported by others using a murine 10T1/2 cell line.[16]

Discussion

Here, we show that human postnatal EPCs and MPCs isolated from either blood or bone marrow have an inherent vasculogenic ability that can be exploited to create functional microvascular networks in vivo. Using Matrigel as a supporting scaffold,[15] we have shown that coimplantation of EPCs with either bmMPCs or cbMPCs into immunodeficient mice resulted in formation of extensive vascular networks after 1 week. The presence of human EPC-lined lumens containing erythrocytes (>100 vessels/mm^2) throughout the implants indicated not only a process of vasculogenesis from the 2 cell types but also the formation of functional anastomoses with the host circulatory system. In addition, MPCs were shown to reside in perivascular locations around the engineered lumens, confirming their active participation in blood vessel assembly. In vitro, MPCs were shown to differentiate into smMHC-positive cells when cocultured with EPCs, an indication that the MPCs achieved a mature smooth muscle phenotype. In a recent report, human mesenchymal stem cells combined with human umbilical vein ECs were shown to facilitate blood vessel assembly and adopt a perivascular location,[36] but our study differs from this report in that we show EPCs from either adult or cord blood, combined with MPCs from adult bone marrow or cord blood, form robust vascular networks in vivo. The extent of the engineered vascular networks was highly influenced by the ratio of EPCs to MPCs, with a progressive increase in vessel density and consistency of vascularized implants achieved when the contribution of MPCs was raised to 60% (Figure 3). This was true for both abEPCs and cbEPCs (Figure 6), demonstrating that both cord blood and adult peripheral blood are excellent sources of ECs for tissue vascularization.

Previous studies suggested the possibility of using mature ECs derived from vascular tissue to create microvascular networks.[7–9,37] However, the clinical use of mature ECs derived from autologous vascular tissue is limited by the difficulty of obtaining sufficient quantities of cells with minimal donor site morbidity.[1] Human ESCs have unlimited expansion capacity, but the therapeutic use of ESCs-derived ECs remains years away from the clinic. Most of these hurdles would be resolved if postnatal progenitor cells with expansion and functional potential were available from individual patients or from dedicated cell banks. In this regard, the in vitro expansion of blood-derived EPCs[12–15] and the recent confirmation of their ability to form vascular networks in vivo[15–17] have constituted major steps forward to resolve the problem of EC sourcing for therapeutic vasculogenesis.

Importantly, these studies have also shown that to produce high density and stable vascular networks, EPCs require coimplantation with perivascular cells. This is consistent with the literature showing interactions between ECs and perivascular cells in the blood vessel wall are critical for normal vascular development.[32–34] In previous attempts to create vascular networks with blood-derived EPCs, either mature SMCs[15] or the mouse embryonic cell line 10T1/2[16] were used to serve as perivascular cells; however, neither source is suitable for clinical application. Therefore, identification of MPCs as a readily obtainable perivascular cell source to partner in vivo with EPCs constitutes a crucial step in the development of therapeutic vasculogenesis. The numbers of human MPCs we were able to obtain in this study are likely to exceed, in the case of bone marrow, and be sufficient, in the case of cord blood, what would be needed for most autologous regenerative therapies.

This study has shown that successful in vivo vascularization depends on several distinct cellular functions. Firstly, both EPCs and MPCs must be present to initiate vasculogenesis, a process that was characterized by the formation of lumenal structures composed of human EPCs surrounded by α-SMA–positive mesenchymal cells. Secondly, an angiogenic response from the host vasculature is needed so that host vessels will be available to form anastomoses with the nascent vasculature. In this regard, we propose that the implanted MPCs stimulated the host angiogenic response. This is based on (1) the ability of bmMPCs alone to recruit murine vessels into the Matrigel implant and (2) the secretion of VEGF from MPCs in vitro (supplemental Figure VIII). EPCs did not secrete VEGF and did not stimulate murine vessel infiltration. Vascularization is achieved when the angiogenic and vasculogenic blood vessels meet, form anastomoses, and establish perfusion of the implants. The fact that perfusion occurred was supported by the presence of erythrocytes within the newly formed vasculature and the delivery of luciferin substrate from the peritoneal cavity to Matrigel implants containing both cbEPCs and bmMPCs. Subsequently, a process reminiscent of in vivo remodeling, characterized by a progressive restriction of α-SMA–expressing cells to perivascular locations, was seen, suggesting a stabilized vasculature.[34] Whether factors secreted or presented by MPCs contribute to such stabilization would be important to elucidate in a future study. Finally, our engineered vascular networks were patent for up to 4 weeks in vivo, confirming the capacity of EPC/MPC-derived vasculature to remain stable and functional.[16]

In summary, we have demonstrated the feasibility of engineering vascular networks in vivo with human postnatal progenitor cells that can be obtained by noninvasive procedures. In addition, we suggest that this murine model of human vasculogenesis is ideally suited for future studies on the cellular and molecular components of microvessel development and pathological neovascular responses and for the development of strategies to enhance neovascularization of engineered human tissues and organs. Further efforts are required to implement these vascularization strategies into tissue regeneration and tissue engineering applications.

Acknowledgments

We thank Dr Joseph C. Wu (Department of Radiology and Molecular Imaging Program, Stanford University School of Medicine,

Calif) for providing the pUb-fluc-GFP construct, Dr Masanori Aikawa (Brigham and Women's Hospital) for providing SMCs, Elke Pravda for confocal microscopy, Sandra R. Smith for VEGF analysis, Jill Wylie-Sears for technical assistance, and Kristin Johnson for figure preparation.

Sources of Funding

This work was supported by US Army Medical Research and Material Command (W81XWH-05-1-0115).

Disclosures

None.

References

1. Jain RK, Au P, Tam J, Duda DG, Fukumura D. Engineering vascularized tissue. *Nat Biotechnol*. 2005;23:821–823.
2. Isner JM, Asahara T. Angiogenesis and vasculogenesis as therapeutic strategies for postnatal neovascularization. *J Clin Invest*. 1999;103:1231–1236.
3. Isner JM, Pieczek A, Schainfeld R, Blair R, Haley L, Asahara T, Rosenfield K, Razvi S, Walsh K, Symes JF. Clinical evidence of angiogenesis after arterial gene transfer of phVEGF165 in patient with ischaemic limb. *Lancet*. 1996;348:370–374.
4. Lee H, Cusick RA, Browne F, Ho Kim T, Ma PX, Utsunomiya H, Langer R, Vacanti JP. Local delivery of basic fibroblast growth factor increases both angiogenesis and engraftment of hepatocytes in tissue-engineered polymer devices. *Transplantation*. 2002;73:1589–1593.
5. Li X, Tjwa M, Moons L, Fons P, Noel A, Ny A, Zhou JM, Lennartsson J, Li H, Luttun A, Ponten A, Devy L, Bouche A, Oh H, Manderveld A, Blacher S, Communi D, Savi P, Bono F, Dewerchin M, Foidart JM, Autiero M, Herbert JM, Collen D, Heldin CH, Eriksson U, Carmeliet P. Revascularization of ischemic tissues by PDGF-CC via effects on endothelial cells and their progenitors. *J Clin Invest*. 2005;115:118–127.
6. Rafii S, Lyden D. Therapeutic stem and progenitor cell transplantation for organ vascularization and regeneration. *Nat Med*. 2003;9:702–712.
7. Koike N, Fukumura D, Gralla O, Au P, Schechner JS, Jain RK. Tissue engineering: creation of long-lasting blood vessels. *Nature*. 2004;428:138–139.
8. Nor JE, Peters MC, Christensen JB, Sutorik MM, Linn S, Khan MK, Addison CL, Mooney DJ, Polverini PJ. Engineering and characterization of functional human microvessels in immunodeficient mice. *Lab Invest*. 2001;81:453–463.
9. Schechner JS, Nath AK, Zheng L, Kluger MS, Hughes CC, Sierra-Honigmann MR, Lorber MI, Tellides G, Kashgarian M, Bothwell AL, Pober JS. In vivo formation of complex microvessels lined by human endothelial cells in an immunodeficient mouse. *Proc Natl Acad Sci U S A*. 2000;97:9191–9196.
10. Levenberg S, Rouwkema J, Macdonald M, Garfein ES, Kohane DS, Darland DC, Marini R, van Blitterswijk CA, Mulligan RC, D'Amore PA, Langer R. Engineering vascularized skeletal muscle tissue. *Nat Biotechnol*. 2005;23:879–884.
11. Wang ZZ, Au P, Chen T, Shao Y, Daheron LM, Bai H, Arzigian M, Fukumura D, Jain RK, Scadden DT. Endothelial cells derived from human embryonic stem cells form durable blood vessels in vivo. *Nat Biotechnol*. 2007;25:317–318.
12. Asahara T, Murohara T, Sullivan A, Silver M, van der Zee R, Li T, Witzenbichler B, Schatteman G, Isner JM. Isolation of putative progenitor endothelial cells for angiogenesis. *Science*. 1997;275:964–967.
13. Ingram DA, Mead LE, Tanaka H, Meade V, Fenoglio A, Mortell K, Pollok K, Ferkowicz MJ, Gilley D, Yoder MC. Identification of a novel hierarchy of endothelial progenitor cells using human peripheral and umbilical cord blood. *Blood*. 2004;104:2752–2760.
14. Lin Y, Weisdorf DJ, Solovey A, Hebbel RP. Origins of circulating endothelial cells and endothelial outgrowth from blood. *J Clin Invest*. 2000;105:71–77.
15. Melero-Martin JM, Khan ZA, Picard A, Wu X, Paruchuri S, Bischoff J. In vivo vasculogenic potential of human blood-derived endothelial progenitor cells. *Blood*. 2007;109:4761–4768.
16. Au P, Daheron LM, Duda DG, Cohen KS, Tyrrell JA, Lanning RM, Fukumura D, Scadden DT, Jain RK. Differential in vivo potential of endothelial progenitor cells from human umbilical cord blood and adult peripheral blood to form functional long-lasting vessels. *Blood*. 2008;111:1302–1305.
17. Yoder MC, Mead LE, Prater D, Krier TR, Mroueh KN, Li F, Krasich R, Temm CJ, Prchal JT, Ingram DA. Redefining endothelial progenitor cells via clonal analysis and hematopoietic stem/progenitor cell principals. *Blood*. 2007;109:1801–1809.
18. Pittenger MF, Mackay AM, Beck SC, Jaiswal RK, Douglas R, Mosca JD, Moorman MA, Simonetti DW, Craig S, Marshak DR. Multilineage potential of adult human mesenchymal stem cells. *Science*. 1999;284:143–147.
19. Simper D, Stalboerger PG, Panetta CJ, Wang S, Caplice NM. Smooth muscle progenitor cells in human blood. *Circulation*. 2002;106:1199–1204.
20. Kim JW, Kim SY, Park SY, Kim YM, Kim JM, Lee MH, Ryu HM. Mesenchymal progenitor cells in the human umbilical cord. *Ann Hematol*. 2004;83:733–738.
21. Le Ricousse-Roussanne S, Barateau V, Contreres JO, Boval B, Kraus-Berthier L, Tobelem G. Ex vivo differentiated endothelial and smooth muscle cells from human cord blood progenitors home to the angiogenic tumor vasculature. *Cardiovasc Res*. 2004;62:176–184.
22. Lee OK, Kuo TK, Chen WM, Lee KD, Hsieh SL, Chen TH. Isolation of multipotent mesenchymal stem cells from umbilical cord blood. *Blood*. 2004;103:1669–1675.
23. Traktuev D, Merfeld-Clauss S, Li J, Kolonin M, Arap W, Pasqualini R, Johnstone BH, March KL. A population of multipotent CD34-positive adipose stromal cells share pericyte and mesenchymal surface markers, reside in a periendothelial location, and stabilize endothelial networks. *Circ Res*. 2008;102:77–85.
24. Marion NW, Mao JJ. Mesenchymal stem cells and tissue engineering. *Methods Enzymol*. 2006;420:339–361.
25. Madsen CS, Regan CP, Hungerford JE, White SL, Manabe I, Owens GK. Smooth muscle-specific expression of the smooth muscle myosin heavy chain gene in transgenic mice requires 5′-flanking and first intronic DNA sequence. *Circ Res*. 1998;82:908–917.
26. Miano JM, Cserjesi P, Ligon KL, Periasamy M, Olson EN. Smooth muscle myosin heavy chain exclusively marks the smooth muscle lineage during mouse embryogenesis. *Circ Res*. 1994;75:803–812.
27. Digirolamo CM, Stokes D, Colter D, Phinney DG, Class R, Prockop DJ. Propagation and senescence of human marrow stromal cells in culture: a simple colony-forming assay identifies samples with the greatest potential to propagate and differentiate. *Br J Haematol*. 1999;107:275–281.
28. Wall ME, Bernacki SH, Loboa EG. Effects of serial passaging on the adipogenic and osteogenic differentiation potential of adipose-derived human mesenchymal stem cells. *Tissue Eng*. 2007;13:1291–1298.
29. Antonelli-Orlidge A, Saunders KB, Smith SR, D'Amore PA. An activated form of transforming growth factor beta is produced by cocultures of endothelial cells and pericytes. *Proc Natl Acad Sci U S A*. 1989;86:4544–4548.
30. Hirschi KK, Rohovsky SA, D'Amore PA. PDGF, TGF-beta, and heterotypic cell-cell interactions mediate endothelial cell-induced recruitment of 10T1/2 cells and their differentiation to a smooth muscle fate. *J Cell Biol*. 1998;141:805–814.
31. Wu X, Rabkin-Aikawa E, Guleserian KJ, Perry TE, Masuda Y, Sutherland FW, Schoen FJ, Mayer JE Jr, Bischoff J. Tissue-engineered microvessels on three-dimensional biodegradable scaffolds using human endothelial progenitor cells. *Am J Physiol Heart Circ Physiol*. 2004;287:H480–H487.
32. Darland DC, D'Amore PA. Blood vessel maturation: vascular development comes of age. *J Clin Invest*. 1999;103:157–158.
33. Folkman J, D'Amore PA. Blood vessel formation: what is its molecular basis? *Cell*. 1996;87:1153–1155.
34. Jain RK. Molecular regulation of vessel maturation. *Nat Med*. 2003;9:685–693.
35. Fukumura D, Ushiyama A, Duda DG, Xu L, Tam J, Krishna V, Chatterjee K, Garkavtsev I, Jain RK. Paracrine regulation of angiogenesis and adipocyte differentiation during in vivo adipogenesis. *Circ Res*. 2003;93:e88–e97.
36. Au P, Tam J, Fukumura D, Jain RK. Bone marrow derived mesenchymal stem cells facilitate engineering of long-lasting functional vasculature. *Blood*. 2008;111:4551–4558.
37. Shepherd BR, Chen HY, Smith CM, Gruionu G, Williams SK, Hoying JB. Rapid perfusion and network remodeling in a microvascular construct after implantation. *Arterioscler Thromb Vasc Biol*. 2004;24:898–904.

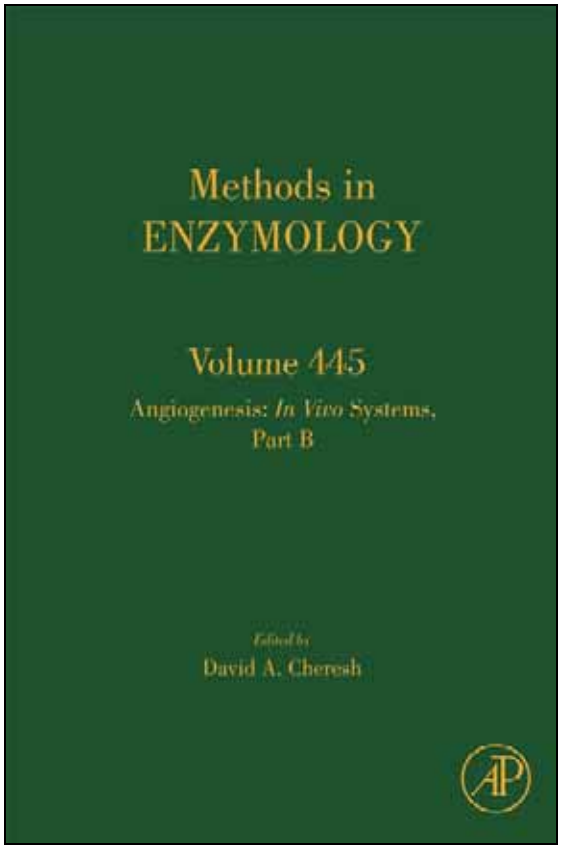

From: Juan M. Melero-Martin and Joyce Bischoff, An *In Vivo* Experimental Model for Postnatal Vasculogenesis.
In David A. Cheresh, editor, Methods in Enzymology, Vol 445,
Burlington: Academic Press, 2008, pp.303-329.
ISBN: 978-0-12-374314-5

CHAPTER THIRTEEN

An *In Vivo* Experimental Model for Postnatal Vasculogenesis

Juan M. Melero-Martin *and* Joyce Bischoff

Contents

Abstract

Rapid and complete vascularization of ischemic tissues and thick engineered tissues is likely to require vasculogenesis. Therefore, the search for clinically relevant sources of vasculogenic cells and the subsequent development of experimental models of vasculogenesis is of utmost importance. Here, we describe a methodology adapted from the Matrigel plug assay to deliver human blood–derived endothelial progenitor cells (EPCs) and mature smooth muscle cells (SMCs) subcutaneously into immunodeficient mice. One week after

Vascular Biology Program and Department of Surgery, Children's Hospital, Boston, Harvard Medical School, Boston, Massachusetts

Methods in Enzymology, Volume 445
ISSN 0076-6879, DOI: 10.1016/S0076-6879(08)03013-9

implantation, an extensive microvascular network composed of the human EPCs and SMCs is formed within the Matrigel. The presence of human EPC-lined lumens containing host erythrocytes can be seen throughout the implants indicating not only the formation (*de novo*) of a vascular network, but also the development of functional anastomoses with the host circulatory system. This is a very versatile assay that allows (1) dialing the final microvessel density by varying either the total number of cells in the original cell suspension or the ratio between EPCs and SMCs, (2) studying the effect of substituting another type of perivascular cell for mature SMCs or another type of endothelial cell, (3) tracking each of the implanted cell types by labeling (e.g., GFP tagging) prior to implantation, and (4) studying the effect of genetically modifying the cells prior to implantation. Additionally, this assay is relatively simple to perform and it does not require an incision or surgical procedure. This murine model of human vasculogenesis is ideally suited for studies on the cellular and molecular components of microvessel development, pathologic neovascular responses, and for the development and investigation of strategies to enhance neovascularization of engineered human tissues and organs.

1. Introduction

Current strategies to generate vascular networks *in vivo* are based on our understanding of the mechanisms of blood vessel formation. During embryogenesis, blood vessels are first formed *de novo* by the patterned assembly of angioblasts in a process termed ''vasculogenesis'' (Cleaver and Melton, 2003; Flamme *et al.*, 1997; Risau and Flamme, 1995). Thereafter, the formation of new blood vessels occurs primarily via the sprouting of endothelial cells (ECs) from pre-existing vasculature (angiogenesis) (Carmeliet, 2003; Conway *et al.*, 2001; Risau, 1997). After birth and during adulthood, the formation of new blood vessels occurs mainly through angiogenesis in a tightly controlled process where EC proliferation and migration are regulated by secreted cytokines, surrounding cells, and extracellular matrix (Carmeliet, 2003; Risau, 1997). Postnatal vasculogenesis involves the recruitment of endothelial progenitor cells (EPCs) as well as an intricate collaboration with hematopoietic cells (De Palma *et al.*, 2005; Grunewald *et al.*, 2006; Yoder *et al.*, 2007). While EPC-derived ECs line the vessel lumen, accessory cells support vessel formation through secretion of cytokines and alteration of the extracellular matrix (Carmeliet, 2003; Hiraoka *et al.*, 1998; Stetler-Stevenson, 1999; Zentilin *et al.*, 2006). Dysregulated angiogenesis and vasculogenesis have been implicated in the pathogenesis of numerous diseases including vascular retinopathies, rheumatoid arthritis, vascular tumors such as infantile hemangioma, and cancer (Folkman, 1995).

Our understanding of angiogenesis as a mechanism of blood vessel formation has evolved, in part, from numerous experimental assays that recapitulate the multistep angiogenic processes (Carmeliet, 2003; Carmeliet and Jain, 2000; Folkman, 1995, 2007; Risau, 1997). These include *in vitro* assays for endothelial proliferation, migration and capillary morphogenesis and *in vivo* assays such as the corneal micropocket assay (Gimbrone *et al.*, 1974), the chick chorioallantoic membrane (CAM) assay (Auerbach *et al.*, 1974; Ausprunk *et al.*, 1974, 1975; Folkman, 1974), and the Matrigel plug assay (Passaniti *et al.*, 1992), among other models (for review, see Norrby, 2006). Angiogenesis in these *in vivo* models is driven by exogenously added factors or relies on ongoing developmental processes, as is the case in the CAM assay. In some sense, the corneal micropocket and the Matrigel plug assays model regenerative processes in that angiogenesis, an essential component of tissue regeneration, is promoted by the growth of new blood vessels toward an angiogenic signal or factor (Isner and Asahara, 1999; Isner *et al.*, 1996; Lee *et al.*, 2002; Li *et al.*, 2005).

The mechanisms governing vasculogenesis are studied primarily during embryonic development in several model organisms and in murine embryonic stem-cell–derived embryoid bodies *in vitro*. Experimental models for postnatal vasculogenesis are less numerous. However, there is extensive interest in postnatal vasculogenesis because of the potential application(s) in tissue-engineering and regenerative therapies. One approach that stimulated our thinking was the work of Schechner and colleagues (2000), in which they showed the preassembly of human umbilical vein ECs (HUVECs) into nascent microvascular networks *in vitro*, and the ability of these preformed endothelial networks to remodel into functional vessels when implanted subcutaneously into immunodeficient mice. In this pioneering work, HUVECs were plated in three-dimensional (3D) collagen/fibronectin gels *in vitro* for 24 h during which time the HUVECs organized into cellular cords with nascent lumens. The endothelial networks embedded within the collagen/fibronectin gels were then implanted into immunodeficient mice and followed for up to 2 months. Blood vessels lined with human endothelial cells and filled with red blood cells were detected after 1 to 2 months, demonstrating the inherent ability of human endothelial cells to assemble into vascular networks that connect with the host (murine) blood vessels. The HUVECs provided an appropriate starting point for this model, but the cells required transduction of the antiapoptotic gene Bcl-2 to augment survival. Later studies by the same group showed that cord blood and adult blood–derived endothelial cells did not require Bcl-2 transduction to form human vessels in this model (Shepherd *et al.*, 2006). Furthermore, Yoder and colleagues (2007) used this model as a functional assay to demonstrate the crucial distinction between EPCs, called ECFC in their study, and hematopoietic/monocytic cells that express endothelial markers and have been called early EPCs, angiogenic EPCs, or CFU-ECs. (EPCs formed vessels whereas the hematopoietic/

monocytic cells did not.) In summary, although the Schechner model system was developed to study immune cell interactions with human endothelium, it has also provided a valuable tool for investigators to test endothelial cell populations for ''vasculogenic'' potential—that is, the ability to form, *de novo*, networks of new vessels that can connect with the pre-existing host vasculature (Koike *et al.*, 2004; Schechner *et al.*, 2000).

The cellular requirements for building blood vessel networks for tissue engineering and tissue regeneration is an area of active investigation. We showed in 2004 that a combination of human EPC-derived endothelial cells and mature human smooth muscle cells (SMCs) assembled into microvessel-like structures *in vitro* when co-seeded on a biodegradable scaffold of polyglycolic acid/poly-L-lactic acid (PGA/PLLA). In the absence of SMCs, the ECs were viable and maintained endothelial characteristics, but did not undergo morphological rearrangements suggestive of lumen formation (Wu *et al.*, 2004). This study indicated that although endothelial cells have an inherent ability to form vascular cords and lumens, SMCs are required in certain, perhaps less favorable, 3-D environments such as that presented by the PGA/PLLA mesh. It also suggested that a two-cell system composed of ECs and a smooth muscle support cell might prove to be more robust and efficient for building vascular networks *de novo*.

The assay we described here supports this concept. We showed that cord blood–derived EPCs combined with mature human smooth muscle as a single-cell suspension in Matrigel form functional human blood vessel networks within 7 days after implantation into nude mice (Melero-Martin *et al.*, 2007). Cord blood EPCs alone or human SMCs alone do not form vessels and Matrigel without cells is inert. Vessel density can be increased or decreased, over a range from 10 to 100 vessels/mm^2, by varying cell numbers. Human cells can be identified by human specific antibodies or by GFP labeling of the cells. Other sources of human ECs, adult peripheral blood–derived EPCs, HUVECs, and human dermal microvascular endothelial cells (HDMECs) also form vessels at 7 days when combined with human SMCs, albeit at lower microvessel densities at this 80:20 ratio. Hence, this approach offers a versatile, quantifiable, and relatively simple model system to study postnatal vasculogenesis *in vivo* using human cells. The model can be used to study the vasculogenic potential of other sources of human endothelial and perivascular cells, such as human embryonic stem cells differentiated into endothelial and smooth muscle lineages (Gerecht-Nir *et al.*, 2003; Kaufman *et al.*, 2001; Levenberg *et al.*, 2002; Levenberg *et al.*, 2007; Wang *et al.*, 2004). The model can be used to screen for anti- and/or proangiogenic compounds. And finally, the model can be used to study the role(s) of specific genes in the formation and function of a vascular network composed of human endothelium.

We refer to this experimental model as ''postnatal vasculogenesis'' because (1) vessels are formed from cells isolated from postnatal human

blood and tissues, (2) vessels form in an adult animal, and (3) vessels do not arise from pre-existing vessels but instead from single cells suspended in Matrigel. However, angiogenesis plays an important role in this assay because connections to the murine vasculature are needed to achieve red blood cell–filled vessels, the functional read-out in this assay. Whether the ability of human vessels to form productive connections with host vessels should be considered an aspect of vasculogenesis and angiogenesis would likely generate a lively discussion.

2. Isolation of Blood-Derived Endothelial Progenitor Cells

The discovery of EPCs in peripheral blood was exciting because it suggested a promising opportunity to noninvasively obtain large quantities of autologous ECs for either therapeutic vascularization or tissue engineering, both of which require some form of postnatal vasculogenesis. However, the process for obtaining blood-derived EPCs with the ability to form blood vessels *in vivo* has not been straightforward. Most of the original studies identified circulating EPCs as cells expressing CD34, CD133, and the VEGF receptor 2 (KDR) (Asahara *et al.*, 1997; Peichev *et al.*, 2000; Reyes *et al.*, 2002; Shi *et al.*, 1998). However, it is known now that these cellular markers are shared by hematopoietic cells that can be mobilized into circulation from the bone marrow to home sites of neovascularization (Rafii and Lyden, 2003; Yoder *et al.*, 2007). Although the hematopoietic and endothelial cell types are fundamentally different, many studies have referred to blood- or bone-marrow–derived adherent cells that express progenitor and endothelial markers such as CD34, CD133 and VEGFR-2+ cells as EPCs (Prater *et al.*, 2007). The hematopoietic accessory cells have been referred to as ''colony-forming units-ECs'' (CFU-ECs) (Gehling *et al.*, 2000), ''circulating angiogenic EPCs'' (Rehman *et al.*, 2003), ''early EPCs'' (Gulati *et al.*, 2003; Hur *et al.*, 2004), and ''colony-forming units-Hill (CFU-Hill)'' (Hill *et al.*, 2003). On the other hand, the cells with direct involvement as the cellular lining of the blood vessel lumen have been referred to as ''late outgrowth ECs'' (Lin *et al.*, 2000), EPCs (Kaushal *et al.*, 2001), ''late EPCs'' (Hur *et al.*, 2004), and ''endothelial colony-forming cells'' (ECFCs) (Ingram *et al.*, 2004). Thus, the term EPCs has been applied to blood and bone-marrow cells with hematopoietic and endothelial features. Despite the ambiguous terminology, the functional distinction between the two groups of cells is becoming clearer. Yoder and colleagues (2007) demonstrated, in an elegant study, that most of the cells that have been long referred to as EPCs are in fact descendants of hematopoietic stem cells (HSCs); the cells express functional activities of myeloid

cells and have no ability to differentiate into functional ECs in perfused blood vessels *in vivo*.

Cells with *bona fide* blood vessel–forming ability, which we refer to as EPCs, and Yoder and Ingram refer to as ECFCs (Ingram et al., 2004), comprise a very small population of the circulating cells. EPCs are found at a concentration of about two to five cells per milliliter in human umbilical cord blood, and at a concentration of about 0.05 to 0.2 cells/ml in adult peripheral blood (Ingram *et al.*, 2004) and in the vessel wall (Ingram *et al.*, 2005). Both the low frequency of EPCs in circulation and the lack of a unique set of distinctive cellular markers have made the isolation of EPCs by flow cytometry or other immunological techniques very challenging. As a result, the most successful methodology for isolating EPCs is based on methods similar to those originally reported for endothelial outgrowth from peripheral blood (Lin *et al.*, 2000). In this method, adult peripheral blood mononuclear cells (MNCs) or human umbilical cord blood MNCs are collected and plated onto collagen-coated plates in endothelial-specific growth media (Ingram *et al.*, 2004; Lin *et al.*, 2000; Yoder *et al.*, 2007). Nonadherent cells are discarded and EC-like colonies emerge from the adherent cell population 14 to 21 days after plating adult MNCs and 5 to 7 days after plating human umbilical cord blood MNCs. The colonies display a cobblestone appearance typical of ECs, can be plated as single cells and routinely expanded for over 70 population doublings (Ingram *et al.*, 2004, 2005; Lin *et al.*, 2000; Melero-Martin *et al.*, 2007; Yoder *et al.*, 2007). EPCs obtained by this methodology are phenotypically indistinguishable from cultured mature ECs in terms of cobblestone morphology and expression of adhesion molecules and receptors (Ingram *et al.*, 2004, 2005; Lin *et al.*, 2000; Melero-Martin *et al.*, 2007; Yoder *et al.*, 2007). However, in functional assays, EPCs exhibit enhanced migratory and proliferative activity compared to mature ECs derived from existing vasculature (Ingram *et al.*, 2004; Khan *et al.*, 2006; Melero-Martin *et al.*, 2007). More importantly, our group and two other independent groups have shown that EPCs obtained by this methodology possess *de novo* vessel-forming ability *in vivo* (Au *et al.*, 2008; Melero-Martin *et al.*, 2007; Yoder *et al.*, 2007), and therefore these EPCs constitute one of the cellular building blocks for our experimental *in vivo* model of vasculogenesis.

2.1. Materials/reagents

Heparin solution (American Pharmaceutical Partners, cat. # 504011)
19-gauge butterfly needle (Kendall, cat. # 225174)
Ficoll-Paque Plus (Amersham Pharmacia, cat. # 17-1440-02)
50-ml Accuspin tubes (Sigma-Aldrich, cat. # A2055)
Ammonium chloride solution (StemCell Technologies, cat. # 07850)
Endothelial basal medium, EBM-2 (Lonza, cat. # CC-3156)

EGM-2 Singlequot supplements (Lonza, cat. # CC-4176)
Glutamine-penicillin-streptomycin solution, 100× GPS (Mediatech, Inc., cat. # 30-009-CI)
Fetal bovine serum, FBS (Hyclone, cat. # SV30014.03). Heat inactivated at 56 °C for 30 min
Bovine serum albumin, BSA (Sigma-Aldrich, cat. # A7906)
Gelatin (Fisher, cat. # DF0143-17-9)
CD31 Dynal beads solution (DYNAL, cat. # 111.55)
Magnetic particle concentrator (DYNAL, cat. # 120.20)
Trypsin-EDTA solution, 1× (Mediatech, Inc., cat. # 25-052-CI)
Dulbecco's phosphate buffered saline, PBS (Sigma-Aldrich, cat. # D5652)
Glucose (Sigma-Aldrich, cat. # G6152)
Sodium citrate (Sigma-Aldrich, cat. # S4641)
Citric acid (Sigma-Aldrich, cat. # 251275)
Sodium carbonate, Na_2CO_3 (Sigma-Aldrich, cat. # 223530)
Human plasma fibronectin (FN) (Chemicon International, cat. # FC-010)
Cloning rings, 150 μl (Sigma-Aldrich, cat. # C1059)
Sterile double-distilled water, dH_2O

2.2. Recipes

PBS, 1 l
  9.6 g of PBS (Sigma-Aldrich, cat. # D5652)
  1 l of dH_2O
  Autoclaved at 121 °C for 30 min
6% ACD-A solution, 1 l
  22.3 g of glucose
  22 g of sodium citrate
  8 g of citric acid
  1 l of dH_2O
Isolation buffer (PBS/0.6% ACD-A/0.5% BSA), 500 ml
  50 ml of 6% ACD-A solution
  2.5 g of BSA
  450 ml of PBS
  Filter sterilized with a 0.2-μm–pore size vacuum filter
EBM-2/20% FBS, 500 ml (herein called EPC medium)
  395 ml of EBM-2
  100 ml of FBS (20% final)
  5 ml of 100× GPS
  All the EGM-2 Singlequot supplements except for hydrocortisone (i.e., VEGF, hFGF-B, R-IGF-1, hEGF, Heparin, ascorbic acid, and GA-1000)
  Filter sterilized with a 0.2-μm–pore-size vacuum filter, divided into 45-ml aliquots and freeze down (–20 °C) until needed.

Isolation medium, 100 ml
81.24 ml of EPC medium
3.76 ml of FBS (to maintain 20% final)
15 ml of autologous plasma (obtained as described below; 15% final)
Filter sterilize with a 0.2-μm–pore-size vacuum filter
1% gelatin solution, 500 ml
5 g of gelatin
500 ml of PBS
Autoclaved at 121 °C for 30 min. Filter sterilized with a 0.2-μm–pore-size vacuum filter
FN-coating solution (0.1 M Na_2CO_3), 500 ml
5.3 g of Na_2CO_3
500 ml of dH_2O
Adjust pH to 9.4 with HCl
Filter sterilized with a 0.2-μm–pore-size vacuum filter

2.3. Procedures

2.3.1. Isolation of cord blood–derived EPCs (cbEPCs)

1. Coat 100-mm tissue-culture plates with 1% gelatin solution (10 ml per plate) and incubate at 37 °C for 30 to 60 min. Prior to use, remove the gelatin solution and wash the plates once with PBS.
2. Set up 50-ml conical tubes with 10 ml of isolation buffer for blood collection.
3. Add 1 ml heparin solution into the syringe prior to drawing cord blood. Draw blood (typically 20 to 40 ml) from the umbilical vein using a 19-gauge butterfly needle. Collect every 25 ml of blood directly into 50-ml conical tubes with 10-ml isolation buffer. Place conical tubes with blood samples on ice.
4. Add 15 ml of Ficoll-Paque Plus to each 50-ml Accuspin tube. Spin at 1200 rpm for 1 min to sediment the Ficoll-Paque below the frit.
5. Add 30 ml of blood/isolation buffer to the top of each Accuspin tube. Spin at 2700 rpm for 15 min at room temperature (RT) with the brake of the centrifuge off.
6. Gently collect autologous plasma supernatant above the mononuclear cell layer. (Do not disturb the cell layer.) Save this autologous plasma to make up isolation medium. To minimize disturbances, do not remove all the plasma above the cell layer.
7. Using an 18-gauge needle on a 10-ml syringe, collect the mononuclear cell layer and transfer it to a 50-ml conical tube on ice. Add 5 ml of isolation buffer to every 10 ml of cells collected.
8. Spin the mononuclear cells at 2700 rpm for 5 min. Remove supernatant and resuspend the cell pellet in 10 ml of isolation buffer. Transfer to a

15-ml conical tube and spin at 1200 rpm for 10 min. Remove supernatant.

9. Add 1 ml of isolation buffer to dislodge the cell pellet and resuspend the cells. Add 3 ml of ammonium chloride solution to lyse erythrocytes. Incubate on ice for 5 to 10 min.
10. Add 5 ml of isolation buffer and centrifuge at 1300 rpm for 5 min. Remove supernatant. If the cell pellet is not devoid of erythrocytes (i.e., pellet still has a red color), incubate again with 1 ml of isolation buffer and 3 ml of ammonium chloride solution on ice for 5 min. Add 5 ml of isolation buffer and centrifuge at 1300 rpm for 5 min. Remove supernatant.
11. Resuspend the cell pellet in 10 ml of isolation medium per 25 ml of cord blood started with. Take 10 μl to count the cells in a hemocytometer and work out the total number of mononuclear cells per ml of cord blood sampled (approximately 4 to 8 $\times$ 10^7 MNCs in 25 to 50 ml of cord blood).
12. Plate the mononuclear cell solution in 1% gelatin-coated 100-mm tissue culture plates. Use 2$\times$ 100-mm tissue culture plates per 25 ml of cord blood sampled (equivalent to 4.5 cm^2/ml cord blood sampled). Add 10 ml of cells suspended in isolation medium to each 10-cm plate, and place them in a humidified incubator at 37 °C and 5% CO_2 for 48 h.
13. Forty-eight hours after plating, aspirate out the unbound cell fraction (which includes all the unattached hematopoietic cells), and feed the bound-cell fraction with fresh EPC medium.
14. Feed the plates every 2 to 3 days with EPC medium. Screen plates for the presence of EC-like colonies. Cord blood–derived endothelial colonies that display cobblestone morphology will emerge in culture after 1 week (Fig. 13.1). The size, frequency, and time of appearance of these colonies will vary as reported by Ingram *et al.* (2004).
15. Allow colonies to expand such that the plate is covered by a confluent cellular monolayer. Detach the cells using trypsin-EDTA solution and proceed to purify them by selection of CD31-positive cells.

2.3.2. Isolation of adult blood derived–EPCs (abEPCs)

1. Coat six-well tissue culture plates with 1% gelatin solution (2 ml per well) and incubate at 37 °C for 30 to 60 min. Prior to use, remove the gelatin solution and wash the plates once with PBS.
2. Set up 50-ml conical tubes with 10 ml of isolation buffer for blood collection.
3. Add 1 ml heparin sodium into the syringe prior to drawing blood. Draw blood from the vein (typically 50 to 100 ml) using a 19-gauge butterfly needle. Collect 25 ml of blood directly into 50-ml conical tubes with 10 ml of isolation buffer. Place conical tubes with blood samples on ice.

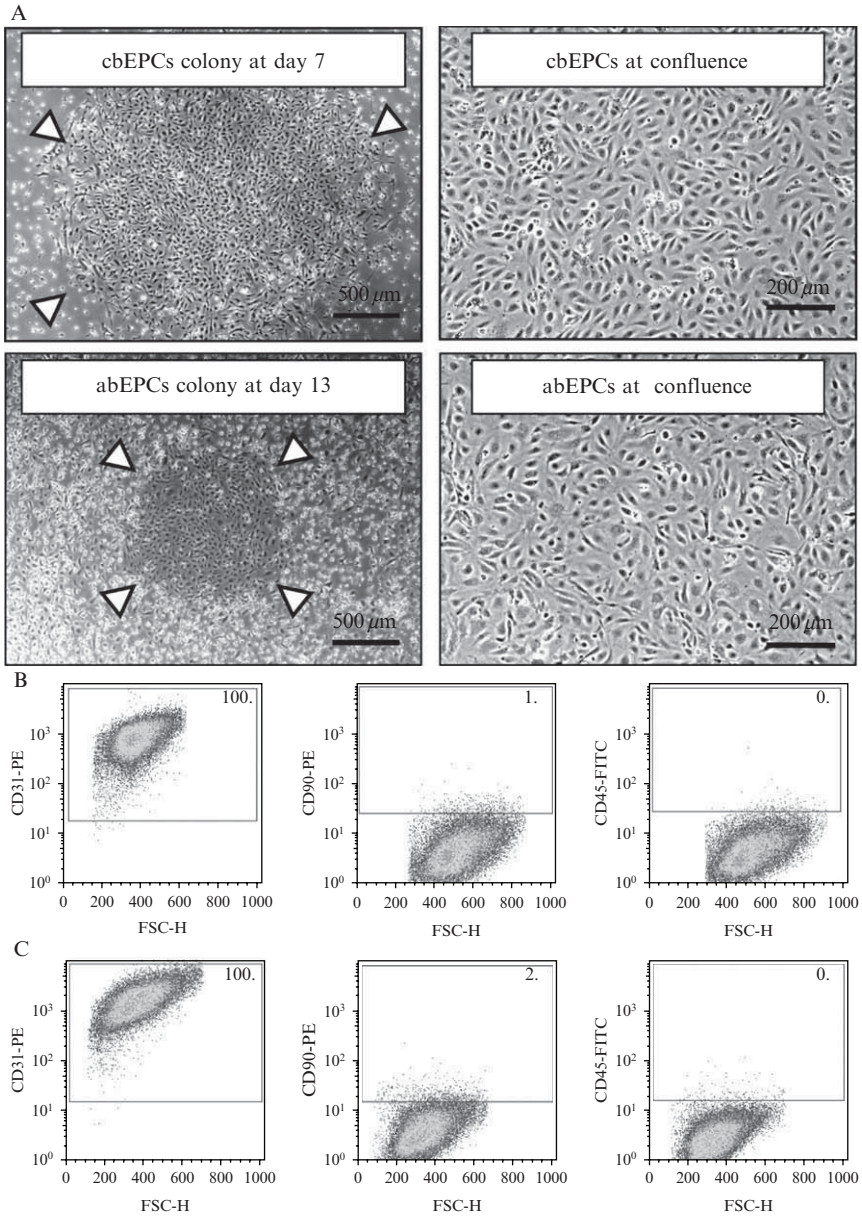

Figure 13.1 Phenotypic characterization of EPCs. (A) EPCs emerge in culture as typical EC colonies, after 5 to 7 days when isolated from cord blood, and after 14 to 21 days when isolated from adult peripheral blood (left panels). CD31-selected EPCs present typical cobblestone morphology at confluence (right panels). Flow cytometric analysis of cultured (B) cbEPCs and (C) abEPCs show uniform expression of EC marker CD31, and negative expression of mesenchymal marker CD90 and hematopoietic markers CD45. This type of analysis should be performed routinely to verify that the cell population to be used for *in vivo* vasculogenesis is not contaminated with either mesenchymal or hematopoietic cells at any stage of their expansion *in vitro*.

4. Add 15 ml of Ficoll-Paque Plus to each 50-ml Accuspin tube. Spin at 1200 rpm for 1 min to sediment the Ficoll-Paque to below the frit.
5. Add 30 ml of blood/isolation buffer to the top of each Accuspin tube. Spin at 2700 rpm for 15 min at RT with the brake of the centrifuge off.
6. Gently collect autologous plasma above the mononuclear cell layer. (Do not disturb the cell layer.) Save this autologous plasma to make up isolation medium. To minimize disturbances, do not remove all the plasma above the cell layer.
7. Using an 18-gauge needle on a 10-ml syringe, collect the mononuclear cell layer and transfer it to a 50-ml conical tube on ice. Add 5 ml of isolation buffer to every 10 ml of cells collected.
8. Spin the mononuclear cells at 2700 rpm for 5 min. Remove supernatant and resuspend the cell pellet in 10 ml of isolation buffer. Transfer to a 15-ml conical tube and spin at 1200 rpm for 10 min. Remove supernatant.
9. Add 1 ml of isolation buffer to dislodge the cell pellet and 3 ml of ammonium chloride solution to lyse erythrocytes. Incubate on ice for 5 to 10 min.
10. Add 5 ml of isolation buffer and centrifuge at 1300 rpm for 5 min. Remove supernatant. If cell pellet is not completely free of erythrocytes (i.e., pellet still has a red color), incubate it again with 1 ml of isolation buffer and 3 ml of ammonium chloride solution on ice for 5 min. Add 5 ml of isolation buffer and centrifuge at 1300 rpm for 5 min. Remove supernatant.
11. Resuspend cells in 12 ml of isolation medium per 25 ml of blood started with. Take 10 μl to count the cells in a hemocytometer and work out the total number of mononuclear cells per ml of blood sampled (approximately 10 to 15 $\times$ 10^7 MNCs in 50 ml of blood).
12. Plate the mononuclear cell solution in 1% gelatin-coated six-well tissue culture plates (2 ml per well). Use one six-well plate for each 25 ml of peripheral blood sampled (equivalent to 2.5 cm^2/ml blood sampled). Place the plates in a humidified incubator at 37 °C and 5% CO_2.
13. Forty-eight hours after plating, add 2 ml of fresh isolation medium to each well. Do not aspirate the unbound cell fraction yet; place the plates back in the humidified incubator at 37 °C and 5% CO_2 for another 48 h.
14. Four days after plating, aspirate the unbound cell fraction and feed the bound cell fraction with fresh EPC medium (2 ml per well).
15. Feed the plates every 2 to 3 days with EPC medium. Screen plates for the presence of EC-like colonies. Peripheral blood-derived endothelial colonies (identified by typical cobblestone morphology) (Fig. 13.1) will emerge in culture after 2 to 3 weeks since isolation. The size, frequency, and time of appearance of these colonies will vary as reported by Ingram *et al.* (2004). Keep feeding the plates and leave the endothelial-like

colonies to grow in size until they reach a diameter of approximately half the diameter of a cloning ring (3 mm).

16. Before proceeding to collect the endothelial-like colonies, coat six-well tissue culture plates with 2 ml of FN-coating solution and 10 μl of human plasma fibronectin (final fibronectin concentration of 1 μg/cm^2) per well. Incubate the plates at 37 °C for at least 60 min. Prior to use, remove the FN-coating solution and wash the plates once with PBS. Add 2 ml of EPC medium to each well where colonies will be plated. Each colony will be collected and replated in an individual well.
17. Mark the location of the colonies of interest on the bottom of the wells with a marker. Verify that the colonies are circled by observing with an inverted microscope. Aspirate the medium from wells where colonies are present and wash each well with PBS. Aspirate the PBS and using a sterile forceps, place a cloning ring over the location of a colony to be selected and press down gently. The grease at the bottom of the cloning ring will help it stick to the culture plate. Add 100 μl of trypsin-EDTA solution inside each cloning ring and incubate at 37 °C until the cells become loosely attached or detached, as observed in the inverted microscope. Transfer the 100 μl of cells in trypsin-EDTA from the cloning ring to the new FN-coated well with 2 ml of EPC medium. Add 100 μl of EPC medium to the cloning ring and gently resuspend any remaining cells inside the cloning ring; transfer this wash to the new FN-coated well with 2 ml of EPC medium. Finally, place the plates in the humidified incubator at 37 °C and 5% CO_2.
18. Feed the plates every 2 to 3 days with EPC medium. At confluence, detach the cells using trypsin-EDTA solution and replate the cells from each well into one 100-mm, FN-coated tissue culture plate. Culture the plates in the humidified incubator at 37 °C and 5% CO_2.
19. Allow cells to reach confluence. Detach the cells using trypsin-EDTA solution and proceed to purify them by selection of CD31-positive cells.

2.3.3. Magnetic bead purification of cultured CD31-positive EPCs

1. Coat 100-mm tissue-culture plates with 5 ml of FN-coating solution and 60 μl of human plasma fibronectin per plate (final fibronectin concentration of 1 μg/cm^2). Incubate the plates at 37 °C for at least 60 min. Before use, remove the FN-coating solution and wash the plates once with PBS.
2. For each confluent 100-mm cultured plate, aspirate the culture medium and wash the cells with 10 ml of PBS. Remove PBS and add 2 ml of trypsin-EDTA solution to each 100-mm plate. Gently rock the plates to evenly distribute the trypsin-EDTA solution. Incubate for 1 to 2 min. Gently tap the plate to facilitate cell detachment and verify under an inverted microscope that cells are detaching and in suspension.

3. When cells completely detach, add 8 ml of EPC medium and collect the cell solution into a 15-ml conical tube. Take 10 μl to count the cells in a hemocytometer and work out the total number of cells harvested.
4. Centrifuge the cells at 1200 rpm for 5 min, remove the supernatant and wash the cell pellet in 5 ml of isolation buffer. Centrifuge the cells at 1200 rpm for 5 min, remove the supernatant and resuspend the cell pellet in 500 μl of isolation buffer. Transfer the cell solution into a 1.5-ml sterile centrifuge tube.
5. Add 12.5 μl of anti-CD31—coated Dynal beads and incubate for 5 min at 4 °C with intermittent mixing. CD31-positive cells will attach to the anti-CD31–coated magnetic beads.
6. Place the centrifuge tube in the magnetic cell concentrator and hold for 1 min. Anti-CD31–coated magnetic beads will move toward the magnet (accumulating on the wall of the tube) leaving the nonattached cells (CD31-negative cell fraction) free in suspension. Gently aspirate the CD31-negative cell fraction.
7. Remove the centrifuge tube from the magnetic cell concentrator. Add 0.5 ml of isolation buffer and mix gently by pipetting. Place the tube back in the magnetic cell concentrator, hold for 1 min, and discard the negative fraction. Repeat the wash a total of three times.
8. After the final wash, resuspend the CD31-positive cells in 10 ml of EPC medium and plate the resulting cell solution on a 100-mm, FN-coated tissue culture plate. These cells can be referred to as passage 1 (P1) EPCs.

2.3.4. Notes

1. During the initial steps of the isolation procedure when the MNC fraction is plated on 100-mm dishes or 6-mm multiwell dishes, cells are fed with EPC medium with 15% of autologous plasma.
2. Because the EPCs comprise a very small population of the mononucleated cells, about two to five cells per milliliter in human umbilical cord blood and 0.05 to 0.2 cells per milliliter in adult peripheral blood (Ingram *et al.*, 2004), the initial period of cell attachment is 2 days for cord blood samples and 4 days for adult peripheral blood samples. Thereafter, the unattached cells should be discarded and the cultures fed with EPC medium without autologous plasma.
3. As reported previously (Ingram *et al.*, 2004; Yoder *et al.*, 2007), EPC colonies should be evident 14 to 21 days after plating adult peripheral blood MNCs. However, since the number of expected colonies from adult peripheral blood is very low, a careful and thorough screening of the culture plates is advised, beginning in the second week after the procedure. To facilitate the screening (and the later picking of colonies), MNCs from adult blood samples can be divided among individual wells of a six-well plate instead of using 100-mm culture plates.

4. Plates from adult peripheral blood preparations will present higher numbers of attached hematopoietic cells (e.g., monocytes and macrophages) than those from cord blood samples (Yoder *et al.*, 2007). The myeloid cells will adhere to and populate the culture plates such that colonies of abEPCs will be left with limited free space to expand. Therefore, investigators are advised to pick the abEPC colonies with cloning rings and transfer the cells to new culture wells where they can be expanded freely from the hematopoietic cells.
5. Due to the inherent heterogeneity of blood samples, one concern about this method is the potential contamination with hematopoietic cells. However, hematopoietic cells that do attach to the culture plates are then difficult to detach during the trypsinization step. If such cells do detach, they do not proliferate appreciably in subsequent passages. Moreover, the superior proliferative capacity of EPCs over hematopoietic cells in culture will rapidly outpace any hematopoietic cells present at passage 1. In addition, the presence of hematopoietic cells is only significant in preparations from adult peripheral blood, wherein the EPC colonies are selected using cloning rings, thereby reducing the chances of contaminating cells.
6. An additional concern is the potential contamination with mesenchymal cells present in the blood samples. Circulating mesenchymal cells have been reported in adult peripheral blood (Simper *et al.*, 2002) and cord blood samples (Kim *et al.*, 2004; Le Ricousse-Roussanne *et al.*, 2004; Lee *et al.*, 2004). Therefore, blood-derived mesenchymal cells constitute a real potential contaminant since they can adhere and proliferate in the culture plates with ease. However, mesenchymal cells do not express the surface cell marker CD31, and therefore they will be depleted from the culture during the magnetic bead purification of CD31-positive EPCs.

3. Expansion and Characterization of Blood-derived Endothelial Progenitor Cells

Prior to their use *in vivo*, EPCs will require a period of culture expansion *in vitro*. Although conditions for expanding EPCs can be found elsewhere in the literature, we have shown that up to 10^{13} cbEPCs (25 ml of cord blood) and 10^{8} EPCs (50 ml of adult peripheral blood) can be obtained after only 40 days in culture following the methods described here (Melero-Martin *et al.*, 2007). Similar expansion potential has been also reported by other authors for both blood-derived EPCs (Ingram *et al.*, 2004; Lin *et al.*, 2000). These remarkable numbers of human EPCs are likely to exceed (in the case of cord blood), and be sufficient (in the case of adult blood), the quantity that would be needed for most autologous regenerative therapies.

However, it is important to consider the effect that culture conditions and the extent of expansion may impose on cellular phenotype and function.

We and others have reported that EPCs expanded *in vitro* are phenotypically indistinguishable from cultured ECs (Ingram *et al.*, 2004, 2005; Lin *et al.*, 2000; Melero-Martin *et al.*, 2007; Yoder *et al.*, 2007). For example, flow cytometric analysis of EPCs shows uniform expression of EC markers CD31, VEGF-R2, and vWF, and negative expression of mesenchymal marker CD90 and hematopoietic markers CD45 and CD14. This type of analysis should be performed routinely to verify that the cell population to be used for *in vivo* vasculogenesis is not contaminated with either mesenchymal or hematopoietic cells at any stage of their expansion *in vitro* (Melero-Martin *et al.*, 2007). Additionally, immunofluorescence staining should show that EPCs express CD31 and VE-cadherin at the cell–cell borders and vWF in a punctuate pattern in the cytoplasm, clear indications of EC properties (Melero-Martin *et al.*, 2007). Despite the consistent and uniform expression of endothelial markers, EPCs can undergo cellular and functional changes in culture. For instance, cord blood–derived EPCs have been reported to change their morphology, growth kinetics, migration, proliferative responses toward angiogenic factors, and *in vivo* vasculogenic ability as they are expanded in culture (Ingram *et al.*, 2004; Khan *et al.*, 2006; Melero-Martin *et al.*, 2007). Therefore, it is important to keep track of the number of population doublings that EPCs undergo *in vitro* prior to their use *in vivo*. In this section we provide details for (1) routine culture of EPCs, (2) evaluation of the accumulative number of population doublings during expansion, and (3) simplified phenotype confirmation by flow cytometry. In summary, we would like to stress the importance of these quality control measures to ensure that the cells to be used are homogenous and have expected endothelial features.

3.1. Additional materials/reagents

High-glucose Dulbecco's Modified Eagle Medium, 1× DMEM (Gibco, cat. # 10564)
MEM nonessential amino acid solution (NEAA), 100× (Sigma-Aldrich, cat. # M7145)
0.5 *M* EDTA solution, pH 8.0 (Gibco, cat. # 15575-038)
Mouse IgG1-PE (BD Pharmingen, cat. # 555787)
Mouse IgG1-FITC (BD Biosciences, cat. # 349041)
CD31-PE (Ancell, cat. # 180-050)
CD90-PE (BD Pharmingen, cat. # 555596)
CD45-FITC (BD Biosciences, cat. # 347463)
Sterile double-distilled water, dH_2O

3.2. Additional recipes

DMEM/10% FBS medium, 500 ml
- 440 ml of DMEM
- 50 ml of FBS (10% final)
- 5 ml of 100× NEAA
- 5 ml of 100× GPS
- Filter sterilized with a 0.2-μm–pore-size vacuum filter

FACS buffer (PBS/0.5% BSA/2m*M* EDTA), 100 ml
- 9.6 ml of PBS
- 0.5 g of BSA
- 0.4 ml of 0.5 *M* EDTA solution

3.3. Procedures

3.3.1. Expansion of blood-derived EPCs

Feed P1 blood-derived EPCs every 2 to 3 days using EPC medium (10 ml of medium per each 100-mm tissue-culture plate). At confluence, subculture the cells as follows:

1. Aspirate out the culture medium and wash the cells with 10 ml of PBS.
2. Remove PBS and add 2 ml of trypsin-EDTA solution to each 100-mm plate. Gently rock the plates to evenly distribute the trypsin-EDTA solution. Incubate for 1 to 2 min. Gently tap the plate to see the detached cells in suspension under an inverted microscope.
3. When cells completely detach, add 8 ml of EPC medium and collect the cell solution into a 15-ml conical tube. Take 10 μl to count the cells in a hemocytometer and work out the total number of cells harvested. Calculate the number of population doublings (PD) as follows:

$$PD = \frac{Ln\left(\frac{XF}{X0}\right)}{Ln(2)}$$

where *X*0 (cells) refers to the initial cell number seeded in this culture, *XF* (cells) refers to the final cell number observed at the time of harvesting, and *PD* refers to the number of doublings that the cell population underwent during this passage.

4. Plate the cells in FN-coated (1 μg/cm^2) tissue-culture plates at a seeding density of 5000 cell/cm^2 using EPC medium. Place the plates in a humidified incubator at 37 °C and 5% CO_2 and feed them every 2 to 3 days with EPC medium. These cells can be referred to as passage 2 (P2) EPCs.

Repeat this procedure for subsequent passages. Keep track of the accumulative value of PD as the cell population is expanded.

3.3.2. Cell characterization by flow cytometry (CD31, CD90, and CD45)

1. Aspirate out the culture medium from one confluent 100-mm culture plate and wash the cells with 10 ml of PBS.
2. Remove PBS and add 2 ml of trypsin-EDTA solution to each 100-mm plate. Gently rock the plates to evenly distribute the trypsin-EDTA solution. Incubate for 1 to 2 min. Gently tap the plate to see the detached cells in suspension under an inverted microscope.
3. When cells completely detach, add 8 ml of DMEM/10% FBS medium and collect the cell solution into a 15-ml conical tube. Take 10 μl to count the cells in a hemocytometer and work out the total number of cells harvested.
4. Centrifuge the cells at 1200 rpm (<300 g) for 5 min. Remove supernatant and resuspend the cell pellet in 10 ml of FACS buffer and centrifuge again at 1200 rpm (<300 g) for 5 min. Remove supernatant.
5. Resuspend the cell pellet in 500 μl of FACS buffer (100 μl per label). Split the cell sample by transferring 100 μl of the cell suspension into five individual 1.5-ml centrifuge tubes. Add 1 μl of conjugated antibody (IgG-FITC, IgG-PE, CD31-PE, CD90-PE, and CD45-FITC) and incubate for 20 min at 4 °C with frequent mixing (tapping).
6. Following incubation, add 1 ml of FACS buffer to the tubes and centrifuge at 3000 rpm (800 g) for 3 min.
7. Wash the pellet in 1 ml of FACS buffer and centrifuge again. Repeat the wash once again.
8. Resuspend the cell pellets in 1% paraformaldehyde (made in PBS) and transfer the cells to FACS tubes. Keep the samples at 4 °C in the dark up to 1 week before analysis. Flow cytometric analyses can be performed using standard instruments (e.g., a Becton Dickinson FACScan flow cytometer) and the collected data analyzed by specialized software (e.g., FlowJo software from Tree Star Inc.).

3.3.3. Notes

1. When expanding cells in culture, it is common among investigators to report the passage number of the cultured cells. However, it is more accurate to keep track of the number of population doublings (PD) to reflect the degree of expansion exerted on them. The functional changes that cultured cells experience as a result of their expansion *in vitro* are likely to correlate with the number of PD, but not necessarily with the number of passages. Two different investigators can easily reach the same number of PD after two different passage numbers.

2. Anti-VE-cadherin (CD144) can be used in place of anti-CD31 to verify endothelial phenotype. PE-conjugated, anti-human VE-cadherin is available from R&D Systems.
3. Expanded EPCs can be cryo-preserved using standard methods (e.g., using 90% FBS and 10% DMSO as freezing medium and liquid nitrogen for storage). We have tested EPCs cryo-preserved at different passages (up to passage 15), and their phenotype as well as their *in vitro* and *in vivo* functions were properly maintained (Melero-Martin *et al.*, 2007).

4. Growth of Human Smooth Muscle Cells

This assay requires SMCs as a source of perivascular cells. Human SMCs can be isolated from discarded vascular tissues (e.g., human saphenous vein-derived SMCs). Additionally, investigators can purchase commercially available human SMCs (e.g., Cell Application, Inc. ScienCell Res Lab; Cascade Biologics; Lonza Inc.).

4.1. Procedure

Plate SMCs in noncoated tissue-culture plates at a seeding density of 10,000 cells/cm^2. Place the plates in a humidified incubator at 37 °C and 5% CO_2 and feed them every 2 to 3 days with DMEM/10% FBS medium (10 ml of medium per 100-mm tissue-culture plate). At 80% confluence, subculture the cells as follows:

1. Aspirate out the culture medium and wash the cells with 10 ml of PBS.
2. Remove PBS and add 2 ml of trypsin-EDTA solution to each 100-mm plate. Gently rock the plates to evenly distribute the trypsin-EDTA solution. Incubate for 1 to 2 min. Gently tap the plate to see the detached cells in suspension under an inverted microscope.
3. When cells completely detach, add 8 ml of DMEM/10% FBS medium and collect the cell solution into a 15-ml conical tube. Take 10 μl to count the cells in a hemocytometer and work out the total number of cells harvested. Calculate the number of PDs with the previous equation.
4. Plate the cells in noncoated tissue-culture plates at a seeding density of 10,000 cell/cm^2 using DMEM/10% FBS medium. Place the plates in a humidified incubator at 37 °C and 5% CO_2 and feed them every 2 to 3 days with DMEM/10% FBS medium.

Repeat this procedure for subsequent passages. Keep track of the cumulative value of PD as the cell population is expanded.

5. *IN VIVO* VASCULOGENIC ASSAY

The Matrigel plug assay was introduced by Passaniti and co-workers in 1992 (Passaniti *et al.*, 1992), and is regarded as a useful assay for *in vivo* screening of potential pro- and anti-angiogenic compounds (Auerbach *et al.*, 2003). Matrigel, which is an extract of the murine Engleberth-Holm-Swarm tumor, is composed of basement membrane proteins. Although it takes the form of a liquid at 4 °C, Matrigel reconstitutes into a gel or plug at body temperature when injected subcutaneously into mice, where it is progressively surrounded by granulation tissue. This assay was originally conceived as a mechanism to study the growth of new vessels into the Matrigel in response to an angiogenic factor. For instance, Matrigel plugs elicit an intense vascular response when supplemented with acidic FGF (Passaniti *et al.*, 1992), basic FGF, or VEGF (Kano *et al.*, 2005). One aspect of this assay that has been often criticized is the fact that Matrigel has not been fully defined chemically. It contains collagen IV, laminin, nidogen/entacin, heparin sulfate proteoglycan, and growth factors such as epidermal growth factor, transforming growth factor beta, platelet-derived growth factor, insulin-like growth factor-1, nerve growth factor, and bFGF (Baatout, 1997; Vukicevic *et al.*, 1992). This suggests that caution should be exercised in the interpretation of experiments on cellular activities related to Matrigel (Vukicevic *et al.*, 1992). However, subcutaneous implantation of Matrigel alone (without any additional angiogenic factor) does not initiate an angiogenic response from the host; when plugs of Matrigel alone are implanted for 1 to 2 weeks into immunodeficient mice, they remain largely inert with no vascular structures inside the implants and only a few cells invading the plugs (Melero-Martin *et al.*, 2007). On the contrary, implantation of Matrigel containing EPCs and SMCs supports the progressive formation of vascular networks, reproducing aspects of postnatal vasculogenesis such as cellular assembly, lumen formation and network remodeling. Additionally, this assay is relatively simple to perform; it does not require an incision or surgical procedure, which reduces the potential influence of wound healing. Finally, the assay can be carried out in either athymic nu/nu or NOD/SCID mice.

5.1. Additional materials/reagents

Phenol-red–free BD Matrigel Matrix (BD Bioscience, cat. # 356237)
Six-week-old male athymic nu/nu mouse (Massachusetts General Hospital, Boston)
Histological Tissue-Tek unicassette (Sakura Finetek, cat. # 4117-02)
Isoflurane liquid for inhalation (Buxter Healthcare Corporation, cat. # NDC 10019-360-40)
10% neutral buffered formalin (Sigma-Aldrich, cat. # HT501128)

5.2. Additional recipes

Matrigel aliquots, 1ml

Matrigel should be divided into aliquots as recommended by the manufacturer. Briefly, thaw 10 ml of Matrigel on ice overnight and transfer the liquid Matrigel into ten 1.5-ml centrifuge tubes (1-ml aliquots). Freeze the Matrigel aliquots at –20 °C until needed. The day of the experiment, thaw the required aliquots on ice 1 to 2 h prior to their use.

5.3. Procedures

Before the experiment, make sure that sufficient EPCs and SMCs are available in culture; 1,500,000 EPCs and 375,000 SMCs will be required for each implant and mouse.

1. Aspirate the medium of each culture plate and wash the cells with 10 ml of PBS. Remove PBS and add 2 ml of trypsin-EDTA solution to each 100-mm plate. Gently rock the plates to evenly distribute the trypsin-EDTA solution. Incubate for 1 to 2 min. Gently tap the plate to see the detached cells in suspension under an inverted microscope.
2. When cells completely detach, add 8 ml of DMEM/10% FBS and collect the cell solution into a 15-ml conical tube. Take 10 μl to count the cells in a hemocytometer and work out the total number of EPCs and SMCs harvested.
3. Transfer 7,500,000 EPCs (5 $\times$ 1,500,000 cells) and 1,875,000 SMCs (5 $\times$ 375,000 cells) together into a single 50-ml conical tube. This is the total amount of cells required for five individual mice. Centrifuge at 1200 rpm and remove the supernatant. The total number of cells/implant can be varied from one-third to three times this amount to achieve lower or higher microvessel density (Melero-Martin *et al.*, 2007). Furthermore, the ratio of EPCs to SMCs can also be varied to achieve different degrees of vessel formation.
4. Resuspend the cell pellet on 1 ml of ice-cold Matrigel. Mix the cells very gently to avoid bubbles within the Matrigel. Load the cell–Matrigel mixture into a 1-ml sterile syringe, and place a 26-gauge needle with its cap on the tip of the syringe. Keep the loaded syringe deep on ice until injection.
5. Prior to the injection, anesthetize the immunodeficient mice by placing them in a gas chamber delivering isoflurane. Allow the mice to inhale the isoflurane for approximately 2 min until they are asleep (monitor their heart beats by inspection). For each mouse, inject 200 μl of the cell–Matrigel mixture subcutaneously into the upper dorsal region using a 26-gauge needle. Matrigel forms a gel at 37 °C so that the implant should form a small bump just under the skin (Fig. 13.2). After the injection,

place the mice on a layer of gauze for comfort and warmth and observe them until they become ambulatory. Then, observe the mice daily for the first 3 days.

6. One week after the injections, euthanize the mice by placing them in a gas chamber delivering compressed CO_2 gas. Once euthanized, cut open the skin near the area of the injection and surgically removed the Matrigel plug (Fig. 13.2). Digital photographs of the retrieved Matrigel plugs with a scale are advised.
7. Place the harvested Matrigel plugs into histological cassettes and deep them into 10% neutral buffered formalin overnight at RT. After fixation, wash the 10% neutral buffered formalin away with dH_2O and place the histological cassettes at 4 °C in PBS until histological evaluation.
8. For histological evaluation, the implants are embedded in paraffin and sectioned (7-μm–thick sections) using standard histological procedures. Standard protocols for hematoxilin and eosin (H&E) can be found elsewhere.
9. Quantify microvessel density by evaluation of 10 randomly selected fields (0.1 mm^2 each) of H&E stained sections taken from the middle part of the implants. Microvessels can be identified as lumenal structures containing red blood cells and counted (Fig. 13.3). Report microvessel density as the average number of red blood cell-filled microvessels from the fields analyzed and expressed as vessels per square millimeter; 93 $\pm$ 18 vessels/mm^2 correspond to the average values plus/minus standard deviation obtained from four individual mice using cbEPCs at passage 3 plus SMCs (Melero-Martin *et al.*, 2007).

5.3.1. Notes

1. The time between resuspension of the cells in Matrigel and injection into the mice should be kept to a minimum (30 to 60 min).

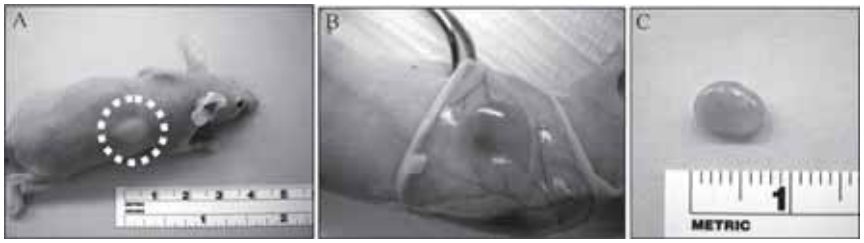

Figure 13.2 Appearance of cell/Matrigel plugs. Human cord blood EPCs and smooth muscle cells were suspended in Matrigel as described in the text. Right panel shows location and appearance of a cell/Matrigel suspension implanted subcutaneously into a nude mouse. Middle panel shows appearance of the cell/Matrigel plug 7 days after implantation. The left panel shows the appearance of the cell/Matrigel plug removed from the mouse after 7 days and prior to processing for histology.

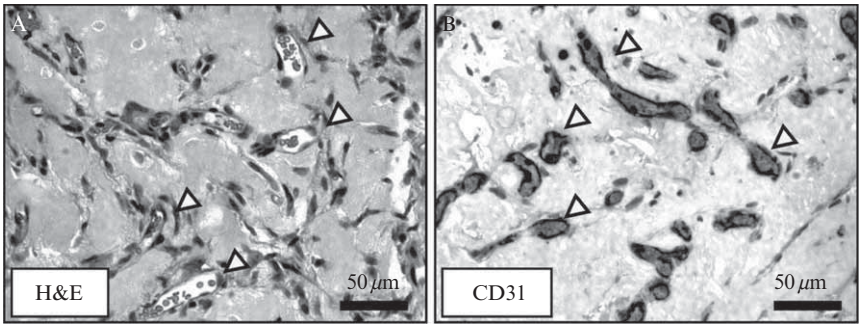

Figure 13.3 *In vivo* vasculogenic potential of EPCs. Matrigel implants containing human EPCs and SMCs were evaluated after 1 week. (A) H&E staining of implants revealed the presence of an extensive network of microvessels containing red blood cells. (B) Immunohistochemical staining at 1 week with anti-human CD31 antibody revealed that the lumenal structures were formed by the implanted EPCs.

2. Note that in this assay it is difficult to generate identical 3D plugs, even though the total Matrigel volume is kept constant (Auerbach *et al.*, 2000). Therefore, injections should be performed gently and the cell–Matrigel mixtures slowly released. In this regard, further improvements can be achieved by using subcutaneous chambers that allow for constant 3D form and volume of the Matrigel plug; these chambers have been reported to make the original Matrigel plug assay more reproducible in mice and rats (Kragh *et al.*, 2003; Ley *et al.*, 2004).
3. To further characterize the microvascular structures detected, sections of the retrieved Matrigel plug should be immunohistochemically stained with a human-specific CD31 antibody using standard staining protocols. Lumenal structures will stain positive for human CD31 (Fig. 13.3), confirming that those lumens are formed by the implanted human EPCs and not by the host cells. This evaluation is important because it demonstrates that the formation of microvascular vessels within the implant is the result of a process of *in vivo* vasculogenesis carried out by the implanted cells, and is not due to blood vessel invasion and sprouting (i.e., an angiogenic response from nearby host vasculature). We recommend using the monoclonal mouse anti-human CD31 antibody from DakoCytomation (Clone JC70A, cat. # M0823) at a 1:20 dilution. The human specificity of this antibody was confirmed by the negative reaction obtained with a diversity of mouse tissue sections that were stained in parallel (Melero-Martin *et al.*, 2007). SMCs can be localized by immunostaining with anti-alpha smooth muscle actin (clone 1A4, Sigma). However, this antibody reacts with both murine and human alpha–smooth muscle actin.

6. Conclusion

Rapid and complete vascularization of ischemic tissues and thick engineered tissues are likely to require vasculogenesis. Therefore, the search for clinically relevant sources of vasculogenic cells and the subsequent development of experimental models of vasculogenesis are of utmost importance. Here, we describe a methodology adapted from the Matrigel plug assay to deliver human blood–derived EPCs and mature SMCs subcutaneously into immunodeficient mice. One week after implantation, an extensive microvascular bed that forms anastomoses with the host vasculature will be created by the implanted cells inside the plugs. The presence of human EPC–lined lumens containing host erythrocytes can be seen throughout the implants indicating not only the formation (*de novo*) of a vascular network, but also the development of functional anastomoses with the host circulatory system. Varying the number of cells in the original cell suspension can be used to manipulate the microvessel density achieved at 7 days. Altering the ratio between EPCs and SMCs, substituting another type of perivascular cell for mature SMCs, and GFP tagging the EPCs or perivascular cells are potential modifications (Melero-Martin *et al.*, 2008). This murine model of human vasculogenesis is ideally suited for studies aimed at cellular and molecular components of microvessel development and pathologic neovascular responses, and for the development and investigation of strategies to enhance neovascularization of engineered human tissues and organs.

ACKNOWLEDGMENTS

This research was supported by funding from the U.S. Army Medical Research and Material Command (W81XWH-05-1-0115).

REFERENCES

Asahara, T., Murohara, T., Sullivan, A., Silver, M., van der Zee, R., Li, T., Witzenbichler, B., Schatteman, G., and Isner, J. M. (1997). Isolation of putative progenitor endothelial cells for angiogenesis. *Science* **275,** 964–967.

Au, P., Daheron, L. M., Duda, D. G., Cohen, K. S., Tyrrell, J. A., Lanning, R. M., Fukumura, D., Scadden, D. T., and Jain, R. K. (2008). Differential *in vivo* potential of endothelial progenitor cells from human umbilical cord blood and adult peripheral blood to form functional long-lasting vessels. *Blood* **111,** 1302–1305.

Auerbach, R., Akhtar, N., Lewis, R. L., and Shinners, B. L. (2000). Angiogenesis assays: problems and pitfalls. *Cancer Metastasis Rev.* **19,** 167–172.

Auerbach, R., Kubai, L., Knighton, D., and Folkman, J. (1974). A simple procedure for the long-term cultivation of chicken embryos. *Dev. Biol.* **41,** 391–394.

Auerbach, R., Lewis, R., Shinners, B., Kubai, L., and Akhtar, N. (2003). Angiogenesis assays: A critical overview. *Clin. Chem.* **49,** 32–40.

Ausprunk, D. H., Knighton, D. R., and Folkman, J. (1974). Differentiation of vascular endothelium in the chick chorioallantois: A structural and autoradiographic study. *Dev. Biol.* **38,** 237–248.

Ausprunk, D. H., Knighton, D. R., and Folkman, J. (1975). Vascularization of normal and neoplastic tissues grafted to the chick chorioallantois. Role of host and preexisting graft blood vessels. *Am. J. Pathol.* **79,** 597–618.

Baatout, S. (1997). Endothelial differentiation using Matrigel (review). *Anticancer Res.* **17,** 451–455.

Carmeliet, P. (2003). Angiogenesis in health and disease. *Nat. Med.* **9,** 653–660.

Carmeliet, P., and Jain, R. K. (2000). Angiogenesis in cancer and other diseases. *Nature* **407,** 249–257.

Cleaver, O., and Melton, D. A. (2003). Endothelial signaling during development. *Nat. Med.* **9,** 661–668.

Conway, E. M., Collen, D., and Carmeliet, P. (2001). Molecular mechanisms of blood vessel growth. *Cardiovasc. Res.* **49,** 507–521.

De Palma, M., Venneri, M. A., Galli, R., Sergi Sergi, L., Politi, L. S., Sampaolesi, M., and Naldini, L. (2005). Tie2 identifies a hematopoietic lineage of proangiogenic monocytes required for tumor vessel formation and a mesenchymal population of pericyte progenitors. *Cancer Cell* **8,** 211–226.

Flamme, I., Frolich, T., and Risau, W. (1997). Molecular mechanisms of vasculogenesis and embryonic angiogenesis. *J. Cell Physiol.* **173,** 206–210.

Folkman, J. (1974). Tumor angiogenesis. *Adv* Cancer Res. **19,** 331–358.

Folkman, J. (1995). Angiogenesis in cancer, vascular, rheumatoid and other disease. *Nat. Med.* **1,** 27–31.

Folkman, J. (2007). Angiogenesis: An organizing principle for drug discovery? *Nat. Rev. Drug Discov.* **6,** 273–286.

Gehling, U. M., Ergun, S., Schumacher, U., Wagener, C., Pantel, K., Otte, M., Schuch, G., Schafhausen, P., Mende, T., Kilic, N., Kluge, K., Schafer, B., *et al.* (2000). *In vitro* differentiation of endothelial cells from AC133-positive progenitor cells. *Blood* **95,** 3106–3112.

Gerecht-Nir, S., Ziskind, A., Cohen, S., and Itskovitz-Eldor, J. (2003). Human embryonic stem cells as an *in vitro* model for human vascular development and the induction of vascular differentiation. *Lab. Invest.* **83,** 1811–1820.

Gimbrone, M. A., Jr., Cotran, R. S., and Folkman, J. (1974). Human vascular endothelial cells in culture. Growth and DNA synthesis. *J. Cell Biol.* **60,** 673–684.

Grunewald, M., Avraham, I., Dor, Y., Bachar-Lustig, E., Itin, A., Jung, S., Chimenti, S., Landsman, L., Abramovitch, R., and Keshet, E. (2006). VEGF-induced adult neovascularization: recruitment, retention, and role of accessory cells. *Cell* **124,** 175–189.

Gulati, R., Jevremovic, D., Peterson, T. E., Chatterjee, S., Shah, V., Vile, R. G., and Simari, R. D. (2003). Diverse origin and function of cells with endothelial phenotype obtained from adult human blood. *Circ. Res.* **93,** 1023–1025.

Hill, J. M., Zalos, G., Halcox, J. P., Schenke, W. H., Waclawiw, M. A., Quyyumi, A. A., and Finkel, T. (2003). Circulating endothelial progenitor cells, vascular function, and cardiovascular risk. *N. Engl. J. Med.* **348,** 593–600.

Hiraoka, N., Allen, E., Apel, I. J., Gyetko, M. R., and Weiss, S. J. (1998). Matrix metalloproteinases regulate neovascularization by acting as pericellular fibrinolysins. *Cell* **95,** 365–377.

Hur, J., Yoon, C. H., Kim, H. S., Choi, J. H., Kang, H. J., Hwang, K. K., Oh, B. H., Lee, M. M., and Park, Y. B. (2004). Characterization of two types of endothelial

progenitor cells and their different contributions to neovasculogenesis. *Arterioscler. Thromb. Vasc. Biol.* **24,** 288–293.

Ingram, D. A., Mead, L. E., Moore, D. B., Woodard, W., Fenoglio, A., and Yoder, M. C. (2005). Vessel wall-derived endothelial cells rapidly proliferate because they contain a complete hierarchy of endothelial progenitor cells. *Blood* **105,** 2783–2786.

Ingram, D. A., Mead, L. E., Tanaka, H., Meade, V., Fenoglio, A., Mortell, K., Pollok, K., Ferkowicz, M. J., Gilley, D., and Yoder, M. C. (2004). Identification of a novel hierarchy of endothelial progenitor cells using human peripheral and umbilical cord blood. *Blood* **104,** 2752–2760.

Isner, J. M., and Asahara, T. (1999). Angiogenesis and vasculogenesis as therapeutic strategies for postnatal neovascularization. *J. Clin. Invest.* **103,** 1231–1236.

Isner, J. M., Pieczek, A., Schainfeld, R., Blair, R., Haley, L., Asahara, T., Rosenfield, K., Razvi, S., Walsh, K., and Symes, J. F. (1996). Clinical evidence of angiogenesis after arterial gene transfer of phVEGF165 in patient with ischaemic limb. *Lancet* **348,** 370–374.

Kano, M. R., Morishita, Y., Iwata, C., Iwasaka, S., Watabe, T., Ouchi, Y., Miyazono, K., and Miyazawa, K. (2005). VEGF-A and FGF-2 synergistically promote neoangiogenesis through enhancement of endogenous PDGF-B-PDGFRbeta signaling. *J. Cell Sci.* **118,** 3759–3768.

Kaufman, D. S., Hanson, E. T., Lewis, R. L., Auerbach, R., and Thomson, J. A. (2001). Hematopoietic colony-forming cells derived from human embryonic stem cells. *Proc. Natl. Acad. Sci. USA* **98,** 10716–10721.

Kaushal, S., Amiel, G. E., Guleserian, K. J., Shapira, O. M., Perry, T., Sutherland, F. W., Rabkin, E., Moran, A. M., Schoen, F. J., Atala, A., Soker, S., Bischoff, J., *et al.* (2001). Functional small-diameter neovessels created using endothelial progenitor cells expanded *ex vivo*. *Nat. Med.* **7,** 1035–1040.

Khan, Z. A., Melero-Martin, J. M., Wu, X., Paruchuri, S., Boscolo, E., Mulliken, J. B., and Bischoff, J. (2006). Endothelial progenitor cells from infantile hemangioma and umbilical cord blood display unique cellular responses to endostatin. *Blood* **108,** 915–921.

Kim, J. W., Kim, S. Y., Park, S. Y., Kim, Y. M., Kim, J. M., Lee, M. H., and Ryu, H. M. (2004). Mesenchymal progenitor cells in the human umbilical cord. *Ann. Hematol.* **83,** 733–738.

Koike, N., Fukumura, D., Gralla, O., Au, P., Schechner, J. S., and Jain, R. K. (2004). Tissue engineering: creation of long-lasting blood vessels. *Nature* **428,** 138–139.

Kragh, M., Hjarnaa, P. J., Bramm, E., Kristjansen, P. E., Rygaard, J., and Binderup, L. (2003). *In vivo* chamber angiogenesis assay: An optimized Matrigel plug assay for fast assessment of anti-angiogenic activity. *Int. J. Oncol.* **22,** 305–311.

Le Ricousse-Roussanne, S., Barateau, V., Contreres, J. O., Boval, B., Kraus-Berthier, L., and Tobelem, G. (2004). *Ex vivo* differentiated endothelial and smooth muscle cells from human cord blood progenitors home to the angiogenic tumor vasculature. *Cardiovasc. Res.* **62,** 176–184.

Lee, H., Cusick, R. A., Browne, F., Ho Kim, T., Ma, P. X., Utsunomiya, H., Langer, R., and Vacanti, J. P. (2002). Local delivery of basic fibroblast growth factor increases both angiogenesis and engraftment of hepatocytes in tissue-engineered polymer devices. *Transplantation* **73,** 1589–1593.

Lee, O. K., Kuo, T. K., Chen, W. M., Lee, K. D., Hsieh, S. L., and Chen, T. H. (2004). Isolation of multipotent mesenchymal stem cells from umbilical cord blood. *Blood* **103,** 1669–1675.

Levenberg, S., Golub, J. S., Amit, M., Itskovitz-Eldor, J., and Langer, R. (2002). Endothelial cells derived from human embryonic stem cells. *Proc. Natl. Acad. Sci. USA* **99,** 4391–4396.

Levenberg, S., Zoldan, J., Basevitch, Y., and Langer, R. (2007). Endothelial potential of human embryonic stem cells. *Blood* **110,** 806–814.

Ley, C. D., Olsen, M. W., Lund, E. L., and Kristjansen, P. E. (2004). Angiogenic synergy of bFGF and VEGF is antagonized by Angiopoietin-2 in a modified *in vivo* Matrigel assay. *Microvasc. Res.* **68,** 161–168.

Li, X., Tjwa, M., Moons, L., Fons, P., Noel, A., Ny, A., Zhou, J. M., Lennartsson, J., Li, H., Luttun, A., Ponten, A., Devy, L., *et al.* (2005). Revascularization of ischemic tissues by PDGF-CC via effects on endothelial cells and their progenitors. *J. Clin. Invest.* **115,** 118–127.

Lin, Y., Weisdorf, D. J., Solovey, A., and Hebbel, R. P. (2000). Origins of circulating endothelial cells and endothelial outgrowth from blood. *J. Clin. Invest.* **105,** 71–77.

Melero-Martin, J. M., Khan, Z. A., Picard, A., Wu, X., Paruchuri, S., and Bischoff, J. (2007). *In vivo* vasculogenic potential of human blood-derived endothelial progenitor cells. *Blood* **109,** 4761–4768.

Melero-Martin, J. M., De Obaldia, M. E., Kang, S-Y., Khan, Z. A., Yuan, L., Oettgen, P., and Bischoff, J. (2008). Engineering robust and functional vascular networks *in vivo* with human adult and cord blood derived progenitor cells. *Circ. Res.* **103,** 194–202.

Norrby, K. (2006). *In vivo* models of angiogenesis. *J. Cell. Mol. Med.* **10,** 588–612.

Passaniti, A., Taylor, R. M., Pili, R., Guo, Y., Long, P. V., Haney, J. A., Pauly, R. R., Grant, D. S., and Martin, G. R. (1992). A simple, quantitative method for assessing angiogenesis and antiangiogenic agents using reconstituted basement membrane, heparin, and fibroblast growth factor. *Lab. Invest.* **67,** 519–528.

Peichev, M., Naiyer, A. J., Pereira, D., Zhu, Z., Lane, W. J., Williams, M., Oz, M. C., Hicklin, D. J., Witte, L., Moore, M. A., and Rafii, S. (2000). Expression of VEGFR-2 and AC133 by circulating human CD34(+) cells identifies a population of functional endothelial precursors. *Blood* **95,** 952–958.

Prater, D. N., Case, J., Ingram, D. A., and Yoder, M. C. (2007). Working hypothesis to redefine endothelial progenitor cells. *Leukemia* **21,** 1141–1149.

Rafii, S., and Lyden, D. (2003). Therapeutic stem and progenitor cell transplantation for organ vascularization and regeneration. *Nat. Med.* **9,** 702–712.

Rehman, J., Li, J., Orschell, C. M., and March, K. L. (2003). Peripheral blood "endothelial progenitor cells" are derived from monocyte/macrophages and secrete angiogenic growth factors. *Circulation* **107,** 1164–1169.

Reyes, M., Dudek, A., Jahagirdar, B., Koodie, L., Marker, P. H., and Verfaillie, C. M. (2002). Origin of endothelial progenitors in human postnatal bone marrow. *J. Clin. Invest.* **109,** 337–346.

Risau, W. (1997). Mechanisms of angiogenesis. *Nature* **386,** 671–674.

Risau, W., and Flamme, I. (1995). Vasculogenesis. *Dev. Biol.Annu. Rev. Cell Dev. Biol.* **11,** 73–91.

Schechner, J. S., Nath, A. K., Zheng, L., Kluger, M. S., Hughes, C. C., Sierra-Honigmann, M. R., Lorber, M. I., Tellides, G., Kashgarian, M., Bothwell, A. L., and Pober, J. S. (2000). *In vivo* formation of complex microvessels lined by human endothelial cells in an immunodeficient mouse. *Proc. Natl. Acad. Sci. USA* **97,** 9191–9196.

Shepherd, B. R., Enis, D. R., Wang, F., Suarez, Y., Pober, J. S., and Schechner, J. S. (2006). Vascularization and engraftment of a human skin substitute using circulating progenitor cell-derived endothelial cells. *FASEB J.* **20,** 1739–1741.

Shi, Q., Rafii, S., Wu, M. H., Wijelath, E. S., Yu, C., Ishida, A., Fujita, Y., Kothari, S., Mohle, R., Sauvage, L. R., Moore, M. A., Storb, R. F., *et al.* (1998). Evidence for circulating bone marrow-derived endothelial cells. *Blood* **92,** 362–367.

Simper, D., Stalboerger, P. G., Panetta, C. J., Wang, S., and Caplice, N. M. (2002). Smooth muscle progenitor cells in human blood. *Circulation* **106,** 1199–1204.

Stetler-Stevenson, W. G. (1999). Matrix metalloproteinases in angiogenesis: A moving target for therapeutic intervention. *J. Clin. Invest.* **103,** 1237–1241.

Vukicevic, S., Kleinman, H. K., Luyten, F. P., Roberts, A. B., Roche, N. S., and Reddi, A. H. (1992). Identification of multiple active growth factors in basement membrane Matrigel suggests caution in interpretation of cellular activity related to extracellular matrix components. *Exp. Cell Res.* **202,** 1–8.

Wang, L., Li, L., Shojaei, F., Levac, K., Cerdan, C., Menendez, P., Martin, T., Rouleau, A., and Bhatia, M. (2004). Endothelial and hematopoietic cell fate of human embryonic stem cells originates from primitive endothelium with hemangioblastic properties. *Immunity* **21,** 31–41.

Wu, X., Rabkin-Aikawa, E., Guleserian, K. J., Perry, T. E., Masuda, Y., Sutherland, F. W., Schoen, F. J., Mayer, J. E., Jr., and Bischoff, J. (2004). Tissue-engineered microvessels on three-dimensional biodegradable scaffolds using human endothelial progenitor cells. *Am. J. Physiol. Heart Circ. Physiol.* **287,** H480–H487.

Yoder, M. C., Mead, L. E., Prater, D., Krier, T. R., Mroueh, K. N., Li, F., Krasich, R., Temm, C. J., Prchal, J. T., and Ingram, D. A. (2007). Redefining endothelial progenitor cells via clonal analysis and hematopoietic stem/progenitor cell principals. *Blood* **109,** 1801–1809.

Zentilin, L., Tafuro, S., Zacchigna, S., Arsic, N., Pattarini, L., Sinigaglia, M., and Giacca, M. (2006). Bone marrow mononuclear cells are recruited to the sites of VEGF-induced neovascularization but are not incorporated into the newly formed vessels. *Blood* **107,** 3546–3554.

Adv Biochem Engin/Biotechnol (2009) 112: 209–229
DOI:10.1007/10_2008_12

Methodology for Optimal In Vitro Cell Expansion in Tissue Engineering

J.M. Melero-Martin, S. Santhalingam, and M. Al-Rubeai

Abstract Expansion of the cell population in vitro has become an essential step in the process of tissue engineering and also the systematic optimization of culture conditions is now a fundamental problem that needs to be addressed. Herein, we provide a rational methodology for searching culture conditions that optimize the acquisition of large quantities of cells following a sequential expansion process. In particular, the analysis of both seeding density and passage length was considered crucial, and their correct selection should be taken as a requisite to establish culture conditions for monolayer systems. This methodology also introduces additional considerations concerning the running cost of the expansion process. The selection of culture conditions will be a compromise between optimal cell expansion and acceptable running cost. This compromise will normally translate into an increase of passage length further away from the optimal value dictated by the growth kinetic of the cells. Finally, the importance of incorporating functional assays to validate the phenotypical and functional characteristics of the expanded cells has been highlighted. The optimization approach presented will contribute to the development of feasible large scale expansion of cells required by the tissue engineering industry.

Keywords Cell expansion, Progenitor cells, Regenerative medicine, Stem cells, Tissue engineering.

J.M. Melero-Martin
Vascular Biology Program and Department of Surgery, Children's Hospital Boston, Harvard Medical School, Boston, MA, USA

S. Santhalingam
Department of Chemical Engineering, School of Engineering, University of Birmingham, Birmingham, B15 2TT, UK

M. Al-Rubeai (✉)
School of Chemical and Bioprocess Engineering and Centre for Synthesis and Chemical Biology, University College Dublin, Belfield, Dublin 4, Ireland

Contents

1 Introduction

1.1 Tissue Engineering in Regenerative Medicine

Organs and tissues often necessitate reconstruction or replacement due to damage produced from congenital disorders, cancer, and trauma, among other conditions [1]. These defects are normally treated by either replacement with autologous tissue or by allogeneic organ transplantation. However, both approaches present important constrains: (1) autologous treatment imposes serious problems of morbidity for most tissues, and (2) there is a severe shortage of donor organs, which is worsening with aging of the world population. In addition, any of the mentioned approaches rarely replace the entire function of the original organ, and tissues used for reconstruction often lead to complications due to their inherent different functional parameters.

An alternative therapy for the repair of damaged tissue resides in the tissue engineering approach. Tissue engineering is an interdisciplinary field that applies principles and methods of engineering and the life sciences toward the development of biological substitutes that restore, maintain, and improve the function of damaged tissues and organs [2]. Such a tissue reconstitution process can be conducted either entirely in vitro or partially in vitro and then completed in vivo. Tissue engineering strategies based on autologous cells are normally initiated from a small piece of donor tissue (biopsy), from which individual cells are isolated. These cells are expanded in culture, attached to a support matrix (scaffold), and re-implanted into the host. Major advances have been achieved in this field within the past decade, resulting in the creation of functional tissues such as small diameter vascular grafts [3], heart valves [4, 5], and urinary bladder [6] among others.

1.2 Cell Sources for Tissue Engineering

Establishing a reliable source of cells is a principal priority for tissue engineers [7]. Cells used in tissue engineering may be drawn from a variety of sources, including primary tissues and cell lines. Primary tissues may be xenogeneic (from different species), allogeneic (from different members of the same species), syngeneic (from a genetically identical individual), or autologous (from the same individual). Ideally, both structural and functional tissue replacement will occur with minimal complications. Although animal cells are a possibility, ensuring that they are safe remains a concern, as does the high likelihood of their rejection by the immune system [1, 8]. Currently, the clinical use of allogeneic cells is still limited by the need for host immunosuppression. However, with the advent of techniques to render cells immunologically "transparent," the use of banked allogeneic cells may become a clinical reality [7]. An alternative cell source for bioengineering of tissues and organs is therapeutic cloning, wherein patient-specific embryonic stem cells (ESCs) can be derived from pre-implantation stage embryos produced by somatic cell nuclear transfer, therefore obtaining histocompatible cells for engraftment [9]. Stem cells derived from this source might have the potential to replace and regenerate damaged tissues; however, the mechanisms controlling their differentiation must be fully understood, and ethical issues surrounding their use must be resolved prior to their implementation in therapeutic strategies.

Until further advances allow other cell sources to become a clinical reality, autologous cells are the preferred cells to use in regenerative medicine. To acquire autologous cells, a biopsy of tissue is obtained from the host, the cells are dissociated and expanded in culture, and the expanded cells are implanted into the same host. The use of autologous cells, although it may cause an inflammatory response, avoids rejection, and thus the side effects of immunosuppressive medications can be avoided. In addition, the use of autologous adult stem cells is ethically sound and accepted worldwide [1].

1.3 In Vitro Expansion of Autologous Cells

Most adult human cells have a limited lifespan, and after repeated divisions, they eventually enter replicative senescence, a state in which they are still viable, yet no longer divide and display reduced functionality. This presents a challenge to using differentiated autologous cells as a cell source for tissue engineering. Moreover, engineered tissues must contain a sufficient amount of cells to remain functional over clinically relevant time periods [10]. Therefore, one of the major limitations of applying cell-based regenerative medicine techniques to organ replacement is the inherent difficulty of growing specific cell types in large quantities [1]. This problem affects the majority of differentiated human cells. For

example, articular chondrocytes in culture rapidly undergo dedifferentiation [11]. As a result, chondrocytes isolated from their tissue-specific extracellular matrix fail to produce cartilage matrix after extensive expansion in monolayer culture, a phenomenon that limits their availability in sufficient quantities for tissue engineering applications [12]. Similar constrains are found in the field of vascular and urinary bladder tissue engineering, where the acquisition of large quantities of endothelial [13] and urothelial [1] cells from differentiated functional tissues is enormously challenging.

To overcome this expansion limitation, researchers have been exploring alternatives to obtain sufficiently large, functional autologous cell populations for tissue engineering and regenerative medicine applications. One area of interest is the use of autologous adult stem or progenitor cells. By studying the sites for stem or progenitor cells in specific organs, as well as exploring the conditions that promote their differentiation, it may be possible to overcome the obstacles that limit cell expansion in vitro. For example, the identification of chondroprogenitor cells in the superficial zones of articular cartilages [14], has provided an alternative avenue to obtain chondrocytes that retain their ability to form cartilage after extensive expansion in culture [15, 12]. For vascular tissue engineering, the identification of endothelial progenitor cells (EPCs) in blood has offered an opportunity to noninvasively obtain large quantities of functional endothelial cells [16, 17, 18, 13]. Similar advantages are found with the identification of urothelial progenitor cells for urinary bladder tissue engineering [19]. All these studies indicated that it is possible to collect autologous cells from human patients, expand them in culture, and return them to the donor in sufficient quantities for reconstructive purposes. Major advances have been achieved within the past decade in the possible expansion of a variety of progenitor cells and adult stem cells, with specific techniques that make the use of autologous cells possible for clinical application.

One of the challenges that tissue engineers will have to address in the near future is the development of feasible large-scale cell-expansion processes. Routine tissue culturing methodologies can hardly cope with the scale of cell production required for the clinical generation of tissue-engineered products. Expansion of the cell population in vitro has become an essential step in the process of tissue engineering, and optimization of the culture conditions and expansion protocols are fundamental issues that need to be addressed. In fact, the enhanced expansion potential of stem and progenitor cells in culture opens up the possibility for more intense expansion processes that may enable the generation of large cell banks for use in regenerative medicine. The aim of this article is to provide a rational methodology for searching culture conditions that optimize the acquisition of large quantities of cells following a sequential expansion process. The proposed methodology uses mathematical expressions that relate the growth curve of the cells with expansion process parameters, and it facilitates the optimal selection of routine culture conditions irrespective of the source of autologous cells under investigation.

2 Definitions

2.1 Parameters Related to Cell Growth in a Single Passage

Several parameters can be defined concerning cell expansion in a single monolayer passage (see Fig. 1):

I_p (cells): initial cell number available at the beginning of the passage.

$X0_p$ (cell cm^{-2}): initial cell density used at inoculation.

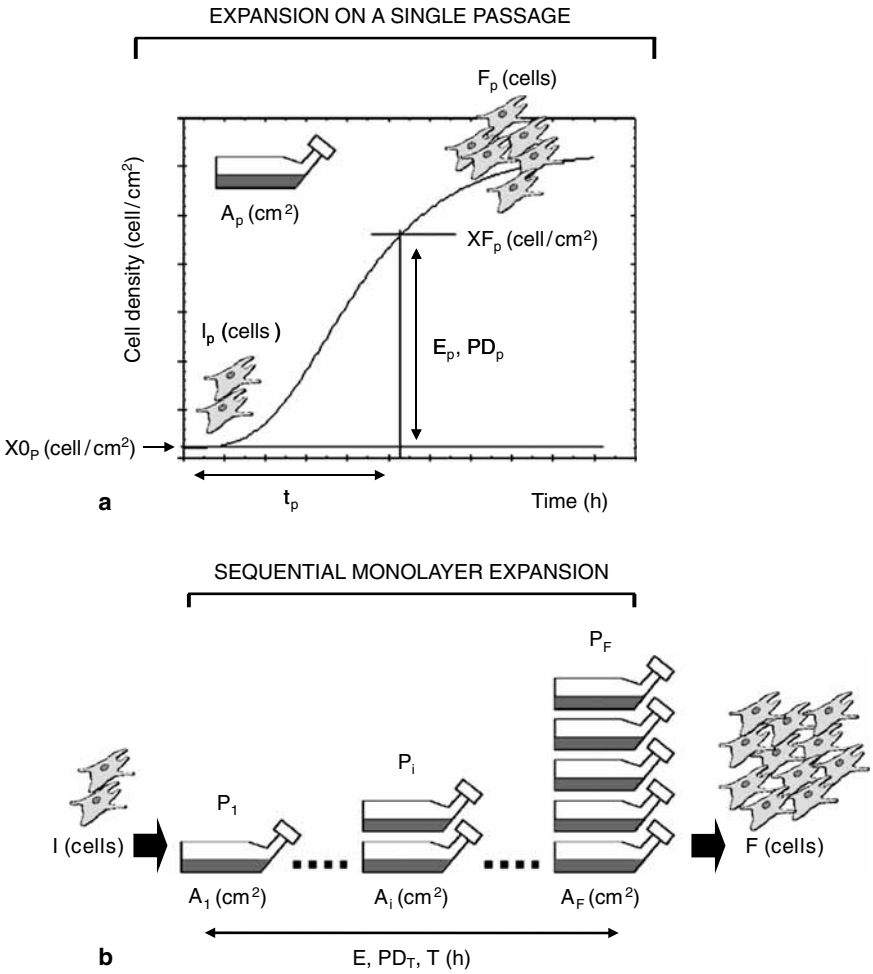

Fig. 1 Schematic diagrams of cell expansion in a monolayer. (**a**) Growth of the cell population during a single monolayer passage. (**b**) The overall expansion process is constituted by sequential monolayer expansion steps

XF_p (cell cm^{-2}): final cell density observed at the time of harvesting.

PD_p (–): passage population doubling corresponds to the number of doublings that cells undergo from inoculation to harvesting.

t_p (h): passage length corresponds to the duration of the passage, from inoculation to harvesting.

E_p (–): passage expansion factor corresponds to the factor by which the viable cell density is multiplied from inoculation to harvesting.

Given these definitions of single passage parameters, the following equations apply:

$$E_p = \frac{XF_p}{X0_p} \tag{1}$$

$$2^{PD_p} = \frac{XF_p}{X0_p} \tag{2}$$

$$E_p = 2^{PD_p} \tag{3}$$

2.2 Parameters Related to a Sequential Monolayer Expansion

Additionally, the following parameters can be defined concerning a sequential monolayer expansion process (see Fig. 1):

I (cells): initial cell number available at the beginning of the expansion process.

F (cells): final cell number available at the end of the expansion process.

PD_T (–): total population doubling corresponds to the final number of doublings that cells undergo during the expansion process.

T (h): total expansion time corresponds to the duration of the expansion process.

N (–): total number of passages that the cells undergo during the expansion process.

E (–): total expansion factor corresponds to the factor by which the viable cell density is multiplied during the expansion process.

Given these definitions of sequential expansion parameters, the following equations apply:

$$PD_T = \sum_{p=1}^{N} PD_p \tag{4}$$

$$T = \sum_{p=1}^{N} t_p \tag{5}$$

$$E = \prod_{p=1}^{N} E_p \tag{6}$$

$$2^{\mathrm{PD_T}} = \frac{F}{I} \tag{7}$$

$$E = 2^{\mathrm{PD_T}} \tag{8}$$

$$E = \frac{F}{I} \tag{9}$$

3 Determination of Growth Curves

Optimization of cell expansion relies on the analysis of cell growth curves at different culture conditions. Elaboration of detailed cell growth curves (evolution of cell density over time) is normally done in the laboratory by using small-scale experiments in which cells are plated in sufficient replicated tissue culture wells, and manually counted at intervals using a hemocytometer. This microscopy technique is limited by inter user variability, laborious and often time-consuming data collection, user fatigue, and small sampling size (i.e., a few hundred cells) [20]. There is interest in the potential benefits of replacing standard cell counting methods with an automated systems. In this regard, several direct methods to monitor cell concentration have been proposed. Such methods include optical techniques based on light absorbance and or scattering, real-time imaging, particle size analysis, and techniques to measure culture fluid density [21, 22, 23, 24]. However, most of these techniques are not applicable to monitor anchorage-dependent cell concentration and viability accurately at all the stages of the culture [25]. Alternative automated systems such as Microcyte flow cytometer [26], NucleoCounter [27], and Guava PCA are being introduced into laboratories for rapid and accurate determination of viable cell numbers. However, these automated systems are mainly designed for suspended cell cultures, and not for routine evaluations of anchorage-dependent primary cells. For these reasons, trypan blue dye exclusion assay, DNA content, MTT assay, and nuclei counting are still the most commonly utilized methods for the determination of cell density of primary cells.

Each type of primary cell presents a specific growth curve that needs to be determined using the culture conditions under evaluation. Although some authors

still use the exponential growth approach to characterize the behavior of proliferative cells in culture, this assumption is not accurate for most primary cells. The concept of exponential growth by mammalian cells in culture is based upon the apparent linearity of semi logarithmic data plots. Nevertheless, this method of graphical analysis is known to be an unreliable test of the exponential hypothesis. The question of exponential growth was re-examined more than two decades ago by using the more sensitive method of Smith plots, in which specific growth rate is plotted against time. With exponential growth, data points should fall on a horizontal straight line when specific growth rate is plotted against time, but after analyzing the growth of 125 different mammalian and avian cell lines, it was found that only 11 exhibited an exponential phase while the remaining cell lines all had nonexponential growth patterns [28]. The most common of these consisted of an initial period of growth acceleration followed by a later phase of deceleratory growth. Examples of decelerator growth kinetics can be found from very diverse cell sources, including chondroprogenitor cells isolated from the superficial zone of articular cartilages [29], and umbilical cord blood-derived endothelial progenitor cells [13]. As long as essential nutrients and cytokines are provided in sufficient amounts (achieved by adequate feeding), anchorage-dependent primary cell proliferation in culture is controlled by cell–cell contact inhibition. Since this mechanism of control is essentially density-dependent [30], cultures are characterized by a progressive generation of inhibitory contacts that ultimately lead to the appearance of the stationary phase or plateau. The kinetics of decelerating growth can be described with high accuracy by diverse equations such as Gompertz, logistic, inverse cube root and power functions [31, 32, 33]. In particular, Gompertz functions have been proposed to model the growth of a diversity of biological systems, including tumors [34, 35, 36], and normal primary cells [29]. The use of mathematical expressions can be instrumental for modeling the proliferative behavior of the cells in culture, but is not mandatory for the optimization analysis, which can be developed from appropriate experimental data.

The analysis of growth curves may seem straight forward at first examination, however, the election of an optimal growth curve requires careful analysis of the data. To illustrate this, we analyzed the growth curves of chondroprogenitor cells obtained at five different seeding densities (Fig. 2a) [29]. In this example, all culture parameters, with the exception of the seeding density, were kept constant. From Fig. 2a it can be observed how the initial cell density played a central role in the proliferation performance of the cultures, affecting both the kinetics of cell growth and the final cell density achieved. These results were expected since the proliferation of anchorage-dependent primary cells is controlled by cell–cell contact inhibition [15], a mechanism that is essentially density-dependent [30]. Therefore, it could be expected that higher seeding densities will necessarily lead to a more rapid generation of inhibitory contacts and consequently to a more rapid appearance of the stationary phase. While cultures with seeding densities of 10^5 cell cm^{-2} reached the stationary phase at day 5, the cultures with seeding density of 10^4 cell cm^{-2} required 8 days. Although higher initial cell densities had faster growth

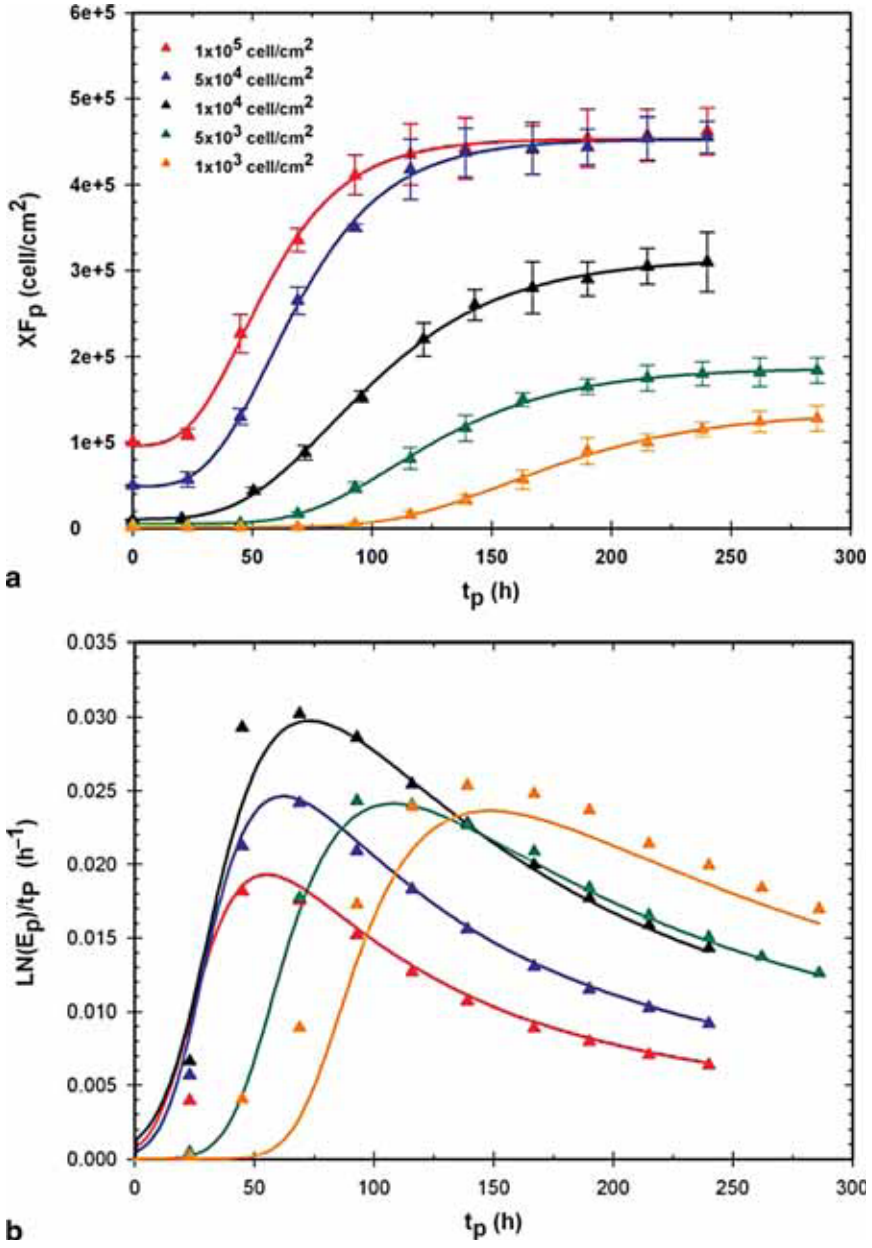

Fig. 2 Expansion of chondroprogenitor cells in a monolayer. (**a**) The effect of initial cell density on cell proliferation was evaluated at five different seeding densities corresponding to 10^5 cells cm^{-2}, 5×10^4 cells cm^{-2}, 10^4 cells cm^{-2}, 5×10^3 cells cm^{-2}, and 10^3 cells cm^{-2}. All the cultures were supplied with 0.3 ml cm^{-2} of DMEM supplemented with 40% FCS and 1 ng ml^{-1} of TGF-β1. Viable cell densities were evaluated at intervals for each of the different seeding densities tested. Each data point represents the mean of three separate cultures ±SD. (**b**) Optimization of passage length at different initial cell densities was determined by the maximum of (In $(E_p)/E_p$). This figure was adapted from [29] with permission from the editor

kinetics (shorter lag phases and sharper growth curves) attention should also be paid to the expansion factor (E_p) achieved for each seeding density. The expansion factors achieved for each of the cultures examined corresponded to 5, 9, 30, 36, and 103 as the initial cell density was increased (10^5, 5×10^4, 10^4, 5×10^3, and 10^3cell cm^{-2}, respectively). Consequently, while higher initial cell densities produced faster growth kinetics, it also imposed a lower value of the expansion factor achievable in a single passage. Moreover, since chondroprogenitor cells (and many progenitor cells) have the ability to form colonies even at very low seeding densities [14] the value of the expansion factor could be potentially improved by further reduction in the initial cell density of the cultures. The problem resides in the detrimental effect that a very low seeding density will have on the growth kinetics (and consequently on the time necessary to achieve the desired expansion factor). From the above example, it is clear that the determination of an optimal seeding density necessarily involves a compromise between the growth kinetic (i.e., time) and the expansion factor achievable, and that it cannot be easily done by simple direct observation of experimental growth curves.

4 Optimal Cell Expansion

The optimal culture conditions for cell expansion correspond to those culture conditions that would allow us to achieve the desired final cell number in the minimal time and with the minimal cost. Additionally, these optimally expanded cells need to maintain the required phenotype for their final therapeutic use. Despite the fact that the definition of optimal culture conditions is straight forward, the number of parameters affecting the growth of cells in culture is enormous and therefore their simultaneous optimization may seem like an unbearable task for most cell-culture investigators. However, from a practical stand point, the decisions that investigators need to make when culturing primary cells are often restricted to four categories: (1) media formulation and feeding strategy, (2) coating of culture plate, (3) seeding density, and (4) length of each passage (e.g., time of harvest and subculture). In fact, out of these four categories, two questions are considered essential for optimal expansion: firstly, it is necessary to determine the seeding density ($X0$). Secondly, for any selected seeding density, it is necessary to establish the value of the passage length (t_p) that makes the expansion process optimal in a serial operation. Once the methodology for optimal selection of both seeding density and passage length is established, it can be used to study the effect that different media formulations, feeding strategies, and/or coating materials have on the expansion performance of the cells under investigation.

Starting with a constant number of cells (I), the expansion optimization can be performed by maximizing the final cell number (F) for a given total expansion time (T)

$$\mathrm{Max}(F) = \mathrm{Max}(E \times I) \tag{10}$$

To ease the analysis and further develop this equation, we can distinguish between unaltered or altered growth kinetics as cells are expanded over a number of passages.

4.1 Unaltered Growth Kinetics

We can initially assume that the growth kinetic of the cells is not significantly altered during all the passages required for the expansion process. From this assumption one obtains the following equations:

$$\mathrm{PD_T} = \sum_{i=1}^{N} \mathrm{PD}_i = N \times \mathrm{PD_p} \tag{11}$$

$$T = \sum_{i=1}^{N} t_i = N \times t_\mathrm{p} \tag{12}$$

$$E = \prod_{i=1}^{N} E_i = (E_\mathrm{p})^N \tag{13}$$

Consequently, Eq. (10) can be written as:

$$\mathrm{Max}(F) = \mathrm{Max}(E \times I) = \mathrm{Max}(E_\mathrm{p})^N \tag{14}$$

$$\mathrm{Max}(F) = \mathrm{Max}(E_\mathrm{p})^N = \mathrm{Max}\left[\left(E_\mathrm{p}\right)^{\frac{T}{t_\mathrm{p}}} \right] \tag{15}$$

$$\mathrm{Max}(F) = \mathrm{Max}\left[\left(E_\mathrm{p}\right)^{\frac{T}{t_\mathrm{p}}} \right] = \mathrm{Max}\left[\frac{T}{t_\mathrm{p}} \times \ln(E_\mathrm{p}) \right] \tag{16}$$

$$\mathrm{Max}(F) = \mathrm{Max}\left[\frac{\ln(E_\mathrm{p})}{t_\mathrm{p}} \right] \tag{17}$$

Therefore, the optimal passage length (t_p) for a given initial cell number (I) and total expansion time (T) can be found by plotting ($\ln(E_\mathrm{p})/t_\mathrm{p}$) against t_p and determining the maximum.

Continuing with the example of chondroprogenitor cells at different seeding densities, and according to Eq. (17), the optimal passage length (t_p) was found by plotting $\ln(E_\mathrm{p})/t_\mathrm{p}$ against t_p and determining the maximum of the resulting curve for each of the seeding densities investigated (Fig. 2b). The optimal seeding density for

chondroprogenitor cells corresponded to 10^4 cell cm^{-2} as reflected by the maximum of the curves. In addition, the optimal passage length for this seeding density corresponded to 73 h (time at which the maximum of the curve was reached). The selection of the adequate passage length is crucial. While longer passage length will lead to higher expansion factor in a single passage (as reflected in the growth curves, Fig. 2a), it would be detrimental in a serial operation process as it would impose longer total expansion time (or lower final expansion factor if the process time is constant). Consequently, although each seeding density is associated with an optimal value of passage length, 10^4 cell cm^{-2} for seeding density with 73 h of passage length is found to be the optimal condition overall for cell expansion.

Although the analysis just presented is suitable for a single passage, the validation of the estimated seeding density and passage length during a sequential expansion relies on the veracity of the unaltered growth kinetic assumption. Only in those situations where cell growth curves remain fairly constant during passaging can the optimization analysis be reduced to a single passage. This is the case of the chondroprogenitor cell growth kinetic, which has been shown to be reasonably unaltered up to seven passages [29].

4.2 Altered Growth Kinetics

Despite that on some occasions the assumption of an unaltered growth kinetic is valid for a number of passages, in some cell types the growth kinetic varies significantly as cells are expanded in culture. One example of cells that present an altered growth kinetic in culture is endothelial progenitor cells. The identification of EPCs in blood a decade ago presented an opportunity to noninvasively obtain endothelial cells for therapeutic applications [16, 17, 18]. For example, blood-derived EPCs have been used to endothelialize small-diameter blood vessels [3], and to form functional vascular networks in vivo [37, 13, 38]. For therapeutic application, extensive expansion of EPCs in vitro is likely to be required, and therefore changes in growth kinetics over time will influence the search for optimal expansion conditions.

To illustrate this concept, an analysis of the growth curves of cord blood-derived EPCs (cbEPCs) obtained at five different passages is made (Fig. 3a) [13]. In this example, all culture parameters were kept constant. From Fig. 3a it can be observed how the passage number played a central role in the proliferation performance of the cultures, affecting both the kinetics of cell growth and the final cell density achieved. In fact, it has been reported that as cbEPCs are expanded in culture, their morphology, growth kinetics, and proliferative responses toward angiogenic factors progressively resemble those of mature microvascular endothelial cells [13]. Since cbEPC growth curves are significantly different at each passage, we cannot assume that the optimal culture conditions found for one passage will remain constant during the sequential expansion of cbEPCs. For example, optimal seeding density may be different at each passage. In addition, the optimal passage length can vary as we expand the cells.

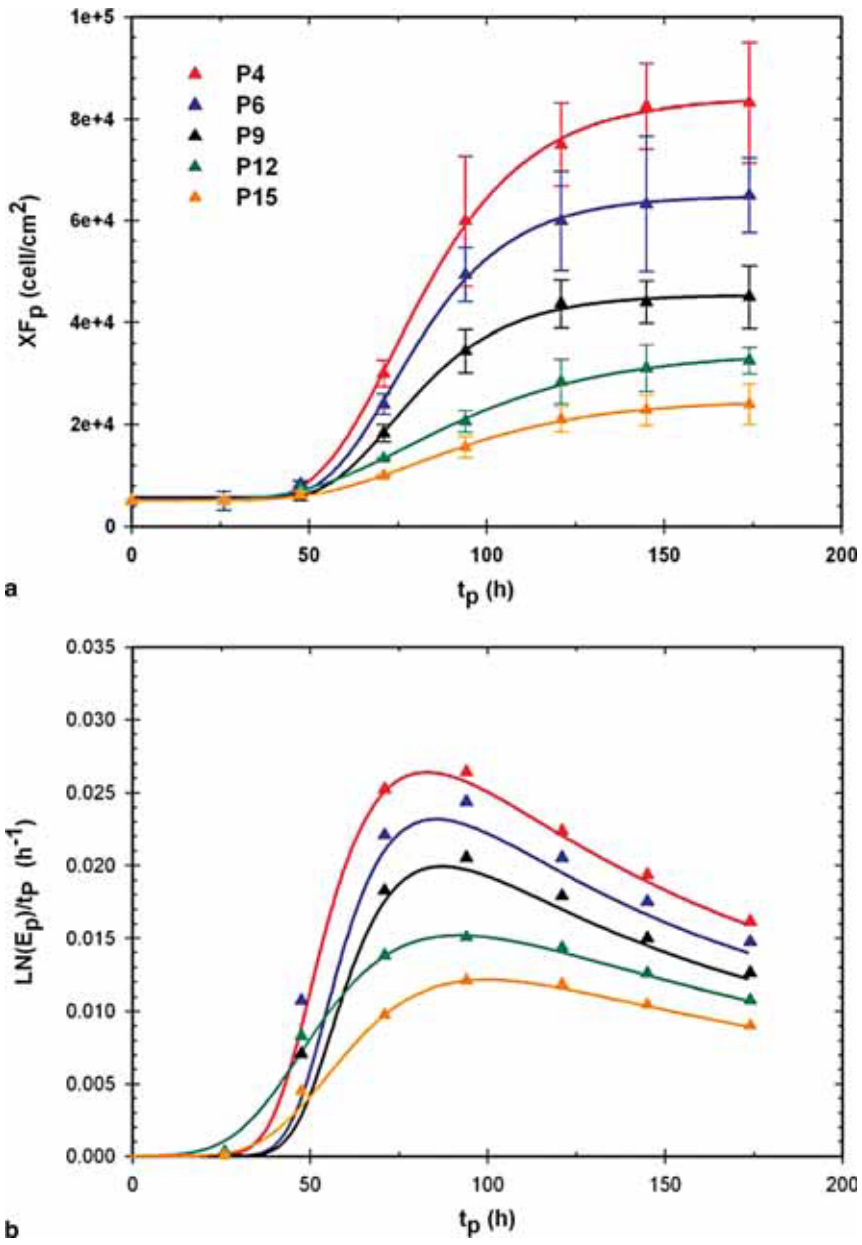

Fig. 3 Expansion of cord blood-derived endothelial progenitor cells in a monolayer. (**a**) Growth curves of cbEPCs at different passage numbers (P4, P6, P9, P12, and P15). Each data point represents the mean of three separate cultures ±SD. All the cultures were supplied with 0.3 ml cm^{-2} of EGM-2 supplemented with 20% FCS. (**b**) Optimization of passage length at different initial cell densities was determined by the maximum of (In $(E_p)/t_p$). Panel (**a**) of this figure was adapted from [13] with permission from the editor

Therefore, in cells where the growth kinetic changes (such as cbEPCs), both the optimal seeding density ($X0$) and passage length (t_p) need to be found at different passages by plotting $\ln(E_p)/t_p$ against t_p [Eq. (17)] and determining the maximum of the resulting curve for each of the seeding densities investigated. In the example depicted in Fig. 3, the seeding density of cbEPCs was kept constant (5×10^3 cell cm^{-2}), and the optimal passage length determined at different passages. The optimal passage lengths (t_p) corresponded to 83, 86, 87, 92, and 100 h for EPCs at passages 4, 6, 9, 12, and 15, respectively, illustrating the effect of prolonged culture on expansion optimization (Fig. 3b). As a result, if cbEPCs are to be grown at 5×10^3 cell cm^{-2}, the recommended passage length for optimal sequential expansion needs to be progressively increased as cells are being passaged. Importantly, this example also illustrates that even though the growth kinetic varies dramatically as cells are expanded in vitro, the resulting optimal parameters can eventually oscillate around a narrow range of values. Therefore, some cell types may present important differences in growth kinetic as they are expanded, but their optimal seeding density and/or passage length may remain essentially unchanged. However, this may not be the case for all primary cells, and as a general rule, optimal seeding density and passage length need to be found at each passage (or at least every few passages) for each type of cell under consideration.

5 Exponential Growth Kinetics

Even though most anchorage-dependent primary cells present deceleratory growth patterns, some cell lines that are routinely used by the biopharmaceutical industry proliferate following exponential growth kinetics. This is the case of CHO 320, a gamma-interferon producing cell line. Growth curves of CHO 320 in suspension cultures have been modeled with high accuracy by an exponential growth function [39], given by the following simplified version of the Monod equation [40]:

$$XF = X0 \times \exp\left(\mu \times t_p\right) \tag{18}$$

where μ (h^{-1}) corresponds to the specific growth rate, and remains essentially constant during the growth phase of the culture. The Monod equation [Eq. (18)] has been used extensively for the description of the growth of animal cells [40]. This model assumes an exponential cell growth until the amount of an essential substrate becomes limiting. This simplified version of the Monod equation does not take into consideration death rate by accumulation of toxic compounds, and therefore it can only be applied to stages of the culture where cell viability is high. The confirmation of an exponential growth pattern will have important implications for the expansion optimization of a cell line, and it will be necessarily different from that shown for primary cells with a deceleratory growth kinetic [29].

Using the exponential growth Eq. (18), the expansion factor of each passage can be estimated by (19)

$$E_p = \frac{XF}{X0} = \frac{X0 \times \exp\left(\mu \times t_p\right)}{X0} = \exp\left(\mu \times t_p\right) \tag{19}$$

and the evaluation of $(\ln(E_p)/t_p)$ results in

$$\frac{\ln(E_p)}{t_p} = \frac{\mu \times t_p}{t_p} = \mu \tag{20}$$

Therefore, determining the maximum of $(\ln(E_p)/t_p)$ in a culture system that follows a true exponential growth is equivalent to determining the maximum specific growth rate. This means that for any given initial amount of cells, the culture conditions (including seeding density) that maximize the specific growth rate of the cells will be the optimal conditions to achieve the highest number of cells in a given constant culture time. Even though this analysis may seem obvious at first examination, it is important to remember that not all mammalian cell-culture systems will lead to the same conclusion. For instance, during the evaluation of primary chondroprogenitor cells (Fig. 2) [29], the values of specific growth rate were far from constant throughout the growth period of the culture. As a result, the optimal seeding density was found to be a compromise between the growth kinetic and the expansion factor achievable (i.e., not always the highest specific growth rate corresponded to the optimal). Only when a culture follows a true exponential growth can the value of specific growth rate be taken as the sole parameter for cell expansion optimization.

In the study of CHO 320 [39], the maximum specific growth rate (and therefore optimal expansion) was found for the lowest seeding density evaluated (0.5×10^5 cell ml^{-1}). This finding led us to speculate that lowering the initial cell density beyond the optimal 0.5×10^5 cell ml^{-1} could be beneficial for the expansion process. However, this should be evaluated carefully; by lowering the seeding density of the culture, we could eventually reach a threshold seeding density that results in an inferior specific growth rate due to a very sparse distribution of the suspended cells. Also, very low initial cell densities are known to result in nonexponential growth patterns [41], and therefore the straight forward correlation between specific growth rate and optimal expansion condition will no longer be valid.

Another consequence of an exponential growth kinetic is found in the determination of optimal passage lengths. From Eq. (20), the answer to this question seems straight forward: as long as we can maintain the value of specific growth rate constant, it should not matter at what point we passage the cells. However, this statement should be looked at more carefully by taking into account additional considerations concerning the cost of the expansion process. Independently of the seeding density, the selection of the passage length will have a direct influence on the final cost of the expansion process (discussed below). Although the optimal cell expansion will be identical as long as the specific growth rate remains constant, longer values of passage length will eventually result in lower total process cost by reducing the

total number of passages required (each passage involves evident costs in labor, materials, and services). Therefore, from costing considerations, it will be beneficial to maintain the cells in culture as long as its specific growth rate remains constant. To optimize transfer times between passages (passage length) with a minimal cost, it is recommended to maintain the cells in culture until the end of the exponential growth phase.

6 Running Cost of the Expansion Process

Independently of the seeding density, the selection of the passage length will have a direct influence on the final cost of the expansion process. Although the optimal passage length will always give the desired expansion factor in a minimal process time, longer values of the passage length could eventually create a situation where the same desired expansion factor is achieved with a lower total process cost (in detriment of the process time) by reducing for example the number of passages required. To illustrate this concept, we can define the following costing parameters and equations:

C_{MPA} ($ cm^{-2}): corresponds to the cost of culture medium per unit of area necessary to carry out one single passage. For a given cell type, the concentration of medium used (expressed in ml cm^{-2}) and the cost of the medium ($ ml^{-1}) can be considered as constants, independent of the passage length. The value of C_{MPA} ($ cm^{-2}) depends directly on the number of medium changes performed during the extent of the passage. However, if the feeding strategy is constantly maintained (typically medium is replenished every 2–3 days), the value of C_{MPA} ($ cm^{-2}) can be considered as a constant for every passage.

C_{FPA} ($ cm^{-2}): corresponds to the cost of tissue culture flasks expressed per unit of area. For a given kind of tissue culture flasks, this value can be considered as a constant, independent of the passage length.

C_{XPA} ($ cm^{-2}): corresponds to the rest of the running cost of any single passage expressed per unit of area (excluding the cost considered in C_{MPA} and C_{FPA}). This cost includes concepts such as PBS buffer and trypsin-EDTA solution required for cell harvesting, labor cost, and all the other operating costs. By its own definition, it is clear that the value of this parameter depends on the length of the passage. Nevertheless, to ease the analysis, this value was considered as a constant. The reasons for such hypothesis are based on the fact that some of the costs included in this parameter are independent of the passage length (e.g., the cost of PBS buffer and trypsin-EDTA solution required for cell harvesting, and the labor cost attributed to the inoculation and cell harvesting). Taking also into consideration that C_{XPA} is added to C_{MPA} and C_{FPA} on the overall passage running cost, the hypothesis of considering C_{XPA} as a constant is reasonable.

C_{PA} ($ cm^{-2}): corresponds to the total running cost per unit of area necessary to carry out one single passage. C_{PA} can be estimated by the following equation:

$$C_{\mathrm{PA}} = C_{\mathrm{MPA}} + C_{\mathrm{FPA}} + C_{\mathrm{XPA}} \tag{21}$$

Since C_{MPA}, C_{FPA}, and C_{XPA} can be considered as constants (for given culture conditions and under the hypotheses stated before), the value of C_{PA} can also be considered as a constant.

A_i (cm^2): corresponds to culture area utilized during passage number i. For a given constant seeding density ($X0$), A_i can be expressed as:

$$A_i = \frac{I_i}{X0} \tag{22}$$

C_{Pi} (\$): corresponds to the total running cost necessary to carry out passage number i. C_{Pi} can be estimated by the following equation:

$$C_{\mathrm{Pi}} = C_{\mathrm{PA}} \cdot A_i \tag{23}$$

C (\$): corresponds to the total running cost of the expansion process. This parameter can be calculated by summing the cost of every single passage constituting the expansion process

$$C = \sum_{i=1}^{N} C_{\mathrm{Pi}} = C_{\mathrm{PA}} \sum_{i=1}^{N} A_i = \frac{C_{\mathrm{PA}}}{X0} \sum_{i=1}^{N} I_i \tag{24}$$

I_i can be expressed as a function of the expansion factors preceding passage number i as follows:

$$I_i = I_{i-1} \times E_{i-1} = I_{i-2} \times E_{i-2} \times E_{i-1} = I_{i-3} \times E_{i-3} \times E_{i-2} \times E_{i-1} = ... = I \prod_{z=1}^{i-1} E_z \tag{25}$$

Therefore, Eq. (24) can be written as:

$$C = \frac{C_{\mathrm{PA}}}{X0} \sum_{i=1}^{N} I_i = \frac{C_{\mathrm{PA}} I}{X0} \sum_{i=1}^{N} \left(\prod_{z=1}^{i-1} E_z \right) \tag{26}$$

ξ (–): corresponds to a dimensionless expression of the total running cost of the expansion process, C, and is defined by the following expression:

$$\xi = \frac{C}{\frac{C_{\mathrm{PA}} I}{X0}} \tag{27}$$

Combining Eqs. (26) and (27), the dimensionless running cost of the expansion process can be expressed as follows:

$$\xi = \sum_{i=1}^{N} \left(\prod_{z=1}^{i-1} E_z \right) \tag{28}$$

From this equation, it is clear that the running cost of the expansion process is highly influenced by the values of the expansion factors (E) achieved in each passage. In other words, the selection of the length of each passage will have a tremendous effect on the running cost of the process, and this cost will be continuously decreased as we prolong the extent of each passage. The optimal culture conditions for cell expansion (based on growth kinetic) are not necessarily the most economical ones. Although the optimal passage length will always give the desired expansion factor in a minimal process time, longer values of the passage length could lead to the same desired expansion factor with a lower total process cost (in detriment of the process time) by reducing for example the number of passages required. The selection of culture conditions will be a compromise between optimal cell expansion (growth kinetics) and acceptable running cost. This compromise will normally translate into an increase of passage length further away from the optimal value dictated by the growth kinetic of the cells. This is the case, for instance, for chondroprogenitor cells, where the selection of longer passage lengths (120 h instead of the optimal 73 h) was shown to reduce the running cost of the expansion process by more than 60% at the expense of suboptimal proliferation and process time [29].

7 Preservation of Cell Phenotype

When selecting culture conditions for optimal cell expansion, it is crucial to ensure that the expanded cell population retains the required phenotype and functional characteristics for their final therapeutic use. Therefore, any expansion optimization approach should be accompanied by assays to evaluate the preservation of functional cell phenotypes. For instance, when dealing with chondroprogenitor cells, we need to ensure that the optimal expansion conditions do not compromise their ability to differentiate and produce cartilage-like extracellular matrix. After following the methodology proposed above, the chondroprogenitor cell population was grown in pellet cultures and was able to synthesize a cartilage-like matrix that stained strongly with safranin-O, indicating the presence of sulfated proteoglycans. In addition, immunohistochemistry analysis of the pellets showed the presence of collagen type II, another cartilage marker. These results proved the ability of chondroprogenitor cells to differentiate into chondrocytes and to synthesize cartilage-like matrix after serial expansion in monolayer using optimized culture conditions, an ability that ultimately validated the selection of those optimal conditions [15, 42].

In the case of cbEPCs, the endothelial phenotype of the expanded population was confirmed up to passage 15 [13]. cbEPCs consistently expressed endothelial markers CD34, VE-cadherin, VEGF-R2, CD146, CD31, eNOS, vWF, and CD105. In addition, cbEPCs were negative for mesenchymal marker CD90 and hematopoietic markers CD45 and CD14, confirming that the cells were not contaminated with either mesenchymal or hematopoietic cells at any stage of the expansion process.

Expanded cbEPCs were also able to up-regulate leukocyte adhesion molecules E-selectin, ICAM-1, and VCAM-1 in response to the inflammatory cytokine TNF-α. This response to an inflammatory cytokine is characteristic of endothelial cells and suggests that the use of cbEPCs in vivo could also provide physiologic proinflammatory properties.

The maintenance of an appropriate phenotype (e.g., expression of cellular surface markers), although essential, may not be sufficient depending on the application, and functional assays must be performed before establishing definitive expansion culture conditions. In this regard, despite their phenotypical stability, cbEPCs have been shown to undergo cellular changes during their expansion in vitro. In particular, the migratory capacity of cbEPCs in vitro decreased over time in culture [43]. Also, it has been shown that as cbEPCs are expanded in culture, their vasculogenic ability in vivo decreases [13]. Therefore, if cbEPCs are to be used for tissue vascularization, these functional changes can either impose a limitation on the extent to which cbEPCs could be expanded in vitro prior to implantation, or redefine the conditions for their final therapeutic use. The latter was actually the case of cbEPC at high passages, where the partial loss of vasculogenic ability in vivo was compensated by increasing the number of cells seeded into the implants [13].

8 Conclusions

Here, we provide a rational methodology for searching culture conditions that optimize the acquisition of large quantities of cells following a sequential expansion process. The methodology starts with the evaluation of growth kinetics in monolayer cultures, and leads to the selection of both optimal seeding density and passage length. The mathematical elucidation for the selection of optimal culture conditions has been specifically presented for those situations where the cell population presents either unaltered or altered growth kinetics during routine passaging. Additionally, a simplified set of equations was introduced to ease the analysis of cells that grow with exponential kinetics. This methodology also introduces additional considerations concerning the running cost of the expansion process, and shows that the selection of culture conditions should be a compromise between optimal cell expansion and acceptable running cost. This compromise will normally translate into an increase of passage length further away from the optimal value dictated by the growth kinetic of the cells. Finally, the importance of incorporating functional assays to validate the phenotypical and functional characteristics of the expanded cells has been highlighted. The optimization approach presented is expected to contribute to the development of feasible large-scale expansion of cells required by the tissue engineering industry.

Acknowledgments Part of this research was supported by funding from the US Army Medical Research and Material Command (W81XWH-05-1-0115).

References

1. Eberli D, Atala A (2006) Tissue engineering using adult stem cells. Methods Enzymol 420: 287–302.
2. Langer R, Vacanti JP (1993) Tissue engineering. Science 260 (5110): 920–926.
3. Kaushal S, Amiel GE, Guleserian KJ, Shapira OM, Perry T, Sutherland FW, Rabkin E, Moran AM, Schoen FJ, Atala A, et al. (2001) Functional small-diameter neovessels created using endothelial progenitor cells expanded ex vivo. Nat Med 7(9): 1035–1040.
4. Hoerstrup SP, Sodian R, Daebritz S, Wang J, Bacha EA, Martin DP, Moran AM, Guleserian KJ, Sperling JS, Kaushal S, et al. (2000) Functional living trileaflet heart valves grown in vitro. Circulation 102 (19 Suppl 3): III44–III49.
5. Sutherland FW, Perry TE, Yu Y, Sherwood MC, Rabkin E, Masuda Y, Garcia GA, McLellan DL, Engelmayr GC, Jr, Sacks MS, et al. (2005) From stem cells to viable autologous semilunar heart valve. Circulation 111 (21): 2783–2791.
6. Oberpenning F, Meng J, Yoo JJ, Atala A (1999) De novo reconstitution of a functional mammalian urinary bladder by tissue engineering. Nat Biotechnol 17 (2): 149–155.
7. Vacanti JP, Langer R (1999) Tissue engineering: the design and fabrication of living replacement devices for surgical reconstruction and transplantation. Lancet 354 (Suppl 1): SI32–SI34.
8. Langer RS, Vacanti JP (1999) Tissue engineering: the challenges ahead. Sci Am 280 (4): 86–89.
9. Han Z, Vandevoort CA, Latham KE (2007) Therapeutic cloning: status and prospects. Curr Opin Mol Ther 9 (4): 392–397.
10. Petersen T, Niklason L (2007) Cellular lifespan and regenerative medicine. Biomaterials 28 (26): 3751–3756.
11. Holtzer H, Abbott J, Lash J, Holtzer A (1960) The loss of phenotypic traits by differentiated cells in vitro, I. Dedifferentiation of cartilage cells. Proc Natl Acad Sci U S A 46 (4): 1533–1542.
12. Melero-Martin JM, Al-Rubeai M (2007) In vitro expansion of chondrocytes. In: Ashammakhi N, Reis R, Chiellini E (eds.) Topics in tissue engineering, vol 3, Chap 2. University of Oulu, Finland, pp.1–37.
13. Melero-Martin JM, Khan ZA, Picard A, Wu X, Paruchuri S, Bischoff J (2007) In vivo vasculogenic potential of human blood-derived endothelial progenitor cells. Blood 109 (11): 4761–4768.
14. Dowthwaite GP, Bishop JC, Redman SN, Khan IM, Rooney P, Evans DJ, Haughton L, Bayram Z, Boyer S, Thomson B, et al.(2004) The surface of articular cartilage contains a progenitor cell population. J Cell Sci 117 (Pt 6): 889–897.
15. Martin JM, Smith M, Al-Rubeai M (2005) Cryopreservation and in vitro expansion of chondroprogenitor cells isolated from the superficial zone of articular cartilage. Biotechnol Prog 21 (1): 168–177.
16. Asahara T, Murohara T, Sullivan A, Silver M, van der Zee R, Li T, Witzenbichler B, Schatteman G, Isner JM (1997) Isolation of putative progenitor endothelial cells for angiogenesis. Science 275 (5302): 964–967.
17. Ingram DA, Mead LE, Tanaka H, Meade V, Fenoglio A, Mortell K, Pollok K, Ferkowicz MJ, Gilley D, Yoder MC (2004) Identification of a novel hierarchy of endothelial progenitor cells using human peripheral and umbilical cord blood. Blood 104 (9): 2752–2760.
18. Lin Y, Weisdorf DJ, Solovey A, Hebbel RP (2000) Origins of circulating endothelial cells and endothelial outgrowth from blood. J Clin Invest 105 (1): 71–77.
19. Yoo JJ, Meng J, Oberpenning F, Atala A (1998) Bladder augmentation using allogenic bladder submucosa seeded with cells. Urology 51 (2): 221–225.
20. Nielson LK, Smyth GK, Grrenfield PF (1991) Hemocytometer cell count distributions: implication of non poison behaviour. Biotechnol Prog 7: 560–563
21. Kell DB, Markx GH, Davey CL, Todd RW (1990) Real-time monitoring of cellular biomass: methods and applications. Trends Anal Chem 9: 190–194.
22. Konstantinov K, Chuppa S, Sajan E, Tsai Y, Yoon S, Golini F (1994) Real-time biomass-concentration monitoring in animal-cell cultures. Trends Biotechnol 12 (8): 324–333.

23. Olsson L, Nielsen J (1997) On-line and in situ monitoring of biomass in submerged cultivations. Trends Biotechnol 15: 517–522.
24. Sonnleitner B, Locher G, Fiechter A (1992) Biomass determination. J Biotechnol 25 (1–2): 5–22
25. Ducommun P, Ruffieux P-A, Furter M-P, Marison I, von Stockar U (2000) A new method for on-line measurement of the volumetric oxygen uptake rate in membrane aerated animal cell cultures. J Biotechnol 78 (2): 139–147.
26. Harding CL, Lloyd DR, McFarlane CM, Al-Rubeai M (2000) Using the Microcyte flow cytometer to monitor cell number, viability, and apoptosis in mammalian cell culture. Biotechnol Prog 16 (5): 800–802.
27. Shah D, Naciri M, Clee P, al-Rubeai M (2006) NucleoCounter – an efficient technique for the determination of cell number and viability in animal cell culture processes. Cytotechnology 51: 39–44.
28. Skehan P, Friedman SJ (1984) Non-exponential growth by mammalian cells in culture. 17 (4): 335–343.
29. Melero-Martin JM, Dowling MA, Smith M, Al-Rubeai M (2006b) Optimal in-vitro expansion of chondroprogenitor cells in monolayer culture. Biotechnol Bioeng 93 (3): 519–533.
30. Dietrich C, Wallenfang K, Oesch F, Wieser R (1997) Differences in the mechanisms of growth control in contact-inhibited and serum-deprived human fibroblasts. 15 (22): 2743–2747.
31. Buchanan RL, Whiting RC, Damert WC. (1997) When is simple good enough: a comparison of the Gompertz, Baranyi, and three-phase linear models for fitting bacterial growth curves. Food Microbiol 14: 613–626.
32. Deakin MA (1970) Gompertz curves, allometry and embryogenesis. Bull Math Biophys 32 (3): 445–452.
33. Skehan P, Friedman SJ (1982) Deceleratory growth by a rat glial tumor line in culture. 42 (5): 1636–1640.
34. Heegaard S, Spang-Thomsen M, Prause JU (2003) Establishment and characterization of human uveal malignant melanoma xenografts in nude mice. Melanoma Res 13 (3): 247–251.
35. Lloyd HH (1975) Estimation of tumor cell kill from Gompertz growth curves. Cancer Chemother Rep 59 (2 Pt 1): 267–277.
36. Spratt JA, von Fournier D, Spratt JS, Weber EE (1993) Decelerating growth and human breast cancer. Cancer 71 (6): 2013–2019.
37. Au P, Daheron LM, Duda DG, Cohen KS, Tyrrell JA, Lanning RM, Fukumura D, Scadden DT, Jain RK (2008) Differential in vivo potential of endothelial progenitor cells from human umbilical cord blood and adult peripheral blood to form functional long-lasting vessels. Blood 111 (3): 1302–1305.
38. Yoder MC, Mead LE, Prater D, Krier TR, Mroueh KN, Li F, Krasich R, Temm CJ, Prchal JT, Ingram DA (2007) Redefining endothelial progenitor cells via clonal analysis and hematopoietic stem/progenitor cell principals. Blood 109 (5): 1801–1809.
39. Santhalingam S (2007) Monitoring, optimisation and expansion issues of CHO cells producing gamma interferon in serum-supplemented and serum-free cultures [Ph.D. thesis]. University of Birmingham, Birmingham, UK.
40. Fox SR, Patel UA, Yap MG, Wang DI (2004) Maximizing interferon-gamma production by Chinese hamster ovary cells through temperature shift optimization: experimental and modeling. Biotechnol Bioeng 85 (2): 177–184.
41. Harada JJ, Porter CW, Morris DR (1981) Induction of polyamine limitation in Chinese hamster ovary cells by alpha-methylornithine. J Cell Physiol 107 (3): 413–426.
42. Melero-Martin JM, Dowling MA, Smith M, Al-Rubeai M (2006a) Expansion of chondroprogenitor cells on macroporous microcarriers as an alternative to conventional monolayer systems. Biomaterials 27 (15): 2970–2979.
43. Khan ZA, Melero-Martin JM, Wu X, Paruchuri S, Boscolo E, Mulliken JB, Bischoff J (2006) Endothelial progenitor cells from infantile hemangioma and umbilical cord blood display unique cellular responses to endostatin. Blood 108 (3): 915–921.